Structural and magnetic properties of ultrathin Fe_3O_4 films: cation- and lattice-site-selective studies by synchrotron radiation-based techniques

Dissertation

zur Erlangung des Grades Doktor der Naturwissenschaft (Dr. rer. nat.)
dem Fachbereich Physik der Universität Osnabrück
vorgelegt von

Tobias Pohlmann, M.Sc.

Osnabrück, Februar 2021

Examiners:

Prof. Dr. Joachim Wollschläger
Dr. Florian Bertram

Contents

1. Introduction

The iron oxide magnetite, Fe_3O_4, is often regarded as attractive for utilization as non-toxic nanoparticles in medicine [1,2] or for catalysis [3,4]. It is a ferrimagnetic half-metal [5,6], which means that at the Fermi energy, all its electrons have the same spin state – denoted spin-up in the following. Because of this property, it has been a long-standing candidate to serve as a source for spin-polarized currents for all-oxide thin-film spintronic devices [7–12].

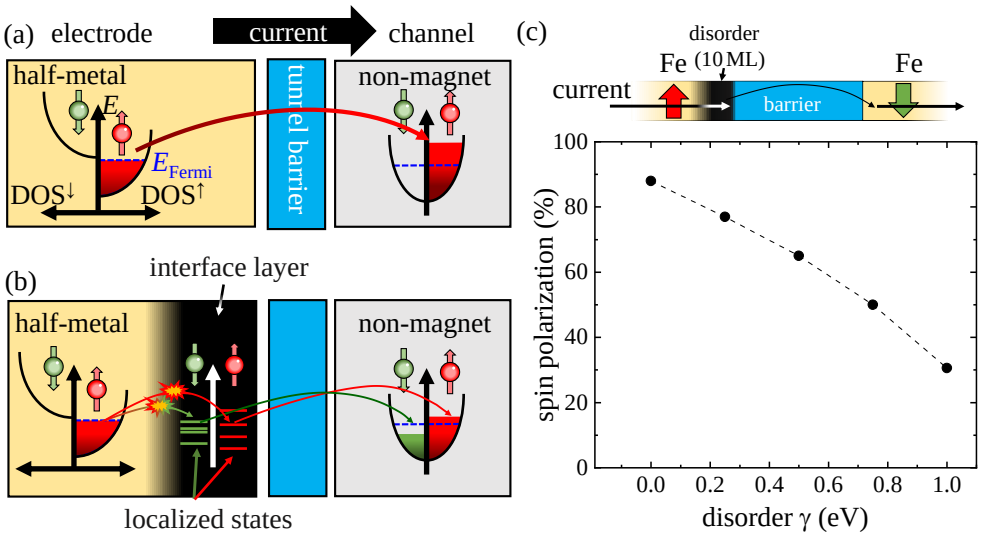

Fig. 1.1: (a) Sketch of the concept of spin injection, reproduced after Ref. [13]. A half-metal has only spin-up states at the Fermi energy. When the spin-polarized electrons enter a non-magnetic material across a tunnel barrier, their spin is preserved and a non-equilibrium spin accumulation develops in the non-magnet. (b) If a interface layer is present, electrons from the half-metallic band scatter into non-polarized interface states, from where they tunnel into the non-magnet. (c) Simulation of 10 disordered monolayers at one interface in a Fe/insulator/Fe junction. The tunneling spin polarization rapidly drops with increasing disorder strength γ. Taken from Ref. [14].

One of the key tasks of spintronics is *spin injection*, the generation of an accumulation of spin-polarized electrons in a non-magnetic channel material [13,15,16]. The most prevalent way to accomplish electric spin injection is spin-dependent tunneling from ferromagnets, which utilizes the fact that in a tunneling process, the spin polarization is preserved [10]. It is easy to see that half-metals are particularly suitable spin injection materials, because in a half-metal the electrons that contribute to the transport are 100% spin-polarized. This is illustrated in Fig. 1.1(a). In the half-metal, there is only density of states (DOS) available for spin-up states, and if a electric current is driven from the half-metal into the non-magnet across an insulating tunnel barrier, the spin polarization is translated into the non-magnet.

However, in the early 2000s, when Fe_3O_4's performance was tested in magnetic tunnel junctions, the results were disappointing, as magnetite proved to be more than 15 times less efficient in magnetic tunnel junctions than other half-metals such as $La_{0.67}Sr_{0.33}MnO_3$ [12, 14, 17–19]. The reason for this poor performance is not yet clear – however, it was speculated that the culprit might be the interfaces [17]. Spin dependent-tunneling is extremely sensitive to disorder at the ferromagnet-insulator interface, because spin-injection relies on the fact that the electrons tunnel from the spin-polarized bands of the ferromagnet directly into the non-magnet, so that their spin is preserved [20]. However, if non-magnetic interface states are present, this might be undermined, as sketched in Fig. 1.1(b). If electrons go through a non-spin-preserving scattering process into the disordered interface states, they tunnel into the channel material from these non-magnetic interface states, resulting in a reduced spin accumulation in the channel material. As an illustration, Tsymbal et al. simulated the disorder at the interface of a Fe/insulator/Fe junction [14], shown in Fig. 1.1(c). The on-site atomic energy of Fe was randomly varied with a disorder strength γ in a range of 10 monolayers at the interface, resulting in a rapid drop of the tunneling spin polarization with the disorder strength.

In the early 2010s, the formation of 2–3 monolayers of iron-deficient wüstite ($Fe_{1-\delta}O$) was observed at the Fe_3O_4/MgO(001) and later on the Fe_3O_4/$SrTiO_3$(001) interface [21, 22], offering a potential explanation of the poor tunneling spin-polarization of Fe_3O_4. However, the exact structure and the – for spintronic purposes arguably more important – magnetic properties of these modifications of the Fe_3O_4/MgO(001) and Fe_3O_4/$SrTiO_3$(001) interfaces, are still elusive. The reason is that it can be very difficult to obtain information on them, because interface and surface modifications can potentially be restricted to layers as thin as a single atomic layer. This is particularly true for the mixed-valence oxide Fe_3O_4, because it requires a way to distinguish between Fe^{2+}_{oct}, Fe^{3+}_{oct} and Fe^{3+}_{tet} cations, which only differ by a single elementary charge or their oxygen coordination.

For this reason, this work is dedicated to utilize a set of novel techniques in order to gain access to the chemical, structural and magnetic properties of the surface and interface of ultrathin Fe_3O_4 films grown by reactive molecular beam epitaxy (RMBE). Before the results are presented, first the theoretical background of the concepts and methods is given in Chap. 2. Chapter 3 introduces the materials important for this work, including the different iron oxide phases, the substrate materials MgO and $SrTiO_3$, as well as the antiferromagnetic NiO, which is often considered as an exchange bias partner for Fe_3O_4 in magnetic tunnel junctions [17, 23]. All experiments presented in this work have been performed at synchrotron radiation sources; for this reason, Chap. 4 explains the concept of these sources along with the experimental setups and analysis techniques used.

The results are organized in Chaps. 5-7. In Chap. 5, the growth dynamics of Fe_3O_4 films is studied, with the goal to observe the temporal evolution of their structure and electronic structure while the films are deposited. To this end, time-resolved high-energy x-ray diffraction (tr-HEXRD) and time-resolved hard x-ray photoelectron spectroscopy (tr-HAXPES) are used. In order to enable these measurements, a custom-designed ultra-high vacuum (UHV) chamber was constructed which allows to simultaneously deposit the Fe_3O_4 films and collect diffraction data or photoelectron spectra. This way, it is possible to monitor the structural and chemical properties of Fe_3O_4/MgO(001), Fe_3O_4/NiO/MgO(001) and Fe_3O_4/$SrTiO_3$(001) thin films during the growth process.

The second technique introduced in this work exploits the magnetic contrast between the

three cation species to obtain cation- and lattice-site-selective magnetic depth profiles of Fe_3O_4, granting access to the depth distribution of the individual cation species throughout the film. This is achieved by analyzing the x-ray magnetic dichroism (XMCD) spectrum of Fe_3O_4 by means of charge-transfer multiplet (CTM) calculations in order to disentangle the overlapping spectra of the individual cations. Using this information, x-ray resonant magnetic reflectivity (XRMR) curves are recorded at the three x-ray energies with the highest contributions of one respective cation species, allowing conclusions about their depth distribution and magnetization. This technique is used in Chap. 6 in order to resolve the surface composition of Fe_3O_4/MgO(001) films, and in Chap. 7 to investigate the Fe_3O_4/NiO/MgO(001) and the Fe_3O_4/MgO(001) interfaces.

2. Background and methods

In this chapter, the theoretical background and methods necessary to understand this work are introduced. The main focus of this thesis is the cation distribution in thin films of iron oxides, and among those, primarily magnetite (Fe_3O_4). Therefore, as a start, the base framework for the description of crystals, thin film growth and magnetism are presented in the Secs. 2.1 to 2.3, as well as experimental methods to access their crystalline and cation order in the Secs. 2.4 to 2.7. These explanations will be held closely to the example of magnetite, since they will be mainly applied to this specific material.

Most methods used in this work are synchrotron-based, and include x-ray diffraction techniques, which are sensitive to the periodic structure of crystals, x-ray reflectometry, sensitive to the electron density and film thicknesses of the samples, and x-ray spectroscopy, which is sensitive to the electronic structure, magnetic properties and chemical composition. In Sec. 2.4, first the spectroscopic techniques will be discussed. These include x-ray photoelectron spectroscopy (XPS), x-ray absorption spectroscopy (XAS) and x-ray magnetic dichroism (XMCD). Additionally, charge-transfer multiplet (CTM) theory will be explained in detail, which can be used to describe XPS, XAS and XMCD spectra. After that, x-ray reflectivity (XRR) will be introduced in Sec. 2.5, followed up in Sec. 2.6 by XRMR, which is a resonant reflectometry technique combining reflectivity and magnetic dichroism. Finally, x-ray diffraction (XRD) will be presented in Sec. 2.7.

The part about the description of crystals uses the definitions in Ref. [24], and the basic information about thin film growth can be found in Ref. [25]. The basic magnetic definitions are given here according to Refs. [24, 26]. The spectroscopy part mostly follows Refs. [27–29]. The presentation of XRMR is oriented at Ref. [30], and XRR and XRD at Ref. [31]. The section about diffraction on thin films is taken from Ref. [32].

2.1. Description of crystals

Crystals consist of a strictly periodic arrangement of atoms, which means that even infinitely large crystals can be described by, first, describing the rules of their periodicity – done so by the concept of *Bravais lattices* – and, second, describing the entity that is periodically repeated in space: a finite, and often even small, group of atoms called the *basis*.

2.1.1. Lattices

The lattice is an infinite group of points in the three-dimensional space. At each point, a set of atoms – the basis – can be located, so that a crystal is formed. The lattice can be mathematically described by choosing three lattice vectors $\mathbf{a}, \mathbf{b}, \mathbf{c}$, so that every point on the

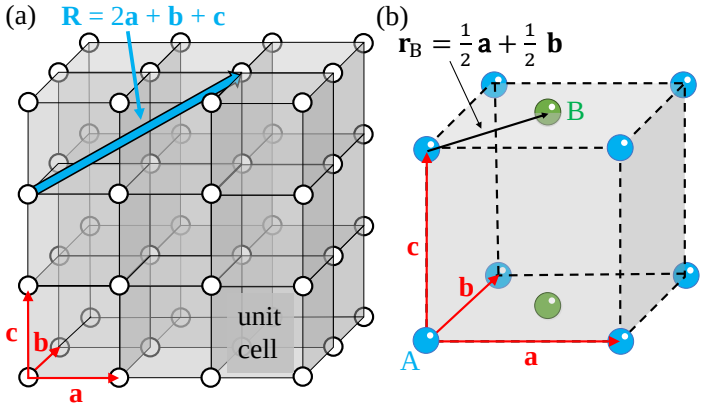

Fig. 2.1: (a) Illustration of a cubic lattice. White points are lattice points, grey cubes indicate unit cells. Red arrows $\mathbf{a}$, $\mathbf{b}$ and $\mathbf{c}$ are the lattice vectors, the blue arrow is an example for a translational vector $\mathbf{R}$. (b) Close-up of a single unit cell. A and B are the basis atoms, $\mathbf{r}_B$ is the basis vector of B.

lattice can be reached by a linear combination with integer parameters u, v, w

$$\mathbf{R} = u \cdot \mathbf{a} + v \cdot \mathbf{b} + w \cdot \mathbf{c} \quad \text{with} \quad u, v, w \in \mathbb{Z} \quad . \tag{2.1}$$

By choosing a set of integer parameters u, v, w and constructing a vector $\mathbf{R}$ by this rule, every lattice point and only lattice points are reached, and the symmetry properties of a lattice are determined by choosing appropriate lattice vectors $\mathbf{a}, \mathbf{b}, \mathbf{c}$. For example, all crystals discussed in this work can be described by cubic lattices. An illustration of a cubic lattice is given in Fig. 2.1(a). A simple cubic (sc) lattice can be described by the lattice vectors

$$\mathbf{a}_{\text{sc}} = a \cdot \begin{pmatrix} 1 \\ 0 \\ 0 \end{pmatrix}, \quad \mathbf{b}_{\text{sc}} = a \cdot \begin{pmatrix} 0 \\ 1 \\ 0 \end{pmatrix}, \quad \mathbf{c}_{\text{sc}} = a \cdot \begin{pmatrix} 0 \\ 0 \\ 1 \end{pmatrix} \quad , \tag{2.2}$$

a being the *lattice constant*, the characteristic length of the lattice. Since the three lattice vectors have all the same length and enclose a 90° angle to each other, the lattice can be thought of consisting of cube-shaped cells, with one lattice point at each corner. This cell is called the *unit cell* of the cubic lattice.

2.1.2. Bravais lattices

A lattice is defined by the symmetry operations that can be used on it to convert it into itself. For instance, cubic lattices are invariant to rotations about 90° around the 3 axes given by the lattice vectors. In addition to rotations, mirror and inversion are symmetry operations to be considered. In three dimensions, there exist 14 lattice types that can be distinguished by their symmetries this way – they are called *Bravais lattices*. They are classified into 7 crystal systems, which can be represented by a parallelepiped with 3 edge lengths a, b and c and the angles α, β and γ between them. Each crystal system can occur in the 4 centering types *primitive, base-centered, body-centered* and *face-centered*. Some combinations of crystal systems and centering types can be shown to be equivalent, so that only the 14 independent Bravais lattices in Tab. 2.1 are left. By picking one Bravais lattice and a suitable basis, each three-dimensional crystal can be represented.

system	type	properties
triclinic	1. primitive	$a \neq b \neq c$ $\alpha \neq \gamma \neq \beta$
monoclinic	2. primitive 3. base-centered	$a \neq b \neq c$ $\alpha = \gamma = 90° \neq \beta$
orthorhombic	4. primitive 5. body-centered 6. face-centered 7. base-centered	$a \neq b \neq c$ $\alpha = \gamma = \beta = 90°$
tetragonal	8. primitive 9. body-centered	$a = b \neq c$ $\alpha = \gamma = \beta = 90°$
cubic	10. primitive 11. body-centered 12. face-centered	$a = b = c$ $\alpha = \gamma = \beta = 90°$
trigonal	13. primitive	$a = b = c$ $\alpha = \gamma = \beta \neq 90°$
hexagonal	14. primitive	$a = b \neq c$ $\alpha = \beta = 90°,\ \gamma = 120°$

Tab. 2.1: The 14 Bravais lattices in three dimensions. Adapted from Ref. [24].

2.1.3. Basis

Besides the lattice, a basis is needed to describe a crystal. It is convenient to use the same vectors $\mathbf{a}, \mathbf{b}, \mathbf{c}$ to construct a vector $\mathbf{r}_j$ that points from a lattice point to the center of the basis atom j. For this, a set of parameters x_j, y_j, z_j is needed with

$$\mathbf{r_j} = x_j\mathbf{a} + y_j\mathbf{b} + z_j\mathbf{c} \quad \text{with} \quad 0 \leq x_j, y_j, z_j \leq 1 \quad . \tag{2.3}$$

This way, for a given lattice, a basis atom position $\mathbf{r}_j$ can be indexed by the indices $B_j = (x_j, y_j, z_j)$. In the simplest case, a basis may be a single atom sitting on a lattice point, described by $B_j = (0, 0, 0)$. Another example is illustrated in Fig. 2.1(b). It shows a single unit cell of the simple cubic lattice, with one atom A sitting on the lattice point, and a different atom B sitting in the center of one face of the cube. This basis can be described by the indices $B_\mathrm{A} = (0, 0, 0)$ and $B_\mathrm{B} = (\frac{1}{2}, \frac{1}{2}, 0)$, resulting in position vectors $\mathbf{r}_\mathrm{A} = \mathbf{0}$ and $\mathbf{r}_\mathrm{B} = \frac{1}{2}\mathbf{a}+\frac{1}{2}\mathbf{b}$.

2.1.4. Unit cells

The unit cell is an element of the crystal that can be infinitely repeated to construct the complete crystal. For instance, for the class of cubic lattices important for this work, the most convenient and conventional unit cell is the cube spanned by $\mathbf{a}_\mathrm{sc}, \mathbf{b}_\mathrm{sc}, \mathbf{c}_\mathrm{sc}$, shown in Fig. 2.1(b). It contains the basis atoms of the crystal and reflects the cubic symmetry of the lattice, and by repeating this cube face to face as in Fig. 2.1(a), it forms the crystal. For this reason, it is usually sufficient to show the unit cell of a crystal in order to discuss its properties.

There are many possible choices for a unit cell for each given lattice; the defining requirements of a unit cell are that it needs to contain at least a single lattice point, and reflect the symmetry of the lattice.

2.1.5. Directions and planes

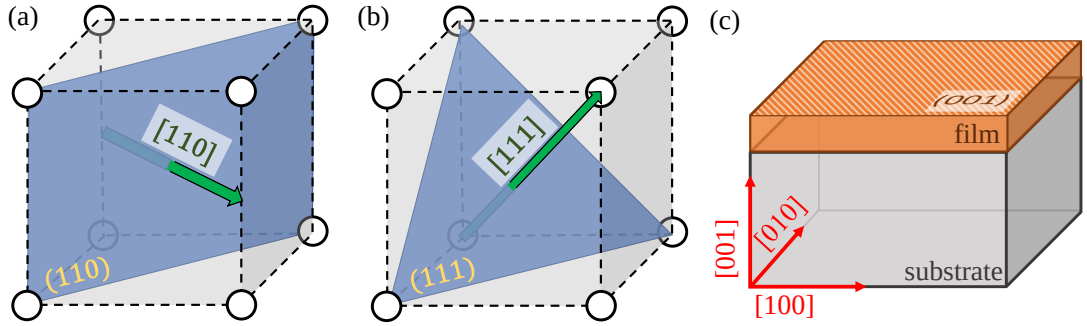

Fig. 2.2: (a) (110) plane of a simple cubic lattice, together with its normal vector [110]. (b) (111) plane of a simple cubic lattice, together with its normal vector [110]. (c) Illustration of the conventional coordinate system for a thin film, with the growth direction being along [001].

It is often necessary to address directions in crystals. This is done in terms of the lattice vectors **a**, **b**, **c**. For instance, the direction parallel to **a** is given by a triplet [100], because it has one component parallel to **a**, and 0 components parallel to **b** and **c**. Two other examples can be found in Figs. 2.2(a),(b). In Fig. 2.2(a), the green arrow has one component along **a** and one along **b**, and is thus denoted as the [110] direction. In Fig. 2.2(b), the green arrow has one component along all three lattice vectors, and thus points into the [111] direction. Following this logic, there would be many equivalent notations for the same direction. For instance, [111] and [222] point into the same direction. Therefore, conventionally they are given by the smallest set of integer indices $[u, v, w]$ that points into the desired direction. They are noted down in square brackets.

Another useful concept is that of *lattice planes*, describing two-dimensional planes in a crystal, which is particularly important when discussing actually two-dimensional entities such as surfaces and interfaces. Lattice planes are denoted by the *Miller indices* (HKL), indicated by round brackets. The general definition of Miller indices for arbitrary lattice types can be found in textbooks (for instance Refs. [24, 33]). However, since this thesis is only concerned with cubic lattices, we can use a much simpler definition: in cubic lattices, the plane described by the Miller indices (HKL) is always the plane orthogonal to the direction $[HKL]$. This is again illustrated in Figs. 2.2(a),(b), where the blue planes represent the (110) and the (111) planes, respectively. The corresponding direction vectors are the surface normals of these planes.

Many lattice planes and directions are equivalent to each other, depending on the symmetry of the lattice. For instance, for an infinite cubic lattice, all directions along edges of the cubes are equivalent (i.e., $[100] \equiv [010] \equiv [001]$), and so are all planes incorporating the cube's faces (i.e.,$(100) \equiv (010) \equiv (001)$). However, while lattices are conceptually infinite, real crystals are not. Particularly, this thesis studies ultrathin films, which have thicknesses of only a few

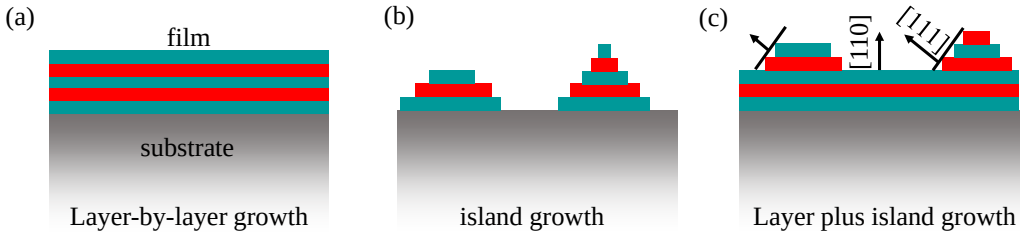

Fig. 2.3: Illustrations of the three major growth modes, (a) layer-by-layer, (b) island and (c) layer-plus-island growth. Black arrows in (c) indicate crystal directions for the example of a Fe_3O_4/MgO(110) film.

nanometres, grown on substrates with lateral sizes of several millimeters. This is sketched in Fig. 2.2(c). If the growth direction is parallel to one of the edges of the cube, it becomes desirable to differentiate between the lattice directions along the very large lateral sizes and the lattice direction along the finite thickness. Conventionally, the z-axis is chosen as the latter direction, so that the [001] direction points along the growth direction, and the surface of the film lies in the (001) plane.

2.2. Thin film growth

In this work, all samples are crystalline ultrathin films that have been grown by evaporating transition metals into a molecular beam directed onto a substrate. The crystal structure of the substrate serves as a template for the deposited material to form crystalline layers as well. This process is known as *epitaxy*. Upon impact on the substrate surface, the atoms engage in four main processes: adsorption, desorption, surface diffusion and nucleation. Their rates depend on the temperature of the substrate, the kinetic energy of the atoms arriving on the substrate and the structural details of the substrate and the emergent film. The substrate offers an attractive potential to the atoms from the beam. Due to their high kinetic energy $k_\mathrm{B}T_\mathrm{source}$ from the evaporation source, they might scatter and leave again into the gas phase, or they will thermalize with the substrate and adsorb, and subsequently diffuse across its surface, where the atoms are left with two options: The heat and momentum reservoir represented by the surface might supply them with enough energy to desorb again, or, as the number of adsorbed atoms on the surface becomes large, they will form clusters and nucleate, eventually leading to the formation of a crystalline film [25]. High substrate temperature allows an increased atom mobility, which usually results in a higher ordered films, since the atoms only settle for energetically very favorable sites. In turn, a very hot substrate may also result in a high desorption rate, making the deposition process inefficient [25]. Another effect triggered by high temperature is interdiffusion between film and substrate: despite the fact that the diffusion of substrate atoms is low compared to the adatoms, as the former are already bound in a stable crystal, sometimes an intermixed phase of substrate and film material is similarly or even more stable than the two distinct phases. In that case, high substrate temperatures can facilitate the interdiffusion of film and substrate atoms, which may [34,35] or may not [36] be desired.

When the film is deposited, three thermodynamic energy terms determine the mode of the growth: the free energy of the substrate surface γ_sub, the free energy of the substrate-film

interface γ_{inter} and the free energy of the film surface γ_{film}. In this picture, the free energy contribution from the crystallinity of the film is still neglected. If the free energy of the substrate is bigger than the sum of the interface and the film surface energy,

$$\gamma_{\text{film}} + \gamma_{\text{inter}} < \gamma_{\text{sub}} \quad , \tag{2.4}$$

it is energetically favorable to minimize the substrate surface area by covering it up, and the film grows in layer-by-layer mode. In this growth mode, the film closes each atomic layer before growing the next, illustrated in Fig. 2.3(a). It is also known as Frank-van-der-Merwe mode.

In the opposite case, when

$$\gamma_{\text{film}} + \gamma_{\text{inter}} > \gamma_{\text{sub}} \quad ,$$

it is thermodynamically favorable to have only little film surface area, and island growth is preferred. This mode, also known as Vollmer-Weber mode, is illustrated in Fig. 2.3(b).

An intermediate case is the layer-plus-island growth mode – or Stranski-Krastanov growth –, for which first closed layers form, and after that islands grow on top, depicted in Fig. 2.3(c). The layer-plus-island growth can serve as relaxation mechanism and often occurs if the substrate promotes a certain growth direction, but the resulting film surface is not the most stable surface of the crystal. An example is Fe_3O_4/MgO(110), illustrated by Fig. 2.3(c). The criterion of Eq. (2.4) favors closed film layers, and the substrate orientation forces a growth in Fe_3O_4[110] direction. However, the Fe_3O_4(111) surface is more stable than the Fe_3O_4(110) surface, so that after the first layer is closed, the film grows in an island mode in order to maximize the Fe_3O_4(111) surface [37]. Another mechanism that can result in layer-plus-island growth is related to the temperature. Equation 2.4 considers the growth mode to be only a relation between film and substrate. However, beyond a critical temperature T_{R} – the *roughening temperature* –, even films that engage in layer-by-layer growth at lower temperature will start to roughen, independent from the substrate. The reason is that the energy necessary for the film surface to form a step – which is governed by the fact that the bonds between the atoms make the formation of closed layers energetically favorable – is compensated at high temperatures by the configuration entropy introduced by the large number of variable shapes a step can take. Consequently, steps form spontaneously above T_{R} [38], and the film forms a layer plus island structure. However, all experiments in this work operate far from typical roughening temperatures [39, 40].

Another factor worth considering about epitaxial growth is the interface of film structure and substrate. In general, the in-plane lattice constant of the substrate a_{sub} and the in-plane bulk lattice constant of the film material a_{film} will differ. This difference is quantified by the lattice mismatch

$$\epsilon = \frac{a_{\text{film}} - a_{\text{sub}}}{a_{\text{sub}}} \quad . \tag{2.5}$$

For the film, it is on the one hand favorable to grow in its bulk lattice constant, but in the interface region, it is on the other hand favorable to fit onto the substrate lattice constant in order to form bonds to the substrate atoms. These competing conditions can be resolved in two different ways:

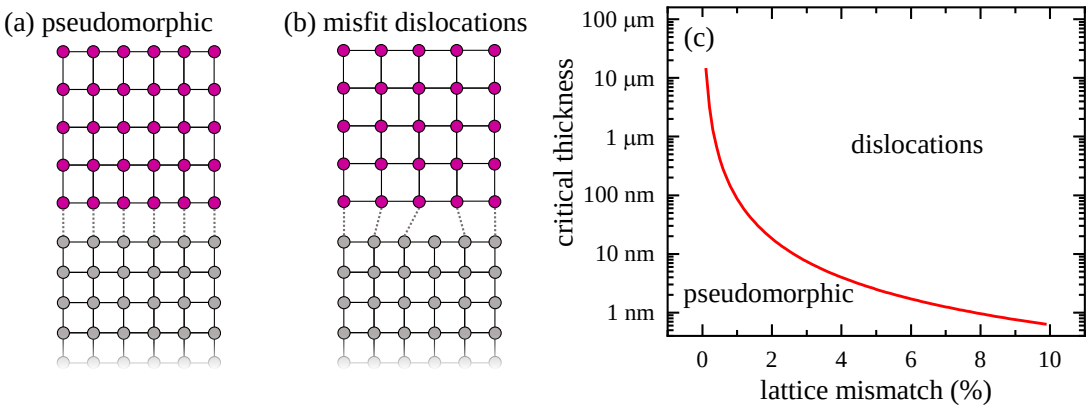

Fig. 2.4: (a) Illustration of pseudomorphic growth. The film is strained, so that its lateral lattice constant matches the one of the substrate. (b) The film grows with a relaxed lattice constant and accounts for the mismatch by developing misfit dislocations at the interface. (c) Critical film thickness, above which pseudomorphic growth is unfavorable, as a function of lattice mismatch. It was calculated following the model of People and Bean in Ref. [41], assuming dislocations along the [110] direction [42] and a Poisson ratio of $\nu = 0.03$ [43].

pseudomorphic growth: the film grows in the lateral lattice constant of the substrate and is therefore strained against its own lattice constant (cf. Fig. 2.4(a)). Usually, the lateral strain $\Delta a/a$ causes the vertical lattice constant c to develop a strain $\Delta c/c$ according to the Poisson ratio ν. This means, if the unit cell is laterally compressed, it will vertically expand, and vice versa. This scenario usually happens if the lattice mismatch is small.

misfit dislocations: the film releases strain by forming dislocations and relaxes to its bulk lattice constant (cf. Fig. 2.4(a)). This usually happens when the strain energy required for pseudomorphic growth becomes big, either because the lattice mismatch is high, or the film thickness and thus the strained material volume becomes big.

There exist several models to calculate the critical film thickness for which pseudomorphic growth becomes unfavorable and misfit dislocations start to occur [41,44,45]. The model of People and Bean [41] employs the condition that the strain energy is equal to the energy necessary to create the dislocations [41], arriving at the expression for the critical film thickness

$$h_c = \frac{1-\nu}{1+\nu} \cdot \frac{1}{16\pi\sqrt{2}} \cdot \frac{b^2}{a} \cdot \frac{1}{f^2} \cdot \ln\left(\frac{h_c}{b}\right) \quad . \tag{2.6}$$

Here, ν is the Poisson ratio, b is the slip distance of a single dislocation, and f is the lattice mismatch. Figure 2.4(c) shows the critical thickness as a function of lattice mismatch between substrate and film.

2.3. Magnetism

Magnetite is a ferrimagnet and the oldest known magnetic material. Because in this work, not only the structural, but also the magnetic properties of magnetite will be investigated, the basic terms of magnetism are introduced here. First, paramagnetism and diamagnetism

will be introduced, and after that the collective magnetic orders of ferromagnetism, antiferromagnetism and ferrimagnetism.

2.3.1. Quantum numbers

The microscopic description of magnetism involves the magnetic moments of the atomic states, which makes it necessary to briefly review the notation of atomic states by quantum numbers. This notation will also become very important in the upcoming Sec. 2.4.2, where spectroscopic techniques and multiplet calculations will be discussed. The information given here is taken from Ref. [29].

The Hamiltonian for the single electron approximation in an atom is given by

$$H_{\text{electron}} = \frac{\boldsymbol{p}^2}{2m_{\text{e}}} + \frac{-Ze^2}{\boldsymbol{r}} \quad . \tag{2.7}$$

The square modulus of its eigenstates $\Psi_{nlm}(\mathbf{r}, \mathbf{p})$ represents the probability to find an electron at position $\mathbf{r}$ with momentum $\mathbf{p}$ and therefore describes where and how the electrons may move around the atom. The probability distribution for the location of an electron with wave function Ψ_{nlm} is called its *orbital*. It is characterized by the quantum numbers n, l and m. n is the principal quantum number. It gives the strongest contribution on the binding energy of the electron and determines its radial distance from the core, but not its angular symmetry. Responsible for the angular symmetry of the corresponding orbital is the orbital angular quantum number l. This is illustrated for $l = 0 - 2$ in Fig. 2.5. Orbitals with $l = 0$ are spherical (cf. Fig. 2.5(a)), while $l = 1$ orbitals are shaped like dumbbells aligned along the three cartesian axes (cf. Fig. 2.5(b)), and of the 5 $l = 2$ orbitals, four consist of four lobes along oriented in different cartesian planes, and one of two lobes pointing along the z-axis together with a doughnut-shaped probability distribution in the xy-plane [46] (cf. Fig. 2.5(c)). The l quantum number is usually denoted in spectroscopic notation; i.e., a quantum state with $l = 0$ is denoted 's' state, a state with $l = 1$ denoted 'p' state, $l = 2$ an 'd' state, and $l = 3$ an 'f' state.

For a given l, the magnetic quantum number can take the values $m_l = l, l-1, ..., -l$. Each orbital may be occupied with electrons that have an intrinsic spin, denoted by the quantum number $s = \frac{1}{2}$. Analogous to the case of m_l, the magnetic spin quantum number m_s of an electron may take the values $m_s = \frac{1}{2}, -\frac{1}{2}$. The orbital angular momenta l and the spin s can be best understood as the amplitudes of the angular momenta, and their magnetic quantum number m can then be understood as their orientation towards a quantization axis [47]. In most practical cases, there exists some distinguished direction (for instance, a magnetic field) which is used as the quantization axis. It is conventionally chosen to be the z-axis, so that the magnetic quantum numbers m_l and m_s can be viewed as the projection of angular momentum vectors of length l and s onto the z-axis. For example, for a single electron the terms 'spin-up' and 'spin-down' are well known and refer to its possible values of $m_s = \frac{1}{2}, -\frac{1}{2}$, respectively. Their orientation towards the z-axis is accessed by the projection operator $\widehat{S}_z$. For the quantum mechanical state $|s = \frac{1}{2}, m_s = -\frac{1}{2}\rangle$ of a single 'spin-down' electron,

$$\widehat{S}_z \, |\frac{1}{2}, -\frac{1}{2}\rangle = m_s \cdot \hbar \; |\frac{1}{2}, -\frac{1}{2}\rangle = -\frac{1}{2} \cdot \hbar \; |\frac{1}{2}, -\frac{1}{2}\rangle \quad . \tag{2.8}$$

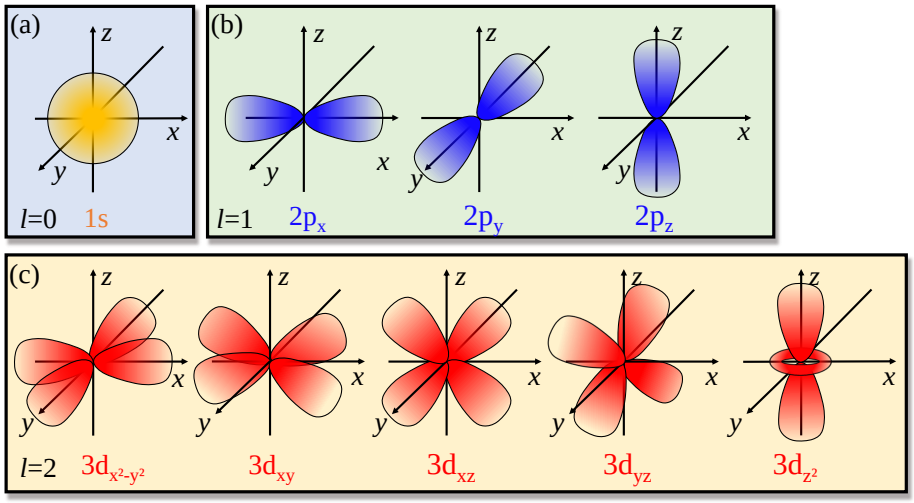

Fig. 2.5: Shapes of the orbitals for (a) l=0 ('s' orbital), (b) l=1 ('p' orbitals) and (c) l=2 ('d' orbitals). Reproduced after Ref. [46].

As will be shown soon, this very operator comes into play for determining the magnetic moment of an atom, which lends the name 'magnetic' to the magnetic quantum numbers.

For electrons with spin $s = \frac{1}{2}$, the orbital angular momentum l and the spin s can be coupled to a total angular momentum $j = l + s$ and $j = l - s$, with an according total magnetic quantum number $m_j = j, j-1, ..., -j$. This coupling is called spin-orbit coupling. The different quantum numbers and their possible values are summarized in Tab. 2.2.

The entirety of occupied states in an atom is called its *configuration*. It is denoted as a series of the occupied orbitals nl^N, with n being the principal quantum number, l the orbital quantum number in spectroscopic notation and N the number of electrons occupying the orbital. For example, the full electron configuration of an iron atom is $1s^2 2s^2 2p^6 3s^2 3p^6 3d^6 4s^2$, which is conventionally abbreviated to $3d^6 4s^2$ by omitting all completely occupied orbitals before the first partially filled one (in this case, the 3d orbital).

The symmetry of the ground state – and thus, the quantum numbers – of a configuration is calculated by adding up the angular momenta. In order to reflect the symmetry of the configuration, it can be denoted by a spectroscopic term symbol ${}^{2S+1}L_J$; S and L are the sums of the momenta s_i and l_i of the individual electrons, and J takes the values from $J = L + S, ..., |L - S|$.

To give an example: For a single electron configuration, i.e, $2p^1$, the principal quantum number is $n = 2$, $L = 1$ (represented by 'p'), the spin is $S = 1/2$ and the total angular momentum may either be $J = L - S = \frac{1}{2}$ or $J = L + S = \frac{3}{2}$. These states have two possible term symbols: ${}^2P_{1/2}$ for $J = \frac{1}{2}$, and ${}^2P_{3/2}$ for $J = \frac{3}{2}$. The ${}^2P_{1/2}$ state additionally splits up into 2 states with $m_J = -\frac{1}{2}, \frac{1}{2}$, and ${}^2P_{3/2}$ into 4 states with $m_J = -\frac{3}{2}, -\frac{1}{2}, \frac{1}{2}, \frac{3}{2}$.

Name	Symbol	Values (single electron)
principal quantum number	n	$n = 1, 2, 3...$
orbital angular momentum quantum number	l	$l = n-1, n-2, ..., 0$
magnetic quantum number	m_l	$m_l = l, l-1, ..., -l$
spin quantum number	s	$s = \frac{1}{2}$
spin magnetic quantum number	m_s	$m_s = -\frac{1}{2}, \frac{1}{2}$
total angular momentum quantum number	j	$j = l + \frac{1}{2}, l\frac{1}{2}$
total magnetic quantum number	m_j	$m_j = j, j-1..., -j$

Tab. 2.2: Summary of the quantum numbers and their possible values for a single electron, adapted from Ref. [29].

2.3.2. Diamagnetism and paramagnetism

If a material is exposed to an external magnetic field $\mathbf{B}_{\text{ext}}$, it will response by aligning its magnetization $\mathbf{M}$ according to

$$\mathbf{M} = \chi \frac{1}{\mu_0} \mathbf{B}_{\text{ext}}, \quad \text{with} \quad \mu_0 : \text{ vacuum permeability} \quad . \tag{2.9}$$

The proportionality constant χ is called *magnetic susceptibility*[1]. A material which has $\chi > 0$ aligns its magnetization $\mathbf{M}$ parallel to the outer field $\mathbf{B}_{\text{ext}}$. If this material has no persistent magnetic order (those will be discussed in the upcoming section), it is called a *paramagnet*, while a *diamagnet* has a susceptibility $\chi < 0$ and directs its magnetization antiparallel to the magnetic field.

In order to understand the underlying mechanisms, a closer look to the magnetic moments on individual atoms has to be taken. Microscopically, the magnetization of a material is the sum over the magnetic moments $\boldsymbol{\mu}$ of all its atoms, normalized to its volume V,

$$\mathbf{M} = \frac{1}{V} \sum_j \boldsymbol{\mu}_j \quad . \tag{2.10}$$

Paramagnetism and diamagnetism have different origins. Diamagnetism can be understood as an atomic equivalent of Lenz' rule: the magnetic field induces an electron current into the atom. This electron current then generates a magnetic field which opposes the external one. Paramagnetism, on the other hand, stems from the fact that the magnetic moment of an atom is inclined to align with the magnetic field. In terms of energy levels, atomic states have a magnetic moment

$$\widehat{\boldsymbol{\mu}} = -g_J \mu_{\text{B}} \widehat{\mathbf{J}} \quad \text{with} \quad \widehat{\mathbf{J}} = \widehat{\mathbf{S}} + \widehat{\mathbf{L}} \quad \text{and} \quad g_J = 1 + \frac{J(J+1) + S(S+1) - L(L+1)}{2J(J+1)}. \tag{2.11}$$

[1] For the upcoming discussion, χ will be a real number, but please note that generally, the magnetization $\mathbf{M}$ does not need to be parallel to the outer magnetic field, and as such, the magnetic susceptibility is actually a tensor $\widehat{\chi}$.

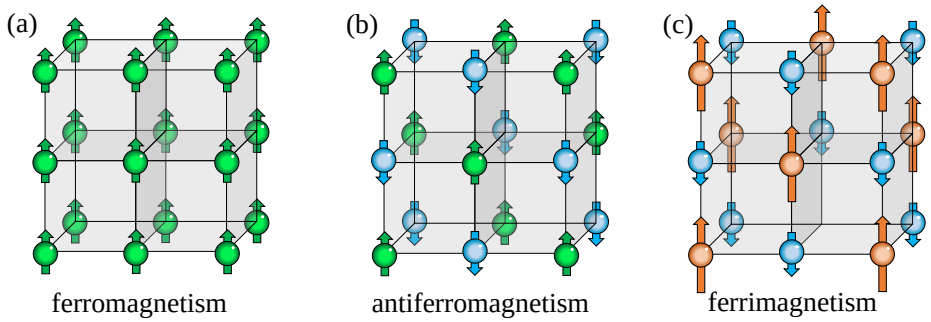

Fig. 2.6: Illustrations for the magnetic order in (a) a ferromagnet, (b) an antiferromagnet and (c) a ferrimagnet.

μ_B is the Bohr magneton, g_J is the Landé factor, and $\widehat{\mathbf{J}}$, $\widehat{\mathbf{S}}$ and $\widehat{\mathbf{L}}$ are the quantum mechanical operators for the total angular momentum, the spin momentum and the orbital momentum, respectively. In a magnetic field with strength B_z in the z direction, an atomic state $|J, m_J\rangle$ experiences an energy shift U

$$-B_z\widehat{\mu_z}\,|J, m_J\rangle = U\ \ |J, m_J\rangle = B_z\, m_J\, g_J\, \mu_\mathrm{B}\ \ |J, m_J\rangle\,. \tag{2.12}$$

Here, the projection operator from Eq. (2.8) is used in the form of $\widehat{\mu}_z = \frac{g_J\,\mu_\mathrm{B}}{\hbar}\widehat{J}_z$. Those states with a magnetic moment $\mu_\mathrm{z} = -m_J\, g_J\, \mu_\mathrm{B}$ parallel to B_z will have lower energy and a higher probability to be populated. According to Eq. (2.10), if more states with parallel magnetic moments μ_j are populated, the magnetization $\mathbf{M}$ increases, resulting in a magnetic ordering of the atoms. Therefore, paramagnetism only occurs in atoms that have electrons in partially filled shells, because otherwise there are no states available to be preferably populated. In the ground state of an atom with localized electrons, the paramagnetism of partially filled shells is called *Langevin* paramagnetism. This represents the strongest form of paramagnetism. In metals, whose electrons are better described in terms of bands than in terms of localized states, the paramagnetism of the conduction electrons is called *Pauli* paramagnetism. At finite temperatures, even for atoms with closed shells in the ground state, some electrons will be excited into states that have a non-zero total angular momentum J. Their paramagnetic response is the *Van Vleck* paramagnetism. Diamagnetism, in turn, occurs in every atom. It can be similarly strong as the Pauli or the Van Vleck paramagnetism, but is much weaker than the Langevin paramagnetism. Consequently, an atom can only be diamagnetic if no contribution from Langevin paramagnetism is present.

Both paramagnetic and diamagnetic materials only have a magnetization if an external magnetic field is applied – without a magnetic field, diamagnets have no magnetic moments at all, and the moments of a paramagnet are randomized, so that no macroscopic magnetization is observed.

2.3.3. Collective magnetism

The phenomenon of retained magnetic order in a material even in the absence of an outer magnetic field is called collective magnetism. Three particularly widespread examples of collective magnetism – the ferromagnet, the antiferromagnet and the ferrimagnet – are sketched

in Fig. 2.6. In ferromagnets, all moments align parallel to each other, resulting in a maximum magnetization (cf. Fig. 2.6(a)). In contrast, the moments in antiferromagnets try to align antiparallel to its neighboring atoms, resulting in vanishing macroscopic magnetization (cf. Fig. 2.6(b)). In a ferrimagnet, there exist antiparallel sublattices, just as in an antiferromagnet, but the magnetic moments on these sublattices have different amplitudes (cf. Fig. 2.6(c)). Consequently, they do not cancel each other out completely, so that a non-zero magnetization develops. There are more complex forms of magnetic order, but these three cover the most basic terms. Collective magnetism only occurs below certain material-specific temperatures. The temperature above which ferro- and ferrimagnetic order is lost in favor of paramagnetism is called Curie temperature T_C, and the antiferromagnetic counterpart is called the Néel temperature T_N. The coupling of spins leading to collective magnetism is called *exchange interaction*, which is vastly unrelated to the mechanisms behind paramagnetism and diamagnetism. It is already obtained by applying the Coulomb repulsion operator to some two-electron wavefunction – such as an atomic state – $|\Psi\rangle$ [29]

$$\langle\Psi|\frac{e^2}{\boldsymbol{r}_{12}}|\Psi\rangle = F + G \quad . \tag{2.13}$$

F and G are the Slater-Condon integrals; F is called the Coulomb – or 'direct' – term and corresponds to the classical repulsion between the electron charges. G is the exchange term, and represents the transition probability to exchange the positions of the two electrons induced by the Coulomb operator. It becomes necessary for the sole reason that the electrons need to be indistinguishable and antisymmetric upon the exchange

$$\Psi(\mathbf{x}_1, \mathbf{x}_2) = -\Psi(\mathbf{x}_2, \mathbf{x}_1) \quad \mathbf{x}_i = (\mathbf{r}_i, s_i) \quad , \tag{2.14}$$

with $\mathbf{r}_i$ being the position and s_i the spin of particle i. The energy for an exchange of two particles is of course tied to the atomic states they are in and thus, also to their spin. If the orbitals of neighboring atoms in a solid overlap, so that the electrons experience their respective Coulomb potential, they will also experience an exchange interaction, which indirectly couples their spins. The value of this exchange energy favors a particular relative orientation of the spins and thus, a magnetic order. Loosely speaking, collective magnetism is caused by the effort of the system to facilitate an easy exchange of electrons.

This explanation may sound technical and unintuitive, especially as there is no classical analogon to the exchange interaction. However, it opens the way to very useful – and arguably intuitive – arguments which explain the spin alignment between atoms depending on how easily it allows delocalization of electrons across its overlapping orbitals. Such exchange schemes will be discussed in Sec. 2.3.4.

For completeness, the Heisenberg model shall be mentioned here. As discussed before, magnetic order expresses itself in the alignment of the electronic spins and angular momenta of the atoms, although they are not directly coupled to each other. However, for some applications the magnetic order can be modeled by constructing a lattice where the atoms are represented by interacting spins $\widehat{\mathbf{S}}$. These atoms do not contain the spatial wavefunctions and thus, no actual exchange interaction. The exchange interaction is then described by the

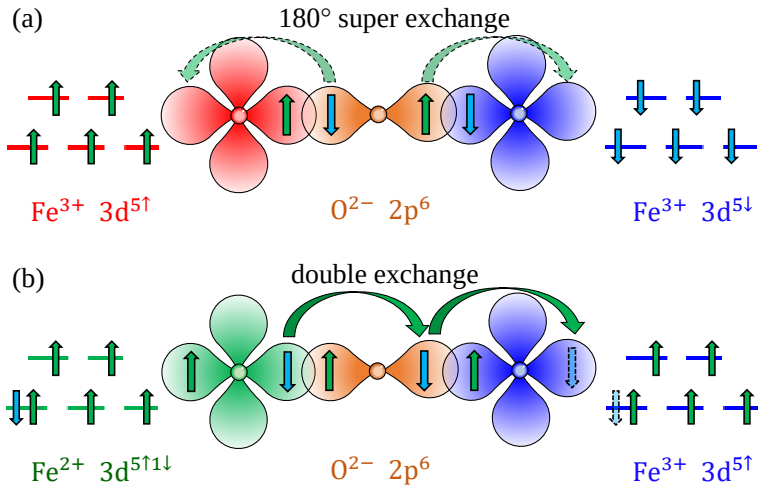

Fig. 2.7: (a) Illustration of super exchange between two Fe^{3+} cations. In order to realize a delocalization across the 2p orbitals of O^{2-}, the spins of the cations align antiparallel. (b) Illustration of double exchange between a Fe^{2+} and a Fe^{3+} cation. The spins align parallel in order to facilitate the delocalization of one electron.

Heisenberg Hamiltonian which couples the spins directly

$$H_{\text{Heis}} = - \sum_{\text{pairs } (i,j)} J_{\text{exc}}(i,j)\ \widehat{\mathbf{S}}_i \cdot \widehat{\mathbf{S}}_j \quad , \tag{2.15}$$

with $\widehat{\mathbf{S}}_{i,j}$ being the spins of two neighboring atoms i and j. Here, $J_{\text{exc}}(i,j)$ is the exchange integral between spins i and j, and its sign determines whether the lattice favors ferro- (positive) or antiferromagnetic (negative) spin alignment. This model is more intuitive and can be useful, for example, for qualitative arguments and approximations of the Curie temperature. However, please remember that in reality, there is no such thing in the solid as an exchange field which couples the actual spins in this way.

2.3.4. Super exchange and double exchange

The exchange interaction in metals can often be described in terms of the Stoner criterion, or by a direct exchange interaction in the case of 3d metals, in which a tight-binding model is more appropriate. For those, as well as generally for more details on the topic, please refer to Ref. [26]. Since this work is concerned with metal oxides, these exchange schemes do not apply here. Instead, the most prevalent exchange schemes are those that involve mediation across the oxygen ligands, namely the super exchange and the double exchange. They are illustrated in Fig. 2.7.

Super exchange takes place between two identical cations and is mediated by a ligand, typically O^{2-}. The most common geometry is the 180° M-O-M (metal-oxygen-metal) bond, in which the three ions are arranged in a straight line, and is sketched in Fig. 2.7(a) for two Fe^{3+} cations. Their 3d shells are half filled with 5 electrons, and Hund's rule dictates that they all have the same spin in the ground state. In order to allow both ligand 2p electrons to spread out into the 3d orbitals that they overlap with, the Fe^{3+} cations need to be aligned antiparallel to the respective 2p electron, and consequently also to the other Fe^{3+} cation. This results in a strong antiferromagnetic coupling. In other words, the antiferromagnetic order is a result of the effort of the atoms to facilitate delocalization of the 2p electrons into the 3d orbital, just as described in Sec. 2.3.3. Generally, whether super exchange leads to antiferromagnetic or ferromagnetic coupling depends on the geometry of the bonds, and

there exist a set of rules – the Goodenough-Kanamori rules – that help to quickly determine its effect [26]. According to these rules, the discussion above holds for singly occupied orbitals with large overlap, which is typically the case for orbitals pointing towards each other with angles between 120° and 180°. For singly occupied 3d orbitals with an overlap integral which equals to zero – this is the case for 90° M-O-M arrangements –, in contrast, the super exchange would lead to a weak ferromagnetic coupling. The Goodenough-Kanamori rules further predict a weak ferromagnetic coupling for singly occupied 3d orbitals which overlap with empty or doubly occupied orbitals of the same type.

Double exchange is a mechanism between two cations of the same element, but of different valencies. It is always ferromagnetic and is sketched in Fig. 2.7(b) for the case of Fe^{3+} and Fe^{2+}. The $3d^6$ configuration of the Fe^{2+} cation has an additional electron on top of a half shell, which needs to occupy the first minority spin state. It is written here as $3d^{5\uparrow 1\downarrow}$. This spin-down electron can be delocalized across the neighboring Fe^{3+} cation, but only if this cation has also a $3d^{5\uparrow}$ configuration; otherwise, there would be no empty state available for a spin-down electron. The result is that the two different cations effectively form two identical $Fe^{2.5+}$ cations, between which one electron is delocalized. Therefore, it is energetically favorable for the system to align ferromagnetically. This delocalization process is again mediated by the O^{2-} 2p orbital, which bridges the distance between the cations by hybridization with the two 3d orbitals.

2.4. Core-level spectroscopy

The three spectroscopic techniques introduced in this section – XPS, XAS and XMCD – all belong to the group of core-level spectroscopies. They bear this name not because they are used to *study* the core levels of an atom, but because they utilize the excitation of core level electrons in order to study the valence states [29]: Most properties of solids – conduction, magnetism, binding characteristics – are determined by their outer electrons in the valence states. Solid state physics is therefore mostly concerned with studying these valence states. The binding energies of valence electrons are in the few eV range and are accessible by visible light. In a solid, they take part in the binding process and their properties are largely affected by the environment, and thus their character differs largely from the atomic case. Core-level electrons, on the other hand, have typical binding energies ranging up to several thousand eV. They remain mostly the same even in a solid and are therefore very well described by an atomic description. This is exploited by core-level spectroscopy, whose strategy it is to excite core level electrons into valence states or even remove them from the solid, leaving behind a core hole, and probe the valence states by investigating their reaction. For such an excitation process, x-rays with energies exceeding or matching these binding energies are necessary. The final state, into which the atom is excited, is a superposition of the core hole and the valence state wavefunctions, and therefore allows conclusions towards these unknown valence states and the electronic properties of the solid.

To start with, the one electron picture is considered as a groundwork in Sec. 2.4.1, which effectively assumes that the excitation process does not change the atom at all. Upon this foundation, the more complete picture of CTM theory will be built. This theory fully accounts for the core hole effects as well as the influence of the crystal by introducing crystal field and charge transfer effects.

2.4.1. Single electron picture

The single electron picture is not suited to describe any spectral shapes, but can explain the origin of the characteristic spectra of different elements. In this picture, the density-of-states (DOS) approximation and the core hole approximation are made: it is assumed that the ground state DOS is correct at all times, even if an additional electron is added to the valence states or a core hole is created.

An illustration for the case of the 3d transition metal iron can be found in Fig. 2.8. In an iron atom, electrons are bound in the core levels nl (1s, 2p, 3d, etc.) with certain binding energies $E_{\mathrm{bind}}(nl)$. If it is illuminated by a photon of energy $E_{\mathrm{ph}} > E_{\mathrm{bind}}(nl)$, the photon can be absorbed and promote an electron from the state nl to the Fermi energy or even to leave the solid with a kinetic energy of

$$E_{\mathrm{kin}} = E_{\mathrm{ph}} - E_{\mathrm{bind}} - \Phi \quad . \tag{2.16}$$

Here, Φ is called the work function and represents the energy necessary for an electron at the Fermi energy to leave the solid.

When the x-ray absorption of an atom is measured as a function of the photon energy E_{ph}, at energies $E_{\mathrm{ph}} = E_{\mathrm{bind}}(nl)$ an abrupt jump in absorption is detected (cf. Fig. 2.8(a)). These are called *absorption edges*. At theses energies, all electrons in the state nl are available to directly absorb the photon and be promoted to the lowest empty state, leaving behind a core hole in the state nl.

Similarly, if the same atom is illuminated by x-rays with a constant energy E_{ph}, and the numbers of photoelectrons as a function of their kinetic energy E_{kin} is measured, again at certain energies a dramatic increase in photoelectrons is observed (cf. Fig. 2.8(b)). The reason is the same as before: at these energies $E_{\mathrm{kin}} > 0$, Eq. (2.16) is fulfilled for a binding energy $E_{\mathrm{bind}}(nl)$, and x-ray absorption occurs very efficiently. In the case of XPS, a large number of electrons are excited into the continuum with that particular kinetic energy and can be detected.

The physical process behind both, XAS and XPS, is almost identical. The difference is merely whether the core level electrons are excited to the Fermi level or into the continuum, as illustrated in Fig. 2.8(c). If Φ is known, Eq. (2.16) can be used to present the energy axis of the XP spectrum in terms of E_{bind} instead of E_{kin}, as in Fig. 2.8(b). In this representation, the XAS absorption edges and the XPS peaks are located at the same energies. This series of peaks in the XP and XA spectra at these exact energies is characteristic for each atom and can be used to determine the chemical composition of a sample.

Despite these similarities of both methods, historically some different conventions regarding nomenclature and presentation were established in the XPS and XAS communities. In XPS, the spectroscopic lines are usually denoted according to the energy levels in the atom (1s, 2p, 3d, etc.) from where the photoelectrons are excited from, while in XAS, instead the spectroscopic notation for optical transitions is used (K,L,M, etc.). This is demonstrated by the red labels on the top of Figs. 2.8(a),(b). The energy axes of XA spectra are conventionally labeled 'photon energy' and are organized from low energies on the left to high energies on the right. XP spectra typically use the label 'binding energy' and organize them from high energies on the left to low energies on the right, again demonstrated in Figs. 2.8(a),(b). Both terms – 'photon energy' and 'binding energy' – are linked by Eq. (2.16). The inverted energy

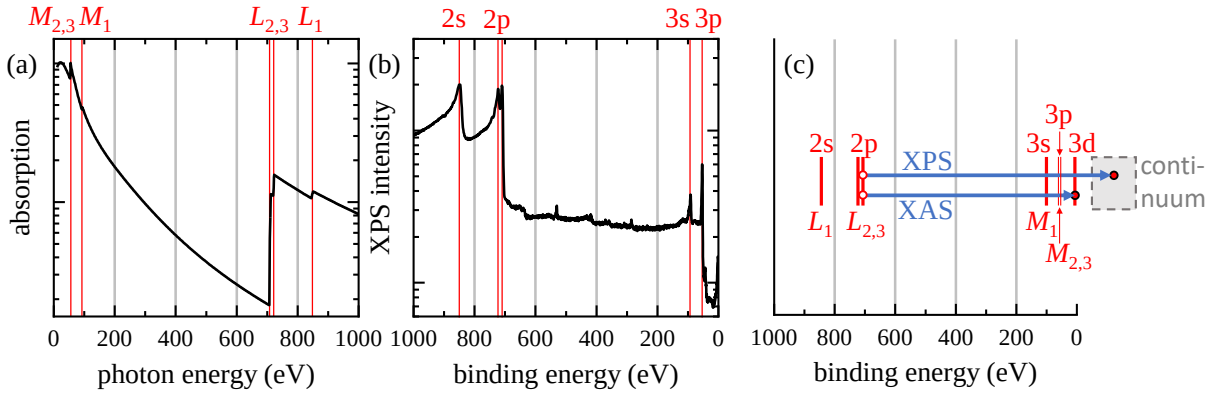

Fig. 2.8: (a) Tabulated values of the x-ray absorption coefficient of Fe (taken from Ref. [48]). (b) XPS survey measurement of Fe. (c) Sketch of the excitations of a 2p electron in an XAS and XPS experiment. Red lines indicate the resonance positions. In XPS, peaks are denoted by energy levels (2p, 3d, etc), in XAS by the spectroscopic notation for optical transitions (*L*,*M*,etc.).

axis reflects the fact that the controlled quantity in XPS is the kinetic energy of the electrons, and the binding energy enters Eq. (2.16) for the kinetic energy with a minus sign.

The central formula for core-level spectroscopy is Fermi's Golden Rule. It describes the probability W of a transition operator $\widehat{T}$ – for instance, excitation by the absorption of a photon of energy E_{ph} – from an initial state i to a final state f, represented by wavefunctions $|\Psi_i\rangle$ and $|\Psi_f\rangle$

$$W(f,i) = \frac{2\pi}{\hbar} |\langle \Psi_f | \widehat{T} | \Psi_i \rangle|^2 \cdot \delta(E_f - E_i - E_{\mathrm{ph}}) \quad . \tag{2.17}$$

The $\delta(E)$ function makes sure that the transition occurs only when the energy difference between f and i is exactly the photon energy E_{ph}. For the transition operator $\widehat{T}$, for the case of absorption of soft x-rays, it is usually sufficient to only consider the dipole operator[2]. The initial state i is usually well known, as it is simply the electronic ground state of the studied atom or ion.

In this one-electron description, both XAS and XPS are merely teaching us the binding energies of the core levels. However, as mentioned earlier, the goal is to learn something about the valence states. Therefore, it becomes clear that the true information is hidden in the final state f, which depends on all electronic reactions of the atom's or ion's local environment to the core hole produced by the excitation. These considerably differ for XPS and XAS and will therefore be discussed separately in Secs. 2.4.3 and 2.4.4.

2.4.2. Charge-transfer multiplet calculations

The theoretical framework in which both XAS and XPS spectra of transition metals are best described is called charge-transfer multiplet (CTM) theory. It utilizes atomic multiplet

[2]Below 10 keV, quadrupole terms are smaller than dipole terms by about $\approx 10^{-4}$ [29]; the discussion here will therefore limit itself to the dipole approximation. In the actual calculations used in this work, both dipole and quadrupole transitions are accounted for.

effects, crystal-field effects and charge-transfer effects in order to describe the initial and the final states, and then employs Eq. (2.17) to evaluate the transition probability between them.

Atomic multiplets

The starting point are atomistic calculations of electron transitions, completely neglecting the crystal environment. For this work, the Fe L edge of Fe^{2+} and Fe^{3+} cations is of particular interest. Therefore, the following explanations will be done on the example of the case of Fe^{2+}. The electron configuration of this cation is $2p^63d^6$. At the L edge, the ion absorbs an x-ray of energy $E_{\mathrm{ph}} \approx 710\,\mathrm{eV}$, so that a core level electron is excited from 2p to 3d, and the resulting final state is thus $2p^53d^7$. In order to find the wave functions $|\Phi_{i,f}\rangle$ describing the iron atom in these configurations, the Schrödinger equation, $H\,|\Psi_{\mathrm{i,f}}\rangle = E_{i,f}\,|\Psi_{i,f}\rangle$, has to be solved using the atomic Hamiltonian

$$H_{\mathrm{atom}} = \underbrace{\sum_i^N \frac{\boldsymbol{p}_i^2}{2m} + \sum_i^N \frac{-Ze^2}{\boldsymbol{r}_i}}_{\text{average energy}} + \underbrace{\sum_{\text{pairs}} \frac{e^2}{\boldsymbol{r}_{ij}}}_{\text{Coulomb repulsion of electrons}} + \underbrace{\sum_i^N \zeta(\boldsymbol{r}_i)\widehat{\mathbf{L}}_i \cdot \widehat{\mathbf{S}}_i}_{\text{spin-orbit coupling}} = H_{\mathrm{avg}} + H_{\mathrm{ee}} + H_{ls} \quad . \tag{2.18}$$

The first two terms describe the electrons' kinetic energy and potential energy in the field of the nucleus. In a given configuration, this term is the same for all electrons and is neglected as an offset. This means that these calculations do not give a total energy, but only the relative energies in a configuration.

The energy contributions resulting from this Hamiltonian can be found in their matrix elements. The values of these matrix elements can be calculated from atomistic Hartree-Fock [49] calculations or can be found for a variety of ions in the literature [50] [3]. In the initial state, the 2p shell is closed and only the spin-orbit coupling of the 3d electron contributes [49]

$$\langle 3d^6|\zeta_{3d}\widehat{\mathbf{L}}_{3d} \cdot \widehat{\mathbf{S}}_{3d}|3d^6\rangle = \epsilon_{3d} \quad . \tag{2.19}$$

$\widehat{\mathbf{L}}$ and $\widehat{\mathbf{S}}$ are the orbital and spin angular momentum operators, and ζ_{3d} is the strength of the coupling.

For a two-electron wavefunction, an eigenstate of the initial state $|2p^63d^6\rangle$ has an energy contribution from the Coulomb repulsion of the 3d electrons:

$$\langle 2p^63d^6|\frac{e^2}{\boldsymbol{r}_{12}}|2p^63d^6\rangle = \sum_k f_k F^k_{\mathrm{dd}} + \sum_k g_k G^k_{\mathrm{dd}} \quad . \tag{2.20}$$

The right-hand side of Eq. (2.20) is a conventional way to separate the radial parts F^k and G^k from the angular parts f_k and g_k of the matrix element. The energies F^k and G^k are called the *Slater-Condon* parameters (or Slater integrals) and denote the Coulomb repulsion

[3] Hartree-Fock methods are ab-initio calculations of the wavefunction of a multi-electron configuration. They are based on the assumption that all electrons are non-interacting and can be represented by single-electron wavefunctions, but experience their mutual Coulomb field and obey the exclusion principle. This method is not exact, but leads to energies of the wavefunction that are accurate within about 1%. More details can be found in Ref. [49].

initial state			⟶	final state						
$2p^6 3d^6$				$2p^5 3d^7$						
F^2_{dd}	F^4_{dd}	ϵ_{3d}		F^2_{dd}	F^4_{dd}	F^2_{pd}	G^1_{pd}	G^3_{pd}	ϵ_{3d}	ϵ_{2p}
10.966	6.815	0.052		11.78	7.33	6.79	5.00	2.84	0.067	8.2

Tab. 2.3: Slater-Condon parameters F^k and G^k as well as spin-orbit splittings ϵ for the initial state $2p^6 3d^6$ (left) and the final state $2p^5 3d^7$ (right) of an x-ray absorption process at the L edge of an Fe^{2+} ion. All values given in eV.

of the electrons and the exchange interaction, respectively, as already mentioned during the discussion of the exchange interaction by means of Eq. (2.13). The angular parts f_k and g_k were separated from the radial parts using the Wigner-Eckhart theorem and represent the basis transformation from the orbital angular momenta l_1 and l_2 of the two electrons to the coupled total angular momentum L. They are non-zero only for some k between 0 and $l_1 + l_2$. The possible values of k depend on the electron configuration; for the case of $2p^6 3d^6$, only F^2_{dd} and F^4_{dd} occur and are given in Tab. 2.3.

In the final state $2p^5 3d^7$, due to the 2p core hole an additional 2p spin-orbit term occurs

$$\langle 2p^5 | \zeta_{2p} \widehat{\mathbf{L}}_{2p} \cdot \widehat{\mathbf{S}}_{2p} | 2p^6 \rangle = \epsilon_{2p} \tag{2.21}$$

as well as a 2p-3d multiplet coupling between the 2p core hole and the 3d electrons

$$\langle 2p^5 3d^7 | \frac{e^2}{\boldsymbol{r}_{12}} | 2p^5 3d^7 \rangle = \sum_k f'_k F^k_{pd} + \sum_k g'_k G^k_{pd} \quad . \tag{2.22}$$

In solids, results are usually better if the Slater-Condon parameters are reduced to about 80% of their Hartree-Fock values [51]. For the case of Fe^{2+}, all relevant parameters (given as their 100% values) for the atomistic multiplet calculations are summarized in Tab. 2.3.

The F^k_{dd} parameters cause both, the initial and final state, to split up into a series of spectroscopic lines. However, at the heart of multiplet effects are the core-valence Slater-Condon parameters F^k_{pd}, G^k_{pd}, which indicate the overlap of the 2p core-hole wavefunction and the 3d valence wavefunctions. For materials in which these parameters are small compared to the spin-orbit coupling (i.e, Pt, Pd), multiplet effects are small and density functional theory (DFT) approaches reproduce spectra well. However, as can be seen from Tab. 2.3, for iron and the other transition metal oxides, $F^k_{pd} = 6.8\,\text{eV}$ and $G^k_{pd} = 5.0\,\text{eV}$ are in the same order of magnitude as the 2p spin-orbit coupling $\epsilon_{2p} = 8.2\,\text{eV}$. Therefore, multiplet effects are strong and need to be adressed in calculations [28].

According to Eq. (2.17), the transition intensities of an x-ray absorption process are obtained by

$$I_{XAS} \sim \langle \Phi_f | \widehat{T} | \Phi_i \rangle \approx \langle 2p^6 3d^6 | \widehat{p} | 2p^5 3d^7 \rangle \quad .$$

In the second step, we identified the transition operator $\widehat{T}$ as the dipole operator $\widehat{p}$, which is well fulfilled in the soft and intermediate x-ray region, in which quadrupole contributions are

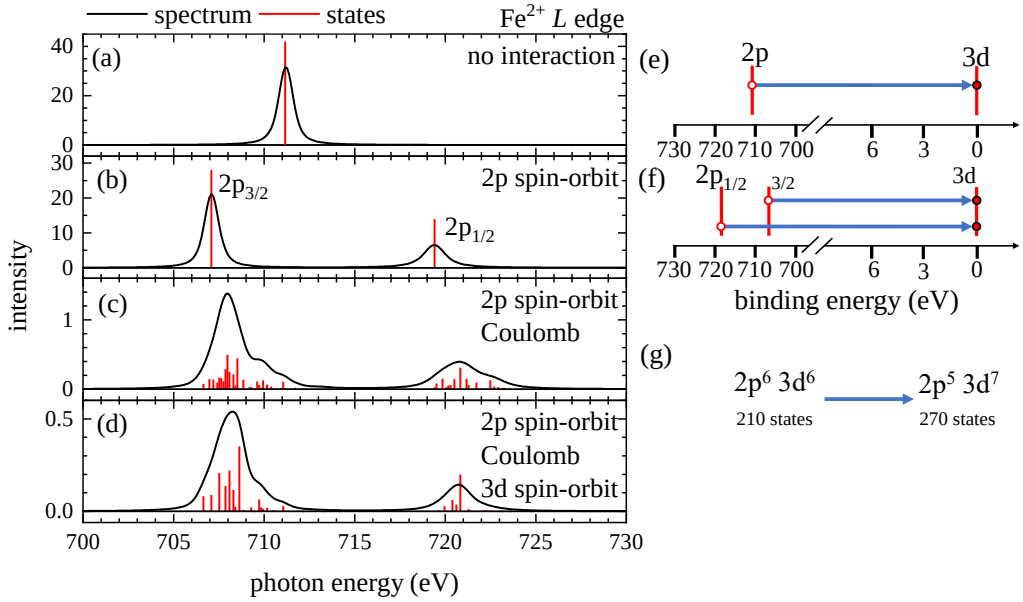

Fig. 2.9: Atomic multiplet calculations of the Fe^{2+} L edge. (a) Calculation with no interactions between the electrons in the initial and final states. (b) Calculation with only the 2p spin-orbit coupling of the final state. (c) Calculation with 2p spin-orbit coupling and the Coulomb interaction between the electrons. (d) Calculation with both 2p and 3d spin-orbit coupling and Coulomb interaction between the electrons. (e) Illustration of the situation in (a) in the single electron picture. (f) Illustration of the transition in (b) in the single electron picture. (g) The coupling of 2p core hole and 3d valence electrons cannot be described in a single electron picture.

weak. The dipole operator chooses viable transition by the dipole selection rules, imposing changes in the total angular momentum of $\Delta J = +1, 0, -1$, preservation of the spin quantum number, $\Delta S = 0$, and a change of the angular momentum quantum number by $\Delta L = \pm 1$.

The effects of the different contributions can be seen in Fig. 2.9. It shows the lines which were determined by the atomic multiplet calculations in red, and a pseudo-Voigt broadening in order to simulate an actual XAS spectrum in black. In Fig. 2.9(a), the atomic multiplet simulation of the Fe^{2+} L edge is displayed with all spin-orbit and Slater-Condon parameters set to 0, so that all possible states within the initial and final state have the same energy. The result is a single line, only stemming from the binding energy of the 2p electron. This scenario can be intuitively understood in the single electron picture, illustrated in Fig. 2.9(e), where an electron is simply promoted from 2p to 3d, overcoming the binding energy of $\sim 711\,\mathrm{eV}$. If the 2p spin-orbit ϵ_{2p} coupling is switched on, the single line intensity is split in a 1:2 ratio into the singlet state $2p_{1/2}$ and the triplet state $2p_{3/2}$, displayed in Fig. 2.9(b). As illustrated in Fig. 2.9(f), the single electron picture still holds up well, since initial and final states do not interact[4]. This changes when the Coulomb interactions between the electrons enters in Fig. 2.9(c). Now multiplet effects not only split up the initial and final state, but in the final state also couple the core hole wavefunction with the valence electrons. In order to evaluate

[4]Please note that the 2p spin-orbit splitting is an effect of the core hole, and therefore a final state effect of the $2p^5 3d^7$ configuration, not of the initial state, as might be suggested by the illustration.

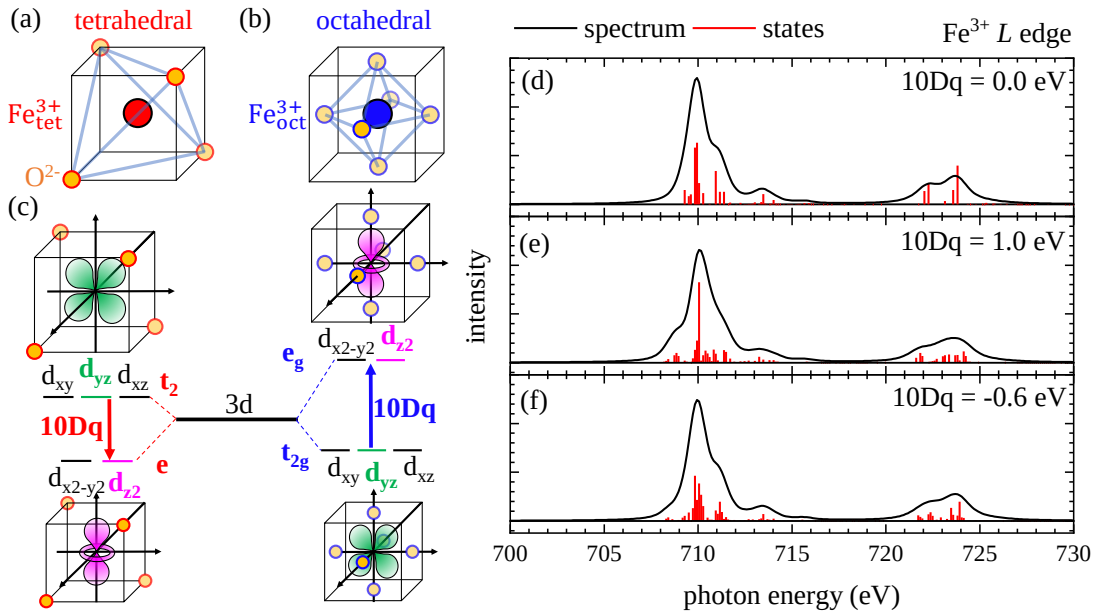

Fig. 2.10: (a) Illustration of a tetrahedrally coordinated Fe^{3+}_{tet} cation. (b) Illustration of an octahedrally coordinated Fe^{3+}_{oct} cation. (c) Energy splitting scheme of the 3d orbitals into e and t_2 states, separated by the energy term 10Dq. For the e states, the orientation of the d_{z^2} orbital is illustrated in the respective orientation, and for the t_2 states, the d_{yz} orbital. (d)-(f) Crystal field multiplet calculations for (d) no crystal field, (e) an octahedral crystal field of 10Dq=1.0 eV and (f) a tetrahedral crystal field of 10Dq= −0.6 eV.

all possible transitions, the individual angular momenta of the $2p^5$ core hole and the $3d^7$ valence states need to be coupled with each other, resulting in a huge increase in possible states. For instance, the initial state of a Fe^{2+} cation, with a $2p^6d^6$ configuration, has in total 34 different states, and the final state of an x-ray absorption process at the L edge $2p^5d^7$ has 110 states, enabling $34 \cdot 110 = 3740$ possible transitions. Whether or not a certain transition is realized depends on the selections rules. In Fig. 2.9(d), finally the 3d spin-orbit coupling ϵ_{3d} is included. As can be seen from Tab. 2.3, ϵ_{3d} is only very small and causes hardly any splitting. However, some of the transitions are rendered forbidden due to the selection rules, so that in total fewer lines occur.

Crystal fields

So far, the discussion was purely atomistic and did not take into account the crystal environment the Fe^{2+} cation is embedded in. This is accomplished by simply modeling the surrounding ligand atoms (O^{2-} in the case of Fe_3O_4) with their electric field working on the iron cation. This electric field is called *crystal field* or *ligand field*. The reason this very simplified approach works is that it fully accounts for the symmetry provided by the crystal environment. The Hamiltonian is simply extended by an additional term H_{cf}

$$H_{\mathrm{Atom}} = H_{\mathrm{avg}} + H_{\mathrm{ee}} + H_{ls} + \underbrace{H_{\mathrm{cf}}}_{=-e\cdot\Phi(\mathbf{r})} \tag{2.23}$$

The crystal field is treated as a perturbation to the atomic result. The actual calculations utilize group theory in order to represent the symmetries of the atomic states in terms of the crystal field, which can be a difficult task. However, for the purposes of this work the situation is fortunately very simple, as it is only concerned with two distinct, but very similar crystal field symmetries. They are illustrated in Figs. 2.10(a) and 2.10(b) at the example of Fe^{3+}_{tet} and Fe^{3+}_{oct}. In Fig. 2.10(a), the oxygen anions surround the Fe^{3+}_{tet} cation in the form of a tetrahedron, which can be represented as 4 anions sitting on 4 corners of a cube. In Fig. 2.10(b), the Fe^{3+}_{oct} cation is surrounded by anions arranged in an octahedron, which can be thought of the anions sitting on the 6 faces of a cube. These two arrangements belong to different symmetry groups (T_d and O_h); however, in combination with the symmetries of the 3d orbitals, they can be conveniently described by a single common variable, 10Dq [51]. The reason is illustrated in Fig. 2.10(c). Without crystal field, the 3d electrons may populate five degenerate orbitals: d_{xy}, d_{yz}, d_{xz}, which are oriented towards the edges of the cube, and $d_{x^2-y^2}$, d_{z^2}, which are oriented towards the faces of the cube. As examples, in Fig. 2.10(c) the d_{yz} orbital and the d_{z^2} orbital are depicted for both the octahedral and the tetrahedral case. Because it is energetically unfavorable for the electrons to populate a state close to a ligand, the degeneracy of the orbitals is lifted. In octahedral symmetry, the $d_{x^2-y^2}$, d_{z^2} orbitals form the e_g state and the d_{xy}, d_{yz}, d_{xz} orbitals form the t_{2g} state, and they are split by the energy term $10Dq = E_{e_g} - E_{t_{2g}} > 0$. In tetrahedral symmetry, the degeneracy is lifted in the same way and the same states e and t_2 are formed[5], only that now the e state is lower in energy than the t_2 state, and thus $10Dq < 0$.

This means that only a single parameter, 10Dq, is needed in the multiplet calculations, and it describes octahedral fields when it is positive and tetrahedral fields when it is negative. This is exemplified in Figs. 2.10(d)-(f). Figure 2.10(d) shows a purely atomic spectrum of a Fe^{3+} cation without crystal field. In Figs. 2.10(e),(f) the spectrum is shown for an octahedral and tetrahedral field, respectively. Due to the additional splitting, the number of lines increases.

Charge transfer

As a last ingredient, charge transfer will be considered. It describes the fact that in a crystal, electrons can be transferred between atoms – in the case of Fe_3O_4, between the iron cation and the oxygen ligands. In this sense, a Fe^{2+}_{oct} cation cannot fully be described by a $2p^63d^6$ configuration, but as a mixture between $2p^63d^6$ and $2p^63d^7\underline{L}$, with the $\underline{L}$ indicating that one electron was donated from a ligand. The second configuration is called charge-transfer state, and the energy separating it from the ground state is the charge-transfer energy Δ. Generally, also higher charge-transfer states exist simultaneously, like $2p^63d^8\underline{L}^2$ etc., but since their energy is high, they are usually not prominent. The charge transfer effect becomes especially important for screening effects in the final state, when the electronical environment of the cation reacts to the creation of the core hole during the x-ray absorption process. The positive charge of the 2p core hole generates an attractive potential for the electrons, which pulls down the 3d states by an energy term U_{pd}. As illustrated in Fig. 2.11(a), this is not very crucial in XAS, because the excited electron remains in the cation and the 2p core hole in the final state gets screened by the additional 3d electron itself. Adding an additional electron to the 3d shell costs the *3d electron correlation energy* U_{dd}, counteracting the gain

[5] The 'g' (abrv. 'gerade') is removed from the e_g and t_{2g} states due to the lack of inversion symmetry for tetrahedral cations.

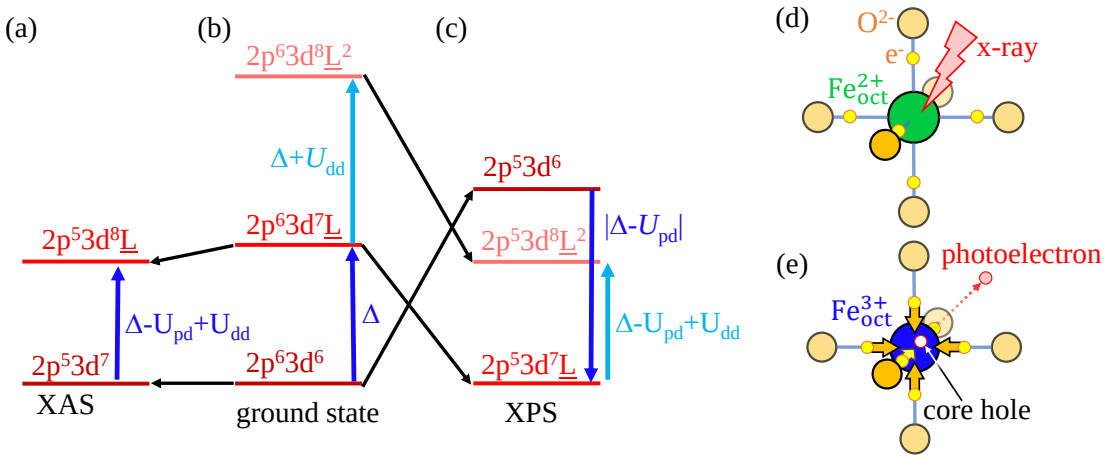

Fig. 2.11: (a),(b),(c) Energy scheme of the charge-transfer states for (b) the ground state and the final states in (a) XAS and (c) XPS. All energy terms are shifted with the lowest state of the three scenarios at zero. Black arrows indicate a dipole transition computed in the multiplet calculation, blue arrows stand for a monopole mixing calculated between charge-transfer states. Reproduced from Ref. [27]. (d),(e) Illustration of the screening effect by charge-transfer from ligands during the photoionization process in XPS.

from the core hole potential[6]. In total, the charge-transfer energy of the final state is

$$\Delta_f^{\mathrm{XAS}} = \Delta - U_{\mathrm{pd}} + U_{\mathrm{dd}} \quad \underbrace{\approx \Delta - 1 \ldots 2\,\mathrm{eV}}_{\text{for transition metal oxides}} \quad . \tag{2.24}$$

In contrast, in XPS, the excitation is an ionizing process, in which the excited electron leaves the cation as a photoelectron. This situation is sketched in Figs. 2.11(d),(e). In Fig. 2.11(d), the $\mathrm{Fe}^{2+}_{\mathrm{oct}}$ cation forms an ionic bond with the surrounding oxygen anions, described by a mixture between a $2\mathrm{p}^6 3\mathrm{d}^6$ and $2\mathrm{p}^6 3\mathrm{d}^7\underline{\mathrm{L}}$ configuration. When it absorbs an x-ray, it ejects a photoelectron, leaving behind a 2p core hole and turning $\mathrm{Fe}^{2+}_{\mathrm{oct}}$ into $\mathrm{Fe}^{3+}_{\mathrm{oct}}$. To this additional charge, the ligand electrons react strongly, and a mixed configuration between $2\mathrm{p}^5 3\mathrm{d}^7$ and $2\mathrm{p}^5 3\mathrm{d}^8\underline{\mathrm{L}}$ forms, and now even $2\mathrm{p}^5 3\mathrm{d}^9\underline{\mathrm{L}}^2$ becomes important. Figures 2.11(a)-(c) summarize the energy schemes of the charge-transfer states for XAS and XPS. While the prevalence of the charge-transfer configuration in XAS does hardly change between initial and final state (compare Figs. 2.11(a) and 2.11(b)), in XPS the charge-transfer state in fact become lower in energy than the regular state (compare Figs. 2.11(b) and 2.11(c)). The reason is that the x-ray absorption process again creates the core hole potential U_{pd} lowering the 3d energies, but no additional correlation energy U_{dd} has to be expended in turn, so that the final state charge-transfer energy is negative

$$\Delta_f^{\mathrm{XPS}} = \Delta - U_{\mathrm{pd}} < 0 \quad .$$

[6] U_{dd} can be thought of as the Coulomb repulsion among the 3d electrons. Its formal definition is the energy it costs to transfer a 3d electron from one metal cation to the other, i.e., realize the configuration shift $3\mathrm{d}^N + 3\mathrm{d}^N \rightarrow 3\mathrm{d}^{N+1} + 3\mathrm{d}^{N-1}$ [28].

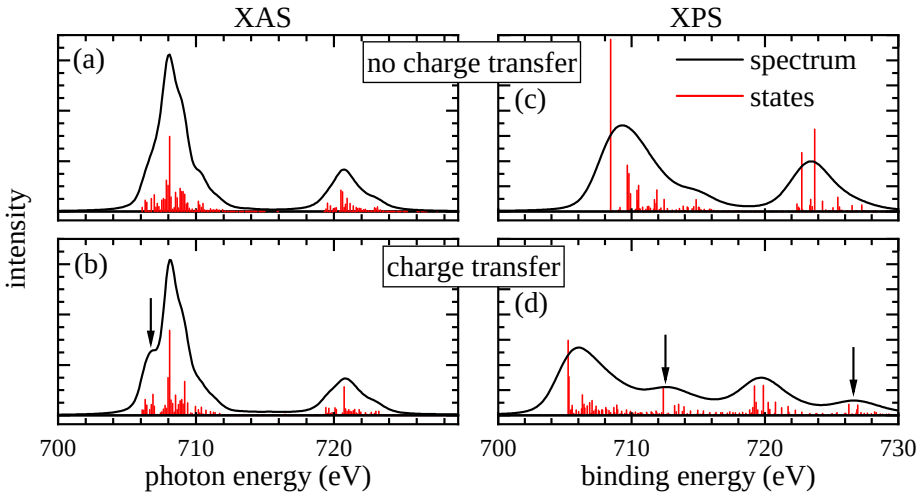

Fig. 2.12: (a),(b) Multiplet calculations of a Fe^{2+}_{oct} XAS spectrum without and with charge transfer included, respectively. (c),(d) Multiplet calculation of the XPS spectrum of Fe^{2+}_{oct} without and with charge transfer included. Black arrows highlight charge-transfer satellites. For the sake of easier comparison to the XA spectra in (a),(b), the energy axis of the XP spectra follow the orientation of the XA spectra.

Essentially, the completed charge transfer in the $2p^5 3d^7 \underline{L}$ state compensates for the photoelectron lost to the excitation. The second charge-transfer configuration $2p^5 3d^8 \underline{L}^2$ is separated from the non-charge-transfer state by $2 \cdot (\Delta - U_{pd}) + U_{dd}$, which is often still negative. This is the reason why charge transfer is the most important effect in XPS [52,53], while XAS spectra of the transition metal L edge can be described well even when neglecting charge transfer altogether [51]. Figures 2.12(a),(b) show XAS spectra of Fe^{2+}_{oct} without and with charge transfer, respectively, and Figs. 2.12(c),(d) the same with XPS spectra. In XAS, a small charge-transfer satellites on the low energy side of Fe L_3 develops, highlighted by a black arrow. In XPS, one strong satellite for each, $Fe2p_{3/2}$ and $Fe2p_{1/2}$ appears, and both peaks shift in energy. This shift, caused by the binding of the cation to its surrounding, is called *chemical shift*, and is much like the charge-transfer satellites extremely sensitive to the valency of the cation. Both can be used to identify the oxidation state of the element in question.

In the multiplet calculation, charge-transfer is implemented by calculating the dipole transition between the charge-transfer states on top of the non-charge-transfer ones (cf. black arrows between Figs. 2.11(a)-(c)), and also the mixing between the charge-transfer states has to be computed (blue arrows in Figs. 2.11(a)-(c))

$$H_{\mathrm{mix,i}} = \langle 2p^6 3d^6 | \frac{\widehat{t}}{\Delta_{\mathrm{i}}} | 2p^6 3d^7 \underline{L} \rangle \tag{2.25}$$

$$H_{\mathrm{mix,f}} = \langle 2p^5 3d^7 | \frac{\widehat{t}}{\Delta_{\mathrm{f}}} | 2p^5 3d^8 \underline{L} \rangle \tag{2.26}$$

$$\tag{2.27}$$

Besides the charge-transfer energies Δ explained earlier, the hybridization parameters $\widehat{t}$ are

important, which describe the mixing strength between the states. Although they can in principle be different for initial and final states, they are usually assumed to be equal. However, usually different hybridization parameters are chosen for e_g and t_{2g} states.

Limitations

CTM calculations are very successful in reproducing spectra for localized electron systems, such as metal oxides. However, some features observed in recorded spectra are not accounted for. First and foremost, CTM is an atomistic simulation at its heart. Band effects are not included in this framework, which is why CTM is not a good starting point for metal spectra, for instance. For those, DFT calculations usually are more suitable [28].

Second, Auger processes are not covered either. When an electron is lifted into an excited state – i.e., a 2p electron into the 3d shell –, this excited electron will eventually decay back to the 2p level, with the need for an outlet for the excess energy. For low x-ray energies, the most prevalent way to achieve this is to transfer the excess energy (710 eV for the Fe L_3 edge) to a weaker bound electron (i.e., a 3d electron), which is in turn ejected from the atom. These ejected Auger electrons have a specific kinetic energy and are measured in XPS alongside the photoelectrons. They cause very similar peaks, which can also be spectroscopically evaluated. In fact, Auger electron spectroscopy is also a widespread technique.

Third, shake-up satellites are not described by CTM. In a shake-up process, the kinetic energy of an ejected photoelectron is partially transferred to a valence band electron, which is lifted to some higher state. The kinetic energy of the photoelectron then does not obey Eq. (2.16) anymore, because it is additionally lowered by the shake-up process. Because another transition between quantized states is involved, these processes again happen at distinct energies, leading to a distinct satellite feature close to an XPS line. These satellites are again not covered by CTM and may appear systematically in measurements, but not in the simulations.

Lastly, inelastic processes are also not covered. A plethora of inelastic processes in the crystal ultimately result in the fact that an x-ray photon of energy E_{ph} can trigger any excitation process with $E < E_{\mathrm{ph}}$. Consequently, even an x-ray with a non-resonant energy may be absorbed by a solid and excite a variety of effects, leading to intensity steps beneath the absorption lines. This is the reason why Fig. 2.8(a) shows steps at the resonant energies instead of sharp lines predicted by multiplet calculations. Analogously for XPS, inelastic scattering of photoelectrons in the crystal cause photoelectrons to be emitted with energies not governed by Eq. (2.16), again leading to a background that increases in steps beneath the main lines, as can be seen in Fig. 2.8(b). These processes generate a background in both XAS and XPS measurements which are not accounted for by CTM calculations. These processes generate a background in both XAS and XPS measurements which have to be subtracted in order to compare CTM simulations to experimental data.

Despite these limitations, CTM calculations can still reproduce most of the characteristic features in transition metal oxides and are a valuable tool to access their electronic structure.

2.4.3. X-ray photoelectron spectroscopy

XPS is a widespread spectroscopic technique, since well-developed lab-based machines have been commercially available since the 1970s [58]. The most basic use is to record the pho-

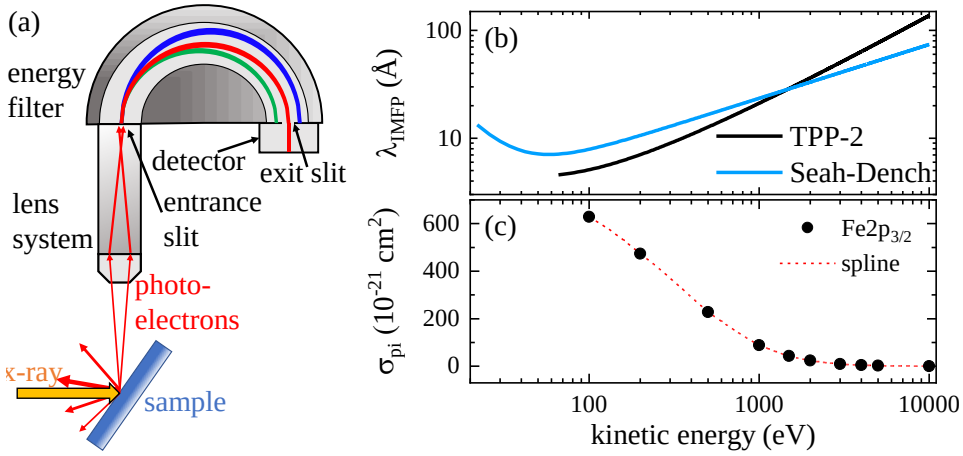

Fig. 2.13: (a) Setup of an XPS measurement. The red arrows are photoelectrons. Blue, green and red arcs in the energy filter represent electron paths for different kinetic energies. Reproduced after Ref. [54]. (b) Inelastic mean free path λ_{IMFP} of electrons in Fe_3O_4 as a function of kinetic energy, calculated from the TPP-2 equation [55] and the equation of Seah and Dench [56]. (b) Subshell photoionization cross section σ_{pi} of the $Fe2p_{3/2}$ state as a function of energy. Data points are tabulated values taken from Ref. [57], dashed line a spline.

toelectron count for a wide energy range and identify the chemical composition from the elements' characteristic line – a different term for XPS is therefore *electron spectroscopy for chemical analysis* (ESCA). From the intensity of the occuring peaks, also the quantitative compositions and stoichiometries of samples can be deduced [34,35,59,60] if the x-ray absorption cross sections are known [57]. In combination with suitable calculation techniques, such as DFT in local spin density approximation [27,61] or CTM theory, even the coordination and hybridization of the atoms in the solid can be examined by XPS [52,53].

The physics behind XPS have alreay been explained in Sec. 2.4.2 along the CTM calculations. The measurement setup is sketched in Fig. 2.13(a). The sample is exposed to an x-ray beam and emits photoelectrons with a broad spectrum of kinetic energies. They are emitted in all directions, but their angular distribution is not uniform, since it depends on the orbital the respective electron is excited from [57]. An analyzer is positioned close to the sample and collects the photoelectrons emitted in its directions. These electrons are collimated in a lens system and decelerated, before they are guided into an analyzer – the most common type in modern setups being the hemispherical energy filter, offering improved resolution and flexibility compared to linear filters, such as cylindrical mirror analyzers [62]. Here, an electric field is applied that forces the electrons on a circular path with a radius that depends on the kinetic energy of the electrons. This is indicated by the differently colored lines in the energy filter in Fig. 2.13(a). Only electrons of a certain kinetic energy will pass through the exit slit and be counted in the detector, controlled by the decelerating voltage in the lens system and the electric field in the hemispherical analyzer. In the so-called fixed transmission mode, the electric field in the hemispherical analyzer is kept constant, so that only electrons arriving at the entrance slit in a energy window around a fixed pass energy E_{pass} can reach the detector. By tuning the deceleration voltage in the lens system, photoelectrons of different initial kinetic energy are decelerated to this pass energy, and this way, a spectrum is recorded.

By using a fixed pass energy, the energy resolution is kept constant for all energies during the measurement. The choice of the pass energy is effectively a trade-off between signal quality and energy resolution: High pass energies improve the electron transmission, resulting in a higher signal, but lower the energy resolution.

XPS is a surface-sensitive technique, since the electrons generated in deeper parts of the sample are reabsorbed before they can leave the sample. The distance that electrons can travel in a material before a $(1 - e^{-1})$ fraction of them is absorbed is called *inelastic mean free path* $\lambda_{\mathrm{IMFP}}(E_{\mathrm{kin}})$ and depends on the kinetic energy E_{kin} of the electron, and shows a similar behavior for all solids. Seah and Dench developed an empirical model which universally describes the quantity $\lambda_{\mathrm{IMFP}}(E_{\mathrm{kin}})/\sqrt{d_{\mathrm{monolayer}}}$ for all materials, where $d_{\mathrm{monolayer}}$ – the thickness of a single monolayer – is the only material-dependent quantity [56]. For Fe_3O_4, this curve is plotted as blue line in Fig. 2.13(b). It captures well the experimentally observed two regimes, which are governed by different excitation mechanisms in the solid [63]. However, better quantitative agreement is reached by the TPP-2 model [55], depicted as black curve in Fig. 2.13(b).

According to Eq. (2.16), this energy for a given binding energy E_{bin} can be controlled by the excitation energy E_{ph}. Therefore, the choice of x-ray energy affects the probing depth of the technique. Typical x-ray sources used in the laboratory are x-ray tubes with Mg ($E_{\mathrm{ph}} = 1254\,\mathrm{eV}$) or Al anode ($E_{\mathrm{ph}} = 1486\,\mathrm{eV}$). Often photoelectron spectroscopy using excitation energies in this range is referred to as XPS, while at excitation energies of about 5 keV and higher, the method is called hard x-ray photoelectron spectroscopy (HAXPES). Other than the used energy the consequently higher probing depth, HAXPES is exactly the same method as XPS.While there are x-ray tubes with hard x-ray energies available (i.e., Cr with $E_{\mathrm{ph}} = 5415\,\mathrm{eV}$), their rather low x-ray flux of tubes (unmonochromatized $\sim 10^{11}\,\frac{\mathrm{photons}}{\mathrm{s}}$ [64], monochromatized $\sim 10^{10}\,\frac{\mathrm{photons}}{\mathrm{s}}$ [65]) becomes a bigger problem in HAXPES, because the photoionization cross sections σ_{cs} of the electronic states in the interesting energy range of $E_{\mathrm{bin}} < 1000\,\mathrm{eV}$ decrease rapidly with the kinetic energy of the photoelectron, depicted in Fig. 2.13 for the $Fe2p_{3/2}$ state. For this reason, the excitation efficiency of these states and consequently the XPS signal becomes small for the excitation with hard x-rays, which are therefore less frequently used in the laboratory. In constrast, HAXPES experiments are often performed at synchrotron facilities with considerably higher photon densities for monochromatized x-rays ($\sim 10^{13}\,\frac{\mathrm{photons}}{\mathrm{s}}$ [66]), counteracting the drop in excitation efficiency.

2.4.4. X-ray absorption spectroscopy

Although XAS is based on the very same physical effect as XPS, it offers some complimentary value. As discussed in Sec. 2.4.2, XA spectra are less sensitive to charge-transfer effects than XPS. Consequently, the distinction of the oxidation state – which heavily influences the charge transfer – is possible, but not as easy as in XPS (cf. Fig. 2.12). In contrast, crystal field effects are better visible in XA spectra than in XP spectra, so it is easier to recognize the coordination of the measured ions in XAS. The most important feature, however, is the fact that XAS spectra are directly proportional the x-ray attenuation coefficient $\alpha_{\mathrm{A}}(E)$ [48]

$$I_{\mathrm{XAS}}(E) \propto \alpha_{\mathrm{A}}(E) \propto f_2(E) \quad . \tag{2.28}$$

This is useful because from this quantity, many other optical quantities describing the interaction of x-rays and the material can be derived. Some of them will be listed here. α_A is closely related to the x-ray absorption length

$$\lambda_\mathrm{A} = \frac{1}{\alpha_\mathrm{A}} \quad , \tag{2.29}$$

and can be used to calculate the transmission T of an x-ray through a material of thickness d

$$T = e^{-d/\lambda_\mathrm{A}} = e^{-d\,\cdot\,\alpha_\mathrm{A}} \tag{2.30}$$

The absorption coefficient is related to the imaginary part of the atomic scattering factor by [48]

$$f_2 = \frac{\alpha_\mathrm{A}}{2\ r_0\ \lambda\ n_V}, \tag{2.31}$$

where n_V is number of atoms per unit volume, r_0 is the classical electron radius and λ is the wavelength of the attenuated x-rays [48]. From $f_2(E)$, the real part of the atomic scattering factor $f_1(E)$ can be obtained by a Kramers-Kronig transformation [31]

$$f_1(E_i) = Z + \frac{2}{\pi}\int_0^\infty \frac{\epsilon^2 f_2(\epsilon)}{E_i^2 - \epsilon^2} d\epsilon \tag{2.32}$$

$$\approx Z + \frac{2}{\pi}\sum_{\epsilon=E_1}^{E_N} \frac{\epsilon f_2(\epsilon)}{E_i^2 - \epsilon} \quad , \tag{2.33}$$

with Z being the atomic number of the element in question. Equation 2.33 is a way to numerically perform the Kramers-Kronig transformation using a discrete dataset of $f_2(E)$ with energies $E_1 ... E_N$. With f_1 and f_2, the index of refraction [48]

$$n_\mathrm{r} = 1 - \frac{1}{2\pi}\ n_V r_0\ \lambda^2 \cdot (f_1 + i f_2) = 1 - \delta + i\beta \tag{2.34}$$

can be obtained. The quantities δ and β are called the optical dispersion and the optical absorption, respectively, and are conventionally used to represent the index of refraction in x-ray optics. The transformation of these quantities into each other is shown in Fig. 2.14. According to Eq. (2.28), the measured XA spectrum can be converted into a physical quantity by using tabulated values, for instance, for α_A or – often more conveniently – f_2 [48,67,68]. The reason is that the optical properties of solids can be well interpolated or calculated based on experimental pre-knowledge under the assumption that the atoms in a solid are non-interacting, as long as the x-ray energies are far from an absorption edge. At the absorption edges, these quantities change rapidly with energy, sensitively depending on the exact state of the atom, and is consequently different from sample to sample. Therefore, the strategy is to measure XAS curves prior to and after the edge wide enough, so that the beginning and end of the measured spectrum becomes comparable to the tabulated values. This is demonstrated in Fig. 2.14(b). The blue dashed line shows tabulated values for $\alpha_\mathrm{A}(E)$, and the red curve is the scaled XA spectrum from Fig. 2.14(a). Typically, the measured spectrum is quite flat prior to the edge and can be easily fit to the tabulated value. However, after the edge,

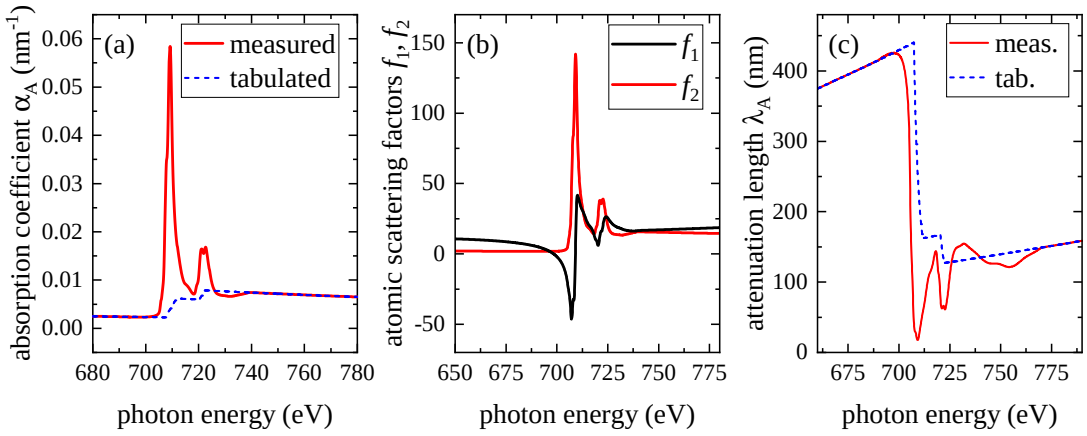

Fig. 2.14: (a) Experimental data (red) scaled to the tabulated absorption edge (blue) of the absorption coefficient α_A [48, 67, 68]. (b) Atomic scattering factors f_1, f_2, obtained by scaling the XA spectrum to tabulated f_2 and performing a Kramers-Kronig transformation (cf. Eq. (2.32)) for f_1. (c) X-ray attenuation length λ_A derived from the spectra in (b) by applying Eq. (2.29).

still some spectral features occur. These are mostly fine structure effects and may make it difficult to reach a satisfying match between tabulated and measured values[7]. From α_A, Eq. (2.31) can be used to obtain the atomic scattering factor f_2. The function $f_2(E)$ is plotted in Fig. 2.14(c) in red. The Kramers-Kronig transformation Eq. (2.32) converts it into the real part of the atomic scattering factor, $f_1(E)$, shown as black line in Fig. 2.14(c). And finally, with Eq. (2.29), from α_A the x-ray attenuation length λ_A can be obtained, displayed in Fig. 2.14(d). It can be seen that the attenuation length for x-rays prior to the edge is about 400 nm, but at the L_3 edge, absorption becomes so strong that it drops as low as 15 nm.

Experimentally, laboratory devices for XAS are not as common as for XPS. The necessity to access a wide band of x-ray wavelengths from x-ray tubes comes at the downside of very low photon fluxes of about $\sim 10^{-2} - 10^{-4} \frac{\text{photons}}{\text{s}}$ [69]. For this reason, XAS is usually performed at synchrotron light sources with scannable x-ray energies. There, recording XA spectra merely requires illumination of the sample with the x-ray beam and a way to detect the absorption. There are four common detection schemes: electron yield (EY), fluorescence yield (FY), luminescence yield (LY) and transmission. In transmission, the sample is placed between the incoming beam and an x-ray detector, and the transmitted intensity of the beam is recorded as a function of energy. This is the most direct access to the absorption coefficient, however, it is unsuitable for ultrathin film samples, which are grown on a substrate and cannot be separately investigated. The other three detection schemes will be discussed in the following.

Electron yield

The EY detection scheme is sketched in Fig. 2.15(a). The probe for the absorbed x-rays are the emitted secondary electrons – mostly Auger electrons –, which are ejected during the relaxation of the excited state into the ground state, and can be detected by putting a wire

[7] They can be valuable in their own right though; the group of spectroscopic techniques of x-ray absorption fine structure (XAFS) is concerned with exactly these features.

on the sample surface, where the accumulation of Auger electrons will cause a small current which is proportional to the x-ray absorption. This current can be measured with a suitably sensitive amperemeter. For this reason, EY can only be used for electrically conductive materials. In the default setup sketched in Fig. 2.15(a), all generated electrons are counted, and the detection scheme is called *total electron yield* (TEY). This is the most widespread method for ultrathin films. It is also possible to apply a filter voltage in order to collect only electrons of certain kinetic energies. This technique is called *partial electron yield* (PEY) and can be useful to further increase the surface sensitivity [70].

EY is a surface-sensitive method, because only electrons that can reach the surface before being reabsorbed can be detected, with the probing depth in magnetite at the Fe L edge being about $20 - 30\,\text{Å}$ [71] in TEY mode. The number of electrons dN_{TEY} arriving at the surface from a layer of thickness dz at a sample depth z is [72]

$$dN_{\text{TEY}}(E,z) = \frac{N_{\text{ph}}}{\lambda_{\text{A}}\sin(\theta)} \cdot e^{-z/(\lambda_{\text{A}}\sin(\theta))} \cdot e^{-z/\lambda_{\text{IMFP}}} dz, \tag{2.35}$$

with θ being the incidence glancing angle of the x-ray. N_{ph} is the number of incident photons. At depth z, their number has been reduced according to $e^{-z/(\lambda_{\text{A}}\sin(\theta))}$, and in the layer of thickness dz a fraction of $dz/(\lambda_{\text{A}}\sin(\theta))$ will be absorbed. This gives the number of secondary electrons at depth z, if it assumed that every absorbed photon generates one secondary electron, and of these a fraction $e^{-z/\lambda_{\text{IMFP}}}$ will arrive at the surface. For a film of thickness d, integration from $z = 0$ to $z = d$ yields the number of electrons $N_{\text{TEY}}(E,z)$

$$\begin{aligned} I_{\text{XAS}} \propto N_{\text{TEY}}(E) \quad &\propto \quad \frac{\lambda_{\text{IMFP}}}{\lambda_{\text{IMFP}} + \lambda_{\text{A}}\sin(\theta)} \cdot (1 - e^{-d\cdot(\frac{1}{\lambda_{\text{A}}\sin(\theta)} + \frac{1}{\lambda_{\text{IMFP}}})}) \\ &\approx \quad \underbrace{\frac{\lambda_{\text{IMFP}}}{\sin(\theta)} \cdot (1 - e^{-d/\lambda_{\text{IMFP}}}) \cdot \frac{1}{\lambda_{\text{A}}(E)}}_{\text{if } \lambda_{\text{IMFP}} \ll \lambda_{\text{A}}(E)\sin(\theta)} \propto \alpha_{\text{A}}(E) \quad . \end{aligned} \tag{2.36}$$

This number depends both on the inelastic mean free path λ_{IMFP} of the electrons and on the x-ray attenuation length $\lambda_{\text{A}}(E)$. According to the TPP-2 model presented in Fig. 2.13(b), the inelastic mean free path is approximately constant at $\lambda_{\text{IMFP}} = 15\,\text{Å}$ in the energy range of the Fe L absorption edge ($\sim 700 - 730\,\text{eV}$). However, as can be seen in Fig. 2.14(d), $\lambda_{\text{A}}(E)$ is rapidly changing with energy at the absorption edge, with a minimum of $\lambda_{\text{A}} = 150\,\text{Å}$. As Eq. (2.36) reveals, the identity of Eq. (2.28), $I_{\text{XAS}} \propto \alpha_{\text{A}}$, holds true as long as the depth sensitivity is limited by the electron escape depth, thus if $\lambda_{\text{A}}\sin(\theta)$ is much bigger than λ_{IMFP}, which is usually true. However, at maximum absorption and at grazing incidence, this might not be the case, because the x-ray becomes significantly damped at sample depths z where electrons could still escape from, and the XA spectrum becomes distorted due to saturation effects. If the distortion is not too strong, it can be corrected. In order to do so, first the approximate absorption coefficient $\alpha'_{\text{A}}(E)$ is determined from the XA spectrum I_{XAS} using the method described earlier in Fig. 2.14. Then, the corrected absorption $\alpha_{\text{A}}(E)$ is determined as [72]

$$\alpha_{\text{A}}(E) = (\frac{1}{\alpha'_{\text{A}}(E)} - \lambda_{\text{IMFP}})^{-1} \quad . \tag{2.37}$$

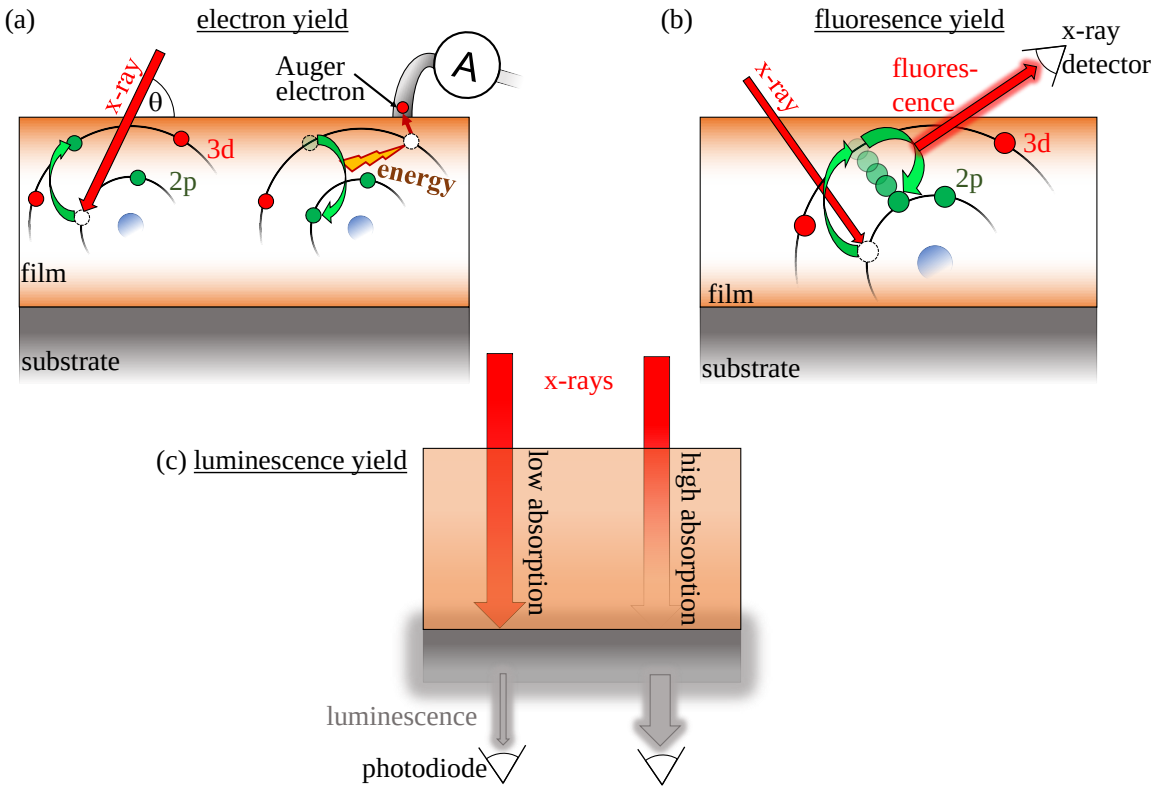

Fig. 2.15: (a) Illustration of the electron yield detection scheme. An x-ray photon excites a 2p electron into a 3d state. Subsequently, an electron relaxes back to fill the 2p core hole, and the excess energy is transferred to a different 3d electron, which leaves the atom as an Auger electron (LMM Auger transition). If it reaches the surface, it can be detected as a charge current. (b) Illustration of fluorescence yield detection. The excited electron decays by emitting the excess energy in form of an x-ray photon, which is then detected as a probe of the absorption strength. (c) Illustration of the luminescence yield detection. The x-ray is transmitted through the sample and excites luminescence in the substrate which can be measured as probe for the x-ray transmission.

Figure 2.16(a) shows TEY spectra of a Fe_3O_4 film before and after the correction.

Fluorescence yield

An alternative approach is to not use the Auger decay channel, but using FY. After the excitation of the 2p electron to the 3d state, it can emit an x-ray photon in order to lose the excess energy. This is illustrated in Fig. 2.15(b). Fluorescent decay happens with less efficiency in the sub-1 keV region than Auger decay [29] and therefore usually leads to a weaker signal. It can be helpful, however, for insulating materials that do not allow for EY detection, or for a higher information depth. Since the depth sensitivity is not limited anymore by the electron escape depth of about $\lambda_{\mathrm{IMFP}} \approx 1.5\,\mathrm{nm}$, but only by the x-ray attenuation length of $\min(\lambda_{\mathrm{A}}(E)) \approx 15\,\mathrm{nm}$. Similar to EY, either all fluorescence photons are counted as total fluorescence yield (TFY) signal, or only photons of particular energies are selected by energy-dispersive detectors. This second method is called *partial fluorescence yield* (PFY). PFY can

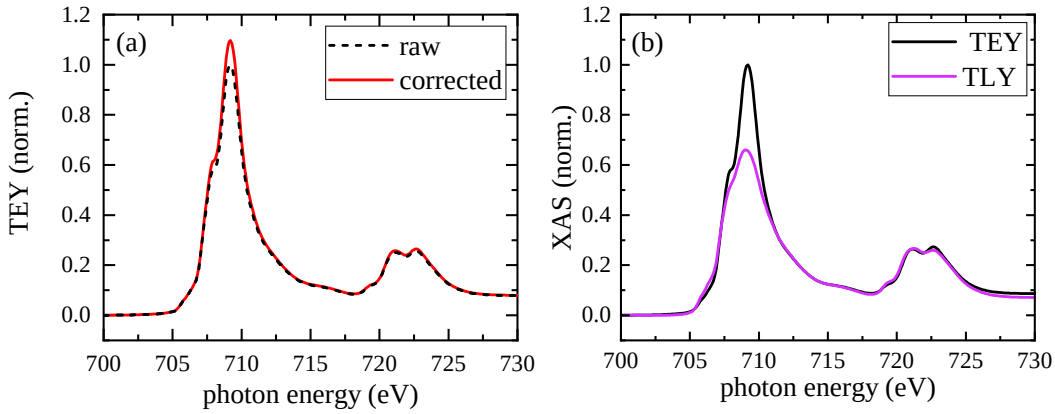

Fig. 2.16: (a) Comparison of the raw TEY data of a 25 nm Fe_3O_4 film and a spectrum corrected using Eq. (2.37) with $\lambda_{\mathrm{IMFP}} = 15$ Å. (b) Comparison of TEY and TLY data recorded simultaneously. The L_3 line of the TLY is strongly distorted.

be considerably more useful than PEY, because certain valence states of the sample can be selected by only detecting fluorescence photons of their respective energy [70].

However, FY unfortunately comes with a number of caveats. First, self-absorption of the fluorescence photons plays a major role. Analogously to Eq. (2.35), an expression for the number of fluorescence photons $dN_{\mathrm{TFY}}(E,z)$ from depth z can be derived

$$dN_{\mathrm{TFY}}(E,z) \propto \frac{1}{\lambda_{\mathrm{A}}(E)\sin(\theta)} e^{-z/(\lambda_{\mathrm{A}}(E)\sin(\theta))} e^{-z/\lambda_{\mathrm{A}}(E_{\mathrm{fluor}})} dz \quad , \tag{2.38}$$

and integrated to

$$N_{\mathrm{TFY}}(E) \propto \frac{\lambda_{\mathrm{A}}(E_{\mathrm{fluor}})}{\lambda_{\mathrm{A}}(E_{\mathrm{fluor}}) + \lambda_{\mathrm{A}}(E)\sin(\theta)} \cdot \left(1 - e^{-d\cdot\left(\frac{1}{\lambda_{\mathrm{A}}(E)\sin(\theta)} + \frac{1}{\lambda_{\mathrm{A}}(E_{\mathrm{fluor}})}\right)}\right) \quad . \tag{2.39}$$

Here, E_{fluor} is the energy of the emitted fluorescence photon and it was assumed that these photons are detected normal to the sample surface. Different to the TEY case, usually the x-ray attenuation length $\lambda_{\mathrm{A}}(E)$ can be expected to be comparable at energies E and E_{fluor}, and at the maximum absorption, even $\lambda_{\mathrm{A}}(E) \leq \lambda_{\mathrm{A}}(E_{\mathrm{fluor}})$. With a solid estimation of $\lambda_{\mathrm{A}}(E_{\mathrm{fluor}})$, a correction can be attempted, but usually the estimation is not easily available, and often the distortion is too strong for a satisfying correction [29]. There are more sophisticated approaches to self-absorption correction [73, 74], but in any case, special care has to be taken.

Another difficulty particularly for the L edge of transition metals is that the efficiency of fluorescence decay can vary across the energy range of the L edge of more than a factor of 4 [75]. This leads to another source of distortion that can only be accounted for by detailed calculations of the different decay efficiencies of the multiplet states.

Luminescence yield

Another detection technique is offered by total luminescence yield (TLY). It is very attractive because it is a transmission technique and therefore offers bulk sensitivity even for ultrathin films. It can be used when the sample substrate can be excited to luminescence by the x-rays

in the used energy range. The principle is sketched in Fig. 2.15(c). The x-rays are transmitted through the film and are ultimately absorbed in the substrate. An additional prerequisite for this detection scheme is therefore that the substrate does not have an absorption edge in the measured energy range. The excited states in the substrate relax to valence holes, which then decay by emitting luminescence, which is typically in the optical energy range [29]. At high absorption in the film, most of the x-rays will be absorbed in the film and less photons are available to produce substrate luminescence. Therefore, the strength of the luminescence serves as a probe of the absorption in the film and is recorded by a photodiode behind the substrate. Examples for suitable substrates are Al_2O_3 or MgO, which are frequently used for Fe_3O_4 thin films [76–78].

The interpretation of TLY spectra is easier as in the TFY case, but is limited to film thicknesses smaller than the minimal x-ray attenuation length λ_A. Otherwise, hardly any x-rays will reach the substrate and the high absorption parts of the XA spectrum will appear compressed. This is displayed in Fig. 2.16(b). The XA spectra were recorded simultaneously in TEY and TLY mode for a 25 nm thick Fe_3O_4 film on MgO(001). They agree very well in low absorption, but at the L_3 peak, at which $\lambda_A \approx 15\,\text{nm}$, the TLY peak is heavily suppressed, making a quantitative evaluation difficult.

2.4.5. X-ray magnetic circular dichroism

A very powerful variation of XAS is offered by the XMCD effect. If two XA spectra are recorded on a magnetic sample using circularly polarized x-rays with opposite helicities (σ^+ and σ^-), the spectra I^{σ^+} and I^{σ^-} are different for both helicities. Their difference is sensitive to the magnetic states in the sample and is called XMCD spectrum

$$I_{\text{XMCD}} = I^{\sigma^+} - I^{\sigma^-} \quad , \tag{2.40}$$

and the 'unpolarized' XAS spectrum can be retained by

$$I_{\text{XAS}} = I^{\sigma^+} + I^{\sigma^-} \quad . \tag{2.41}$$

Figure 2.17(a) introduces the coordinate system for the following explanations. An array of magnetic atoms is ordered in a sample parallel to the yz-plane. The x-ray propagates in its xz incidence plane, with an incidence angle θ to the z-axis. It has a circular polarization σ^+; the polarization vector $\widehat{\epsilon}$ is rotating in the plane normal to the propagation direction. The quantization axis of the magnetic moments of the atoms is z, and the magnetization direction follows an outer magnetic field B_z in the $-z$ direction.

The dichroic component I_{XMCD} depends on the angle θ between the polarization plane – which is normal to the propagation direction of the x-ray – and the magnetization direction ($-z$). If the magnetization direction lies in the polarization plane ($\theta = 90°$), no XMCD signal will be observed, and it will be maximal if the magnetization direction stands perpendicular on the polarization plane ($\theta = 0°$). The XMCD signal I_{XMCD} obtained this way is not yet normalized with respect to the angle. For quantitative comparison, it is more practical to transform the XAS data $I^{\sigma+}$, $I^{\sigma-}$ into the absorption coefficients $\alpha_A^{\sigma+}$, $\alpha_A^{\sigma-}$ and define the

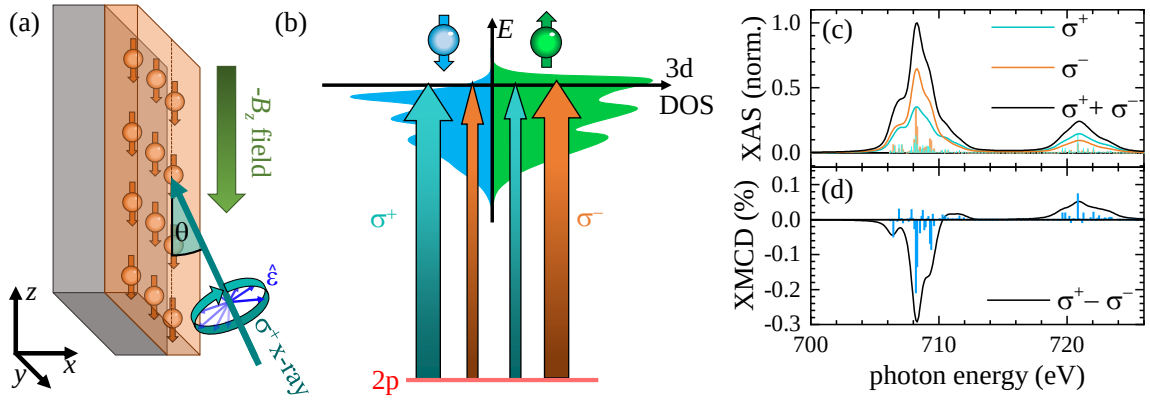

Fig. 2.17: (a) Coordinate system of the magnetic sample. The blue arrows indicate the x-ray's polarization vector. (b) Sketch of the excitation from a spin-orbit split 2p state into a spin-polarized 3d band without spin-orbit coupling. (c),(d) CTM calculations of the (c) XAS and (d) XMCD spectra of a Fe^{2+}_{oct} cation. XA spectra are displayed for both σ^+ and σ^- helicities, and their sum, the unpolarized XA spectrum. They are normalized to the maximum of the unpolarized XA spectrum (cf. Eq. (2.41)).

dichroic absorption coefficient

$$\Delta\alpha_{\mathrm{A}} = \frac{(\alpha_{\mathrm{A}}^{\sigma+} - \alpha_{\mathrm{A}}^{\sigma-})}{\cos(\theta)\cdot \mathrm{DOP}} \quad , \tag{2.42}$$

with DOP being the degree of polarization of the x-rays.

In Sec. 2.4.2, the origin of the L edge XAS shape has been explained by dipole excitations between the multiplet states of the $2p^6 3d^N$ and $2p^5 3d^{N+1}$ configurations. The dipole operator $\widehat{p}$ allows for transitions between states with quantum number differences $\Delta J = -1, 0, 1$, $\Delta S = 0$ and $\Delta L = \pm 1$. This holds true for linearly polarized and unpolarized x-rays. However, for circularly polarized x-rays, an additional selection rule for the total magnetic quantum number m_J comes into play; for positive helicity (σ^+) $\Delta m_J = +1$, for negative helicity (σ^-) $\Delta m_J = -1$. This enables access to the magnetic properties of a material. This is illustrated in Fig. 2.17(b), in which x-rays excite electrons from an 2p state into a spin-polarized 3d band, which has more free spin-up ($m_S = \uparrow$) than spin-down ($m_S = \downarrow$) states at the Fermi energy. Cyan arrows indicate the transition rates for positive helicity, and orange for negative helicity. It can be seen that x-rays with both helicities can excite electrons into both spin bands, but they do so with different efficiency: x-ray photons with σ^+ helicity excite more efficiently into the spin-down band, while x-ray photons with σ^- helicity can more efficiently excite electrons into the spin-up band. Because more spin-up states are available than spin-down states, the absorption of σ^- x-ray photons is stronger than for σ^+ x-ray photons, causing an XMCD signal. This is displayed in Fig. 2.17(c),(d). A more detailed explanation of the origin of the XMCD effect can be found in Appendix A.

Including XMCD effects into CTM calculations requires a single new parameter, the exchange field Δ_{exc}, which controls the splitting of the m_J states. A big splitting will result in a higher occupation of the lower m_J levels and a higher spin-polarization. Typical values for Δ_{exc} are in the range of 0 to 50 meV [23, 79, 80]. This is well in the range of typical thermal energies – for instance, a room temperature of 292 K corresponds to 25 meV, which means that the

splitting of the m_J levels can be thermally overcome. If the thermal energy is much bigger than the splitting due to the exchange field, the XMCD effect will vanish. If the energy terms are in a similar range, their spectral shape remains equal, but are reduced in intensity [29]. In all calculations in this work, thermal population of higher energy levels is accounted for by a Boltzmann distribution.

Additionally, the cubic symmetry introduced by the crystal field has to be lowered further to tetragonal, because the magnetization direction along a certain crystal axis lifts the fourfold rotational symmetry.

Sum Rules

A very widespread analysis technique of XMCD data are the sum rules [81–83]. These allow to extract the spin and the orbital momentum of the electrons from the XAS and XMCD spectra. As discussed in Appendix A, the origin of the $-1:1$ XMCD ratio at the L_3 and L_2 edge, $A_{L_3} + A_{L_2} = 0$, is an expression of the fact that the 2p spin-orbit coupling splits the 2p states into $L+S$ and the $L-S$ states, and is true if the magnetic moment is purely a spin moment. For this reason, the deviation from this ratio is a measure of the orbital moment,

$$\mu_{\mathrm{orb}} = -\frac{4\int_{L_3+L2}(I^{\sigma+} - I^{\sigma-})dE}{3\int_{L_3+L2}(I^{\sigma+} + I^{\sigma-})dE} \cdot n_{\mathrm{h}}\mu_{\mathrm{B}} = -\frac{4}{3}\frac{A_{L_3} + A_{L_2}}{A_{\mathrm{XAS}}} n_{\mathrm{h}}\mu_{\mathrm{B}} \quad . \tag{2.43}$$

The spin moment itself is proportional to the total amplitude of the oppositely oriented areas $(A_{L_3} - 2 \cdot A_{L_2})$

$$\begin{aligned}\mu_{\mathrm{spin}} + 7\,\langle \widehat{T}_z \rangle &= -\frac{6\int_{L_3}(I^{\sigma+} - I^{\sigma-})dE - 4\int_{L_3+L2}(I^{\sigma+} - I^{\sigma-})dE}{\int_{L_3+L2}(I^{\sigma+} + I^{\sigma-})dE} \cdot n_{\mathrm{h}}\mu_{\mathrm{B}} \\ &= -\frac{2\cdot(A_{L_3} - 2A_{L_2})}{A_{\mathrm{XAS}}} \cdot n_{\mathrm{h}}\mu_{\mathrm{B}} \quad . \end{aligned} \tag{2.44}$$

In these equations, μ_{B} is the Bohr magneton and n_{h} is number of 3d holes per formula unit. For instance, Fe_3O_4 has $n_{\mathrm{h}} = 14$ holes per formula unit, 4 stemming from the Fe^{2+}_{oct} species and 5 each from the Fe^{3+}_{oct} and Fe^{3+}_{tet} species[8]. The obtained moments then also refer to one formula unit of Fe_3O_4. The spin moment μ_{spin} is never obtained alone, but always together with the expectation value of the magnetic dipole operator $\langle \widehat{T}_z \rangle$, which is usually not known. However, in most publications it is considered to be small and consequently omitted [23, 85, 86]. In Ref. [79], it is estimated to contribute about 2% to the spin moment for Fe^{2+} cations and 0.007% for Fe^{3+} cations. It has to be noted, however, that in Ref. [84] the contribution by $7\,\langle \widehat{T}_z \rangle$ is estimated per local spin density approximation calculations to be about 4% per octahedral cation. We will omit the term in the following, but the uncertainty introduced by it should be kept in mind.

The sum rules are very attractive because they can easily be applied to experimental data by extracting the areas A_{XAS}, A_{L_3} and A_{L_2} from the XA and XMCD spectra. The typical way to do this is explained in Fig. 2.18 [82]. Figure 2.18(a) sketches a typical layout for an XAS/XMCD experiment: A magnetic field is applied parallel to the film plane to determine

[8] Due to charge transfer effects, n_{h} might deviate from 14. Some publications use $n_{\mathrm{h}} = 13.5$ instead, as derived from local spin density approximation calculations [84].

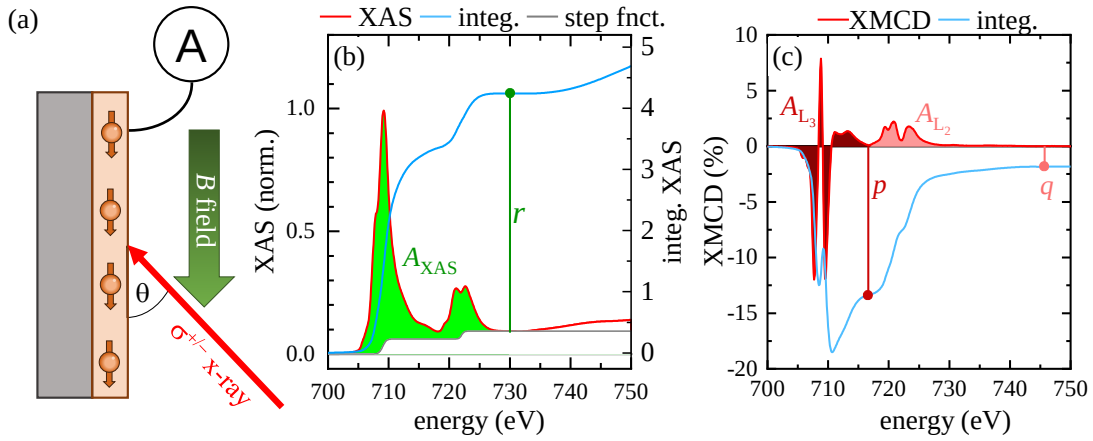

Fig. 2.18: (a) Sketch of an XMCD experiment. A magnetic field is applied in-plane to set the magnetization axis. Circularly polarized x-rays hit the sample under an angle θ. (b) XAS data from a Fe_3O_4 film in red. A step function is plotted grey as background, and the blue line (right y-axis) represents the integral over the XA spectrum. The area $A_{XAS}=r$ beneath the XA spectrum is green. (c) XMCD data corresponding to the XA data in (b). Blue is the integral over the XMCD spectrum. Dark red is the area beneath the L_3 edge A_{L_3}, and light red the area beneath the L_2 edge A_{L_2}. q is the value of the integral above the L_3 edge, p the value above both edges.

the magnetization axis. The x-rays are circularly polarized with a polarization degree DOP and hit the sample under an angle of θ. The unpolarized XA spectrum and the XMCD spectrum are obtained according to Eqs. (2.41) and (2.40), and are shown in Figs. 2.18(b),(c), respectively, for a Fe_3O_4 film. For the XA spectrum, a step-function has to be subtracted as background (grey line), and subsequently the integral is taken across the entire $L_{2,3}$ edge (blue line). The value of the integral $r = A_{\mathrm{XAS}}$ can be taken in the flat region above the L_2 edge. Similarly, the integral over the XMCD spectrum is shown as blue line in Fig. 2.18(c). The value $q = A_{L_3}$ is taken in the flat region of the integral above L_3, and $p = A_{L_3} + A_{L_2}$ is taken from above the L_2 edge. With these, Eqs. (2.43) and (2.44) become

$$\mu_{\mathrm{orb}} = \frac{-4q}{3r} \cdot n_{\mathrm{h}}\mu_{\mathrm{B}} \cdot \frac{1}{\mathrm{DOP} \cdot \cos(\theta)} \quad . \tag{2.45}$$

$$\mu_{\mathrm{spin}} = C \cdot \frac{-(6p - 4q)}{r} \cdot n_{\mathrm{h}}\mu_{\mathrm{B}} \cdot \frac{1}{\mathrm{DOP} \cdot \cos(\theta)} \tag{2.46}$$

The experimental parameters DOP and θ are accounted for in the last term, and C is a correction factor due to electron-electron Coulomb interaction across the $2p$ state, as will be discussed in the following.

The sum rules are based on the assumption that the large spin-orbit interaction fully separates the L_3 from the L_2 edge. This is mostly justified, however, the electron-electron Coulomb interaction does still cause a multiplet mixing even between $2p_{3/2}$ and $2p_{1/2}$ states. Teramura et al. performed atomic multiplet calculations in order to estimate the impact of the electron-electron Coulomb interaction on the sum rule results, and calculate the correction factor C.

cation	Fe^{2+}	Fe^{3+}	Ni^{2+}	Ni^{3+}	Co^{2+}	Co^{3+}
C	1.143	1.46	1.086	1.083	1.086	1.144

Tab. 2.4: Coulomb correction factors of transition metal cations for the spin sum rule as determined by Teramura et al. [79] Determined for crystal fields with 10Dq= 1.5 eV and an exchange field of $\Delta_{\text{exc}} = 10$ meV.

The results are summarized in Tab. 2.4 for some transition metal cations.

2.5. X-ray reflectivity

XRR is a technique that can be used to determine electron density depth profiles of thin film samples. It is based on the interference between x-rays that are reflected from the surface and the interfaces of a thin film samples. The reflection of an x-ray beam depends on the wavelength λ, the incident angle θ and the profile of the refractive index $n_{\text{r}}(z)$ along the film depth z perpendicular to the film surface. Therefore, by measuring the reflected intensity $I_{\text{r}}(\theta)$ as a function of incidence angle θ, the optical density of the film can be retrieved, including film thicknesses d and roughnesses σ. More complete descriptions of XRR can be found in Refs. [30, 31].

Figure 2.19(a) shows the reflection of an x-ray of wave vector $\mathbf{k}_i$ from an interface. It hits the interface of two optical media, with refractive indices n_{r1} and n_{r2}, under a glancing angle θ[9]. Some of the x-ray intensity will be reflected ($\mathbf{k}_f$) under the same reflection angle, θ, and some will be refracted ($\mathbf{k}_t$) into the second medium under the refraction angle θ'. Because the incident and the emergent angle are identical, the momentum transfer vector

$$\mathbf{q} = \mathbf{k}_f - \mathbf{k}_i \tag{2.47}$$

is always perpendicular to the interface. In order to arrive at a representation that does not depend on the x-ray energy, the total value of the momentum transfer vector q_z can be conveniently used instead of the incident angle θ

$$|\mathbf{q}| = q_z = \frac{4\pi}{\lambda}\sin(\theta) \quad . \tag{2.48}$$

The relation between the angles θ' and θ is given by Snell's law [31]

$$n_{\text{r1}} \cdot \cos(\theta) = n_{\text{r2}} \cdot \cos(\theta') \quad . \tag{2.49}$$

In the case of x-rays, the refractive index n_{r} is very close to 1 for almost all materials. As already briefly mentioned in Sec. 2.4.4, usually only its deviations from 1 are given, represented by the form

$$n_{\text{r}} = 1 - \delta + i\beta. \tag{2.34}$$

[9] Please note that in optics, the incident angle θ usually refers to the angle from the surface normal. However, in x-ray reflection and diffraction, θ conventionally denotes the glancing angle.

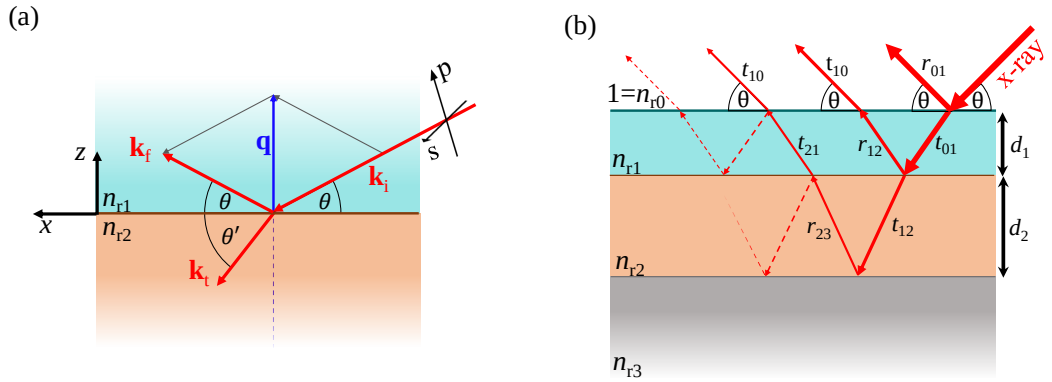

Fig. 2.19: (a) An x-ray $\mathbf{k}_i$ hitting an interface between two optical media with refractive indices n_{r1} and n_{r2} under an angle θ is partly reflected ($\mathbf{k}_f$) and partly refracted ($\mathbf{k}_t$) under the refraction angle θ'. 'p' and 's' indicate the polarization axes, and $\mathbf{q}$ is the scattering vector. (b) Reflectivity from a multilayer. At each interface of the multilayer, x-rays are reflected and refracted according to the Fresnel coefficient r_{ij} and t_{ij}, coming from layer i to layer j. For x-rays, incident, emergent and refracted angles are approximately identical. Solid arrows are first-order reflected partial beams, dashed arrows indicate beams that were reflected twice.

The real part δ is called the optical dispersion, and the imaginary part β is called the optical absorption of the material, and both typically range from $\delta \sim 10^{-6}, \beta \sim 10^{-8}$ in the hard x-ray region to $\delta, \beta \sim 10^{-3}$ in the soft x-ray region. The dispersion δ and the absorption β are closely related to the atomic scattering factors f_1 and f_2, which have been discussed in Eq. (2.34) in Sec. 2.4.4:

$$\delta = \frac{r_0\ \lambda^2\ n_V}{2\pi} f_1 = \frac{r_0\ \lambda^2}{2\pi}\rho_e \quad , \qquad \beta = \frac{r_0\ \lambda^2\ n_V}{2\pi} f_2 = \frac{\lambda}{4\pi}\alpha_A \quad , \tag{2.50}$$

with ρ_e being the electron density.

The refractive index in the vacuum is $n_{r1} = 1$, and for all materials smaller than one (save for absorption edges), $n_{r2} < 1$. If an x-ray enters a solid from the vacuum, Snell's law Eq. (2.49) requires for the refracted angle θ'

$$\cos(\theta') = \frac{n_{r1}}{n_{r2}} \cdot \cos(\theta) > 1 \quad . \tag{2.51}$$

However, this inequality is violated if θ is smaller than a critical angle

$$\theta_{crit} = \arccos(\frac{n_{r2}}{n_{r1}}) \approx \sqrt{2\delta} \quad ,$$

In that case, Eq. (2.51) has no real solution for θ', and total reflection occurs.

The fraction of the reflected intensity $|r|^2 = \frac{I_r}{I_0}$ is given by the Fresnel coefficients [30]

$$r = \frac{k_{f,z} - k_{t,z}}{k_{f,z} + k_{t,z}} \quad . \tag{2.52}$$

Here, $k_{f,z}$ and $k_{t,z}$ are the z-components of the reflected wave vector $\mathbf{k}_f$ and the refracted

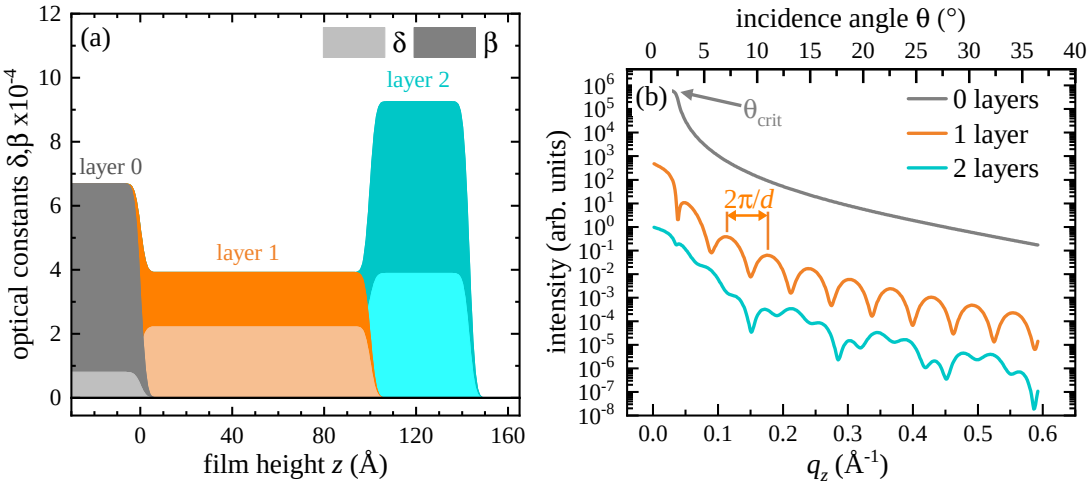

Fig. 2.20: (a) Simulated depth profiles of the optical constants δ,β of a thin film system consisting of a substrate (layer 0) and two thin films (layer 1 and layer 2). (b) XRR simulations for the reflection from a bare substrate (layer 0 in (a)), a single layer of 100 Å thickness (layer 0 + layer 1), two layers of 100 Å and 43 Å thickness (layer 0 + layer 1 +layer 2).

wave vector $\mathbf{k}_\mathrm{t}$ in Fig. 2.19(a). In terms of angles, this can be written as [30]

$$r_\mathrm{s} = \frac{n_{\mathrm{r}1}\cdot\sin(\theta) - n_{\mathrm{r}2}\cdot\sin(\theta')}{n_{\mathrm{r}1}\cdot\sin(\theta) + n_{\mathrm{r}2}\cdot\sin(\theta')} \quad , \quad r_\mathrm{p} = \frac{n_{\mathrm{r}1}\cdot\sin(\theta') - n_{\mathrm{r}2}\cdot\sin(\theta)}{n_{\mathrm{r}1}\cdot\sin(\theta') + n_{\mathrm{r}2}\cdot\sin(\theta)} \tag{2.53}$$

for x-rays with the electrical field vector perpendicular (s-polarization, r_s) and parallel (p-polarization, r_p) to the scattering plane. For hard x-rays, for which $\theta \approx \theta'$, the coefficients barely change for the two polarization channels; however, the polarization becomes important for soft x-rays, and especially at resonant energies, as will be discussed in detail in Sec. 2.6.

If an x-ray illuminates a multilayer sample, at each interface of these layers reflection and refraction occurs, characterized by the Fresnel coefficients $r_{j,j+1}$ and $t_{j,j+1}$ at the interface between layers j and $j+1$, and the total reflected intensity will be a superposition of all partial waves leaving the sample, as sketched in Fig. 2.19(b). The Fresnel coefficients have been used by Parratt to create a recursive algorithm which determines the reflected intensity from a multilayer system [87]. By posing the continuity condition that at each interface the amplitudes E of the transmitted and reflected waves have to be continous and follow the Fresnel coefficients r, the ratio of reflected E^R and transmitted amplitude E^T at an interface between layers j and $j+1$ is [30]

$$R_{j,j+1} = \frac{E_j^\mathrm{R}}{E_j^\mathrm{T}} = \frac{r_{j,j+1} + R_{j+1,j+2}\mathrm{e}^{\mathrm{i}k_{\mathrm{z,j+1}}\mathrm{d_{j+1}}}}{1 + r_{j,j+1}\cdot R_{j+1,j+2}\mathrm{e}^{\mathrm{i}k_{\mathrm{z,j+1}}\mathrm{d_{j+1}}}} \quad , \qquad \frac{I_R}{I_0} = |R_0|^2 \quad , \tag{2.54}$$

with layer thicknesses d_j. I_R is the measured reflected intensity, and requires only knowledge of R_0, which can be recursively obtained assuming that no x-rays are transmitted from the substrate. By introducing the phase factor, interference effects from different partial waves that traveled different path lengths are introduced.

In order to model real sample systems, roughnesses σ between all layers have to be accounted

for, since actual interfaces are usually not sharp. One popular way to achieve this was introduced by Névot and Crocet [88]. By assuming an error function-shape of the interface roughness, the problem can be solved analytically by simply modifying the Fresnel coefficient with an exponential damping factor

$$r_{j,j+1}^{\text{rough}} = r_{j,j+1} \mathrm{e}^{-k_{z,j} k_{z,j+1} \sigma^2}. \tag{2.55}$$

Here, $k_{z,j}$ is the normal components of the wave vector in layer j. This modified expression for the Fresnel coefficient is then inserted into Eq. 2.54. The error function profile has the advantage that it leads to a simple exponential factor for the Fresnel coefficient, and allows to continue to use the Parrat algorithm. However, it is quite limiting, because real roughness profiles may deviate from an error function profile [30,31]. It also produces bad results in cases for which the film thicknesses are similar to the roughnesses. An alternative, more flexible way to model the roughness is to represent the interface regions by a series of very thin layers with continuously changing density. This technique is preferable, but usually more demanding in terms of computing. In practice, several softwares for XRR fitting already exist and implement the Parratt algorithm described above, and can be used to fit reflectivity data [89]. For this work, the software ReMagX by Sebastian Macke has been used, which specializes in magnetic reflectivity fits [30]. Those will be described in more detail in Sec. 2.6.

Some example simulations using the Parratt formalism are shown in Fig. 2.20. A model for the depth profile of the absorption $\beta(z)$ and the dispersion $\delta(z)$ of a double layer sample are displayed in Fig. 2.20(a). The XRR signals resulting from this double layer according to the Parratt formalism outlined above are shown in Fig. 2.20(b). For the bare substrate without a film on top, the grey curve is obtained. For small angles, total reflection occurs, visible as a small plateau. After that, the intensity drops with a characteristic $\propto q_z^{-4}$ proportion. If a single layer is added (orange line), interference of the partial waves reflected at the surface and at the substrate interface lead to periodic maxima and minima, called *Kiessig* fringes. In the case of a single layer, from the length $\Delta q_z \approx \frac{2\pi}{d}$ of such a fringe the film thickness d can be immediately determined. In a system of 2 layers of different thicknesses (43 Å on top of 100 Å, cyan line), a superposition of two oscillations – caused by the 2 layer thicknesses – emerges. The strategy in an XRR experiment is to record the XRR curves from a sample, and then to find a model for optical depth profiles, like those in Fig. 2.20(a), which reproduce the data.

2.6. X-ray resonant magnetic reflectivity

XRMR is a combination of XMCD and XRR. It is either performed by recording two subsequent XRR curves with positive and negative helicity at resonant x-ray energies. Alternatively, the two XRR curves can be recorded using the same x-ray helicity, but with opposite magnetization direction.

The XMCD spectrum is simply the difference between the XAS signals from measurements with left circularly and right circularly polarized x-rays. As discussed in Sec. 2.4.4, the XAS signal is proportional to the atomic scattering factor f_2 and, via the Kramers-Kronig transformation, to f_1. These in turn are closely related to the optical constants δ and β by Eq. (2.50), which determine the shape of the XRR curves. At a dichroic resonance, the XAS intensity is different for both helicities. Accordingly, also f_2 differs, and so do the optical

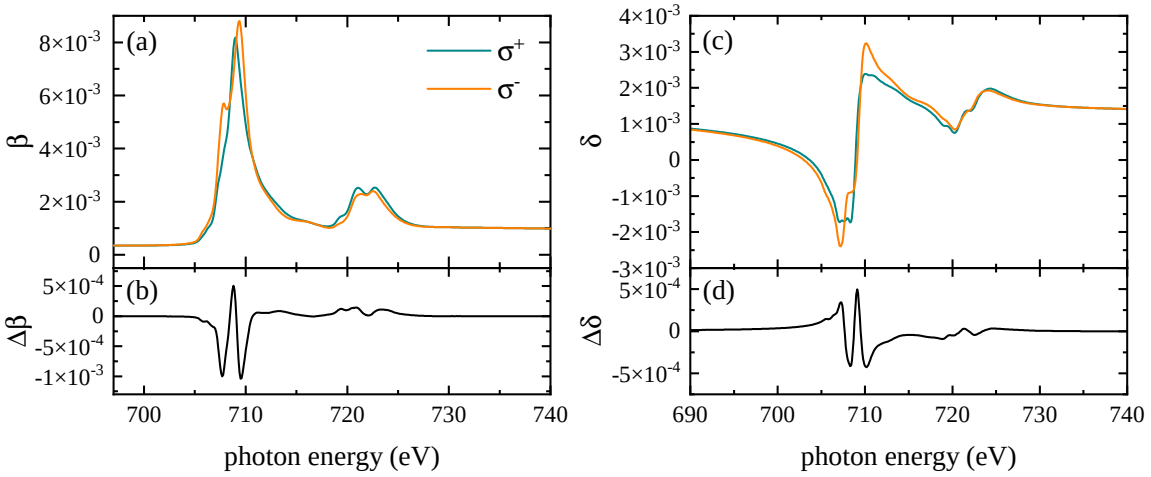

Fig. 2.21: (a) Optical absorption β of a Fe_3O_4 film for left and right circularly polarized x-rays, acquired from an XAS measurement at the Fe L edge. (b) Magnetooptical absorption $\Delta\beta$, obtained from the difference of the curves in (a) (cf. Eq. (2.57)). (c) Optical dispersion δ for both helicities, derived as Kramers-Kronig transform of the curves in (a). (d) The magnetooptical dispersion $\Delta\delta$ is the half the difference of the curves in (c) (cf. Eq. (2.56)).

constants for both helicities from the non-dichroic parts δ_0, β_0 by $\Delta\delta$,$\Delta\beta$ [30]

$$\delta = \delta_0 \pm \Delta\delta \cdot \cos(\theta) \quad , \qquad \delta_0 = \frac{\delta^+ + \delta^-}{2} \quad , \qquad \Delta\delta = \frac{\delta^+ - \delta^-}{2} \quad , \tag{2.56}$$

$$\beta = \beta_0 \mp \Delta\beta \cdot \cos(\theta) \quad , \qquad \beta_0 = \frac{\beta^+ + \beta^-}{2}, \qquad \Delta\beta = \frac{\beta^+ - \beta^-}{2} = \frac{\lambda}{4\pi}\frac{\Delta\alpha_\mathrm{A}}{2} \quad . \tag{2.57}$$

Here, θ is the incidence angle of the x-ray, and it is assumed that the magnetization direction is in-plane and parallel to the x-ray propagation, according to Fig. 2.17. Figure 2.21 illustrates the 4 quantities δ_0, β_0, $\Delta\delta$ and $\Delta\beta$. In Fig. 2.21(a), the optical absorption β is shown of a Fe_3O_4 film is shown for x-rays of different helicities at the Fe L edge, obtained from XAS data. The half of their difference, the magnetooptical absorption $\Delta\beta$, is proportional to the XMCD spectrum α_A (cf. Fig. 2.18(c)) and plotted in Fig. 2.21(b). The Kramers-Kronig transformation of the curves in Fig. 2.21(a) leads to the dispersion δ for both helicities in Fig. 2.21(c), and half their difference is the magnetooptical dispersion $\Delta\delta$ displayed in Fig. 2.21(d). The optical constants for unpolarized x-rays, δ_0 and β_0, are obtained as the averages of the values for the two helicities.

From these relations, the mechanism of XRMR can be already fully understood. If two XRR curves are recorded using left and right circularly polarized x-rays and at an x-ray energy E_r which coincides with a dichroic resonance, the x-rays experience different optical constants δ,β and produce different reflectivity curves I^+ and I^-. Their normalized difference is called the *asymmetry ratio* [90]

$$\Delta I_\mathrm{R} = \frac{I^+ - I^-}{I^+ + I^-} \quad . \tag{2.58}$$

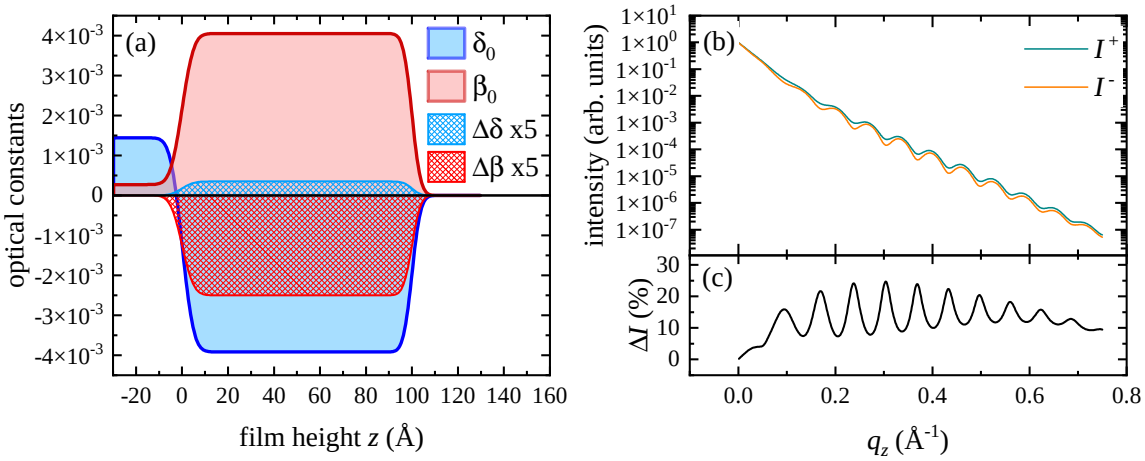

Fig. 2.22: (a) Model optical depth profiles $\delta(z)$,$\beta(z)$ (filled blue and red areas) and magnetooptical depth profiles $\Delta\delta(z)$,$\Delta\beta(z)$ (hatched blue and red areas) for a single film illuminated at a resonant x-ray energy. Magnetooptical profiles are multiplied by 5 for better visibility. (b) Simulation of the reflectivity curves I^+,I^- resulting from the simulated sample in (a) with x-ray helicities σ^+ and σ^-, respectively. (c) Asymmetry ratio obtained as the normalized difference of the curves in (a) (cf. Eq. (2.58)).

and their sum gives the non-dichroic, resonant XRR curve

$$I_\mathrm{R} = \frac{I^+ + I^-}{2} \quad . \tag{2.59}$$

As can be seen in Figs. 2.21(a),(c), the optical constant absorption β is considerably enhanced at the resonance L_3, and the dispersion δ even becomes negative. Additionally, both differ depending for x-rays with different helicities. At such a resonance, the optical depth profiles of a single homogeneously magnetized layer of 100 Å thickness may be represented like in Fig. 2.22(a). Shown are depth profiles of the unpolarized optical constants $\delta_0(z)$,$\beta_0(z)$ and of the magnetooptical constants $\Delta\delta(z)$ and $\Delta\beta(z)$. Simulated dichroic reflectivity curves I^+ and I^- for this model are shown in Fig. 2.22(b). The frequency of the Kiessig fringes is identical between both reflectivity curves, but slightly out-of-phase, due to a magnetically induced difference in dispersion for both helicities, and with less pronounced oscillation amplitudes for I^+, due to a higher absorption for the σ^+ helicity. The resulting asymmetry ratio ΔI is shown in Fig. 2.22(c).

Analyzing XRMR data again requires to find a model for these depth profiles which reproduce the data. To this end, first the non-dichroic reflectivity curve I_R is fitted to find a model for the optical depth profiles $\delta_0(z)$ and $\beta(z)_0$. On this foundation, a model for the two magnetooptical depth profiles, $\Delta\delta(z)$ and $\Delta\beta(z)$, represented in Fig. 2.22(c) as blue and red hatched areas, has to be found which produce a fit to the experimental asymmetry ratio ΔI_R. This procedure is equivalent to simply fitting both XRR curves I^+ and I^-, with the advantage that the structural and the magnetic properties are separated already during the modeling of the depth profiles. As discussed before, $\Delta\beta$ is proportional to the XMCD signal, so that the magnetooptical depth profile $\Delta\beta(z)$ can be interpreted as a depth profile of the XMCD signal at energy E_r. This allows a deduction of the magnetization of a film along

its sample depth, and thus the identification of magnetic dead layers or layers of magnetic enhancement.

However, the Parratt algorithm is not a good choice for the fitting of XRMR curves. Generally, the x-ray polarization changes while the x-ray propagates through the material, which is not accounted for in the Parratt algorithm [30]. The Parratt algorithm treats the polarization channels 'p' and 's' independently from one another, which becomes inaccurate for soft x-rays and especially for resonant energies, as discussed in Sec. 2.5. The full treatment of the polarization can be achieved by finding a solution of a stable electric field of the x-ray $\mathbf{E}$ settling in the layer system. Assuming a time-dependence of the electric field of the form $\mathbf{E}(\mathbf{r},t) = \mathbf{E}(\mathbf{r})e^{-i\omega t}$, the following differential equation can be derived from the Maxwell equations [30]

$$\nabla^2\mathbf{E} - \nabla(\nabla\cdot\mathbf{E}) = -k_0^2\,\widehat{\epsilon}\,\mathbf{E} \quad . \tag{2.60}$$

The dielectric tensor $\widehat{\epsilon}(\mathbf{r})$ defines the interaction of the material with the electric field, analogously to the optical index n_r in the Parratt algorithm; in an isotropic film, it is simply $\widehat{\epsilon} = n_\mathrm{r}^2\ \mathbf{1}$, and the results are identical to the Parratt results. Like the optical index n_r, it is assumed that the dielectric tensor $\widehat{\epsilon}$ is constant within each film, and therefore only changes spatially in the z direction, $\widehat{\epsilon}(\mathbf{r}) = \widehat{\epsilon}(z)$. As boundary conditions, it is imposed that the in-plane components of the electric field $\mathbf{E}$ and the magnetic field $\mathbf{B}$ are continuous at the interfaces, analogous to the Parratt case. The solution then represents the stable wave field forming in the film system. From the amplitude of this wave entering the vacuum from the sample surface, the reflectivity R_0 can be retrieved. Because all components of the electric field are calculated, polarization is inherently accounted for. Equation (2.60) can be analytically solved (please refer to Ref. [30]), but is more computing intensive than the Parratt algorithm.

All necessary formalisms for the analysis of XRMR data have been implemented by Sebastian Macke into his software ReMagX [30].

2.7. X-ray diffraction

XRD is a method to study the periodic structure of crystals. It is based on the interference of x-rays which are scattered at the electron distribution of the periodically arranged crystal planes. This can be understood in terms of the famous Bragg equation, which is illustrated in Fig. 2.23. An x-ray with incident wave vector $\mathbf{k}_i$ and wavelength λ falls onto a lattice plane (HKL) under an angle θ, and is reflected under the same angle with a wave vector $\mathbf{k}_f$. Similarly as for XRR, this scattering process is characterized by the scattering vector $\mathbf{q} = \mathbf{k}_f - \mathbf{k}_i$. Because of the periodic structure of the crystal, an equivalent lattice plane can be found at distance d_{HKL}. The same happens at each equivalent lattice plane of the crystal, so that from each of these scattering processes a partial wave with parallel wave vector $\mathbf{k}_f$, but with a path difference $2\cdot\Delta s = 2\cdot d_{HKL}\cdot\sin(\theta)$ leaves the crystal. The interference of these partial waves is constructive if the path difference is equal to a multitude of the x-ray wavelength λ

$$2\ \Delta s = 2\ d_{HKL}\cdot\sin(\theta) = n\lambda \quad , \qquad n\in\mathbb{N} \quad . \tag{2.61}$$

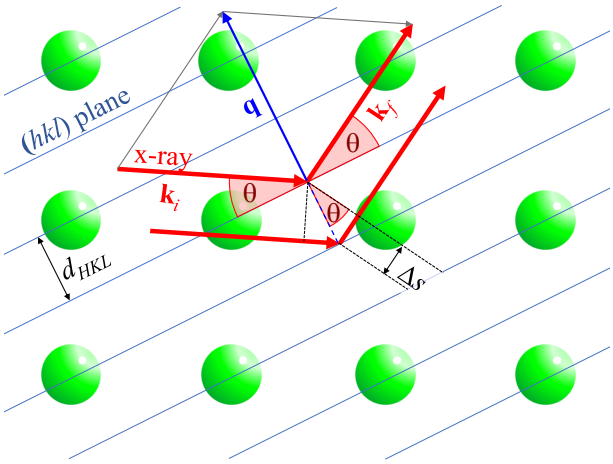

Fig. 2.23: Illustration of the Bragg condition. An x-ray with wave vector $\mathbf{k}_i$ falls on to a lattice plane (blue lines) under the angle θ and is reflected under the same angle. An equivalent x-ray reflected from a parallel lattice plane is scattered into the same direction, but with a path difference $2 \cdot \Delta s$. Blue arrow is the scattering vector $\mathbf{q}$ of the scattering process.

This condition is called *Bragg condition*, and if it is fulfilled, a bright x-ray reflection – called Bragg reflection – is observed under the angle θ (provided the reflection is not structurally forbidden, as will be explained very soon) [91].

A less intuitive, but mathematically more convenient way to identify those scattering vectors $\mathbf{q}$ which cause a Bragg reflection are the Laue equations [92]

$$\mathbf{q} \cdot \mathbf{a} = 2\pi H \quad , \quad \mathbf{q} \cdot \mathbf{b} = 2\pi K \quad , \quad \mathbf{q} \cdot \mathbf{c} = 2\pi L \quad , \quad H, K, L \in \mathbb{Z} \quad . \tag{2.62}$$

$\mathbf{a}$, $\mathbf{b}$ and $\mathbf{c}$ are the basis vectors of the lattice as introduced in Sec. 2.1, and H, K, L are the Miller indices. If $\mathbf{q}$ fulfills these equations, a Bragg reflection from the lattice plane (HKL) is observed. These equations open the avenue to construct a set of basis vectors $\mathbf{a}^*$, $\mathbf{b}^*$ and $\mathbf{c}^*$ so that each reciprocal lattice vector

$$\mathbf{G} = H \cdot \mathbf{a}^* + K \cdot \mathbf{b}^* + L \cdot \mathbf{c}^* \tag{2.63}$$

fulfills the Laue equations $\mathbf{q} = \mathbf{G}$. These basis vectors can be obtained from the basis vectors of the crystal lattice $\mathbf{a}$, $\mathbf{b}$ and $\mathbf{c}$

$$\mathbf{a}^* = 2\pi \frac{\mathbf{b} \times \mathbf{c}}{\mathbf{a} \cdot (\mathbf{b} \times \mathbf{c})} \quad , \quad \mathbf{b}^* = 2\pi \frac{\mathbf{c} \times \mathbf{a}}{\mathbf{a} \cdot (\mathbf{b} \times \mathbf{c})} \quad , \quad \mathbf{c}^* = 2\pi \frac{\mathbf{a} \times \mathbf{b}}{\mathbf{a} \cdot (\mathbf{b} \times \mathbf{c})} \tag{2.64}$$

$\mathbf{a}^*$, $\mathbf{b}^*$ and $\mathbf{c}^*$ have the dimension of an inverse length, usually given in Å^{-1}, and – analogously to $\mathbf{a}$, $\mathbf{b}$ and $\mathbf{c}$ forming the crystal lattice – they form the *reciprocal lattice*. Each point of this reciprocal lattice $\mathbf{G}$ represents a scattering vector that potentially produces a Bragg reflection if it is structurally allowed. These reflections are labeled by the Miller indices HKL used to construct $\mathbf{G}$ (cf. Eq. (2.63)).

The Bragg and the Laue equations can be used to identify the possible positions of the reflections from a crystal, but they do not offer information about their brightness. In order to determine the intensity of the peaks, the scattering processes from the individual atoms and from the unit cell have to be taken into account.

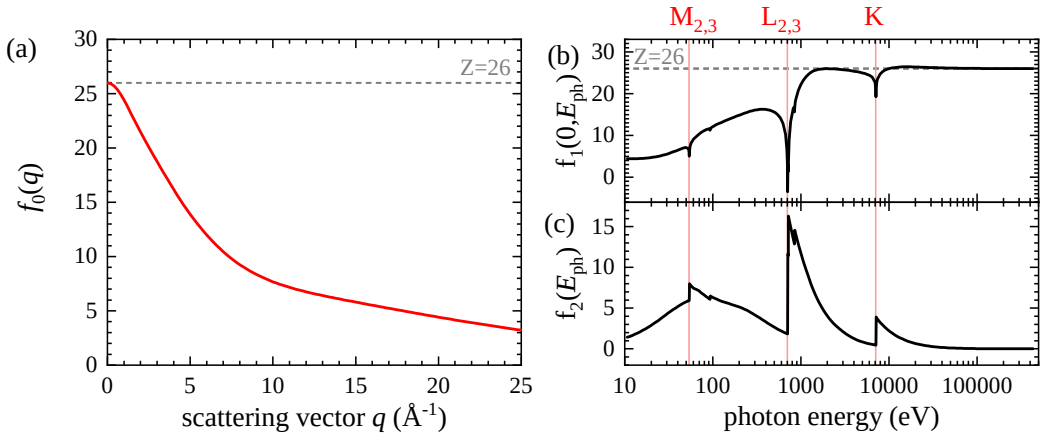

Fig. 2.24: (a) Dependence of the atomic form factor $f_0(q)$ on the scattering vector q. At $q = 0$, $f_0(0) = Z$. Data taken from Ref. [93]. (b) $f_1(E_{\mathrm{ph}})$ and (c) $f_2(E_{\mathrm{ph}})$ as functions of the photon energy. Red lines indicate resonances, at which the tabulated values become inaccurate. Data taken from Ref. [48].

Atomic form factor

Responsible for the x-ray scattering from an atom is mostly the Thomson scattering from its electrons. In an atom with an electron density $\rho(\mathbf{r})$, the scattering amplitude scales with the atomic form factor

$$f_0(\mathbf{q}) = \int \rho(\mathbf{r}) e^{i\mathbf{q}\cdot\mathbf{r}} d^3r \quad , \tag{2.65}$$

which is simply the Fourier transformation of the electron density. For practical purposes, $\rho(\mathbf{r})$ can be well approximated as spherical, so that the atomic form factor only depends on the absolute value of $\mathbf{q}$, $f_0(\mathbf{q}) = f_0(q)$, and may be represented as a sum of 4 Gaussian functions

(2.66)

The values for a_i,b_i and c are tabulated for many ions in Ref. [93]. For $q = 0$, the form factor simply becomes the atomic number, $f_0(0) = Z$.

For a complete description, the assumption that the scattering from the electrons of an atom is the same as the scattering from a cloud of free electrons, is too simple and has to be extended by two energy dependent terms [31]

$$f(q,E) = \underbrace{f_0(q) + f'(E_{\mathrm{ph}})}_{=f_1(q,E_{\mathrm{ph}})} + i f_2(E_{\mathrm{ph}}) \quad . \tag{2.67}$$

The terms $f_1(q, E_{\mathrm{ph}})$ and $f_2(E_{\mathrm{ph}})$ can be identified with the atomic scattering factors introduced in Sec. 2.4.4, for which the dependence of $f_1(q, E_{\mathrm{ph}})$ on the scattering vector q was omitted. For atomic iron ($Z = 26$), $f_0(q)$ is shown as a function of q in Fig. 2.24(a), and $f_1(0, E_{\mathrm{ph}})$ and $f_2(E_{\mathrm{ph}})$ are depicted in Figs. 2.24(b),(c) as functions of the photon energy E_{ph}. It can be seen that for high photon energies ($E_{\mathrm{ph}} > 20\,\mathrm{keV}$) $f_1(0, E_{\mathrm{ph}})$ tends to

$f_1 = f_0(0) = Z$ and f_2 approaches 0. This means that in the case of iron, for energies $E_{\mathrm{ph}} > 20\,\mathrm{keV}$, $f(q, E) \approx f_0(q)$, effectively meaning that the Thomson scattering picture becomes accurate. For these high energies, the x-rays are only weakly interacting with the matter. Refraction and absorption can be neglected, because for x-rays the refractive index n_{r} is close to 1, and multiple scattering is disregarded as well due to the very small scattering cross section. This framework is then called kinematical approximation.

Structure factor

The structure factor $F(\mathbf{q})$ takes into account the structure of the unit cell to the scattering process. It is given by the sum over the scattering amplitudes of all atoms j in the unit cell

$$F(\mathbf{q}) = \sum_j f_j(q) e^{i\mathbf{q}\cdot\mathbf{r_j}} \quad . \tag{2.68}$$

The consequence of this term is that x-rays scattered from different atoms in the unit cell may interfere constructively or destructively with each other, so that the intensity of each Bragg reflection varies. In fact, a reflection HKL which fulfills the Laue equations can even have zero intensity, and thus be invisible. Those reflections are called *forbidden* reflections. For instance, a simple cubic lattice has only a single atom per unit cell at position $\mathbf{r}_0 = (0, 0, 0)$, so that the structure factor $F(\mathbf{q}) = f(q)$ has intensity for all Bragg reflections allowed by the lattice, only dampened for high q due to the atomic form factor. In contrast, a body-centered cubic has an additional atom at the position $\mathbf{r}_1 = (\frac{1}{2}, \frac{1}{2}, \frac{1}{2})$, and the structure factor is

$$F^{\mathrm{bcc}}(\mathbf{q}) = f(q) + f(q) \cdot e^{-i\pi(H+K+L)} = f(q) \cdot (1 + e^{-i\pi(H+K+L)}) \quad .$$

If the sum $(H+K+L)$ is an uneven number, $e^{-i\pi(H+K+L)} = -1$, and consequently $F^{\mathrm{bcc}} = 0$, and the corresponding reflection has no intensity. That means, for example the (002) or the (222) reflections are visible for bcc lattices, but the (111) or the (003) reflections are not. These invisible reflections are called structurally forbidden. This effect leads to a unique diffraction pattern for each crystal structure.

Debye-Waller factor

A modification of the atomic form factor becomes necessary due to the fact that in a real crystal the atom positions which have been considered rigid in the previous description are merely average positions about which the atoms are vibrating. These vibrations occur even at 0 K, but are strongly amplified thermally at finite temperatures. They can be accounted for by an exponential term

$$f^{\mathrm{D}}(q) = f_0(q) e^{-D\,q^2} \quad , \tag{2.69}$$

into which the scattering vector amplitude enters quadratically. This has the consequence that because of thermal vibrations, the intensity of reflections with higher scattering vectors (and thus, higher HKL values) are stronger damped, but their width is not increased.

Scattering from a crystal

The scattering amplitude from a single crystal is given by

$$A(\mathbf{q}) = A_0 C \sum_n \underbrace{\sum_j f_j^D(q) e^{i\mathbf{q}\cdot\mathbf{r_j}}}_{\text{structure factor } F(\mathbf{q})} \cdot e^{i\mathbf{q}\cdot\mathbf{r}_n} \quad , \quad C = \frac{e^2}{m_e c^2 R_0} \quad . \tag{2.70}$$

A_0 is the incident wave amplitude and C is a constant stemming from the Thomson scattering at an individual electron. The first sum spans over all unit cells n at positions $\mathbf{r}_n$, and the second sum is the structure factor, including all atoms j at position $\mathbf{r}_j$ in a single unit cell.

2.8. Thin film and surface diffraction

For an infinite three-dimensional crystal, the scattering vector $\mathbf{q}$ has to satisfy one Laue condition for each of the three dimensions, and the resulting Bragg peaks are perfectly sharp points in reciprocal space, as illustrated in Fig. 2.25(a). For a two-dimensional crystal, only two Laue conditions exist and instead of zero-dimensional Bragg peaks, x-ray diffraction produces one-dimensional diffraction rods, shown in Fig. 2.25(b). In this work, diffraction is used to study surfaces and thin films. A crystal surface can be regarded as infinite laterally, but is semi-infinite vertically, since it has to be truncated in one direction to exhibit a surface. The surface of such a semi-infinite crystal produces Bragg spots which are vertically smeared out, depicted in Fig. 2.25(c). These are called crystal truncation rods (CTR). The diffraction pattern of a thin film shows diffraction spots together with oscillations along the vertical direction, stemming from the interference between x-rays scattered at the individual atomic layers of the film. These oscillations are known as Laue fringes and are illustrated in Fig. 2.25(d).

An instructive way to derive these behaviors is to rewrite the scattered amplitude of a crystal (cf. Eq. (2.70)) by representing the vector $\mathbf{r}_n$ pointing to the origin of the unit cell n through the lattice vectors

$$\mathbf{r}_n = n_1\mathbf{a} + n_2\mathbf{b} + n_3\mathbf{c} \quad . \tag{2.71}$$

Equation 2.70 then becomes [32]

$$A(\mathbf{q}) = A_0 C \sum_n \sum_j F(\mathbf{q}) \sum_{n_1}^{N_1-1} \sum_{n_2}^{N_2-1} \sum_{n_3}^{N_3-1} e^{i\mathbf{q}\cdot(n_1\mathbf{a}+n_2\mathbf{b}+n_3\mathbf{c})} \quad . \tag{2.72}$$

These sums can be identified as geometric sums and represented by the N-slit function $S_N(x)$

$$S_N(x) = \sum_{n=0}^{N-1} e^{inx} = \frac{1-e^{ixN}}{1-e^{ix}} \quad . \tag{2.73}$$

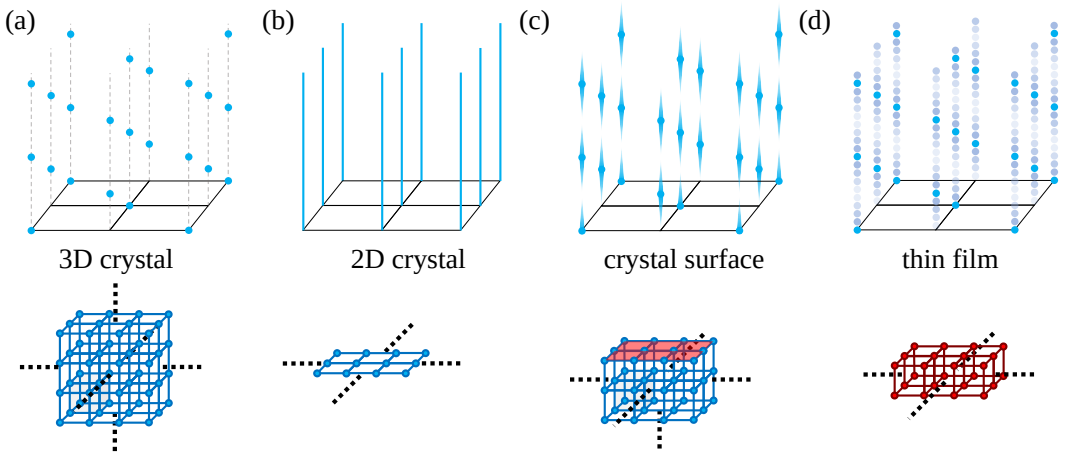

Fig. 2.25: Diffraction patterns from different crystal types. (a) Diffraction from an infinite 3D crystal results in point-like Bragg peaks. (b) A 2D crystal lying in the horizontal plane produces diffraction rods in the vertical direction. (c) Diffraction from the surface of a semi-infinite crystal gives Bragg peaks that are vertically smeared out into CTRs. (d) Diffraction from a thin film leads to CTRs superposed by Laue oscillations. Image adapted from Refs. [32, 94], recreated after a design by Martin Hoppe.

With this, Eq. (2.72) can be expressed as a product of N-slit functions

$$A(\mathbf{q}) = A_0 CF(\mathbf{q}) \cdot S_{N_1}(\mathbf{q}\cdot\mathbf{a}) \cdot S_{N_2}(\mathbf{q}\cdot\mathbf{b}) \cdot S_{N_3}(\mathbf{q}\cdot\mathbf{c}) \quad . \tag{2.74}$$

If N approaches infinity, the N-slit function becomes a sum of δ functions

$$\lim_{N\to\infty} S_N(x) = \sum_{n=0}^{\infty} \delta(x - 2\pi\cdot n) \quad . \tag{2.75}$$

For an infinite crystal, this reproduces the sharp Bragg spots as expected.

The scattering amplitude is a complex quantity and accessible in a diffraction experiment usually only as its square modulus in terms of the scattered intensity

$$I(\mathbf{q}) = |A(\mathbf{q})|^2 \quad .$$

For this reason, the properties of the N-slit function that are reflected in experiments are also mostly those of its square modulus

$$|S_N(x)|^2 = \frac{\sin^2(Nx/2)}{\sin^2(x/2)} \quad . \tag{2.76}$$

The function $|S_N(x)|^2$ is plotted in Fig. 2.26(a) for $N = 3$ and $N = 6$ (which can be interpreted as a one-dimensional crystal consisting of 3 and 6 unit cells, respectively). At integer multiples of 2π, $x = 2\pi\cdot n$, the N-slit function has strong main maxima, and in between it exhibits $N-2$ side maxima. The amplitude of the main maxima is N^2, and their full-width

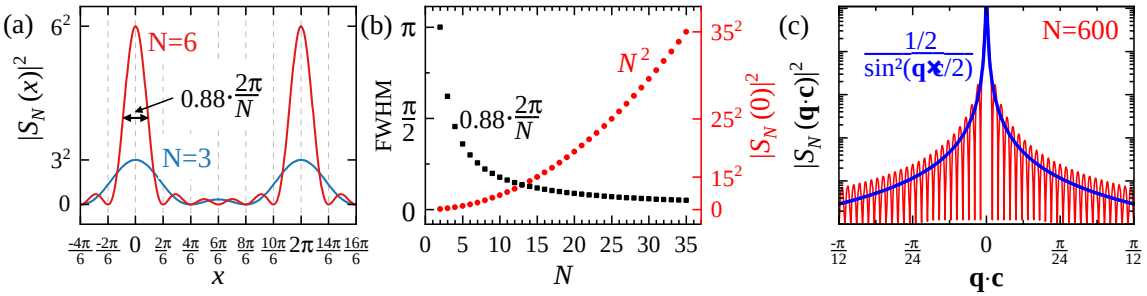

Fig. 2.26: (a) Square modulus of the N-slit function for N=3 and N=6, adapted from Ref. [32]. (b) FWHM of the main maxima (black squares, left axis) and maximum of $|S_N(x)|^2$ (red, right axis) as a function of N. (c) Square modulus of the N-slit function for N=600 (red), in semi-logarithmic scale. Blue is a Pseudo-Voigt profile enveloping the rapidly oscillating N-slit function.

half maximum value (FWHM) is [95]

$$\text{FWHM} = K \cdot \frac{2\pi}{N} \quad , \quad K = 0.89 \quad . \tag{2.77}$$

This means that as N increases, the main maxima become sharper and higher, while the side maxima become more numerous and smaller. The FWHM and the intensity of the main maxima are displayed in Fig. 2.26(b) (black and red, respectively).

Returning to the interpretation in terms of x-ray diffraction, the main maxima can be identified as the Bragg peaks, and the side maxima as the Laue fringes seen in Fig. 2.25(d). The number of Laue fringes between two Bragg peaks scale as $N-2$ with the number of unit cells. Equation 2.77 is known as the *Scherrer* formula, and is a very useful tool to determine the size of the crystalline domains in a sample [95]. K is the shape factor. In the ideal case of a block-shaped crystal as assumed here, it takes the value $K = 0.89$, but in practice it depends on the actual shape of the crystallites. It typically is about $K \approx 0.89...\ 0.94$ [96]. By analyzing the FWHM of a Bragg peak, it is possible to derive the average number N of unit cells per crystallite of a film in a given direction, even if no Laue oscillations are visible.

With this, it is easy to understand the origin of the diffraction patterns in Fig. 2.25. As already noticed, for a thin film with a small number of atomic layers N, the main maxima correspond to the diffraction spots, and the side maxima to the Laue fringes, as illustrated in Fig. 2.25(d). If a crystal becomes very large in one direction and the number of unit cells N approaches infinity, the N-slit function $S_N(x)$ of that direction in Eq. (2.74) can be replaced by a δ-function, according to Eq. (2.75). In that case, the reflection becomes infinitely sharp and bright in the corresponding dimension. If the crystal is infinite in all three dimensions, this results in Bragg spots, and if it is only infinite in two dimensions, diffraction rods occur (cf. Figs. 2.25(a),(b)).

The shape of CTRs between the Bragg spots can be understood by the behavior of the N-slit function for large, but finite N. The numerator $\sin^2(Nx/2)$ will be rapidly oscillating between 0 and 1, and can be approximated by its average value 1/2, so that the N-slit function itself

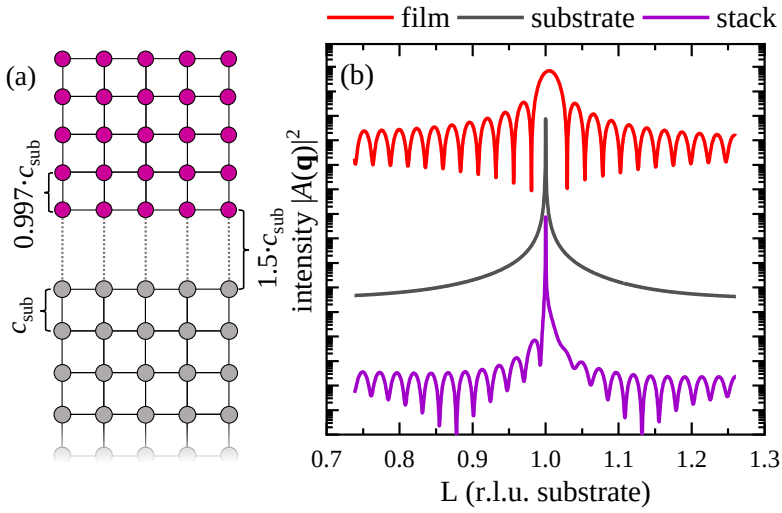

Fig. 2.27: Simulation of the 00L-CTR of a film grown on a substrate. (a) Sketch of the simulated system. The vertical film lattice constant is 0.3% smaller than the one of the substrate, and the interface distance corresponds to one and a half lattice constants. (b) Individual simulations of the diffraction patterns of the film (red), the substrate (grey) and the full system (purple).

becomes [32]

$$|S'_N(x)|^2 = \frac{1/2}{\sin^2(x/2)} \quad . \tag{2.78}$$

To illustrate the consequence for the diffraction pattern, an N-slit function $|S_{N_3}(\mathbf{q}\cdot)\mathbf{c}|^2$ for $N_3 = 600$ is shown in Fig. 2.26(c). Note that the intensity axis is in on a logarithmic scale. The N-slit function (red) oscillates rapidly with the scattering vector $\mathbf{q}$, and approaches the form of Eq. (2.78) (blue), resembling the smeared out intensity distribution sketched in Fig. 2.25(c). The distinct diffraction pattern of CTRs can therefore be understood as an N-slit function with a frequency too high to be experimentally resolved. Note that the description by Eq. (2.78) is only an approximation and fails close to the Bragg peaks, since for $x = 0$, it becomes infinite. In order to lift this restriction, the N-slit function limit for large N can be slightly altered to [32]

$$S''_N(x) = \frac{1}{1 - \mathrm{e}^{-ix-\epsilon}} \quad , \tag{2.79}$$

where ϵ is an absorption parameter, effectively suppressing diffracted amplitude coming from the deeper layers of the semi-infinite crystal.

In order to describe the diffraction pattern of a thin film on a substrate, the amplitudes of both, as given in Eq. (2.72), have to be added

$$A(\mathbf{q}) = A_{\mathrm{substrate}}(\mathbf{q}) + \mathrm{e}^{i\,\mathbf{q}\cdot\mathbf{p}} A_{\mathrm{film}}(\mathbf{q}) \quad . \tag{2.80}$$

The vector $\mathbf{p}$ is a phase vector that describes the shift between the two crystals at the interface. The results for a simulated sample system can be seen in Fig. 2.27. It resembles the situation of Fe_3O_4/MgO(001), with the film lattice constant being 99.7% of the substrate lattice constant, and a shift of $\mathbf{p} = 1.5 \cdot \mathbf{c}_{\mathrm{sub}}$ between the interfaces. Figure 2.27(b) shows the simulated results for the film and the substrate individually, and the full system. The diffraction pattern from the full system is the sum of the amplitudes $A(\mathbf{q})$, not of the intensities $|A(\mathbf{q})|^2$, and therefore differs from the direct sum by their phase factors.

3. Materials

This work focuses on ultrathin films of the iron oxide magnetite (Fe_3O_4) which are grown by RMBE. As substrates, MgO(001) and $SrTiO_3$(001) were used. Additionally, the antiferromagnet NiO served as an interlayer material to create Fe_3O_4/NiO/MgO(001) bilayers. For this reason, these four materials will be introduced here.

Besides magnetite, there exist other iron oxide phases: wüstite ($Fe_{1-\delta}O$), maghemite (γ-Fe_2O_3) and hematite (α-Fe_2O_3). Because these can, depending on the preparation conditions, form instead or alongside magnetite, they will be discussed as well. Finally, some additional properties which specifically emerge in Fe_3O_4 thin films will be discussed. The basic information about the iron oxides presented here stem from in Ref. [97]. The unit cell figures have been created with the software VESTA [98].

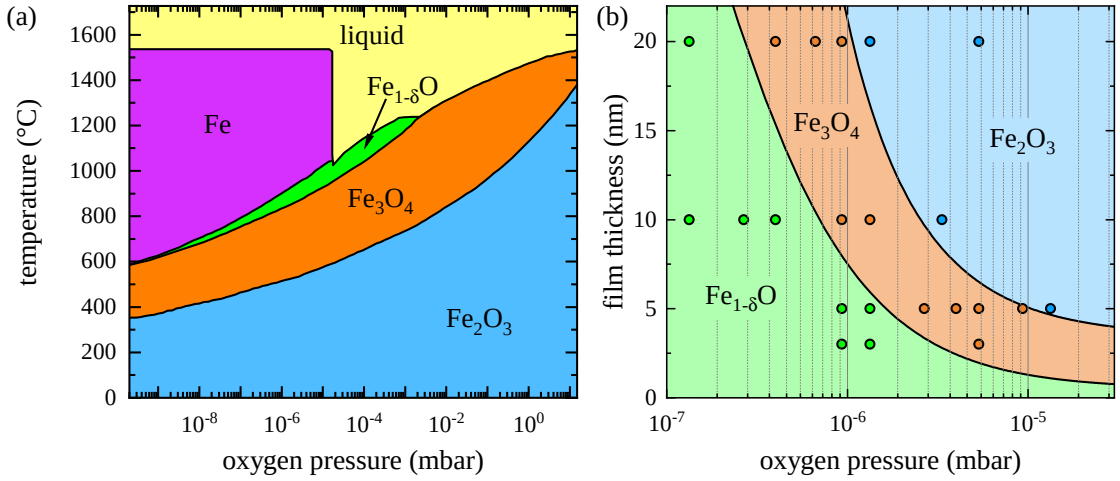

Fig. 3.1: (a) Calculated phase diagram as a function of oxygen pressure and temperature for bulk iron oxide, taken from Ref. [99], data extracted using the software WebPlotDigitizer [100]. (b) Phase diagram of ultrathin iron oxide films grown by RMBE on MgO(001) at a substrate temperature of 250°C, as a function of film thickness and oxygen pressure, taken from Ref. [101]. Colored areas are a guide to the eye.

3.1. Iron oxides

Iron oxides exist in several phases. The lowest oxidation state is represented by wüstite ($Fe_{1-\delta}O$), which contains exclusively divalent Fe^{2+} cations. The highest oxidized iron oxide phase, Fe_2O_3, occurs in two modifications: hematite (α-Fe_2O_3) and maghemite (γ-Fe_2O_3), which only contain trivalent Fe^{3+} cations. Hematite rarely forms on the substrates used

in this work and will therefore not be discussed here. Magnetite is an iron oxide of mixed valency – it contains both Fe^{2+} and Fe^{3+} cations.

Which phase of iron oxide is the most stable depends on the environmental conditions. Figure 3.1(a) shows a phase diagram of the iron oxides for bulk materials calculated by Ketteler et al. [99], indicating that at ambient conditions Fe_2O_3, is the most stable phase, while $Fe_{1-\delta}O$ is stable only in a very small range of conditions. Figure 3.1(b) depicts a phase diagram for ultrathin iron oxide films grown on MgO(001) by RMBE at a substrate temperature of 250°C, obtained by Alraddadi et al. [101]. Their preparation resembles very closely the samples used in this work[1]. For lower film thicknesses, preferably lower-oxidized iron oxides form, and Fe_3O_4 is only the preferred phase for an intermediate range of oxygen pressures and film thicknesses.

3.1.1. Magnetite (Fe_3O_4)

Magnetite is a half-metal at high temperatures, with a band gap of about 0.1 eV [97] and a specific resistivity in the range of $\sigma = 10^{-3} - 10^{-4}\,\Omega \cdot \mathrm{m}$ [103]. Below a temperature of about 120 K, it undergoes a phase transition called the Verwey transition: its crystal structure changes from cubic to monoclinic, and it becomes insulating. All measurements in this work have been performed in the high-temperature phase, so that the explanations in the following will be restricted to this case.

Crystal structure

Magnetite's crystal structure above the Verwey transition temperature is depicted in Fig. 3.2(a), showing a single unit cell with a lattice constant of $a_{Fe_3O_4} = 8.3964\,\text{Å}$. The spinel structure can be described as consisting of three face-centered cubic sublattices: an oxygen sublattice (yellow in Fig. 3.2), an octahedral sublattice with 1/2 of its sites randomly populated by an equal amount of Fe^{2+}_{oct} and Fe^{3+}_{oct} cations (green and blue), and a tetrahedral sublattice which has 1/8 of its sites populated with Fe^{3+}_{tet} cations (red). The octahedral sublattice is offset from the oxygen lattice by $r_{oct} = (\frac{1}{4}, 0, 0)$, and the tetrahedral sublattice is offset from the oxygen lattice by $r_{tet} = (\frac{1}{8}, \frac{1}{8}, \frac{1}{8})$, so that all its sites are tetrahedrally coordinated by oxygen anions. The sites of the tetrahedral lattice are called *A-sites* and the sites of the octahedral lattice *B-sites*.

Figure 3.3 shows the unit cell split up in its layers along the [001]-direction. Each layer consists of an octahedral layer at height z, in which oxygen and B-site iron ions are located, and a tetrahedral layer located at $z + \frac{1}{8} \cdot a_{Fe_3O_4}$. Tab. 3.1 lists all atom positions in the Fe_3O_4 unit cell. In ultrathin films, often the growth direction is particularly interesting. Figure 3.2(b) shows a projection onto the (100) plane, in order to highlight the structure in growth direction. The distances between subsequent octahedral layers, $\Delta z_{oct-oct} = 2.099\,\text{Å}$, and between octahedral and tetrahedral layers, $\Delta z_{oct-tet} = 1.05\,\text{Å}$, are also displayed.

[1] It has to be noted that in their work, they were able to produce wüstite, magnetite and maghemite on MgO(001) by RMBE. However, due to its instability at temperatures below ≈ 570°C, $Fe_{1-\delta}O$ thin films are difficult to prepare using RMBE [102]. Our own experience also rather finds that at low oxygen pressures, rather metallic Fe alongside Fe_3O_4 forms instead of a $Fe_{1-\delta}O$ phase.

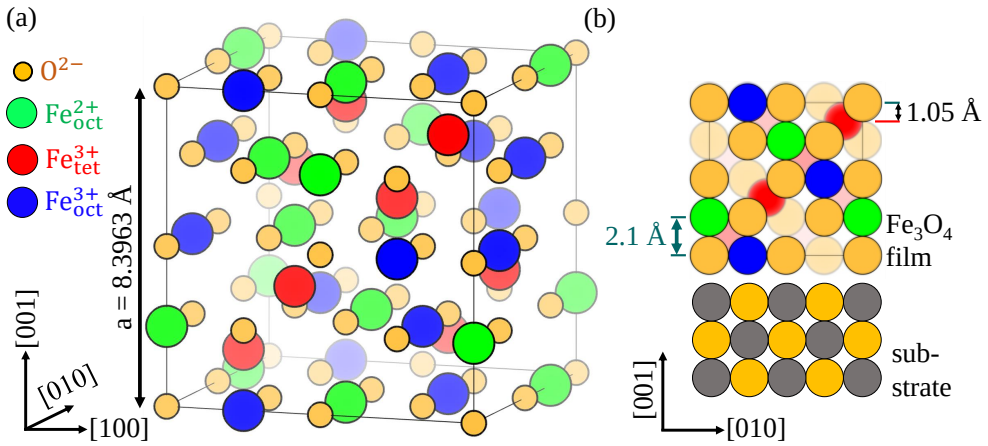

Fig. 3.2: (a) Unit cell of Fe_3O_4, created with the software VESTA [98]. Note that Fe^{2+}_{oct} and Fe^{3+}_{oct} are distributed randomly over the octahedral sites. (b) View of of the unit cell projected onto the (100) plane, to illustrate the stacking order for ultrathin films grown in [001] direction.

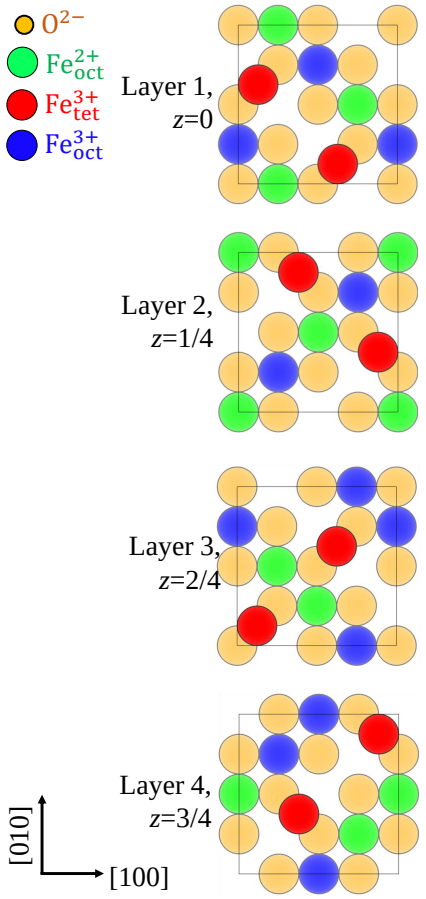

Fig. 3.3: Layer-wise projection of the unit cell in Fig. 3.2(a) onto the (001) plane. Coordinates of all atoms can be found in Tab. 3.1.

Layer	1B	2B	3B	4B
O^{2-}	$(0,0,0)$	$(\frac{1}{4},0,\frac{1}{4})$	$(0,0,\frac{1}{2})$	$(\frac{1}{4},0,\frac{3}{4})$
	$(\frac{1}{2},0,0)$	$(\frac{3}{4},0,\frac{1}{4})$	$(\frac{1}{2},0,\frac{1}{2})$	$(\frac{3}{4},0,\frac{3}{4})$
	$(\frac{1}{4},\frac{1}{4},0)$	$(0,\frac{1}{4},\frac{1}{4})$	$(\frac{1}{4},\frac{1}{4},\frac{1}{2})$	$(0,\frac{1}{4},\frac{3}{4})$
	$(\frac{3}{4},\frac{1}{4},0)$	$(\frac{1}{2},\frac{1}{4},\frac{1}{4})$	$(\frac{3}{4},\frac{1}{4},\frac{1}{2})$	$(\frac{1}{2},\frac{1}{4},\frac{3}{4})$
	$(0,\frac{1}{2},0)$	$(\frac{1}{4},\frac{1}{2},\frac{1}{4})$	$(0,\frac{1}{2},\frac{1}{2})$	$(\frac{1}{4},\frac{1}{2},\frac{3}{4})$
	$(\frac{1}{2},\frac{1}{2},0)$	$(\frac{3}{4},\frac{1}{2},\frac{1}{4})$	$(\frac{1}{2},\frac{1}{2},\frac{1}{2})$	$(\frac{3}{4},\frac{1}{2},\frac{3}{4})$
	$(\frac{1}{4},\frac{3}{4},0)$	$(0,\frac{3}{4},\frac{1}{4})$	$(\frac{1}{4},\frac{3}{4},\frac{1}{2})$	$(0,\frac{3}{4},\frac{3}{4})$
	$(\frac{3}{4},\frac{3}{4},0)$	$(\frac{1}{2},\frac{3}{4},\frac{1}{4})$	$(\frac{3}{4},\frac{3}{4},\frac{1}{2})$	$(\frac{1}{2},\frac{3}{4},\frac{3}{4})$
$Fe^{2+/3+}_{oct}$	$(0,0,\frac{1}{4})$	$(0,0,\frac{1}{4})$	$(\frac{3}{4},0,\frac{1}{2})$	$(\frac{1}{2},0,\frac{3}{4})$
	$(0,\frac{1}{4},0)$	$(\frac{1}{4},\frac{1}{4},\frac{1}{4})$	$(\frac{1}{2},\frac{1}{4},\frac{1}{2})$	$(\frac{3}{4},\frac{1}{4},\frac{3}{4})$
	$(\frac{3}{4},\frac{1}{2},0)$	$(\frac{1}{2},\frac{1}{2},\frac{1}{4})$	$(\frac{1}{4},\frac{1}{2},\frac{1}{2})$	$(\frac{1}{4},\frac{3}{4},\frac{3}{4})$
	$(\frac{1}{2},\frac{3}{4},0)$	$(\frac{3}{4},\frac{3}{4},\frac{1}{4})$	$(0,\frac{3}{4},\frac{1}{2})$	$(\frac{1}{4},\frac{3}{4},\frac{3}{4})$

Layer	1A	2A	3A	4A
Fe^{3+}_{tet}	$(\frac{5}{8},\frac{1}{8},\frac{1}{8})$	$(\frac{7}{8},\frac{3}{8},\frac{3}{8})$	$(\frac{1}{8},\frac{1}{8},\frac{5}{8})$	$(\frac{3}{8},\frac{3}{8},\frac{7}{8})$
	$(\frac{1}{8},\frac{5}{8},\frac{1}{8})$	$(\frac{3}{8},\frac{7}{8},\frac{3}{8})$	$(\frac{5}{8},\frac{5}{8},\frac{5}{8})$	$(\frac{7}{8},\frac{7}{8},\frac{7}{8})$

Tab. 3.1: Coordinates of the atoms in a Fe_3O_4 unit cell, in units of the lattice vectors, grouped into layers in [001] direction and A- and B-sites (1B, 2A, etc.). Layers are sketched in Fig. 3.3.

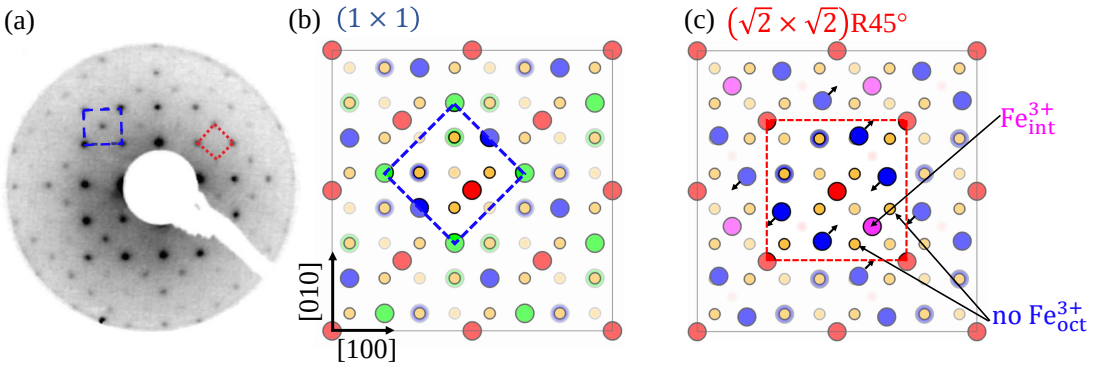

Fig. 3.4: (a) Typical LEED pattern of the $Fe_3O_4(001)$ surface. Blue square indicates the (1×1) pattern, and the red square the $(\sqrt{2} \times \sqrt{2})$R45° reconstruction in reciprocal space (taken from Ref. [94]). (b) Illustration of the (1×1) unit (blue square) on the bulk-cell in real space. (c) SCV model of the $(\sqrt{2} \times \sqrt{2})$R45° reconstruction (red square). Compared to the bulk cell, in the second atomic layer, additional interstitial Fe^{3+}_{int} cations are present (purple), and 2 Fe^{3+}_{oct} cations miss in the third layer. Black arrows indicate small displacements of the Fe^{3+}_{oct} cations as reaction to the interstitial tetrahedral cations.

$Fe_3O_4(001)$ surface structure

It has long been known that the $Fe_3O_4(001)$ surface undergoes a reconstruction, indicated by a $(\sqrt{2} \times \sqrt{2})$R45° pattern observed in Low Electron Energy Diffraction (LEED) [104], as can be seen in 3.4(a). The standard procedure to derive such a surface structure is the Tasker model of the ionic surface, which states that the surfaces of polar oxides need to reconstruct in such a way that the polarity is compensated on the surface [105]. Figure 3.5(a) shows an illustration of this line of reasoning. In [001] direction, Fe_3O_4 consists of alternating octahedral layers with a a total charge of −6 elementary charges, followed by a tetrahedral layer with +6 elementary charges. In the bulk material, these subsequent polar layers compensate each other. The surface, however, needs to possess a total charge of +3 charges in order to compensate the polarity, because otherwise a permanent voltage forms across the entire film ('polar catastrophe'). This model has been successful to predict the surface terminations of some materials, such as TiO, MgO and ZnO [106, 107], and has also frequently been employed to derive models of magnetite's surface structure [80, 108, 109].

The most convincing model of the $Fe_3O_4(001)$ surface to this date has been recently proposed to be a *subsurface cation vacancy* (SCV) structure [110]. This model is illustrated in Fig. 3.4(c). The bulk unit cell of Fe_3O_4, as depicted in Figs. 3.4(b) and 3.5(a), consists of octahedral layers with 4 $Fe^{2+/3+}_{oct}$ cations and tetrahedral layers with 2 Fe^{3+}_{tet} cations. In the SCV structure, the top layer remains a regular octahedral layer, but all cations are exclusively of Fe^{3+}_{oct} valency. In the second layer, an additional interstitial Fe^{3+}_{tet} cation is located (purple in Figs. 3.4(c) and 3.5(b)), with a total of 3 Fe^{3+}_{tet} in that layer. In the third layer, two B-site cations are missing and it only contains 2 Fe^{3+}_{oct} cations. The fourth and fifth layers are again stoichiometric, but still with exclusively Fe^{3+} valencies. In total, the outermost unit cell (grey box in Fig. 3.5(b)) has one cation missing, resulting in a $Fe_{11}O_{16}$ stoichiometry, and a net charge of +3 elementary charges, achieving polarity compensation. Comparison of Figs. 3.4(b),(c) also reveals how this structure gives rise to the $(\sqrt{2} \times \sqrt{2})$R45° reconstruc-

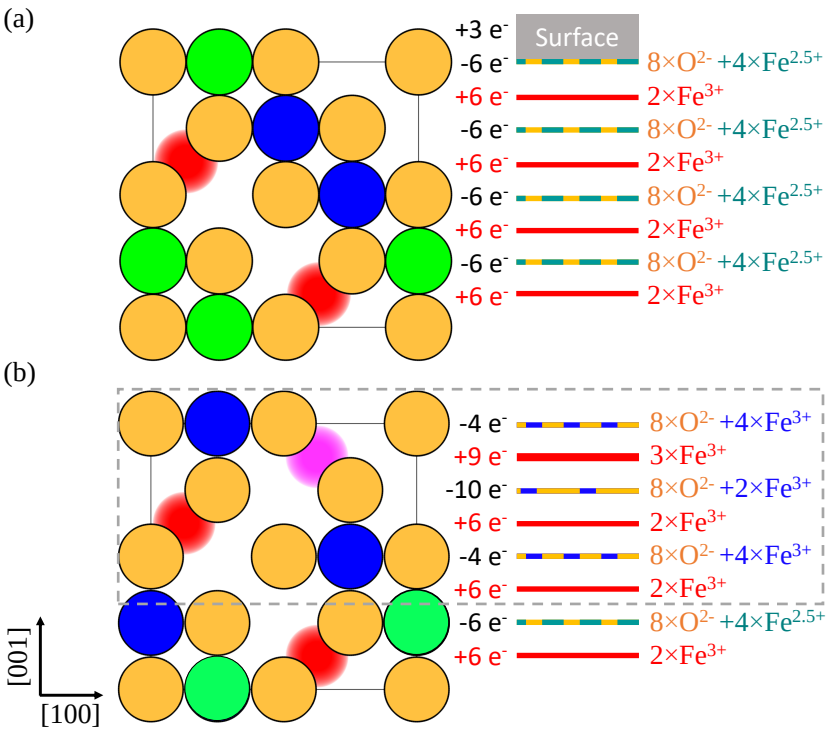

Fig. 3.5: (a) Tasker model of the octahedrally-terminated $Fe_3O_4(001)$ surface. In [001] direction, Fe_3O_4 consists of octahedral layers with a total charge of -6 $\frac{e^-}{u.c.}$ and tetrahedral layers with a $+6\,\frac{e^-}{u.c.}$ charge, calling for a surface reconstruction with $+3\,\frac{e^-}{u.c.}$ to avoid polarity. (b) Polarity compensation in the SCV model. Grey box indicates the reconstructed volume, with a total charge of $+3\,\frac{e^-}{u.c.}$.

tion. On a bulk terminated surface, as in Fig. 3.4(b), the (1×1) pattern corresponds to the smallest repeating surface cell, illustrated by the blue dashed square. With the interstitial tetrahedral cation Fe^{3+}_{int} and the cation vacancies in the third layer in place (see Fig. 3.4(c)), the smallest repeating cell becomes the one indicated by the red square, corresponding to the reconstruction. Note the displacement of the neighboring octahedral cations as reaction of the rearrangement in the tetrahedral layer, emphasized by the small black arrows. While there are other models of $Fe_3O_4(001)$ that both reasonably explain the $(\sqrt{2} \times \sqrt{2})R45°$ reconstruction and achieve polarity compensation [80, 109], the SCV also successfully explains the site-selective adsorption of Au atoms and the incorporation of Co adatoms observed in STM [110, 111].

Magnetism

Magnetite is a ferrimagnet and gave rise to the Néel model of ferrimagnetism [112]: the octahedral sublattice couples ferromagnetically within itself, while there is antiferromagnetic coupling between the octahedral and the tetrahedral sublattices. The experimentally found magnetic moment of Fe_3O_4 of $4.07\,\mu_B$/f.u. can be derived by the individual spin moments of the cations [113], assuming the orbital moments being quenched by the cubic crystal fields. Fe^{3+} cations hold a spin moment of $5\,\mu_B$, and Fe^{2+} has a spin moment of $4\,\mu_B$. The antiferromagnetic coupling effectively cancels out the contributions from the two Fe^{3+} cation species, so that the total moment $\mu_{Fe_3O_4} = 4\,\mu_B$/f.u. matches well the experimental value. However, although this simple line of reasoning leads to a satisfying result, this picture has been called into question. Polarized neutron studies suggest that the tetrahedral A-site cations instead have a magnetic moment of $\mu_{A\text{-site}} = -3.82\,\mu_B$, and the B-site cations form an equivalent $Fe^{2.5+}_{oct}$ species with a magnetic moment of $\mu_{B\text{-site}} = 3.97\,\mu_B$, with a total moment

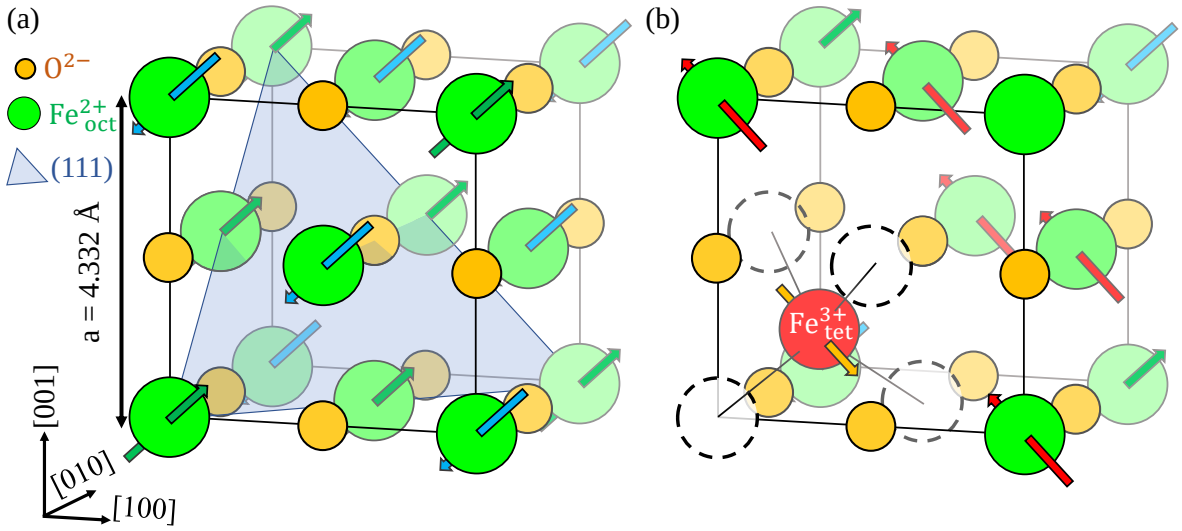

Fig. 3.6: (a) Unit cell of $Fe_{1-\delta}O$. Spins (blue and green arrows) align parallel to the [111] direction. Alternating (111) sheets (shaded area) are ferromagnetic, but couple antiferromagnetically with each other [119, 120]. (b) Koch-Cohen defect in the $Fe_{1-\delta}O$ unit cell. 4 Fe^{2+}_{oct} vacancies surround an interstitial Fe^{3+}_{tet} cation. The spins in the vicinity of the defect align parallel to the ferromagnetic (111) sheets.

of $\mu_{Fe_3O_4} = \mu_{\text{A-site}} + 2 \cdot \mu_{\text{B-site}} = 4.12\,\mu_B$/f.u. [114, 115]. Therefore, the atomic origin of the magnetic moment is not fully settled.

The ferromagnetic coupling on the octahdedral sublattice is due to both, double exchange between the Fe^{2+} and the Fe^{3+} cations [116], and 90°-super exchange via $Fe^{2+/3+}_{oct}$-oxygen-$Fe^{2+/3+}_{oct}$ coupling [117]. The antiferromagnetic coupling between the tetrahedral and octahedral sublattices is due to 120°-super exchange [118] (cf. Sec. 2.3.4). In the bulk, the moments align preferably along the cube diagonals in the [111] direction [97]; however, in ultrathin films, for which the form anisotropy becomes important, this is not necessarily the case.

3.1.2. Wüstite ($Fe_{1-\delta}O$)

Wüstite crystallizes in the rock salt structure, as illustrated in Fig. 3.6(a), with a lattice constant of $a_{FeO} = 4.332$ Å. This crystal structure can be thought of as two face-centered cubic lattices, populated with Fe^{2+} and O^{2-} ions, which are offset by a translational vector $\mathbf{R} = 0.5 \cdot \mathbf{a}$. This results in a FeO formula. However, in nature, wüstite always occurs in an iron-depleted phase and is usually written as $Fe_{1-\delta}O$, with δ ranging from 0.05 to 0.17 [97]. This off-stoichiometric phase is realized by *Koch-Cohen* defects, depicted in Fig. 3.6(b). In this defect, 4 Fe^{2+}_{oct} vacancies coordinate an interstitial Fe^{3+}_{tet} cation. These defects further group into clusters of 13 vacancies surrounding 4 interstitial Fe^{3+}_{tet} cations [97].

Wüstite has a bandgap of 2.4 eV [121], and is a prototypical candidate of a superexchange-mediated antiferromagnet. Preferably, the spins form alternating ferromagnetic (111) sheets. Within these, they are oriented along the [111] direction, perpendicular to the (111) plane. This order is modified by the Koch-Cohen defects. The interstitial Fe^{3+}_{tet} cation aligns parallel to the (111) plane instead, and the surrounding Fe^{2+}_{oct} cations align antiparallel to it [119, 120].

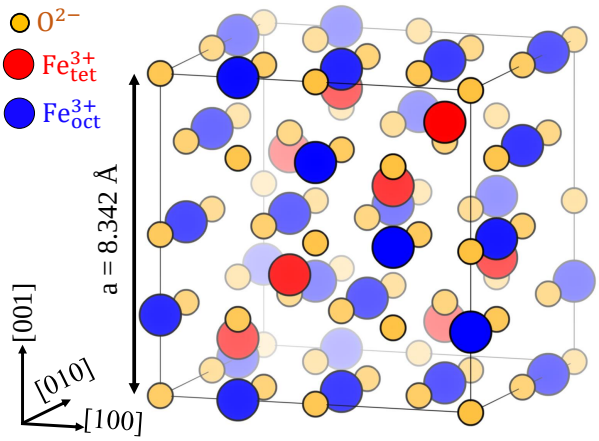

Fig. 3.7: Unit cell of γ-Fe_2O_3. B-sites populated with vacancies are chosen randomly in this representation.

The individual magnetic moments of the Fe^{2+}_{oct}cations have been estimated to be about $4.2\,\mu_B$ [119], corresponding mostly to its spin moment. Its Néel temperature is at 200 K, making it paramagnetic at room temperature.

3.1.3. Maghemite (γ-Fe_2O_3)

Maghemite is structurally very similar to magnetite. It crystallizes in the (regular) spinel structure with a lattice constant of $a_{Fe_2O_3} = 8.342\,\text{Å}$ [122], illustrated in Fig. 3.7. The tetrahedral lattice has 1/8 of its sites populated by Fe^{3+}_{tet} cations – exactly like in the case of Fe_3O_4. However, on the octahedral sites only Fe^{3+}_{oct} cations and randomly distributed vacancies are present. For comparison, if Fe_3O_4 is transcribed as $(Fe^{3+}_8)_{tet}[Fe^{3+}_8Fe^{2+}_8]_{oct}O_{32}$, then Fe_2O_3 can be written in the same form as $(Fe^{3+}_8)_{tet}[Fe^{3+}_{\frac{40}{3}}\square_{\frac{8}{3}}]_{oct}O_{32}$, with $\square$ denoting a vacancy.

Typically, the distribution of the vacancies and the Fe^{3+}_{oct} cations are thought to be random. However, there are recent reports suggesting that the energetically most favourable state of γ-Fe_2O_3 involves an ordering of the iron vacancies in a $1 \times 1 \times 3$ supercell, spanning 3 unit cells in one direction [122,123]. Maghemite is typically regarded an n-type semi-conductor with a band gap of 2.03 eV, in which the delocalized vacancies serve as a means of charge transport [97]; however, in the vacancy-ordered model, the band gap can be reproduced assuming a charge-transfer insulator, for which hopping conduction may happen when electrons are transferred from the O^{2-} anions to unoccupied Fe^{3+}_{oct} states.

Below its Curie temperature of $T_C = 620°C$ [124], maghemite is a ferrimagnet just as well as magnetite, with the octahedral and the tetrahedral lattice coupling antiferromagnetically. The magnetic saturation moment of $2.5\,\frac{\mu_B}{\text{f.u.}}$ can be obtained by the same basic logic as in the case of magnetite: of the $13\frac{1}{3}$ Fe^{3+}_{oct} cations in the unit cell, 8 are compensated by antiferromagnetically coupled Fe^{3+}_{tet} cations, so that the total magnetization arises from the $5\frac{1}{3}$ uncompensated cations, each of which is in a high-spin state with $5\,\mu_B$. In the unit cell $Fe_{\frac{64}{3}}O_{32}$, this gives a magnetic moment of $\frac{16/3}{\text{u.c.}} \cdot 5\,\mu_B = 26\frac{2}{3}\,\frac{\mu_B}{\text{u.c.}}$, and in the formula unit Fe_2O_3 a moment of $2.5\,\mu_B$.

3.1.4. Diffraction patterns

Figure 3.8 shows a schematic of a $\sqrt{H^2+K^2}$ vs L-reciprocal space map (RSM) summarizing the allowed reflections for the spinel crystal structure and the rock salt crystal structure. Examples for spinels are magnetite and maghemite, as discussed before, and examples for the rock salt structure include wüstite, but also NiO and MgO, which will be introduced later in Secs. 3.2 and 3.3. Red disks represent contributions of the tetrahedral sublattice to the spinel diffraction pattern, and blue diamonds contributions of the octahedral sublattice. For this depiction, it was assumed that the lattice constant of the spinel is double the lattice constant of the rock salt structure, $a_{\mathrm{spinel}} = 2 \cdot a_{\mathrm{rocksalt}}$, and the axes are in reciprocal lattice units of the spinel structure.

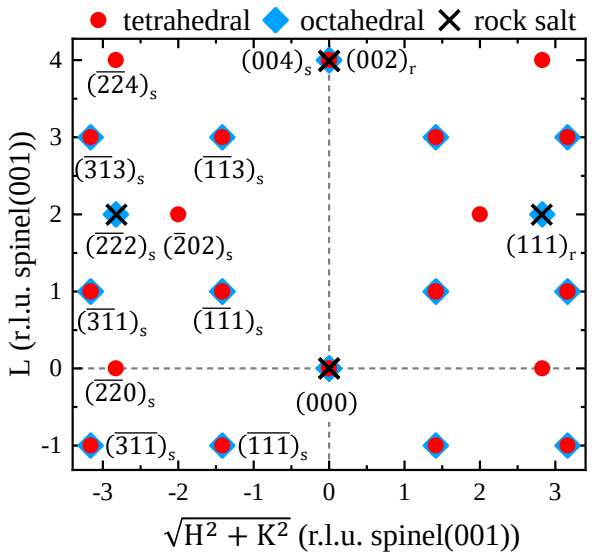

Fig. 3.8: Schematic of a $\sqrt{H^2+H^2}$ vs L-map for a spinel and a rock salt crystal structure with $a_{\mathrm{spinel}} = 2 \cdot a_{\mathrm{rocksalt}}$. Red disks correspond to reflections with contributions from the tetrahedral sublattice and blue diamonds to reflections with contributions from the octahedral sublattice of the spinel structure. Axes are in reciprocal lattice units of the spinel. Indices 's' and 'r' at reflection labels indicate spinel and rock salt reciprocal lattice units, respectively.

HKL	F_{A}	F_{B}	F_{O}
000	8	16	32
004	-8	16	32
111	$-4i^{1/2}(1+i)$	$8i$	0
113	$-4i^{1/2}(1+i)$	$8i$	0
115	$-4i^{1/2}(1+i)$	$8i$	0
202	-8	0	0
204	0	0	0
206	-8	0	0
222	0	-16	32
224	8	0	0
226	0	-16	32
404	8	16	32
313	$4i^{1/2}(1+i)$	$-8i$	0
333	$-4i^{1/2}(1+i)$	$-8i$	0

Tab. 3.2: Contributions from the tetrahedral (F_{A}), the octahedral (F_{B}) and the oxygen sublattice (F_{O}) to the structure factors of some reflections of Fe_3O_4.

The rock salt structure allows those reflections HKL in which the three Miller indices are either all even or all uneven. All reflections forbidden for the rock salt structure are also forbidden for the spinel, and there are some additionally forbidden reflections (for example, the 002 and the 204). The structure factor $F(H,K,L)$ of magnetite can be expressed as a sum of the three sublattice contributions

$$F_{\mathrm{Fe_3O_4}} = f_{\mathrm{Fe^{3+}}} \cdot F_{\mathrm{A}} + \frac{1}{2}(f_{\mathrm{Fe^{2+}}} + f_{\mathrm{Fe^{3+}}}) \cdot F_{\mathrm{B}} + f_{\mathrm{O^{2-}}} \cdot F_{\mathrm{O}} \quad . \tag{3.1}$$

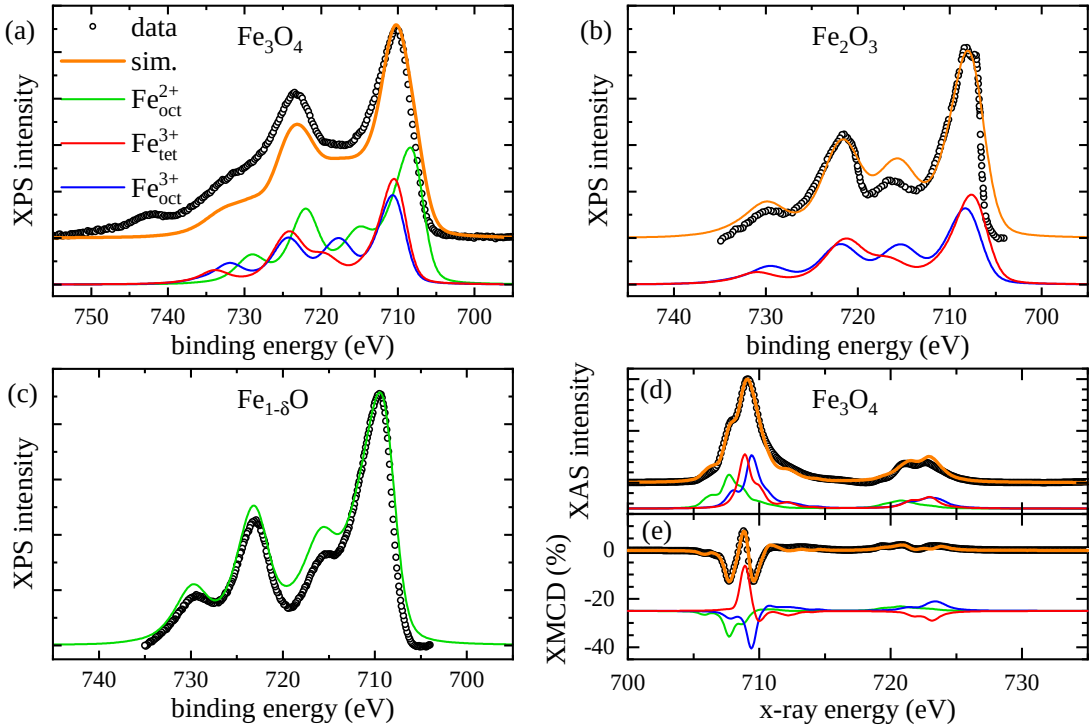

Fig. 3.9: HAXPES data of the Fe2p spectrum for (a) a $Fe_3O_4/SrTiO_3(001)$ sample, (b) a γ-Fe_2O_3 powder sample (data taken from Ref. [125]) and (c) a $Fe_{1-\delta}O$ single crystal sample. The data are compared to the sums of CTM calculations (orange) according to their respective cation stoichiometry of the three cation species Fe^{2+}_{oct} (green), Fe^{3+}_{tet} (red) and Fe^{3+}_{oct} (blue). (d),(e) CTM calculations compared to the (d) XAS and (e) XMCD data of a $Fe_3O_4/MgO(001)$ sample at the Fe L edge, recorded in an outer magnetic field of 4 T. Parameters of the calculations are given in Tab. 4.1.

The individual contributions of the tetrahedral, the octahedral and the oxygen sublattice (F_A, F_B and F_O, respectively) are summarized for some reflections in Tab. 3.1. They were obtained by inserting the positions given in Tab. 3.1 into Eq. (2.68). The octahedral and the oxygen sublattice have non-zero intensity for the same set of reflection – however, there are reflections that are structurally allowed for the tetrahedral lattice, but not for the octahedral lattices, and vice versa. Examples are the 222 reflection, which has $F_A = 0$, but is visible for the other sublattices, and the 224, which has intensity from the tetrahedral lattice, but not from the other lattices. This can also be seen in Fig. 3.8 by means of the red and blue symbols. This offers a pathway to distinguish between octahedral and tetrahedral ordering in the spinel lattice of Fe_3O_4.

3.1.5. Spectroscopic features

The structural similarity between Fe_3O_4 and γ-Fe_2O_3 requires a careful quantitative analysis in order to distinguish the two materials via diffraction methods, since they share the same crystal structure and the lattice constant of γ-Fe_2O_3 is only 0.6% smaller than the one of Fe_3O_4. The diffraction patterns of both materials look like the one shown in Fig. 3.8, with

only slightly offset Bragg positions.

Their photoemission spectra, in contrast, allow to tell them apart at first glance because of their sensitivity to charge-transfer effects. Figures 3.9(a)-(c) show the signature XP spectra of Fe_3O_4, Fe_2O_3 and $Fe_{1-\delta}O$, together with CTM calculations. XPS is particularly well suited to distinguish valencies, because its sensitivity to charge-transfer effects gives rise to a large difference between the iron valency states. The charge-transfer satellite between the $2p_{3/2}$ and the $2p_{1/2}$ for the individual cation spectra is well separated from the main lines. Purely trivalent (red and blue lines in Fig. 3.9(a)) or purely divalent (green line) display a distinct satellite. However, for Fe_3O_4 the shift between the Fe^{2+} and the Fe^{3+} spectra results in an overlap of the charge-transfer satellites, so that their sum (orange line) seemingly shows no apparent satellite at all, but a flat plateau between the lines. This can be taken as a reliable fingerprint of a Fe_3O_4 phase.

XPS data from a Fe_2O_3 sample are shown in Fig. 3.9(b), together with multiplet calculations of Fe^{3+}_{oct} and Fe^{3+}_{tet} cations. Compared to the XP spectrum of Fe_3O_4, a satellite in the center between the two main line appears. As can be seen from the simulation, the reason is the lack of Fe^{2+}_{oct} cations, which contribute intensity at the high-energy flank of the $2p_{3/2}$, and an increase in Fe^{3+}_{oct} relative to the Fe^{3+}_{tet} cations, which are in an $8:8$ ratio in Fe_3O_4, but in an $13\frac{1}{3}:8$ ratio in Fe_2O_3. This peak structure between the two main lines can be used to easily identify a Fe_2O_3 stoichiometry.

The $Fe_{1-\delta}O$ phase is also well distinguishable. $Fe_{1-\delta}O$ is the lowest oxidized iron oxide, and contains only Fe^{2+}_{oct} cations (save for the Koch-Cohen defects). Its XP spectrum can be seen in Fig. 3.9(c). The spectrum is well described by a CTM of the Fe^{2+}_{oct} species. Its fingerprint feature is the charge-transfer satellite between the two main lines, which is located close to the high-energy flank of the $Fe2p_{3/2}$. Comparison with the spectra in Figs. 3.9(a),(b) usually allows a quick determination of the iron oxide phase by the means of the position of the charge-transfer satellite.

The XA and XMCD spectra of Fe_3O_4 are shown in Figs. 3.9(d),(e). Compared to XPS, the charge-transfer splitting is not as pronounced in XAS and no strong satellite features develop in between the L_3 and the L_2 edge. This fact, together with the strong overlap of the individual cation spectra which lead to an unremarkable XA spectrum of Fe_3O_4, makes it more ambigious to determine the valence state. The XMCD data of Fe_3O_4 show three peaks at the L_3 edge, caused by the fact that the tetrahedral cations couple antiferromagnetically to the other two species. This is reflected in the sign of its XMCD spectrum, giving rise to the very characteristic three-peak XMCD structure. This magnetic contrast between the Fe^{2+}_{oct}, Fe^{3+}_{tet} and Fe^{3+}_{oct} cations makes it possible to use XAS together with XMCD to fit experimental data from Fe_3O_4 and extract the cation stoichiometry [23, 35, 80, 126]. This procedure will be discussed in Sec. 4.5.

3.2. Nickel oxide (NiO)

Similar to wüstite, nickel oxide is an insulating (band gap of 4.3 eV [129]), antiferromagnetic transition metal oxide, crystallizing in the rock salt structure (cf. Fig. 3.10(a)). Different to wüstite, it is in its antiferromagnetic phase at room temperature with a Néel temperature of 523 K. In single crystals, the magnetic moments preferably group in ferromagnetic (111)

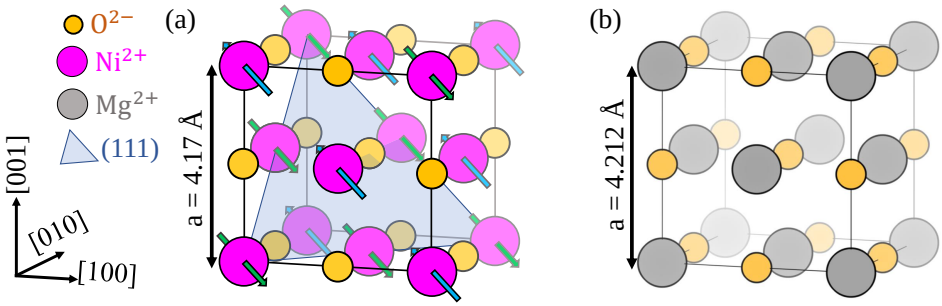

Fig. 3.10: Unit cells of (a) NiO and (b) MgO. Spins in NiO (blue and green arrows) align antiferromagnetically within the (111) plane (shaded area) [127, 128].

sheets and align parallel within these planes in no specified direction, unless a magnetic field is applied, in which case they align perpendicular to the field [127].

Ultrathin film stacks of Fe_3O_4 and NiO are very interesting from a spintronic perspective, because the exchange bias between the ferrimagnetic magnetite and the antiferromagnetic nickel oxide can be exploited for magnetic tunnel junctions [23, 130–133]. This effect causes a shift of the coercive fields of the ferromagnetic film, and can be used to pin its magnetization state. There are, however, hints that the situation is not quite as simple. Bulk NiO is an antiferromagnet at room temperature, but size-effects of the magnetic properties of NiO, including ferromagnetic behaviour at room temperature, have been frequently reported before, mostly for NiO nanoparticles [134–138]. For Fe_3O_4/NiO ultrathin films, a spin-flop coupling of NiO to the Fe_3O_4(001) interface has been reported [132]. In that case, the antiferromagnetic order of NiO aligns perpendicular to the magnetization of Fe_3O_4, but with a canting of the Ni^{2+} moments, resulting in a magnetization component parallel to the ferrimagnet. This reaction of NiO to outer magnetic fields has also been confirmed by spin-hall magnetoresistance measurements [128, 139]. Therefore, the magnetic ordering in NiO appears to heavily depend on the size and environment of the films.

3.3. Magnesium oxide (MgO)

Magnesium oxide is used as a substrate for the iron oxide films in this work. It crystallizes in the rock salt structure with a lattice constant of $a_{MgO} = 4.212\,\text{Å}$, illustrated in Fig. 3.10(b). The RSM of the diffraction pattern of a MgO(001) substrate therefore corresponds to the rock salt reflections in Fig. 3.8. Magnesium oxide is insulating, with a band gap of about 7.8 eV [140], and diamagnetic.

3.4. Strontium titanate ($SrTiO_3$)

Another frequently used substrate for Fe_3O_4 films is strontium titanate ($SrTiO_3$). $SrTiO_3$ is a diamagnetic insulator with a band gap of 3.2 eV, and crystallizes in the perovskite structure with a lattice constant of $a_{SrTiO_3} = 3.905\,\text{Å}$ [141]. The unit cell is shown in Fig. 3.11. It consists of a cubic close-packed structure made of a O^{2-}- and a Sr^{2+}-fcc-sublattice, with 1/4 of the octahedral sites occupied by a Ti^{4+} ion. In [001] direction, $SrTiO_3$ consists of

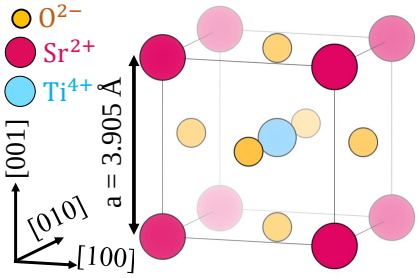

Fig. 3.11: Unit cell of the perovskite structure of $SrTiO_3$. It consists of a cubic close-packed structure made of O^{2-} and Sr^{2+} ions, with 1/4 of the octahedral sites occupied by a Ti^{4+} ion.

alternating TiO_2 and SrO layers. Consequently, the (001) surface, which serves as substrate surface in this work, is terminated by either one of these layers. However, the surface unit cells of both are of the same size and orientation [142], so that no crucial impact on the structure of the film is to be expected.

3.5. Magnetite thin films

3.5.1. MgO versus $SrTiO_3$ substrates

The properties of a thin film sample is always influenced by its substrate. In some cases, it might be desirable to have little effect of the substrate on the film in order to retain, as far as possible, the properties of the film material. In others, the properties of the film material can be tuned by the substrate influence, such as strain on the film lattice [143]. MgO(001) is the substrate used most frequently for Fe_3O_4 films, because its doubled unit cell has a small lattice mismatch of 0.3% to magnetite and is electrically and magnetically inert [21, 80, 117, 144–148]. This allows for pseudomorphic growth of Fe_3O_4/MgO(001) with low coupling of the electronic states or the magnetic order of Fe_3O_4 to the substrate. Since Fe_3O_4 is often considered as an electrode material for spinelectronic devices and MgO is widely used as a tunnel barrier material, Fe_3O_4/MgO stacks are also interesting from an application point of view [12, 17].

As explained in Sec. 2.2, high growth temperatures often result in higher crystalline order of the films. MgO substrates limit the growth and annealing temperatures to 250°C, because beyond this Mg starts to interdiffuse into the magnetite film [36]. An alternative is $SrTiO_3$ [34, 143, 149, 150], whose doubled unit cell has a lattice mismatch of −7.5% to magnetite. $SrTiO_3$ is – just as MgO – diamagnetic and insulating, but may be doped by Niobium in order to tune its conductivity [23]. This is useful from an experimental point of view, because insulating substrates make application of some techniques – especially electron diffraction and synchrotron-based XPS – difficult. The reason is that charging of the sample cannot be compensated if the film is not electrically connected to some electron reservoir. The developing electrostatic potential deflects electrons and skews the binding energies. This can be avoided by connecting a wire to the film in some cases, but this is usually not suitable for *in situ* studies, for which the films are grown and studied without breaking the vacuum. A solution is using a conductive substrate, such as Nb-doped $SrTiO_3$. To this end, the $SrTiO_3$ substrates in this work are doped with 0.05wt% Nb.

The left half of Fig. 3.12(a) shows a schematic RSM summarizing the Bragg positions of MgO(001) and Fe_3O_4(001), and Fig. 3.12(b) the same for $SrTiO_3$(001) and Fe_3O_4(001). The right halves show measurements of a Fe_3O_4/MgO(001) and a Fe_3O_4/$SrTiO_3$(001) thin film sample. The vertical streaks that can be seen crossing the reflections in Fig. 3.12(a) – most

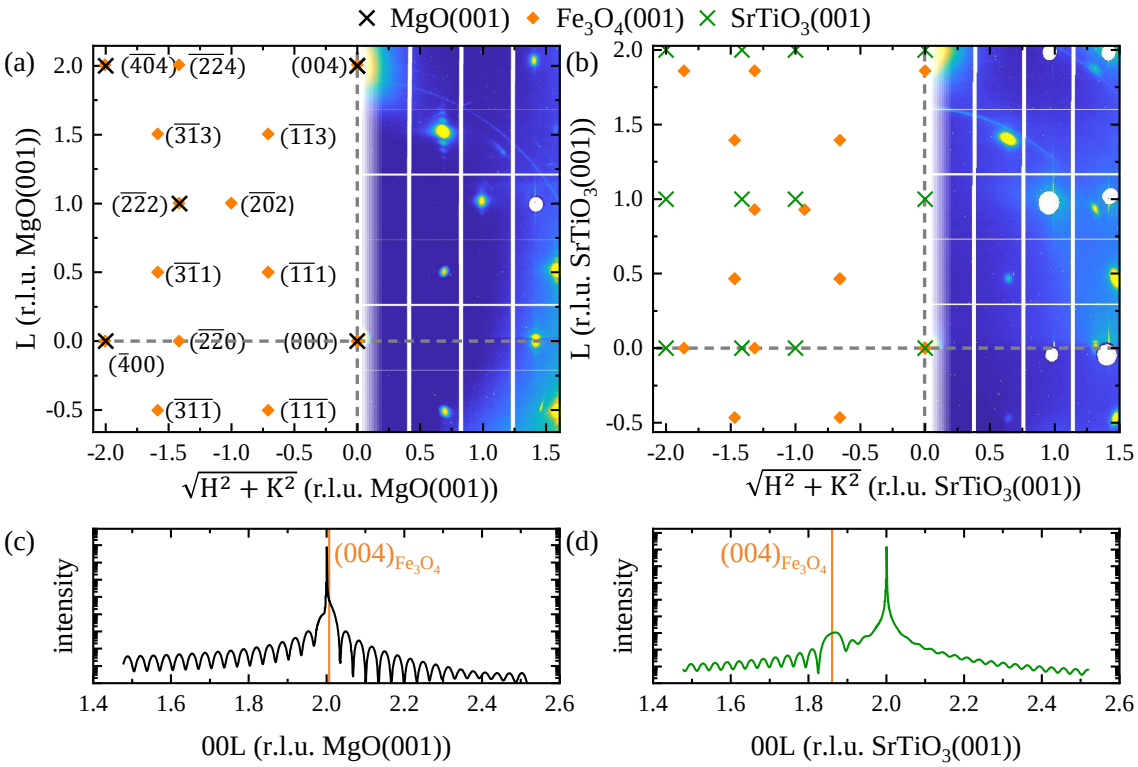

Fig. 3.12: (a) Right half: $\sqrt{H^2+K^2}$ vs L-map of a Fe_3O_4/MgO(001) sample. The white circle at the (222) position is a semi-transparent beam stop protecting the detector from the bright substrate (111) reflection, and the white grid stem from module borders of the detector. Left half: schematic of the Bragg positions for Fe_3O_4(001) and MgO(001). Axes are in reciprocal lattice units of the substrate, reflection labels in units of Fe_3O_4(001). (c) Simulation of the 002-CTR of a 17.6 nm-thick Fe_3O_4/MgO(001) film, produced following the description in Sec. 2.8. Orange line corresponds the position of the $(004)_{Fe_3O_4}$ reflection. (b),(d) Analogous plots for a Fe_3O_4/$SrTiO_3$(001) sample.

notably the (113) – are diffraction rods with Laue fringes, as introduced in Sec. 2.8. Because these Laue fringes are strongly damped for disorder in the film, their occurence serves as a good first indicator for well ordered films. Fe_3O_4/$SrTiO_3$(001) films are usually not as well ordered as Fe_3O_4/MgO(001) films [34], and do not exhibit Laue fringes in Fig. 3.12(b).

The small lattice mismatch between Fe_3O_4 and MgO has the consequence that their reflections strongly overlap. For $SrTiO_3$, actually every reflection HKL is allowed, but the lattice mismatch results in well separated reflections, which can be another reason to choose $SrTiO_3$ as a substrate. This is emphasized by Figs. 3.12(c),(d), which show simulations of the 00L-CTRs of Fe_3O_4/MgO(001) and Fe_3O_4/$SrTiO_3$(001) close to the (002) reflection. The simulations were performed as described in Sec. 2.8, assuming a Fe_3O_4 film consisting of 17 unit cells in the vertical direction. Both CTRs exhibit Laue fringes due to the finite film thickness. The Fe_3O_4/$SrTiO_3$(001) sample additionally shows a pronounced Bragg peak due to the $(004)_{Fe_3O_4}$ film reflection, indicated by the orange line. In the case of Fe_3O_4/MgO(001), the $(004)_{Fe_3O_4}$ reflection is very close to the $(002)_{MgO}$ reflection, and the intensity of the substrate reflection is several order of magnitudes higher than the one of the film. This large

intensity discrepancy has usually the consequence that the substrate reflection cannot be recorded simultaneously with the CTR and the film reflection, but requires higher attenuation. For this reason, the substrate reflections have been blocked by beam stops attached to the detector, visible as white disks in the right halves of Figs. 3.12(a),(b).

3.5.2. Antiphase boundaries

The fact that the lattice constant of Fe_3O_4 is roughly double the lattice constants of both MgO(001) and $SrTiO_3$(001) means that a single unit cell of Fe_3O_4 covers 4 unit cells of the substrate. This has the consequence that distinct islands on the surface may nucleate in a way that their shift cannot be represented by a translational vector. Thus, when they merge, they cannot retain the periodicity of the Fe_3O_4 lattice, and instead form antiphase domains, separated by antiphase boundaries (APB)[2]. Figure 3.13(a) shows the different in-plane shift vectors possible for Fe_3O_4/MgO(001). In reference to the unit cell 'A', the cell 'B' is shifted by half a lattice constant in [100] direction with a shift vector $\frac{1}{2}$[100]. The cell 'C' is shifted with a shift vector of $\frac{1}{4}$[110]. The unit cell 'D' can be obtained by rotating the unit cell 'A' by 90°. When the film grows past the first monolayer, this gives rise to out-of-plane shift vectors of the $\frac{1}{4}$[101]-type. Experimentally, it has been found that about 44% of the antiphase boundaries are of the $\frac{1}{4}$[110]-type, and 55% are of the out-of-plane $\frac{1}{4}$[101]-type, while only about 1% are of the $\frac{1}{2}$[100]-type [117].

Across the APB, electronic transport and the exchange interaction differs from the bulk. This manifests in a higher resistivity [151], magnetoresistance [152] and in lower saturation magnetization [146, 153–155] for thin Fe_3O_4 films, in which the APB density is substantially higher than in bulk Fe_3O_4 [117].

The modified magnetic coupling across APBs is illustrated in Figs. 3.13(b),(c), which show the APB of the $\frac{1}{4}$[110]-type for the first 2 layers of a Fe_3O_4/MgO(001) film, accounting for about 44% of the APBs. In the bulk, the ferromagnetic order in the octahedral sublattice is established by double exchange and 90° super exchange (black arrows in Fig. 3.13(b)), and the antiferromagnetic coupling between the octahedral and the tetrahedral sublattice by 120° super exchange (blue arrows in Fig. 3.13(b)). In the first layer, the antiferromagnetic super exchange between the two sublattices is continued across the APB, but additionally an antiferromagnetic direct exchange between neighboring Fe^{3+}_{tet} cations is possible. In the second layer, an antiferromagnetic 180° super exchange within the octahedral sublattice occurs across the APB (blue arrows in Fig. 3.13(c)). These additional coupling schemes can favour antiferromagnetic alignment between domains, resulting in an overall lower magnetization [117, 156]. This is consistent with the observation that the saturation magnetization becomes smaller with decreasing film thickness [23, 146, 148].

The formation energy of the $\frac{1}{4}$[110] APBs is very low, so that it is perhaps difficult to completely prevent their presence [156]. However, there have been reports that in Fe_3O_4/MgO(001) and Fe_3O_4/$SrTiO_3$(001), the APB density can be reduced by post-deposition annealing [155]. Alternatively, substrates with a spinel crystal structure are an option to reduce APB formation [157]. Nevertheless, on spinel substrates with considerable lattice mismatch, such as $MgAl_2O_4$(001) with a mismatch of 3.4%, APBs still occur as a means to relax strain.

[2] Note that antiphase boundaries do not exclusively occur in thin films grown on higher-symmetry substrates, but are also present in single crystals. However, their density in thin film samples is much higher [117].

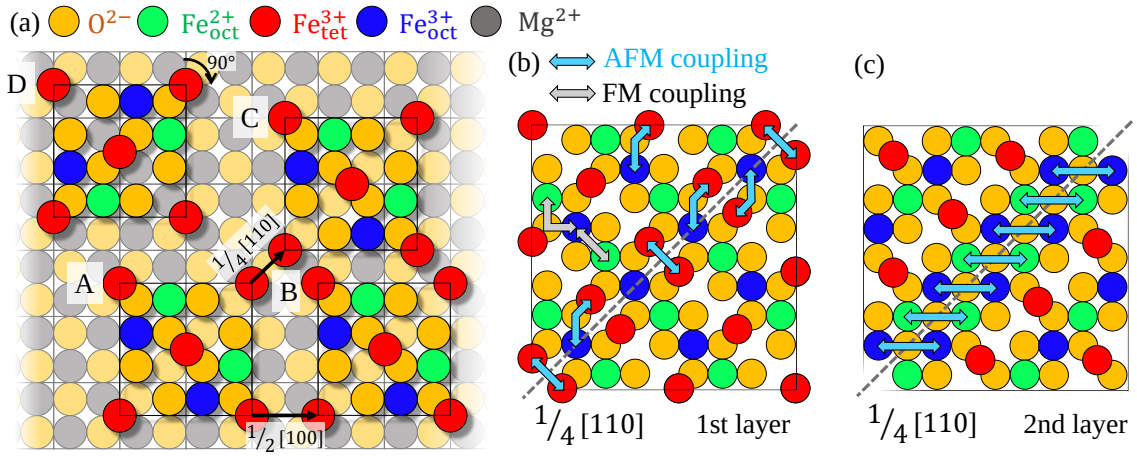

Fig. 3.13: (a) Possible antiphase shifts of Fe_3O_4 monolayers on MgO(001). The reference unit cell 'A' can be shifted by translational vectors $\frac{1}{2}$[100] (cell 'B') or $\frac{1}{4}$[110] (cell 'C'), or be rotated by 90°. (b),(c) Magnetic coupling across an $\frac{1}{4}$[110]-type APB. Blue arrows indicate antiferromagnetic exchange couplings, grey arrows ferromagnetic exchange couplings. Besides the three exchange coupling mechanisms present in bulk Fe_3O_4, (b) in the first monolayer an additional antiferromagnetic direct exchange is present between tetrahedral iron cations across the APB, and (c) in the second monolayer an antiferromagnetic super exchange between octahedral cations. Adapted from Ref. [117].

This happens by the formation of misfit dislocations with a $\frac{1}{4}$100]-shift vector, which locally improves the matching of the film to the substrate lattice at the cost of a APB in the film [158].

3.5.3. Substrate interface

Sec. 3.1.1 discussed the surface structure of Fe_3O_4(001) which experiences a reordering of the cations due to the crystal truncation at the film surface. Similar effects can happen at the interface of the film to the substrate. Figure 3.14(a) shows an illustration of the ideal stacking at the Fe_3O_4/MgO(001) interface. However, the transition from the rock salt structure of the substrate to the spinel structure of the film can be accompanied by the formation of an interlayer of $Fe_{1-\delta}O$, representing a continuation of the rock salt substrate into the iron oxide film. Formation of such $Fe_{1-\delta}O$-like interlayers have been reported earlier on both metal and oxide substrates [159–162], and also on MgO(001) [21] and $SrTiO_3$(001) [22]. In Ref. [21], 3 monolayers of $Fe_{1-\delta}O$ with an intermediate stoichiometry between FeO and Fe_3O_4 are observed using kinematic diffraction analysis. This is illustrated in Fig. 3.14(b). Please note that it is depicted there as a purely stoichiometric FeO layer, but the exact cationic stoichiometry is yet unclear. For all three interface distances – between substrate and film d_{s-f}, between substrate and interlayer d_{s-i} and between interlayer and film d_{i-f} – it has been found that they are either $d = 2.05 \pm 0.1$Å or $d = 3.2 \pm 0.2$Å, roughly corresponding to either 1 or 1.5 vertical layer distances of the substrate [21,144].

A different model for the interface region has been proposed by Chang et al. [80] They present a model for the growth dynamics of Fe_3O_4/MgO(001). By multiplet analysis of the XAS spectra of a series of few monolayer films, they derive an absence of tetrahedral Fe^{3+}_{tet} cations

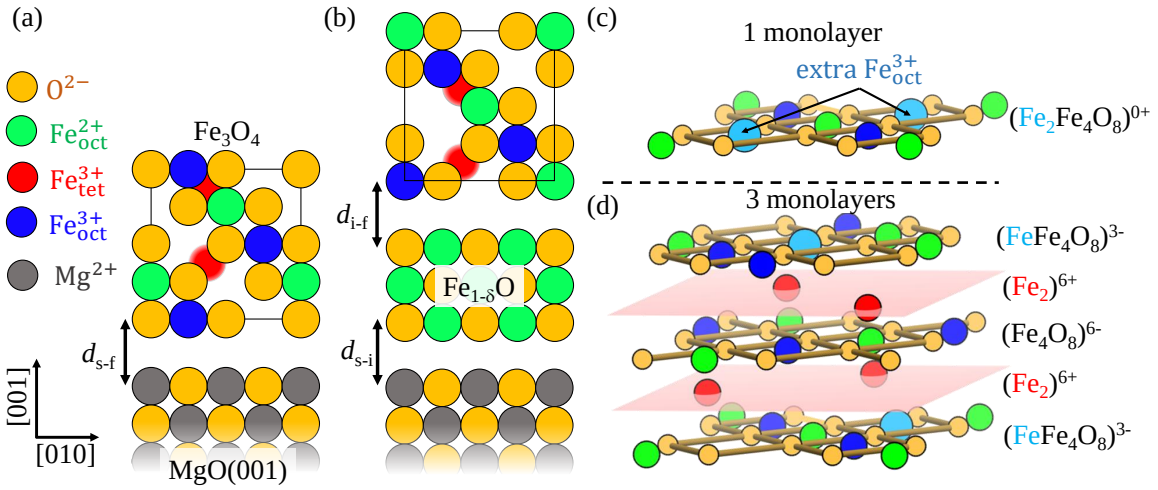

Fig. 3.14: (a) Ideal stacking of Fe_3O_4/MgO(001). (b) 3 monolayers of $Fe_{1-\delta}O$ form an interlayer between Fe_3O_4 and MgO. $d_{s\text{-}f}$, $d_{s\text{-}i}$ and $d_{i\text{-}f}$ are the interface distances of substrate to film, substrate to interlayer and interlayer to film, respectively. Adapted from Ref. [21]. (c),(d) Dynamic atomic reconstruction model of the interface. (c) For a single monolayer of Fe_3O_4/MgO(001), the two Fe^{3+}_{tet} cations occupy octahedral sites instead. (d) If 3 or more monolayers are grown, both the uppermost and lowermost layer are octahedral and have an additional Fe^{3+}_{oct} cation in order to avoid polarity. Adapted from Ref. [80].

in the first monolayer, but their presence in the second one. This behavior is explained by the need for a polarity-compensation mechanism for few-layer films which is different to that of the bulk. The model they suggest is depicted in Figs. 3.14(c),(d). In the first monolayer, no cations populate the tetrahedral sites, but instead two additional Fe^{3+}_{oct} cations per Fe_4O_8 unit are found in the octahedral layer, so that the stoichiometry remains Fe_3O_4, but no polarity can occur. If a film of three monolayers is grown, both the lowermost and the uppermost layer are octahedral layers with one additional Fe^{3+}_{oct} cation and thus, a Fe_5O_8 stoichiometry, so that their total charge is $3-$. In between these two layers, the regular inverse spinel structure develops, consisting of alternating tetrahedral layers with a charge of $+6$ and octahedral layers with a charge of -6. This satisfies the Tasker criterion of non-polarity discussed in Sec. 3.1.1. Given the wide success of the SCV model of the surface structure of $Fe_3O_4(001)$, this model's prediction for the surface is most likely incorrect, at least for films thicker than a few monolayers. However, it might offer a model for the initial growth stage of Fe_3O_4 films and perhaps for the interface stoichiometry.

The interface region may also be affected by interdiffusion of the film and substrate materials. For instance, it is well known that Mg^{2+} ions start to diffuse into Fe_3O_4 if a Fe_3O_4/MgO sample is heated above 250°C [36]. A similar effect is observed for the interface of Fe_3O_4/NiO, where for annealing temperatures above 400°C both films start to interdiffuse to form $NiFe_2O_4$. For Fe_3O_4/NiO films deposited at 400°C, high-resolution transmission electron microscopy images show generally sharp interfaces between the rocksalt structure of NiO and the spinel structure of Fe_3O_4 [131,133]. Complementary electron energy loss spectroscopy (EELS) shows that for Fe_3O_4/NiO stacks deposited at 400°C, the interface appears to be chemically sharp as well [131].

4. Experimental setups

In this chapter, the experimental concepts and setups important for this work are introduced. All experiments in this work study thin film samples prepared by RMBE, and the vast majority employ x-rays produced at synchrotrons. For this reason, first the generation of x-rays at synchrotron facilities is explained in Sec. 4.1. In the following Sec. 4.2, the concept of RMBE is presented. A number of experiments in this work has been performed using a custom-made ultra-high vacuum chamber which allowed time-resolved HEXRD and HAXPES experiments. This chamber and the experiments performed with it will be introduced in Sec. 4.3. After that, the setup used for the XRMR measurement is presented in Sec. 4.4. In Sec. 4.5, methods for the multiplet analysis of XPS and XAS/XMCD data is discussed.

The general information about the generation of synchrotron radiation is taken from Ref. [31].

4.1. Generation of synchrotron radiation

For scientific purposes, x-ray are usually generated in one of two ways: by x-ray tubes or by synchrotron radiation sources, such as storage rings or free electron lasers. X-ray tubes are widely available for lab-based devices and are often used for XPS, XRD or XRR, among other techniques [58]. Synchrotron radiation sources, on the other hand, are large-scale facilities to which the access is usually limited for individual researchers [31]. Since most of the data of this work have been recorded at storage rings, this section focuses on x-ray generated at these. Synchrotron radiation offers a set of advantages: the photon flux is usually orders of magnitude higher (i.e., $\sim 10^8 \frac{\text{photons}}{\text{mm}^2 \cdot \text{s} \cdot 0.1\%\text{bw}}$ vs $\sim 10^{16} \frac{\text{photons}}{\text{mm}^2 \cdot \text{s} \cdot 0.1\%\text{bw}}$ [69]), allowing for faster measurements; also the size and the divergence of the beam are smaller, resulting in better resolution in energy as well as in both real and reciprocal space, and higher coherence. Additionally, the photon flux of x-ray tubes is high only at a material-specific energy – the Kα energy –, so that only this particular energy can be used, unless a flux decrease of at least a factor of 10^4 is accepted [69]. In contrast, the x-ray energy for synchrotron-radiation can not only be arbitrarily picked, but also scanned during the experiment. This means that experiments that require tunable photon energies such as XAS are almost exclusively done at synchrotrons. The quality of an x-ray beam is usually denoted by the brilliance B [94]

$$B = \frac{\text{photon flux}}{(\text{horizontal} \times \text{vertical divergence}) \cdot (\text{beam size}) \cdot (0.1\% \text{ energy bandwidth})} \quad , \quad (4.1)$$

summarizing the qualities discussed above in a single number.

The physical effect that is exploited in synchrotrons to generate x-rays is the fact that charged particles which are accelerated emit electromagnetic radiation – the so-called *synchrotron radiation*. Since the intensity of the emitted radiation scales with the particle mass as $\sim \frac{1}{m^4}$, the only viable choice to produce x-rays are electrons or positrons. Therefore, the strategy is

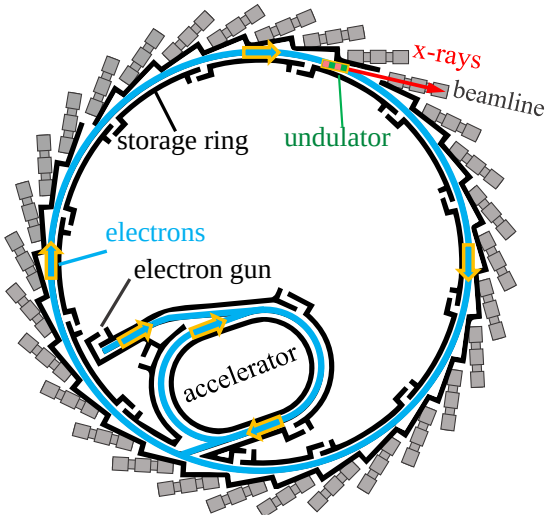

Fig. 4.1: Sketch of a synchrotron facility. Electrons are generated in the electron gun, accelerated to their target speed in the pre-accelerator, and then injected into the storage ring, around which they travel at a relativistic speed. At the undulator, they produce an x-ray beam (red), which escapes into one of the beamlines (grey) surrounding the storage ring. Adapted from Ref. [163].

to accelerate electrons to a relativistic speed and then deliberately force them onto circular arcs, causing them to emit synchrotron radiation.

A typical synchrotron facility is shown in Fig. 4.1. In the electron gun, electrons are generated and fed into a pre-accelerator. There they are accelerated to a speed close to the speed of light, and then introduced into a storage ring, in which the beam of electrons travels at this constant speed. The storage 'ring' of a modern synchrotron has the form of a polygon, consisting of straight sections which are connected by bending magnets. At these bending magnets, the electrons change direction from one straight section to the next and emit synchrotron radiation into a narrow cone with an opening angle determined by the electron energy – the *natural opening angle* –, which then leaves the ring tangentially. At these positions, beamlines can be set up in which the experiments are located (grey in Fig. 4.1). However, more brilliant radiation than from bending magnets can be obtained by using insertion devices in the straight sections [31]: Both wigglers and undulators consist of a series of magnets which lead the electrons onto an oscillatory path, effectively working as a sequence of bending magnets. In undulators, the amplitude of these oscillatory motions is in in the order of the natural opening angle, while it is much wider in wigglers. For this reason, the horizontal divergence of wiggler radiation is much wider than for undulator radiation. Nowadays, the most widespread insertion devices at modern 3rd generation synchrotron radiation sources is the undulator.

Figure 4.2(a) shows the basic concept of an undulator, which is very similar to a wiggler. Just as the wiggler, it consists of an array of magnets of alternating orientation. This way, electrons traveling across the undulator are exposed to alternating magnetic fields and forced onto an oscillating path. These turns in the path lead to the emission of synchrotron radiation. The difference to a wiggler is that the period of these oscillations is designed in a way that the waves emitted at each turn are in phase with one another (constructive interference), so that the total amplitude of the emitted x-rays is given by the sum of each partial wave. This results in an increased brilliance [31]. Another convenient property of undulators is that the x-ray energy can be tuned by varying the gap between the magnetic poles. This changes the magnetic field the electrons are exposed to and consequently its path. The polarization of x-rays produced this way lies in the plane in which the oscillatory motion happens, and

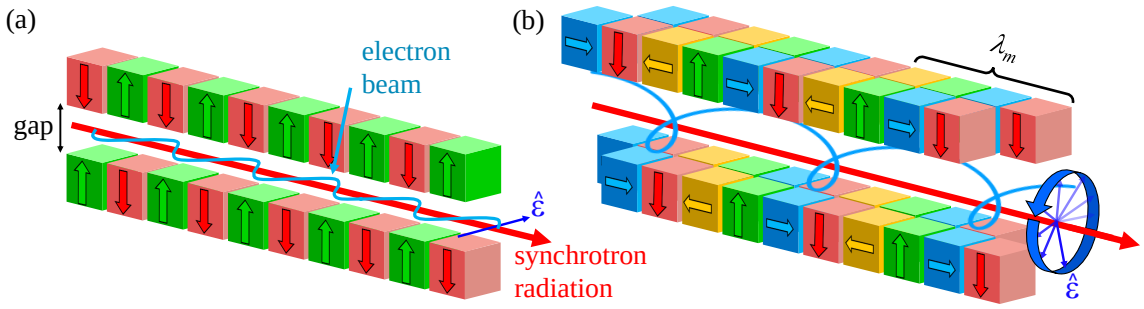

Fig. 4.2: (a) Sketch of an undulator. Red and green boxes indicate magnets of opposite alignment. The alternating magnets force the electron beam (blue) onto an oscillating path, on which it emits synchrotron radiation (red). The polarization vector $\hat{\epsilon}$ lies in the horizontal plane. The gap between the magnet array can tune the photon energy. (b) Sketch of an Apple-II undulator. It consists of 4 rows of magnets with 4 orientations. The rows can be shifted against one another. In a parallel alignment, they produce horizontal polarization as in (a), but if they are shifted by 1/4 of a period length λ_m, the electrons move on a spiral path and produce circularly polarized synchrotron radiation. Adapted from [94, 164].

is therefore linear horizontal. However, some experiments require more flexibility regarding the polarization; for instance, XMCD and XRMR experiments can only be performed with circularly polarized light. Variable polarization can be produced at the undulator. Figure 4.2(b) shows a schematic of an Apple-II undulator [165]. In contrast to the version in Fig. 4.2(a), each of the two magnet arrays consists of two rows of magnets, in which 4 magnet blocks of different orientation are organized in repeating periods. The polarization of the synchrotron radiation can be freely chosen by shifting the rows against the other two. If all 4 aligned with no shift, horizontally polarized x-rays are produced just as in Fig. 4.2(a). If two diagonally opposing rows are shifted against the other two by 1/4 of a period length λ_m, as shown in Fig. 4.2(b), the electrons are forced onto a spiral path through the undulator and produce a circular polarization. Different shift configurations can virtually produce any desired polarization.

A sketch of a typical beamline can be seen in Fig. 4.3. The electron beam passes the undulator and generates the x-ray beam, and is subsequently deflected into the next straight section by a bending magnet. In the optics hutch, the x-ray beam is usually focused by x-ray lenses onto the monochromator. The accessible x-ray energies and the brilliance of a beamline is pre-determined by its undulator. Each undulator has a distinctive spectral characteristic, and reaches its highest brilliance at a energy dictated by its design, mostly its period length. Next to this characteristic energy, the x-ray beam from an undulator contains other wavelengths, and is therefore often called *pink beam*. However, most experiments require a monochromated beam of a narrow energy bandwidth. The dominant monochromator design for x-rays in the intermediate and hard x-ray regime ($E_\mathrm{ph} > 2\,\mathrm{keV}$) is called a double-crystal monochromator [31]. The first crystal is aligned in such a way that the desired x-ray energy fulfills the Bragg condition for a certain reflection – most commonly the Si(111) reflection. The second crystal is then aligned so that the diffracted beam fulfills the same Bragg condition, and ultimately only photons of this single energy can pass. For soft x-rays ($E_\mathrm{ph} < 1\,\mathrm{keV}$), more often grating plates are used [166]. Here, the x-rays coming from the undulator are reflected onto a diffraction grating which diffracts x-rays in different directions

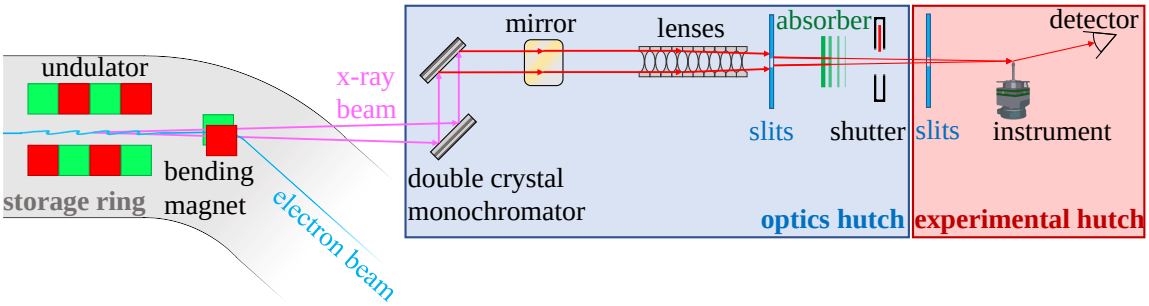

Fig. 4.3: Sketch of a typical beamline. The x-ray beam is generated in the undulator. In the optics hutch, it is collimated monochromatized by a double crystal monochromator, and higher harmonics are filtered using x-ray mirrors. Slits are used to control the size of the beam and absorbers to control the intensity. A shutter is used to quickly block the beam. In the experimental hutch, the experimental instrument and the detector is located.

depending on their energy, which can then be selected by an exit slit.

Photon energies that are integer multiples of the target energy are called higher harmonics and cannot be filtered by the monochromator, because if photons with energy E_{ph} fulfill the Bragg condition at a given incident angle, photons with energy $n \cdot E_{\mathrm{ph}}$ will as well. In order to remove these higher harmonic photons from the beam, x-ray mirrors are used, which utilize the fact that the critical angle of the incident x-rays changes with energy. The mirrors are positioned in a way that the x-rays of the desired energy are totally reflected, while higher harmonic photons are partially transmitted into the mirror and can be partially absorbed [94]. In order to further focus or collimate the beam arriving at the experiment, it usually passes additional x-ray optics such as refractive lenses. In order to control the size of the beam, a set of slits can be employed to cut off portions of the beam. The intensity can be lowered by a set of absorbers which can be moved in and out of the beam path and the combination of which determines the intensity arriving at the sample. A shutter is placed before the experimental hutch in order to fully block the beam. In the experimental hutch, the instrument and the detector is located. In Fig. 4.3, a diffractometer is shown as an example, but it can generally be any kind of sample environment, depending on which experiment shall be performed.

4.2. Molecular beam epitaxy

The thin films in this work have been grown by molecular beam epitaxy. A sketch for the growth of a Fe_3O_4/MgO is shown in Fig. 4.4. The strategy is to create a molecular beam from a solid target and position a substrate in this stream of atoms (and ions), so that the evaporated material condensates and forms a thin film. This process has to be performed in a high-vacuum environment, because otherwise the mean-free path of the molecular beam becomes too small. The main components of an evaporator are a solid target and a filament which generates free electrons by thermionic emission. The electrons are accelerated by a high voltage towards the iron target and locally heat it up to evaporation temperature. The evaporated atoms leave the target radially and are shaped by slits into a molecular beam. The molecular beam passes a fluxmeter which senses a small current from the ions in the molecular beam and serves as a measure of its flux, allowing to control the deposition rate [167].

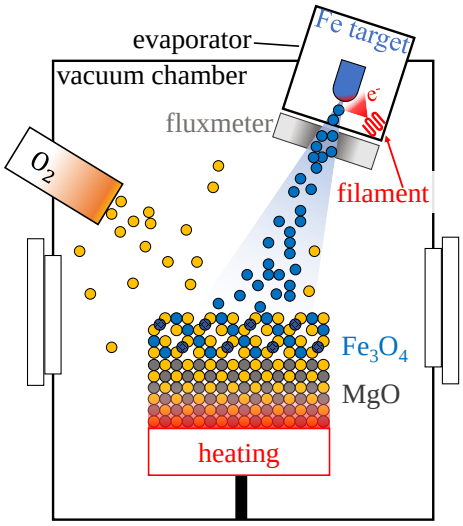

Fig. 4.4: Sketch of an RMBE setup for the growth of Fe_3O_4/MgO. A vacuum chamber is filled with a low oxygen atmosphere and contains a substrate located on a heater. An evaporator generates a molecular beam of iron atoms by accelerating electrons from a filament onto an iron target. A fluxmeter measures the flux of the beam leaving the evaporator. The beam of iron atoms is directed onto a MgO substrate, on which they condensate and react with the oxygen environment to form a Fe_3O_4 film.

One way to grow iron oxide films is to directly deposit it from an oxide target onto a substrate. However, evaporating oxides requires very high temperatures, and the oxygen content is predetermined by the target and may vary depending on the target temperature, because the oxygen evaporates faster than the metal. Alternatively, it is possible to evaporate from a metallic iron target in an oxygen atmosphere, so that the iron condensating on the substrate surface reacts to iron oxide [7]. For this reason, the vacuum chamber is filled with a low oxygen atmosphere (typically $p_{O_2} = 10^{-7}$... 10^{-5} mbar). This procedure is called reactive molecular beam epitaxy. Upon adsorbing on the substrate, the iron atoms diffuse across the surface and organize themselves to form a crystalline film. As explained in Sec. 2.2, this process is often benefited by heating the substrate up to higher temperature in order to offer more thermal energy. Therefore, the substrate is located on a heater to control the substrate temperature.

In an RMBE setup, the main parameters to control the growth process are the oxygen partial pressure p_{O_2}, the substrate temperature T and the deposition rate r. In this work, the deposition procedure followed those described in Refs. [23, 168, 169]. Before deposition, the MgO and the Nb-doped (0.05 wt%) $SrTiO_3$ substrates were annealed at 400°C for one hour in an oxygen atmosphere of $p_{O_2} = 10^{-4}$ mbar for cleaning. NiO/MgO(001) films were grown by evaporating Ni from a metal target in an oxygen atmosphere of either $p_{O_2} = 5 \cdot 10^{-6}$ mbar or $p_{O_2} = 1 \cdot 10^{-5}$ mbar at 250°C substrate temperature. Fe_3O_4 films were deposited on MgO(001) and on NiO/MgO(001) by evaporating Fe at $p_{O_2} = 5 \cdot 10^{-6}$ mbar and a temperature of 250°C, in order to avoid interdiffusion of Mg into the films [36]. The $Fe_3O_4/SrTiO_3$(001) films were deposited in oxygen atmospheres of $p_{O_2} = 1 \cdot 10^{-6}$ mbar and $p_{O_2} = 5 \cdot 10^{-6}$ mbar, at higher substrate temperatures of 350°C and 400°C.

4.3. Time-resolved growth studies

4.3.1. Ultra-high vacuum chamber

For parts of this work, a custom-designed ultra-high vacuum deposition chamber was used which allows tr-HEXRD and tr-HAXPES experiments during the deposition of epitaxial thin

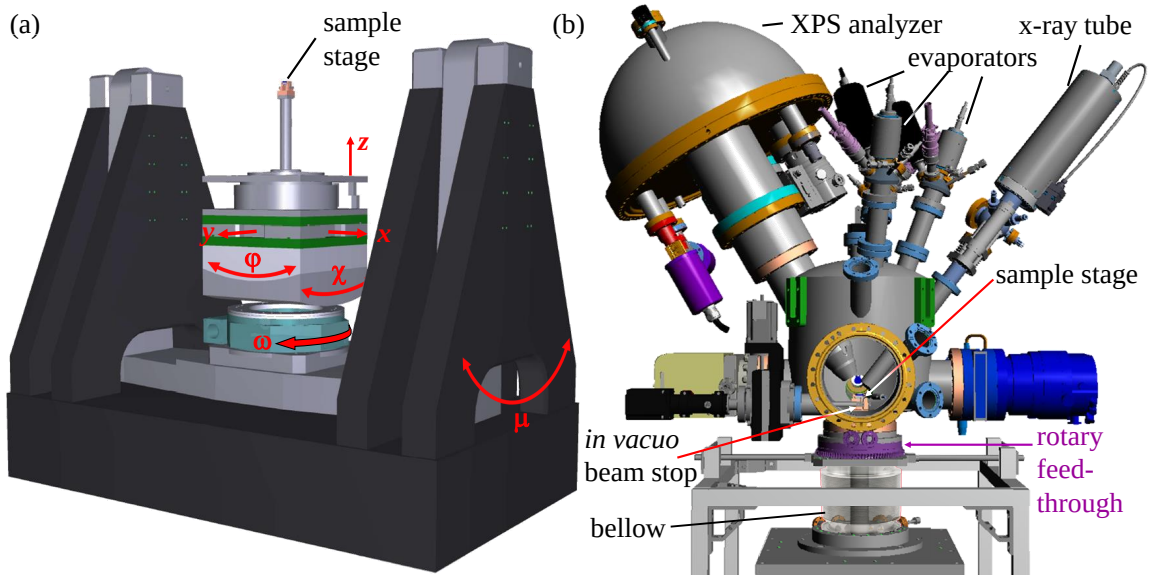

Fig. 4.5: (a) Diffractometer installed at P07/EH2. It offers translational movement in three directions (x, y, z) and rotational movement around 4 axes (ω, χ, φ, μ). The sample stage and the steel tube located on top are parts of the custom UHV chamber. (b) UHV chamber to be installed at P07 on the diffractometer in (a), designed by Jan Röh. The part above the rotary feedthrough (purple) remains still in place, while the bellow and the sample stage moves with the diffractometer. Bellow picture taken from Ref. [170].

films by MBE. The chamber was made to fit the surface diffractometer at the high-energy materials science beamline P07/EH2 at PETRA III, which is depicted in Fig. 4.5(a). It offers the manipulation of 3 translational degrees of freedom (x, y, z), a rotation around the z-axis (ω), two tilting angles – one around the x-axis (χ) and one around the y-axis (φ) – and an incident angle (μ). On top of the diffractometer, the sample is located on a sample stage.

The deposition chamber is shown in Fig. 4.5(b). The base plate at the bottom of the picture is the z-stage of the diffractometer in Fig. 4.5(a). The sample is located at the center of the window framed by the yellow flange. On the top, three evaporators are installed that are directed towards the sample location, allowing for growth of multilayer or mixed oxide films. The chamber is also equipped with a Specs Phoibos 150 hemispherical photoelectron analyzer, which offers a maximum analyzer voltage of 7 keV, making it suitable for HAXPES experiments. An x-ray tube with a Magnesium and a Chromium anode produces x-rays with $E_{\mathrm{Mg}} = 1,486\,\mathrm{eV}$ and $E_{\mathrm{Cr}} = 5,415\,\mathrm{eV}$. This allows XPS measurements both for pre-studies in the laboratory and at the location of the diffraction experiments, so that the chemical composition of the grown samples can be checked *in situ*. It can also be employed for HAXPES measurements at dedicated beamlines. The chamber is pumped by two turbo molecular pumps – one connected to the main chamber corpus (dark blue), and one located at the XPS analyzer – and an ion-getter pump.

In the projection of Fig. 4.5(b), the x-ray beam enters the chamber from the back of the image, is diffracted by the sample on the sample stage and leaves it through the yellow window. It was designed in a way that the manipulation by the diffractometer is translated to the sample in the vacuum without moving any other part of the chamber, in order to avoid scattering of

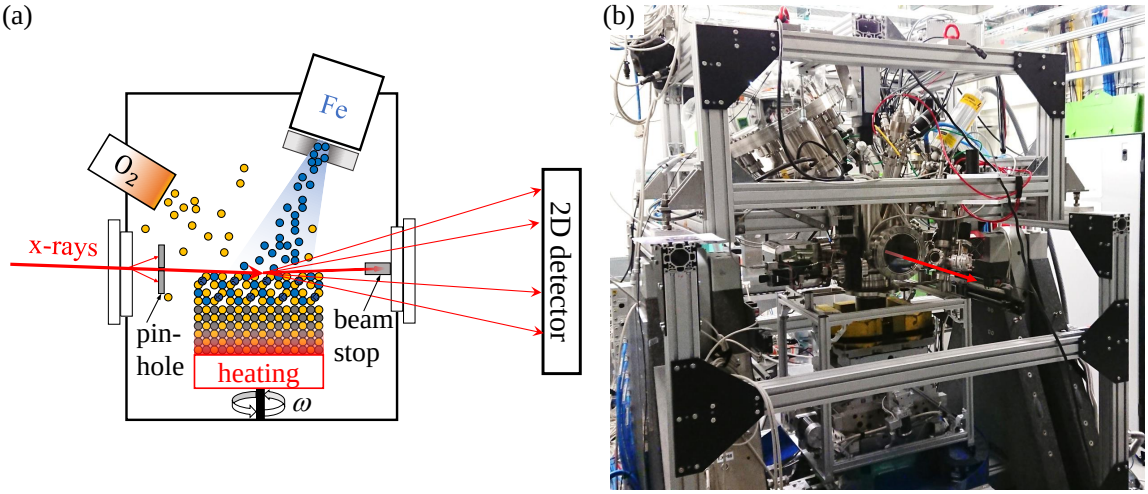

Fig. 4.6: (a) Illustration of the concept of the tr-HEXRD measurements. During the deposition of a Fe_3O_4 film, the x-rays entering the deposition chamber cross a pinhole and are diffracted by the film which is azimuthally rotated over the angle ω. The main beam is blocked by a beam stop, while the diffracted x-rays are cast onto a large area 2D detector. (b) Photograph of the deposition chamber installed at P07/EH2. Red arrow indicates the direction of the x-ray beam.

the x-ray beam on the chamber. This is achieved by connecting the sample stage, which is rigidly fixed to the diffractometer, to the chamber via a rotary feedthrough and a bellow. The bellow can be deformed under translational motions, and the differentially pumped rotary feedthrough allows to rotate the diffractometer against the chamber without breaking the vacuum. This way, the part below the rotary feedthrough plus the sample stage moves with the diffractometer, while the entire part above stays in place. To further avoid undesired scattering, a pinhole is installed behind the entrance window (not visible in Fig. 4.5(b)), which captures intensity scattered from the window. Before the exit window, an *in vacuo* beam stop is located in order to absorb the main beam before it is scattered at the exit window. This way, the diffraction pattern on the detector is almost exclusively due to Bragg reflections from the sample.

The main chamber shown in Fig. 4.5(b) is extended by two side chambers: the first is a small transfer chamber, across which samples can be imported and exported without breaking the vacuum of the main chamber. The small volume of the transfer chamber can be pumped to vacuum condition sufficient for sample transfer into the main chamber rather quickly. In the second side chamber, another sample heater and two more evaporators are located, allowing for the preparation of a sample even if the main chamber is occupied with another sample. Additionally, a LEED system is integrated in this side chamber, so that the surface structure of the prepared samples can be studied *in situ*.

4.3.2. Time-resolved high energy x-ray diffraction at P07

The tr-HEXRD experiments, for which the chamber has been designed, have been performed at P07/EH2 of PETRA III at Deutsches Elektronen-Synchrotron (DESY). P07 is designed

for experiments with high x-ray energies, providing a photon flux of $5 \cdot 10^{12}$ $\frac{\text{photons}}{\text{s} \cdot 0.2\%\text{bw}}$ at $E_{\text{ph}} = 80\,\text{keV}$ [171]. High photon energy corresponds to a small wavelength λ, and consequently to a large scattering vector $|\mathbf{q}| \sim 1/\lambda$. This means that the Bragg condition (cf. Eq. (2.61)) for a given reflection HKL can be achieved already at low angles θ

$$\sin(\theta) = \frac{\lambda}{2 \cdot d_{HKL}} \quad .$$

The combination of a high x-ray energy and a large 2D area detector allows to monitor a high number of Bragg reflections simultaneously by rotating the sample azimuthally. This technique was first introduced by Gustafson et al. [172]. Examples for measurements from these experiments are the RSMs shown in Figs. 3.12(a),(b).

The concept of these experiments is summarized in Fig. 4.6(a), and a photograph of the installed chamber can be seen in Fig. 4.6(b). The goal is to perform HEXRD on ultrathin Fe_3O_4 films during their deposition via RMBE, in order to record RSMs for different stages of the film growth. The x-rays are produced by an *in vacuo* undulator, monochromatized by a Si(111) double crystal monochromator [171] to an energy of 74 keV and focused by 2D aluminum compound refractive lenses (CRL). The x-ray beam enters the deposition chamber through a glass window, behind which a pinhole captures x-rays scattered from the glass. The x-rays that pass the pinhole hit the sample surface at an incidence glancing angle of $\theta = 0.03°$ during the deposition of the thin film. The bright main beam is blocked by an *in vacuo* beam stop, while the diffracted x-rays leave the chamber through another window, behind which the diffraction pattern is recorded on a 2D area detector.

At a given azimuthal angle ω, the area detector covers a portion of the reciprocal space with some scattering vectors $\mathbf{q}(H(\omega), K(\omega), L)$. In order to record a $\sqrt{H^2 + K^2}$ vs L-RSM as shown in Figs. 3.12(a),(b), the sample is rotated about the azimuthal angle ω, effectively integrating over all Miller indices $H(\omega)$ and $K(\omega)$. The cubic symmetry of the crystals investigated in this work implies a fourfold rotational symmetry about the azimuthal rotation axis. For this reason, an azimuthal rotation about 90° suffices in order to cover symmetry equivalent values for $H(\omega)$ and $K(\omega)$. A single data point in this time-resolved HEXRD experiment corresponds to one of these integrated $\sqrt{H^2 + K^2}$ vs L-RSMs. Therefore, the time resolution $1/\Delta t$ with which the series of RSMs documents the growth process is given by the time these azimuthal rotations take. In order to increase the time resolution, the sample was not rotated about the full 90° range, but only over a smaller range $\Delta\omega$ that covers a particularly interesting set of reflections (HKL).

For this reason, immediately before start of the deposition the sample is azimuthally aligned to an angle ω_{111} at which the substrate 111 reflection is best visible on the detector. During deposition, the sample is continuously rotated between $\omega_{111} \pm \Delta\omega$, with $\Delta\omega = 5°$ or $\Delta\omega = 7°$, at an angular speed of 2°/sec, in order to observe the development of the $(22L)_{Fe_3O_4}$ rod during growth. The detector images obtained during each one of these rotations are then summed up to obtain one $\sqrt{H^2 + K^2}$ vs L-RSM every $\Delta t = 12...14$ seconds. After the growth of the sample, a RSM with a full rotation of 90° is recorded with a rotation speed of 0.5°/sec, and an XRR curve was recorded. The electronic structure and chemical composition of the as-grown sample is characterized by XPS, using the Al anode of the installed x-ray tube.

4.3.3. Time-resolved hard x-ray photoelectron spectroscopy at P22

In order to obtain information on the cations stoichiometry of magnetite films during the growth, time resolved HAXPES measurements of $Fe_3O_4/SrTiO_3(001)$ films have been performed. To this end, the same custom-designed UHV-deposition chamber used for the tr-HEXRD measurements is installed at P22 of PETRA III at DESY [66]. The sample is illuminated by an x-ray beam under a glancing angle of 3° at a photon energy of 4.6 keV, and photoelectrons are collected using the Phoibos HSA 150 hemispherical analyzer at a $\alpha = 30°$ angle from the surface normal. The information depth ID(95) from which 95% of the photoelectrons escape can be calculated as [23] $\mathrm{ID}(95) = \lambda_{\mathrm{IMFP}} \cdot \cos(\alpha) \cdot \ln(1 - \frac{95}{100})$, and is about $\mathrm{ID}(95) = 16\,\mathrm{nm}$ in this experiment. The inelastic mean-free path $\lambda_{\mathrm{IMFP}} = 6.2\,\mathrm{nm}$ has been estimated using the TT2p equation [55]. The photoelectron spectra of the Fe 2p is recorded by scanning from high to low binding energies. Recording of a single spectrum takes 120 seconds, which means that the film thickness was changing during a single measurement. After the growth of the sample, more detailed spectra of the Fe2p, the O1s and the Fe3p peaks are measured.

4.4. X-ray magnetic reflectivity experiments at beamline UE46_PGM-1

The XRMR measurements presented in this work have been recorded at the beamline UE46_PGM-1 [173] of BESSY II. X-rays in the energy range of $E_{\mathrm{ph}} = 690...1000\,\mathrm{eV}$ are produced by an Apple-II undulator, enabling a variable polarization (cf. Sec. 4.1), and monochromatized by a plane grating [166]. In order to avoid scattering and absorption of the soft x-rays on air, the entire beam path from the undulator to the detector is evacuated.

The sample setup is illustrated in Fig. 4.7(a). In order to magnetize the sample in the direction of the x-ray propagation, it is located in a magnetic field of about $B = 200\,\mathrm{mT}$. This field is produced by two permanent magnets surrounding the sample. In order to ensure a homogeneous magnetic field at the sample location, the magnets slightly exceed the sample surface vertically. This has the consequence that at very low incident angles θ, the sample is shadowed by the magnets, reducing the intensity for small scattering vectors q_z.

A wire is contacted to the edge of the sample surface by a spot of silver epoxy glue, and directed to a current amplifier, in order to measure XAS and XMCD spectra in TEY mode. The sample is positioned to the x-ray beam with an incident angle of $\theta = 30°$, and the x-ray energy is scanned across the Fe L edge ($E_{\mathrm{ph}} = 690 - 760\,\mathrm{eV}$), successively for left and right circularly polarized x-rays (σ^+, σ^-). From the XMCD spectrum obtained this way, resonance energies which correspond to a strong dichroism in the signal are determined, at which the XRMR measurement is to be performed.

XRMR measurements are done in a θ-2θ geometry, sketched in Fig. 4.7(b): the path of the x-ray beam is fixed along the x direction, towards which the sample is rotated by an angle θ. The x-rays are reflected from the sample surface under the same angle θ, so that the detector has to be positioned at an angle of $2 \cdot \theta$ to the x-axis in order to capture the reflected beam. Two XRR curves are recorded with both helicities one after the other in order to obtain the asymmetry ratio (cf. Sec. 2.6).

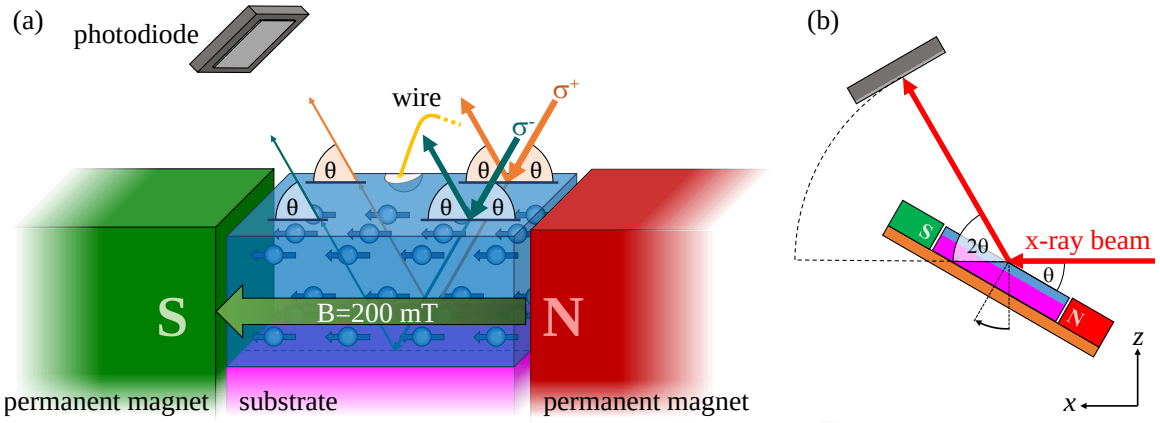

Fig. 4.7: (a) Sample setup for the XRMR measurements at UE_PGM-1. The sample is located between two permanent magnets, which produce a magnetic field of about 200 mT. A wire is connected to the sample surface to measure an XAS TEY signal. Two XRR curves are subsequently measured with both helicities using a photodiode detector. (b) θ-2θ geometry of the XRR measurement. The x-ray propagates along the x direction, the sample – together with the magnets – is rotated by an angle θ, and the detector by an angle of $2 \cdot \theta$ towards the x axis.

4.5. Analysis of spectroscopic data

4.5.1. X-ray photoelectron spectroscopy

Figure 4.8(a) shows XPS data of the Fe2p of a $Fe_3O_4/SrTiO_3(001)$ sample. The intensity difference to the right and the left of the peaks is due to an inelastic background, which is usually undesirable and has to be subtracted in order to compare the measurement to multiplet simulations. The most widespread way to do this is by using a Shirley background [174], shown as purple line in Fig. 4.8(a). The data with background subtracted are shown in Fig. 4.8(b), together with the individual cation spectra of the Fe^{2+}_{oct}, Fe^{3+}_{oct} and Fe^{3+}_{tet} species and their sum. The result of a CTM calculation is a series of lines with relative energy shifts and intensities, which have to be multiplied with a peak function in order to be compared with the data. The broadening of a peak is considered to have a Gaussian *instrumental* component, stemming from the inaccuracy in energy introduced by the x-ray beam and the analyzer, and a Lorentzian *lifetime* component, stemming from the energy-time uncertainty introduced by the lifetime of the excited states. They are represented by a Pseudo-Voigt peak function, obtained by the direct sum of Gaussian and a Lorentzian. The instrumental broadening depends on the setup at hand, and the lifetime broadening is usually unknown and is manually chosen to match the data. Typical values for the lifetime broadening are 0.3 eV for the $Fe2p_{3/2}$ and 0.6 eV for the $Fe2p_{1/2}$ edge. Another manually selected parameter are the absolute binding energies. Since CTM calculations do not provide absolute binding energies, the energy positions of the three individual spectra have to be manually shifted in order to reproduce the data.

The simulation seen in Fig. 4.8(b) captures its main features well, but fails at delivering an actual fit to the data. For once, a shake-up satellite is present at ≈ 742 eV which cannot be described by CTM. However, more severely, the relative intensities of the $2p_{3/2}$ and the $2p_{1/2}$

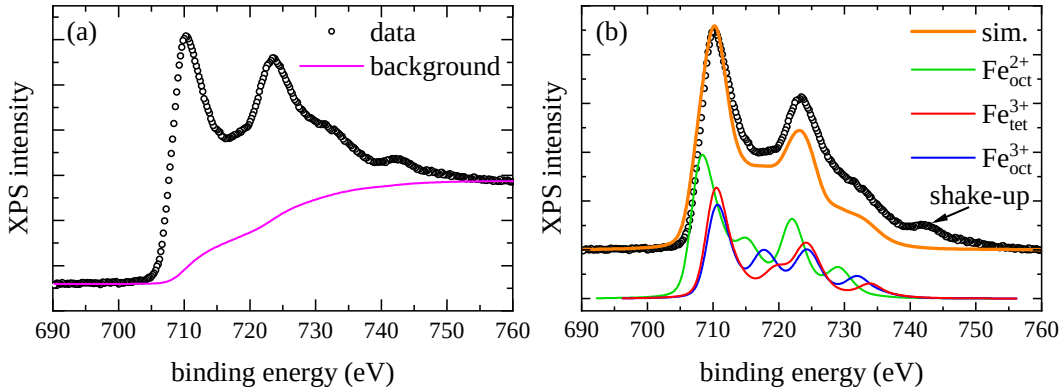

Fig. 4.8: (a) XPS data from a $Fe_3O_4/SrTiO_3(001)$ sample, together with a Shirley background. (b) Data from (a) with the background subtracted, together with CTM calculations of the individual cation spectra and their sum. This is the same image as Fig. 3.9(a), repeated for reader convenience.

are misjudged by the calculation. This is neither a shortcoming exclusive to this work's calculations nor exclusive to iron oxides, but is found similarly in other publications and for other systems [52, 53, 175, 176]. Its origin is still elusive – it is typically vaguely attributed to sources not accessible by the work at hand: charge-transfer cluster-models (without multiplets) assisted by explicit inclusion of inelastic energy-loss backgrounds attribute it to multiplet effects or interference effects from Coster-Kronig decays [175], and multiplet calculations without access to inelastic backgrounds attribute it to inelastic background effects [176]. Ultimately, CTM calculations for XP spectra are quite successful in qualitatively reproducing spectral features, but cannot be used for actual fitting to experimental data.

4.5.2. X-ray absorption spectroscopy and x-ray magnetic dichroism

In contrast to XPS, data fitting to CTM calculations is often possible for XAS and XMCD. In this work, the Cowan code by Theo Thole [177] has been used to perform the multiplet calculations with assistance of the software CTM4XAS [28, 178]. In order to more efficiently perform the calculations and compare them to data, a graphical user interface (GUI) to the Cowan code has been implemented in Python for this work, *Ferridor Magnetowitsch Dostöchjewskij* (FMD). It computes CTM spectra of a set of cations, adds them to a total simulation and compares them to data sets of XAS and XMCD spectra. The GUI is shown in Fig. 4.9. It supports multiplet calculations of the $L_{2,3}$ edges for divalent and trivalent ions of the elements Fe, Ni and Co in octahedral and tetrahedral coordination. Additionally, it offers an interface to process XAS and XMCD data for the sum rule evaluation. The individual multiplet and sum rule functionalities are accessible as tabs (black box). In Fig. 4.9, the multiplet tab for iron is displayed. The green box contains the Slater-Condon parameters for Coulomb interaction (Fdd, Fpd, Gdd) and spin-orbit coupling (SOC_2p, SOC_3d). They are given relative to the values obtained from Hartree-Fock calculations. Typically, the spin-orbit coupling terms are left at 100%, and the Coulomb parameters are set to 80% [51]. The blue box contains the broadening parameters of the Pseudo-Voigt function which is multiplied with the line intensity obtained from the CTM calculation. Gauss refers to the instrumental broadening, Lorentz1 to the lifetime broadening for the $Fe2p_{3/2}$ states and Lorentz2 to the

Fig. 4.9: GUI of the software FMD, used for multiplet analysis in this work. The black box shows tabs offering multiplet fitting or sum rule analysis for different elements. In the green box are input fields for the Slater-Condon parameters. The red box contains a list of the used cation and the used multiplet simulation parameters. The weight and the energy position of the individual cation spectra can be set by using the sliders in the yellow box. In the three graph windows at the bottom, the XAS and XMCD data are compared to the weighted sum of the cation spectra, and the corresponding cation stoichiometry is displayed.

lifetime broadening for the $Fe2p_{1/2}$ states, and are given in eV. The input line labeled as 'resolution' sets the energy resolution of the simulations. The red box contains a list of all selected cations, in which the simulation parameters can be set (for details on the multiplet parameters printed in bold, see Sec. 2.4.2):

- **EG2**: corresponds to the charge-transfer energy Δ of the ground state
- **EG2-EF2**: EF2 is the charge-transfer energy Δ_f of the final state. According to Eq. (2.24), it is typically 1... 2 eV smaller than Δ. For this reason, the software uses EG2 − EF2 as input.
- **Crystal field**: the energy split 10Dq of the e_g and the t_{2g} states of the 3d orbitals in a cubic crystal field
- *Exchange*: sets the Zeeman splitting Δ_{exc} energy of the m_J states, as discussed in Sec. 2.4.5
- **ds**: the energy term Ds is related to 10Dq and necessary to describe the crystal field energy in tetragonal symmetry. It has been implemented because it can be used to account for strained unit cells which are not strictly cubic anymore. However, in this

	cation	Δ (eV)	10Dq (eV)	U_{pd} (eV)	U_{dd} (eV)	t_{eg} (eV)	t_{t2g} (eV)
XPS	Fe^{2+}_{oct}	4.0	1.0	7.5	7.0	2.3	-1.15
	Fe^{3+}_{tet}	2.0	-0.6	7.5	7.0	1.35	-2.7
	Fe^{3+}_{oct}	2.0	1.0	8.0	7.5	2.2	-1.1
XAS	Fe^{2+}_{oct}	6.0	1.0	7.0	6.0	2.0	1.0
	Fe^{3+}_{tet}	6.0	-0.6	7.0	6.0	2.0	1.0
	Fe^{3+}_{oct}	6.0	1.0	7.0	6.0	2.0	1.0

Tab. 4.1: Typical parameters for charge-transfer multiplet calculations of Fe_3O_4 for XPS and XAS. The XPS parameters are taken from Ref. [53], XAS parameters from Ref. [23].

work all calculations have been performed assuming cubic unit cells, thus Ds = 0 eV.

- *weight*: the weight of the corresponding cation spectrum in the sum
- *Eshift*: the relative energy position of the spectrum
- **egMix**: mixing strength t between the charge-transfer states of the e_g orbitals
- **t2gMix**: mixing strength t between the charge-transfer states of the t_{2g} orbitals

A CTM calculation for a single cation is quite computing-intensive and can take up to 50 seconds on a regular office PC. A quick variation of the multiplet parameters is therefore not possible. Exceptions are the weight and the Eshift parameters, which only affect the way the cation spectra are added. Since they do not require a new CTM calculation, they can be varied on the fly using the sliders in the yellow box. The software saves the results of the multiplet calculations in a database, so that calculations with a parameter set that has been previously performed does not need to be repeated. The results of the CTM calculations and their sum are plotted below for both XAS and XMCD, together with the experimental data. Additionally, the cation stoichiometry resulting from the weights of the individual cation spectra is given in the bottom column graph.

Generally, multiplet simulations describe XAS and XMCD data well for transition metal oxides. A systematic weakness is the high-energy flank of the L_3 peak, which is always underestimated [23,35,51], while all other features are well captured. This can even be enhanced if XMCD data are available. If the same CTM calculation that produces the fit to the XAS data simultaneously achieves the fit to the corresponding XMCD, the cation stoichiometry can be usually confidently obtained. This can in principle also be achieved if only XAS data are available, but leads usually to ambiguous results.

Table 4.1 summarizes typical multiplet parameters used for XPS, XAS and XMCD calculations for Fe_3O_4.

5. Time-resolved diffraction and photoelectron spectroscopy investigation of the reactive molecular beam epitaxy of Fe_3O_4 ultrathin films

Tobias Pohlmann, Martin Hoppe, Jannis Thien, Arka Dey, Andreas Alexander, Kevin Ruwisch, Olof Gutowski, Jan Röh, Andrei Gloskovskii, Christoph Schlueter, Karsten Küpper, Joachim Wollschläger, and Florian Bertram

Abstract

We present time-resolved high energy x-ray diffraction (tr-HEXRD) and time-resolved hard x-ray photoelectron spectroscopy (tr-HAXPES) data of the reactive molecular beam epitaxy (RMBE) of Fe_3O_4 ultrathin films on various substrates. Reciprocal space maps are recorded during the deposition of Fe_3O_4 on $SrTiO_3(001)$, MgO(001) and NiO/MgO(001) in order to observe the temporal evolution of Bragg reflections sensitive to the octahedral and tetrahedral sublattices of the inverse spinel structure of Fe_3O_4. A time delay between the appearance of rock salt and spinel-exclusive reflections reveals that during growth of the first 1.1 nm, the iron oxide films grow in a $Fe_{1-\delta}O$ rock salt structure, for which only octahedrally coordinated lattice sites are occupied, before the inverse spinel structure of Fe_3O_4 develops. This is confirmed by tr-HAXPES data, which demonstrate an excess of Fe^{2+} cation in growing films thinner than 3.2 nm. This rock salt phase only appears during growth and vanishes after the supply of the Fe molecular beam is stopped. Thus, it can be concluded the rock salt structure of the interlayer is a property of the dynamic growth process.

5.1. Introduction

Iron oxides grow in a variety of crystal structures and stoichiometries, and their electronical and magnetic properties vary significantly between these phases. Both hematite (α-Fe_2O_3) and maghemite (γ-Fe_2O_3) are semiconductors and represent the iron oxides with the highest oxidation state, with all iron ions occuring in the Fe^{3+} charge state [123, 179]. α-Fe_2O_3 crystallizes in a corundum structure [180] and is a canted antiferromagnet at room temperature with a Néel temperature $T_N = 683°C$ [97], while γ-Fe_2O_3 is ferrimagnet with a Curie temperature of $T_C = 620°C$ [124] and grows in a defect spinel structure [97]. Magnetite (Fe_3O_4) is a half-metallic ferrimagnet with a Curie temperature of $T_C = 580°C$. It crystallizes in the inverse spinel structure ($a_{Fe_3O_4} = 8.396$ Å) and exhibits mixed valences of Fe^{2+} and Fe^{3+} cations [26]. Wüstite ($Fe_{1-\delta}O$) – a semiconducting antiferromagnet with a Néel temperature

of $T_N = -75°C$, crystallizing in the rock salt structure ($a_{FeO} = 4.332$ Å) [119,181] – represents the lowest oxidized polymorph. Wüstite is often found in a defect stoichiometry and typically denoted as $Fe_{1-\delta}O$, with δ ranging from 0.05 to 0.17 [111,181].

Because of this variability of their properties, thin films of iron oxides are often regarded as attractive for spintronics. For instance, magnetite is a long-standing candidate to contribute to all-oxide thin-film spintronic devices, as a source for spin-polarized currents [7–12], maghemite has been discussed as a magnetic tunnel barrier for spin-filter [123,182], and exchange bias has been observed in $Fe/Fe_{1-\delta}O$ bilayers.

In order to effectively study thin-film-based spintronic devices, a detailed knowledge of the growth mechanism down to the monolayer level is necessary. The growth mechanism of Fe_3O_4 thin films has been frequently studied. Chang et al. investigated the cation stoichiometry of $Fe_3O_4/MgO(001)$ for very thin films of few monolayers with x-ray absorption spectroscopy (XAS) and concluded that these ultrathin films dynamically redistribute during growth in order to avoid polarity [80]. It has also been reported on an iron-deficient wüstite layer of about 3 monolayers at the $Fe_3O_4/MgO(001)$ interface observed by x-ray diffraction (XRD) [21].

Fe_3O_4 ultrathin films have been grown on a wide array of substrates. The most widespread choice is the rock salt crystal MgO(001), because its lattice constant of $a_{MgO} = 4.212$ Å results in a small mismatch of 0.3% to Fe_3O_4 and grants pseudomorphic growth [17,21,80,117,144–148]. A drawback of MgO(001) substrates is the limitation of growth and annealing temperatures to 250°C, as Mg starts to interdiffuse into the magnetite film at higher temperatures [36]. $SrTiO_3(001)$ substrates, in contrast, crystallize in the perovskite structure and have a lattice constant of $a_{SrTiO_3} = 3.905$ Å and a mismatch of -7.5% to magnetite, offering the possibility to study strain effects on magnetite [22,34,143,149,150]. Different than on MgO, Fe_3O_4 can be grown on $SrTiO_3$ at elevated temperatures with no risk of interdiffusion [34]. On $SrTiO_3(001)$, Fe_3O_4 has been reported to grow in different orientations: for temperatures below 400°, grows with a (001) orientation, while for temperatures of 700° and above, the more stable (111) orientation is favored [183,184]. Ultrathin film bilayers of Fe_3O_4 and NiO, on the other hand, are very interesting from a spintronic perspective, because the exchange bias between the ferrimagnetic magnetite and NiO, which is antiferromagnetic below its Néel temprature of $T_N = 250°C$, can be exploited for magnetic tunnel junctions [23,130–133]. This effect causes an asymmetric hysteresis of the ferromagnetic film, with different switching fields depending on the direction of the external magnetic field.

In previous studies, Fe_3O_4 films were grown by reactive molecular beam epitaxy (RMBE) and subsequently investigated after growth [23,168]. XRD has been used to study thickness dependent structural properties while x-ray photoelectron spectroscopy (XPS) has been applied for electronic and chemical analysis. A more direct access to the growth process can be granted by simultaneously depositing the film and performing XRD [22] and XPS investigations. This is the route taken in this study. Fe_3O_4 ultrathin films are grown on Nb-doped $SrTiO_3(001)$, MgO(001) and NiO/MgO(001) by RMBE, and time-resolved high-energy x-ray diffraction (tr-HEXRD) is used to observe the formation of Bragg peaks of the evolving Fe_3O_4 film which are specific to the order of octahedrally and tetrahedrally coordinated Fe cations during growth. Time-resolved hard x-ray photoelectron spectroscopy (tr-HAXPES) is employed to observe the development of the Fe 2p spectrum of $Fe_3O_4/SrTiO_3$ during the deposition in order to allow conclusions towards the different oxidation states of Fe through the entire film thickness.

5.2. Experimental details

Synchrotron-based tr-HEXRD measurements utilize high energy x-rays in combination with large area 2D detectors to collect time-resolved diffraction data of dynamic processes, such as thin film growth [185] or catalytic processes [172]. In this study, we observe the intensity evolution of the Bragg reflections of Fe_3O_4 during the deposition of the films.

Our tr-HEXRD measurements were performed at beamline P07/EH2 of PETRA III at Deutsches Elektronen-Synchrotron (DESY). A custom-designed UHV-deposition chamber was mounted on the diffractometer, in order to perform grazing-incidence diffraction with a glancing angle of $\theta = 0.03°$ during the deposition of the thin films. The sample preparation followed the procedures in Refs. [23, 168, 169]. Before deposition, the MgO and the Nb-doped (0.05 wt%) $SrTiO_3$ substrates were annealed at 400°C for one hour in an oxygen atmosphere of $p_{O_2} = 10^{-4}$ mbar. For the Fe_3O_4/NiO/MgO(001) sample, first a 5.6 nm thick NiO layer was grown by evaporating Ni from a metal target in an oxygen atmosphere of $p_{O_2} = 5 \cdot 10^{-6}$ mbar at 250°C substrate temperature. Both the Fe_3O_4 films on NiO/MgO(001) and on MgO(001) were deposited by evaporating Fe under the same conditions as the NiO film. The $Fe_3O_4/SrTiO_3(001)$ film was deposited in a reduced oxygen atmosphere of $p_{O_2} = 1 \cdot 10^{-6}$ mbar and a higher substrate temperature of 350°C. Film thicknesses were controlled by calibrating the fluxes of the evaporators. Table 5.1 summarizes the final thicknesses d after growth and growth rates for the three investigated samples.

For the Fe_3O_4/MgO(001) and the $Fe_3O_4/SrTiO_3(001)$ samples, a photon energy of 74 keV was used, and data were recorded on a Dectris Pilatus 3X CdTe 2D area detector. Before the start of the deposition, the samples were azimuthally aligned to an angle $\omega_{(111)}$ at which the Bragg condition for the substrate (111) reflection was fulfilled. During deposition, the samples were continuously azimuthally rotated between $\omega_{(111)} \pm 7°$ with a rotation speed of 2°/sec, in order to observe the development of the $(22L)_{Fe_3O_4}$ crystal truncation rod (CTR) during growth. The detector images obtained during each one of these 14°-rotations were then summed up to obtain one reciprocal space map (RSM) every 12 seconds (cf. right half of Fig. 5.1). After growth, the electronic structure of the samples was characterized *in situ* by XPS, using a Phoibos HSA 150 hemispherical analyzer and an Al Kα anode, in order to probe the stoichiometry of the grown iron oxide, and a RSM with a full rotation of 90° was recorded with a rotation speed of 0.5°/sec.

For the Fe_3O_4/NiO/MgO(001) sample, we followed the same procedure, but using a photon energy of 72 keV and a Perkin-Elmer XRD1621 detector, with a rotation range of $\omega_{(111)} \pm 5°$, and recorded one RSM every 28 seconds. Again, after growth a RSM with a full rotation of 90° was recorded.

Tab. 5.1: Thicknesses and deposition rates of the samples.

	tr-HEXRD			tr-HAXPES	
sample	Fe_3O_4/NiO/MgO	Fe_3O_4/MgO	$Fe_3O_4/SrTiO_3$	continuous	step-wise
$d_{Fe_3O_4}$ (nm)	18.9 ± 0.1	8.6 ± 0.2	12.4 ± 0.5	18.8 ± 0.3	17.1 ± 0.7
rate (nm/min)	2.6	0.86	0.31	0.47	0.86

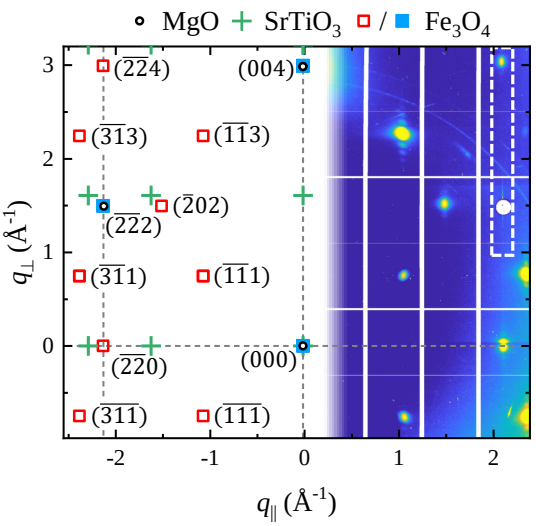

Fig. 5.1: Reciprocal space map of the Fe_3O_4/MgO(001) sample. The right half shows the measurement, the left half a schematic of the Bragg positions for MgO (black circles), $SrTiO_3$ (green crosses) and Fe_3O_4. Open red squares denote Fe_3O_4 reflections that occur exclusively for the spinel structure, while reflections marked by blue squares are also allowed for the rock salt structure. The white dashed box marks the region of the (222) and the (224) reflections whose time evolution during growth is monitored in Figs. 5.3 and 5.5. The white disk at the (222) position is a semi-transparent beam stop protecting the detector from the bright substrate (111) reflection, and the white grid stem from module borders of the detector. The Bragg reflections labeled in the schematic are in Fe_3O_4 lattice units.

In order to obtain information on the temporal evolution of the stoichiometry of the different cations of Fe_3O_4 during the growth, we performed complimentary tr-HAXPES measurements during the growth of Fe_3O_4 films on $SrTiO_3$. To this end, we installed the same custom-designed UHV-deposition chamber used for the tr-HEXRD measurements at beamline P22 of PETRA III at DESY [66]. The samples were illuminated by an x-ray beam under a glancing angle of 3° at a photon energy of 4.6 keV, and photoelectrons were collected using the Phoibos HSA 150 hemispherical analyzer at a $\alpha = 30°$ angle from the surface normal, resulting in an information depth of about $ID(95) = 16\,nm$ [23].

The films were deposited in an oxygen atmosphere of $p_{O_2} = 5 \cdot 10^{-6}$ mbar at a substrate temperature of 400°C. One sample was deposited continuously up to a thickness of 18.8 nm, and one sample was deposited step-wise: After each spectrum taken during the deposition of 1.7 nm Fe_3O_4, the growth was stopped by interrupting the molecular beam, and a Fe 2p spectrum was measured by averaging over 9 scans before the next deposition step. The photoelectron spectra of the Fe 2p were recorded by scanning from high to low binding energies. For the continuously deposited film, the spectra were recorded in 0.2 eV energy steps and an integration time of 0.1 $\frac{sec}{step}$, taking 60 seconds for a single spectrum, which means that the film thickness was changing by 0.5 nm during each measurement. For instance, the first spectrum started recording at a binding energy of 760 eV and a film thickness of 0 nm, and ended at a binding energy of 690 eV with a film thickness of 0.5 nm. We used a linear scaling function on these spectra in order to account for the fact that the intensity of the Fe 2p increases with the film thickness. The step-wise deposited film in energy steps of 0.2 eV and an integration time of 0.2 $\frac{sec}{step}$, taking 120 seconds for a single spectrum. The deposition rates can be found in Tab. 5.1. Charge transfer multiplet (CTM) calculations of the XPS spectra of the three cation species in Fe_3O_4 have been performed using the method and parameter set of Fuji et al [53].

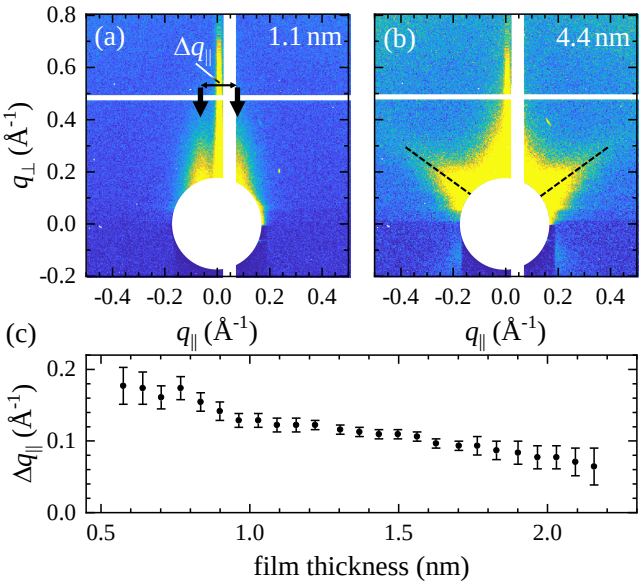

Fig. 5.2: (a) Small angle region of an RSM taken at a thickness of 1.1 nm of the $Fe_3O_4/SrTiO_3$ film. Black arrows indicate two distinct streaks parallel to $q_\perp$. (b) The same region as in (a), but at a film thickness of 4.4 nm. Two streaks at an angle of 55° with respect to the surface normal are highlighted by dashed black lines. (c) Reciprocal space distance $\Delta q_{\parallel}$ of the two streaks in (a) as a function of film thickness.

5.3. Results

Figure 5.1 shows a RSM of the as-grown Fe_3O_4/MgO sample, obtained by a full 90° azimuthal rotation. The right half shows recorded data and the left a schematic of the peak positions from MgO, $SrTiO_3$ and Fe_3O_4.

Information on the early growth stage can be collected by tr-HEXRD by analyzing the grazing incidence small angle x-ray scattering (GISAXS) data in the small angle region of the RSMs (cf. Fig. 5.2). After this stage, the goal of the tr-HEXRD measurements is to record the intensity evolution of the $(222)_{Fe_3O_4}$ and the $(224)_{Fe_3O_4}$ reflection. This endeavor is complicated by the close lattice match of MgO and Fe_3O_4: Fe_3O_4 has roughly double the lattice constant of MgO with a small lattice mismatch of only 0.3%, and consequently, Bragg reflections $(HKL)_{MgO}$ of MgO almost coincide with reflections $(2H, 2K, 2L)_{Fe_3O_4}$ of Fe_3O_4. This can be seen in the schematic RSM in Fig. 5.1, where black circles indicate the MgO reflections, and squares the reflections of Fe_3O_4. The intensity difference between the bright substrate reflections and the weaker film reflections is too high for the detector to record them simultaneously. For this reason, the MgO reflections had to be covered by semi-transparent beamstops on the detector. For instance, on the one hand, the $(222)_{Fe_3O_4}$ has to be blocked (see white disk in the RSM presented in the right half of Fig. 5.1) since it almost coincides with the (111)-reflection of MgO. On the other hand, the $(224)_{Fe_3O_4}$ is fully visible, since the corresponding substrate-related Bragg reflection $(112)_{MgO}$ is forbidden.

In contrast, the perovskite structure of $SrTiO_3$ has more allowed reflections, including the $(112)_{SrTiO_3}$, as illustrated by the green crosses in Fig. 5.1. But since its higher lattice mismatch of -7.5% to Fe_3O_4, the substrate reflections are well separated from the film reflection, making a direct observation of both the $(222)_{Fe_3O_4}$ and the $(224)_{Fe_3O_4}$ reflections possible.

5.3.1. $Fe_3O_4/SrTiO_3$

Figure 5.2(a) shows the small angle region of an RSM taken at a film thickness of 1.1 nm. Two streaks parallel to the $q_\perp$ direction are highlighted by two black arrows. Their reciprocal

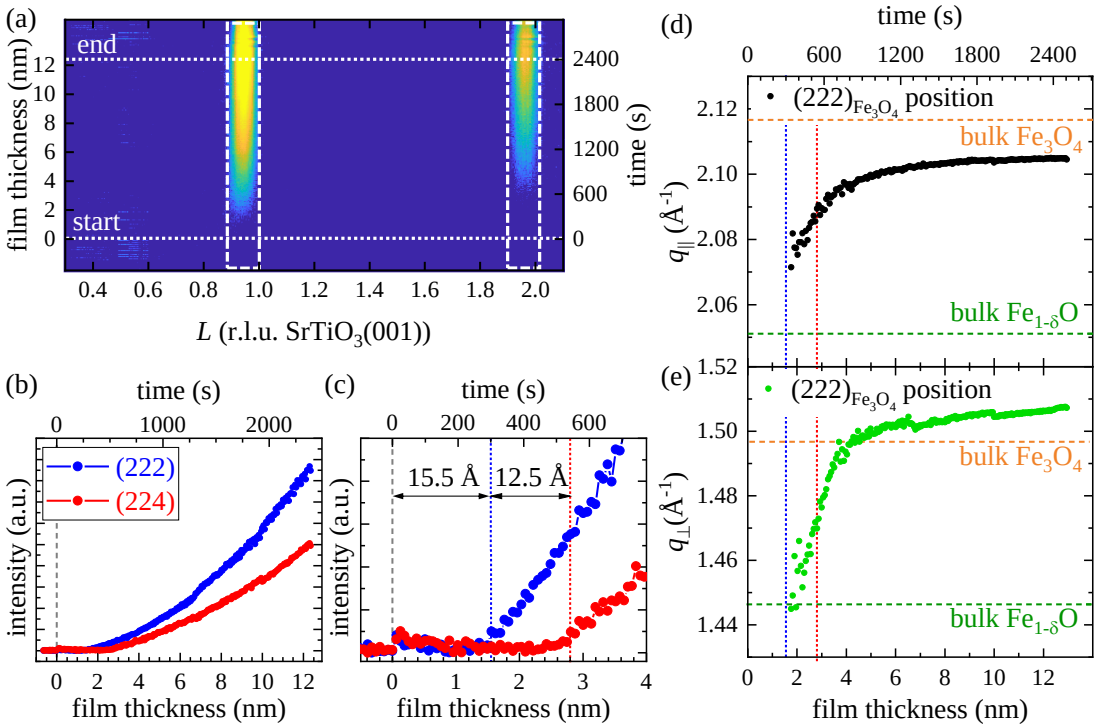

Fig. 5.3: (a) Diffracted intensity along the $(22L)_{Fe_3O_4}$-rod, in the region indicated by the white box in Fig. 5.1, as a function of film thickness. The dotted horizontal white lines indicate the start and end of the deposition process. The white dashed boxes show the regions where the intensities for the $(222)_{Fe_3O_4}$ and $(224)_{Fe_3O_4}$ presented in (b),(c) are taken, respectively. (b) Intensity evolution for the $(222)_{Fe_3O_4}$ and $(224)_{Fe_3O_4}$ during deposition. (c) Close-up of the initial growth stage. Blue and red dotted lines indicate film thicknesses where the $(222)_{Fe_3O_4}$ and $(224)_{Fe_3O_4}$ start to change intensity. (d),(e) Evolution of (d) the in-plane scattering vector $q_\perp$ and (e) the out-of-plane scattering vector $q_\parallel$ of the film (222) reflection. Dashed horizontal lines indicate the expected scattering vectors for bulk Fe_3O_4 and bulk $Fe_{1-\delta}O$. Dotted blue and red vertical lines indicate the thicknesses at which the (222) and the (224) reflections emerge, respectively.

space distance $\Delta q_\parallel$ is plotted as a function of film thickness in Fig. 5.2(c). They become first visible at a film thickness of about 0.5 nm, and then move gradually closer to each other along the $q_\parallel$ direction with increasing film thickness, until they eventually become indistinguishable and merge in the center at a thickness of about 2.2 nm. At a film thickness of 2.9 nm, two new streaks appear, highlighted by black dashed lines in Fig. 5.2(b). In the projection of the RSM, they are tilted by an angle of 55° from the $q_\perp$ direction. These streaks remain present for the rest of the growth process, including the finished film.

In order to gain insight into the growth dynamics of the $Fe_3O_4/SrTiO_3$ film, we used tr-HEXRD to monitor the evolution of the $(222)_{Fe_3O_4}$ and the $(224)_{Fe_3O_4}$ reflections during the deposition. Figure 5.3(a) shows how the intensity along the $(22L)_{Fe_3O_4}$-rod (white dashed box in Fig. 5.1) changes with the film thickness. The color scale corresponds to the intensity, the horizontal axis to the Miller index $(0.93, 0.93, L)_{SrTiO_3}$ and the vertical axis to the film thickness. For the thickness axis, we assumed a linear relation between deposition time

and film thickness. In the color plot of Fig. 5.3(a), it can be seen that at the beginning of the growth, neither the $(222)_{Fe_3O_4}$ nor the $(224)_{Fe_3O_4}$ can be observed. After about 1 nm of growth, intensity is detected at the $(222)_{Fe_3O_4}$ position, and with a slight delay the $(224)_{Fe_3O_4}$ reflection appears. For better quantification, Fig. 5.3(b) shows the L-integrated intensity along the white dashed boxes for the $(222)_{Fe_3O_4}$ and the $(224)_{Fe_3O_4}$ (cf. Fig. 5.3(a)) as a function of film thickness and deposition time for the full growth process, and Fig. 5.3(c) contains a close-up of the early growth stage. Here, the delay between the emergence of the $(222)_{Fe_3O_4}$ and the $(224)_{Fe_3O_4}$ can be determined to be $\Delta d = 1.25 \pm 0.12$ nm. It can also be seen that the $(222)_{Fe_3O_4}$ does not appear before a coverage of 1.55 nm has been reached.

The position of the $(222)_{Fe_3O_4}$ has been fitted to draw conclusions towards the lattice constant during growth. Figures 5.3(d),(e) show the evolution of the in-plane component $q_{\parallel}$ and the out-of-plane component $q_{\perp}$ of the scattering vector of the $(222)_{Fe_3O_4}$. Both components move from a smaller position at low film thicknesses to a larger position at thicker films. This corresponds to a compression of the lattice parameters in both vertical and lateral direction. The dashed lines indicate the scattering vector components expected for bulk Fe_3O_4 and for bulk $Fe_{1-\delta}O$. It can be seen that the position of the (222) reflection is close to the expected value for $Fe_{1-\delta}O$ at the beginning of the deposition, and settles close to the position expected for Fe_3O_4 when the film grows thicker.

In order to make conclusions about the oxide phase in this early growth phase, we performed tr-HAXPES measurements of the growth of $Fe_3O_4/SrTiO_3$ films. The results are shown in Fig. 5.4. Figure 5.4(a) shows the spectra recorded from the continuously deposited $Fe_3O_4/SrTiO_3$ film. During the measurement of each spectrum, about 0.47 nm of Fe_3O_4 have been deposited. For the films below 1.4 nm thickness, the low signal-to-noise ratio makes it difficult to observe spectral features. However, for film thicknesses from 1.9 nm to 3.3 nm, a satellite feature at the high-energy side of the Fe $2p_{3/2}$ can be observed, highlighted by the arrows. For films thicker than 3.8 nm, this satellite disappears, and the region between the Fe $2p_{3/2}$ and the Fe $2p_{1/2}$ is flat. This effect is even more obvious in a step-wise deposition process, for which spectra could be recorded at higher integration times (cf. Fig. 5.4(b)). It was grown in steps of 1.7 nm. After each deposition step, the growth was interrupted. Spectra were taken during and after each deposition step. The violet, magenta and cyan spectra presented in Fig. 5.4(b) were recorded during the first three deposition steps, and had thicknesses of 1.7 nm, 3.4 nm and 5.1 nm after the end of the corresponding measurement, respectively. The orange spectrum was taken during the interruption after the first deposition step, at a film thickness of 1.7 nm. These deposition steps are illustrated in Fig. 5.4(d), with the step labels 1), 2) and 3) corresponding to the in the spectra in Fig. 5.4(b). For the spectra recorded during the first two deposition steps (purple and magenta), a satellite can be seen on the high-energy side of the Fe $2p_{3/2}$ (purple and magenta arrows), which vanishes for both, films thicker than 5.1 nm and the spectrum taken during the interruption. This satellite is well known to be a charge-transfer satellite stemming from Fe^{2+} cations on octahedral lattice sites. To illustrate this, Fig. 5.4(e) shows CTM calculations of the Fe 2p spectrum for the three cation species in Fe_3O_4. The individual cation spectra show a distinct charge-transfer satellite between the Fe $2p_{3/2}$ and the Fe $2p_{1/2}$ lines at different energies. It is highlighted for the Fe^{2+}_{oct} spectrum by a green arrow. Summing up the three spectra in a 1:1:1 ratio yields the Fe_3O_4 spectrum (black), which does not exhibit any satellite structure between the Fe 2p main lines, because the satellites of the individual cation spectra overlap in such a way that they form a flat plateau [53]. This shape is observed for the spectra during

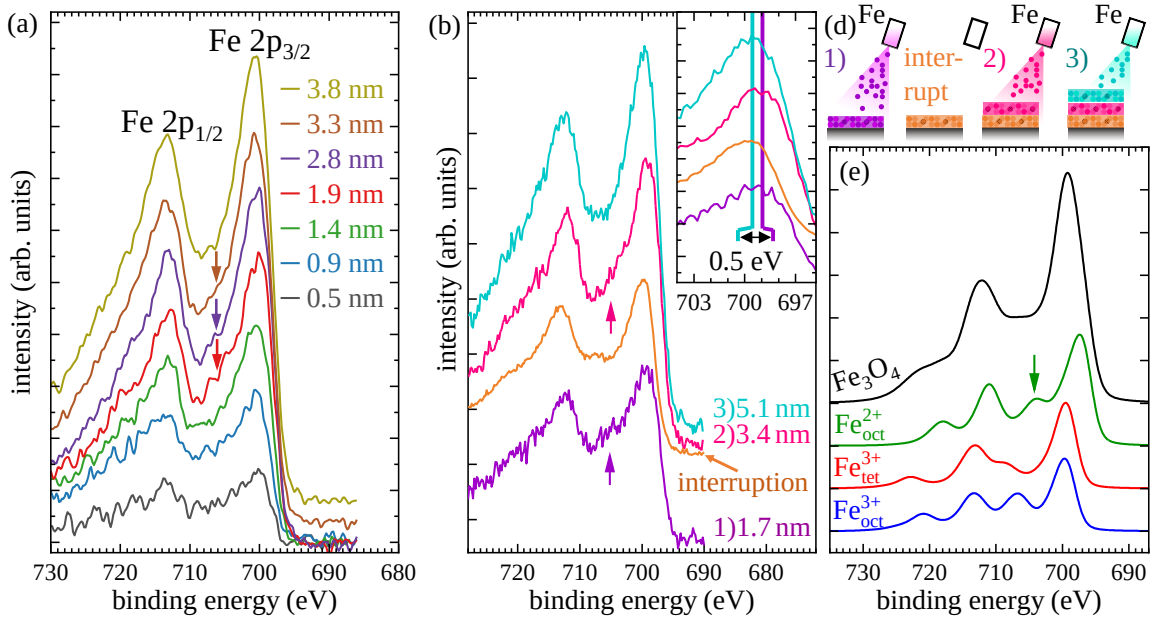

Fig. 5.4: (a) HAXPES data of the Fe 2p recorded during the continuous deposition of a $Fe_3O_4/SrTiO_3$ film. The data was smoothed by a Gaussian filter. (b) HAXPES data of the Fe 2p recorded during the step-wise deposition process of a $Fe_3O_4/SrTiO_3$ film [1) purple, 2) magenta and 3) cyan] and during an interruption of the deposition (orange), as illustrated in (d). At the end of the measurements during deposition, the films were 1.7 nm, 3.4 nm and 5.1 nm thick. (c) Close-up of the Fe $2p_{3/2}$ region; violet and yellow lines indicate center of the peak in the respective spectrum. (d) Sketch of the step-wise deposition process, corresponding to the spectra in (b). (e) CTM calculations of the XPS spectra for the three cation species of Fe_3O_4, Fe^{2+}_{oct} (green), Fe^{3+}_{tet} (red) and Fe^{3+}_{oct} (blue). Grey line is the sum of the Fe^{2+}_{oct} and Fe^{3+}_{oct} spectra, and the black line is the sum of all three spectra, representing the full Fe_3O_4 spectrum. Arrows highlight the charge-transfer satellite characteristic for Fe^{2+} cations.

the third deposition step and in the interruption after the first deposition step in Fig. 5.4(b), and for film thicknesses higher than 3.8 nm in Fig. 5.4(a).

Additionally, we observe a chemical shift of about 0.5 eV for both Fe 2p main lines between the spectrum during the first deposition step on the one hand and the spectra recorded after the first and during the third step on the other hand, shown for the Fe $2p_{3/2}$ peak in the inset of Fig. 5.4(a). The spectrum taken during the second deposition step displays both a weaker satellite as well as a energy position in between the two other spectra.

5.3.2. Fe_3O_4/MgO and Fe_3O_4/NiO/MgO

For the Fe_3O_4 films deposited on MgO, an according evaluation is slightly more difficult because the overlap of the $(222)_{Fe_3O_4}$ and the $(111)_{MgO}$ reflections does not allow for an immediate observation of the $(222)_{Fe_3O_4}$. Particularly, the region around the $(111)_{MgO}$ has to be blocked by a semi-transparent absorber, as can be seen in Fig. 5.1. Therefore, instead of the Bragg peak, we observe the intensity of the CTR at a position $(2, 2, 2-\epsilon)_{Fe_3O_4}$ close to the $(222)_{Fe_3O_4}$ reflection, with $\epsilon = 0.12$. Analogous to Fig. 5.3(a), Fig. 5.5(a) shows

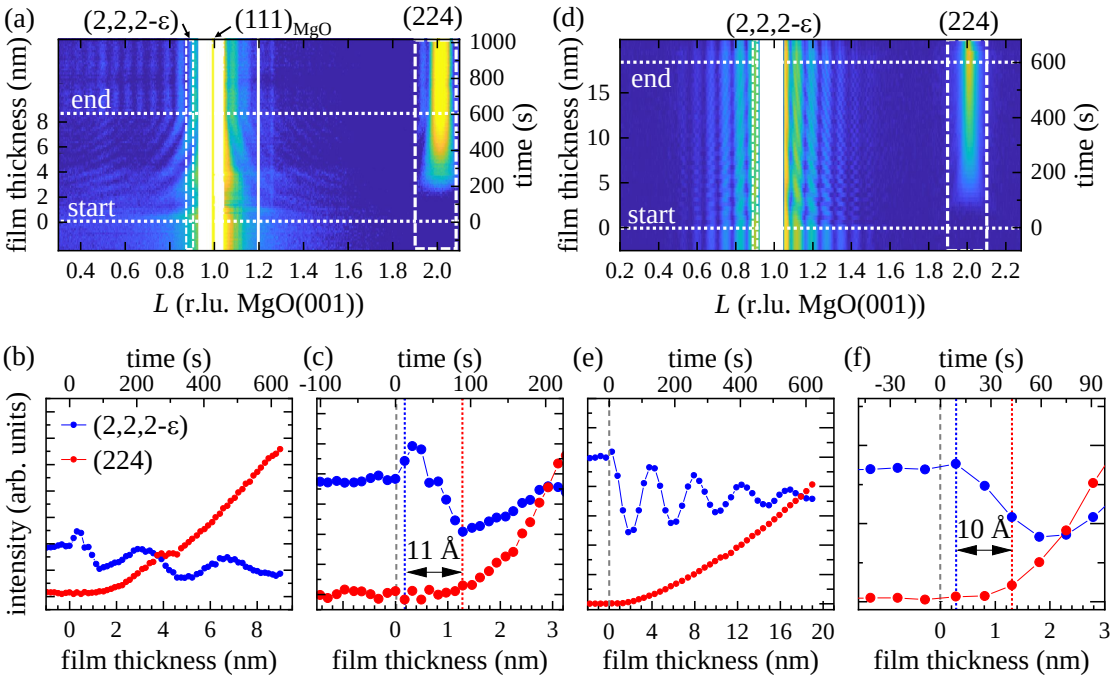

Fig. 5.5: (a),(d) Diffracted intensity along the $(22L)_{Fe_3O_4}$-CTR of the (a) Fe_3O_4film on MgO and the (d) Fe_3O_4/NiO stack on MgO, in the region indicated by the white box in Fig. 5.1, as a function of film thickness. The dotted white lines indicate the start and end of the deposition process. The white area around L=1 is caused by the beam stop for the $(111)_{MgO}$ substrate reflection. The white dashed boxes show the regions in which the intensities for the $(2,2,2\text{-}\epsilon)_{Fe_3O_4}$ and $(224)_{Fe_3O_4}$ in (b),(e) are taken. (b),(e) Intensity evolution for the $(2,2,2\text{-}\epsilon)_{Fe_3O_4}$ and $(224)_{Fe_3O_4}$ during the deposition of (b) the Fe_3O_4/MgO film and (e) the Fe_3O_4/NiO/MgO. (c),(f) Close-up of the initial growth stages in (b),(e) demonstrating the delayed onset of occupation of the tetrahedral sublattice. Data for the $(2,2,2\text{-}\epsilon)_{Fe_3O_4}$ in (f) have been offset for better visibility. Blue and red lines indicate positions where the $(2,2,2\text{-}\epsilon)_{Fe_3O_4}$ and $(224)_{Fe_3O_4}$ start to change intensity.

a false color map of the diffracted intensity during the growth process of the Fe_3O_4 film on MgO. Before starting the growth process, again there is no intensity at the $(224)_{Fe_3O_4}$ position. Around the position of the $(222)_{Fe_3O_4}$ ($L = 1.003$ in Fig. 5.5(a)), however, no intensity (white region) can be detected due to the semi-transparent absorber. At $L = 1$, the $(111)_{MgO}$ reflection is visible as a sharp bright line. The intensity has been corrected for the attenuation by the semi-transparent absorber. In the vicinity of the absorber, the $(111)_{MgO}$-CTR decays monotonically with the L-distance from the main reflection. As soon as the deposition begins, Laue oscillations from the $(222)_{Fe_3O_4}$-reflection emerge, and their period changes with growing film thickness. The $(224)_{Fe_3O_4}$, however, is absent at the beginning, before it gradually appears. Nearing the end of the growth process, it also develops a Laue fringe. After the end of growth, the period of the Laue fringes remains constant, pointing to a stable film thickness and interface roughness.

In Fig. 5.5(b), the L-integrated intensities in the white boxes in Fig. 5.5(a) as a function of

film thickness are plotted, and Fig. 5.5(c) shows a close-up of the temporal evolution during growth of the first 3 nm. Immediately after the beginning of the deposition, the intensity at the $(2, 2, 2-\epsilon)_{Fe_3O_4}$ position starts to oscillate due to the emergence of Laue fringes of the $(222)_{Fe_3O_4}$-reflection, which are changing frequency during the growth. With a delay of about $\Delta d = 11 \pm 1.3$ Å, the intensity of the $(224)_{Fe_3O_4}$ starts to rise, very similar to the case of the $Fe_3O_4/SrTiO_3$.

We used the same procedure to analyze the Fe_3O_4/NiO/MgO sample. The intensity of the $(2, 2, 2-\epsilon)_{Fe_3O_4}$ was analyzed at $\epsilon = 0.09$. The results are shown in Figs. 5.5(d)-(f). In Fig. 5.5(d), Laue oscillations caused by the finite thickness of the NiO film are visible already before the deposition of Fe_3O_4 starts. After start of the deposition, they are superimposed by the Laue-oscillations due to the Fe_3O_4 film, resulting in a Moiré pattern caused by the Laue-oscillations of the two films. As in the case of the Fe_3O_4/MgO sample, the intensity at the $(2, 2, 2-\epsilon)_{Fe_3O_4}$ position starts oscillating immediately after the beginning of the deposition, while the intensity of the $(224)_{Fe_3O_4}$ reacts with a delay of about $\Delta d = 10 \pm 3$ Å.

5.4. Discussion

The GISAXS data of the $Fe_3O_4/SrTiO_3$ film suggest that the film starts to grow in islands. The two distinct vertical streaks observed in the early stage of the growth (cf. Fig. 5.2(a)) are an indicator for a cluster formation on the substrate surface, and their orientation parallel to the $q_\perp$ direction corresponds to the formation of islands of cylindrical or box shape [186]. Their separation distance is a measure of the mean distance of the clusters, and has been observed to decrease with growing film thickness (cf. Fig. 5.2(c)), corresponding to a coarsening process due to, e.g., coalescence of smaller islands to bigger ones. From the film thickness at which the two streaks are not visibly separated anymore, we can conclude that a fully closed film is formed not before a coverage of 2.2 nm. The appearance of the second set of streaks at 2.9 nm, exhibiting a 55° tilt to the out-of-plane direction (cf. Fig. 5.2(b)), is an indication for the formation of (111) facets [187]. This means that after the first layer is closed, the film continues to grow in (001) direction, but develops (111) facets on the surface. The development of (111) facets has been reported earlier for Fe_3O_4 films, and is related to the (111) surface being more stable than the (001) surface [37, 184]. The GISAXS data collected of the Fe_3O_4/MgO(001) film (not shown) displays initially the same behavior: the film grows islands which coalesce to a closed layer at a coverage of about $2-3$ nm. However, no small angle signal indicating the formation of additional nanostructures is observed. This suggests that the Fe_3O_4/MgO(001) film continues to grow in layer-by-layer mode.

The most striking result is the fact that for all three samples, the $(222)_{Fe_3O_4}$ reflections and their diffraction rods appear soon after the start of the deposition, but the spinel-exclusive $(224)_{Fe_3O_4}$ reflection follows only after the film has grown thicker by 1.1 ± 0.15 nm. The inverse spinel structure of Fe_3O_4 can be described as consisting of a cubic close-packed oxygen sublattice, two cation sublattices with double periodicity, one containing the octahedrally coordinated $Fe_{oct}^{2+/3+}$ cations (B-sites) and one containing the tetrahedrally coordinated Fe_{tet}^{3+} cations (A-sites). These sublattices give rise to different Bragg-reflections, some of which are exclusive to the spinel structure while others also occur in a rock salt phase [145]. Figure 5.6 shows the structure factors $|F_{\text{sublattice}}|^2$ for the A-, B- and O^{2-} sublattices. The intensity of the $(222)_{Fe_3O_4}$ has contributions from both the oxygen and the octahedral sublattice, while the

intensity of the $(224)_{Fe_3O_4}$ is purely due to the tetrahedral sublattice. Therefore, the delayed emergence of the $(224)_{Fe_3O_4}$ with respect to the emergence of the $(222)_{Fe_3O_4}$ indicates that in the early growth stage, the iron oxide film grows in a rock salt structure instead of the inverse spinel structure of Fe_3O_4. Additionally, the position of the (222) reflection of the film agrees well with the expected position of the $(111)_{Fe_{1-\delta}O}$ reflection, and only relaxes towards the lattice constant of Fe_3O_4 when the film grows thicker. This suggests that iron oxide films which are grown under conditions that are well-known to grow in the Fe_3O_4 phase [34, 99, 117, 145, 169] begin to grow in a $Fe_{1-\delta}O$ structure with exclusive occupation of octahedral lattice sites, and only after a certain thickness start to form the inverse spinel structure of Fe_3O_4 with Fe cations occupying tetrahedral lattice sites, as well. We determine the thickness of this layer to be about 1 nm, as this is the thickness difference between the emergence of the two reflections consistent for all three samples. This corresponds to about 2–3 unit cells of $Fe_{1-\delta}O$, or about 4–6 atomic layers [21]. We also want to emphasize that this finding is robust although the growth rates differ by almost an order of magnitude between the samples (cf. Tab. 5.1) and different substrates have been used. A similar effect has been reported earlier for Fe_3O_4/MgO(001) films deposited at low temperatures or low deposition rates [145]. It has been attributed to an iron-deficient rock-salt structure which retains the same stoichiometry as Fe_3O_4.

While for the two samples grown on MgO(001), the $(222)_{Fe_3O_4}$-reflection emerges immediately after begin of the deposition, for $Fe_3O_4/SrTiO_3$ the $(222)_{Fe_3O_4}$ appears only after about 1.5 nm are grown already. This implies a lower initial ordering in films below a coverage of 1.5 nm deposited on $SrTiO_3$(001) than for films on MgO(001). Such a distorted interface layer of $Fe_3O_4/SrTiO_3$(001) has been reported before [22]. A possible explanation is that the competition between a (001) and a (111) orientation reported for $Fe_3O_4/SrTiO_3$(001) [183, 184] might cause different orientations for different islands, so that no Bragg peaks develop due to missing long range order during this growth stage. However, our data do not allow a clarification of the structure in this phase.

In our HAXPES data obtained for the growth of Fe_3O_4 on $SrTiO_3$(001), we observe a charge-transfer satellite at the high-energy side of the Fe $2p_{3/2}$ and a chemical shift of the Fe $2p_{3/2}$ and the Fe $2p_{1/2}$ to about 0.5 eV lower energies for iron oxide films with thicknesses between $\sim$ 1.5 nm to $\sim$ 4 nm. Both, the satellite and the chemical shift in Figs. 5.4(a)-(c) are indicators for an excess of Fe^{2+} cations. This also suggests a $Fe_{1-\delta}O$ phase, consistent with the diffraction data. The chemical shift and the satellite are most pronounced for the 1.9 nm

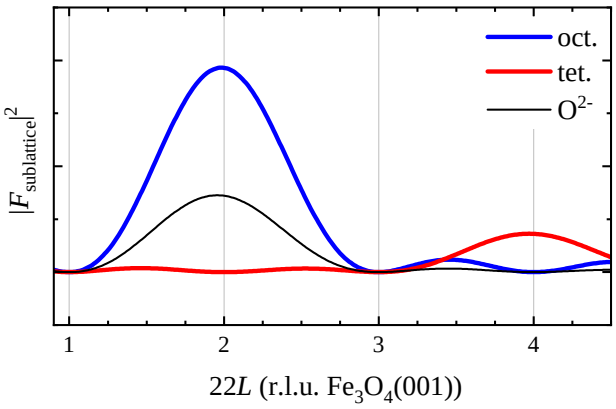

Fig. 5.6: Contributions of the octahedral, tetrahedral and oxygen sublattices to the structure factor $|F_{\text{sublattice}}|^2$ of Fe_3O_4.

and the 1.7 nm-thick films in Figs. 5.4(a) and 5.4(b), respectively. They are weakened after the thickness is increased to 3.3 nm and 3.4 nm, and vanish at thicknesses of 3.8 nm and 5.1 nm. The information depth of our HAXPES measurements is about ID(95) = 16 nm, and therefore accesses the entire film thickness. However, the vanishing of the spectral features does not necessarily imply a vanishing of the Fe^{2+}-rich $Fe_{1-\delta}O$ phase itself, but can also be attributed to its signal is rendered invisible due to the Fe_3O_4 phase forming on top. The tr-HAXPES data of the step-wise deposited film also reveal that the stoichiometry of the film changes when the growth is interrupted (cf. Fig. 5.4(b)). During deposition, the 1.7 nm film clearly shows a Fe^{2+}-charge-transfer satellite, also seen for the continuously deposited sample (cf. Fig. 5.4(a)). However, when the iron supply is cut, the 1.7 nm-thick film exhibits a spectrum characteristic for Fe_3O_4, and as soon as the deposition is continued, the satellite returns. This suggests that this $Fe_{1-\delta}O$ phase is a transient phenomenon and exclusively occurs during the dynamic growth process, but does not remain stable when the deposition is stopped.

5.5. Summary

In summary, the initial growth stage of $Fe_3O_4/SrTiO_3(001)$ appears to occur in 3 steps: First, the film grows in disordered islands of unknown structure. Second, at a coverage of about 1.5 nm, as the islands become bigger, they predominantly form a rock salt structure and show an excess of Fe^{2+}, likely being a $Fe_{1-\delta}O$ phase. Between a coverage of 2.2 nm and 3 nm, the first layer closes, and at about 2.8 nm the film finally starts to grow in an inverse spinel structure in [001] direction, developing (111) facets on the surface.

Fe_3O_4films on MgO(001) and on NiO/MgO(001) start to grow in islands, too, and the first closed layer forms at a coverage of about $2-3$ nm. However, the immediate appearance of the $(222)_{Fe_3O_4}$ reflection after the begin of the deposition suggests that these islands immediately exhibit a well ordered rock salt structure. After a thickness of about 1 nm, they grow in the inverse spinel structure. Given how similar the thickness of the rock salt layer is across all three samples, it seems very likely that it is due to the formation of a $Fe_{1-\delta}O$ layer at the beginning of the growth for all three samples.

The tr-HAXPES measurements of $Fe_3O_4/SrTiO_3(001)$ additionally reveal that the $Fe_{1-\delta}O$ phase in the sub-nanometer range is only stable during the deposition process, but turns into a Fe_3O_4 phase when the deposition is interrupted. We therefore conclude that this is a strictly dynamic property of the growth process.

Original publication: Physical Review B **102**, 220411 (2020),
available at http://dx.doi.org/10.1103/PhysRevB.102.220411

6. Cation- and lattice-site-selective magnetic depth profiles of ultrathin Fe_3O_4(001) films

Tobias Pohlmann, Timo Kuschel, Jari Rodewald, Jannis Thien, Kevin Ruwisch, Florian Bertram, Eugen Weschke, Padraic Shafer, Joachim Wollschläger, and Karsten Küpper

Abstract

A detailed understanding of ultrathin film surface properties is crucial for the proper interpretation of spectroscopic, catalytic and spin-transport data. We present x-ray magnetic circular dichroism (XMCD) and x-ray resonant magnetic reflectivity (XRMR) measurements on ultrathin Fe_3O_4 films to obtain magnetic depth profiles for the three resonant energies corresponding to the different cation species Fe^{2+}_{oct}, Fe^{3+}_{tet} and Fe^{3+}_{oct} located on octahedral and tetrahedral sites of the inverse spinel structure of Fe_3O_4. By analyzing the XMCD spectrum of Fe_3O_4 using multiplet calculations, the resonance energy of each cation species can be isolated. Performing XRMR on these three resonant energies yields magnetic depth profiles that correspond each to one specific cation species. The depth profiles of both kinds of Fe^{3+} cations reveal a 3.9 ± 1.0 Å-thick surface layer of enhanced magnetization, which is likely due to an excess of these ions at the expense of the Fe^{2+}_{oct} species in the surface region. The magnetically enhanced Fe^{3+}_{tet} layer is additionally shifted about 2.9 ± 0.4 Å farther from the surface than the Fe^{3+}_{oct} layer.

7. Structural and magnetic investigation of the interfaces of Fe_3O_4/MgO(001) with and without NiO interlayer

Tobias Pohlmann, Florian Bertram, Jari Rodewald, Jannis Thien, Kevin Ruwisch, Timo Kuschel, Eugen Weschke, Karsten Küpper, and Joachim Wollschläger

Abstract

We present an investigation on the structural and magnetic properties of the Fe_3O_4/MgO(001) and the Fe_3O_4/NiO(001) interfaces by extracting valence- and lattice-site-selective magnetooptical depth profiles by means of x-ray resonant magnetic reflectivity in combination with charge-transfer multiplet simulations of x-ray magnetic circular dichroism data. For Fe_3O_4/MgO(001), the magnetooptical depth profiles at the Fe^{2+}_{oct} and the Fe^{3+}_{oct} resonant energies follow exactly the structural profile, while the magnetooptical depth profile at the Fe^{3+}_{tet} resonance being offset by 3.2 ± 1.3 Å from the interface, consistent with a B-terminated interface of Fe_3O_4 with fully intact magnetic order. For Fe_3O_4/NiO(001), magnetooptical depth profiles agreeing with the structural depth profile are observed at both the Fe^{2+}_{oct} resonance and the Ni L_3 resonance. This implies a ferromagnetic order in the NiO film, and the absence of any magnetic dead layers in the Fe_3O_4 film. However, the interface positions of the magnetooptical depth profiles at the Fe^{3+}_{oct} and the Fe^{3+}_{tet} are dislocated by 3.3 ± 1.4 Å and 2.7 ± 0.9 Å, respectively, not consistent with a magnetically ordered stoichiometric interface. This may be related to an intermixed (Ni, Fe)O layer at the interface.

7.1. Introduction

Magnetite (Fe_3O_4) is a half-metallic ferrimagnet in the inverse spinel structure. This structure consists of a cubic close-packed (fcc) oxygen lattice whose interstitial sites are populated by three different iron species: 1/2 of the octahedral B-sites are occupied randomly by divalent Fe^{2+}_{oct} and trivalent Fe^{3+}_{oct} cations, and 1/8 of the tetrahedral A-sites are occupied by trivalent Fe^{3+}_{tet} cations. The two octahedrally coordinated species Fe^{2+}_{oct} and Fe^{3+}_{oct} are ferromagnetically coupled by double exchange, while the Fe^{3+}_{oct} and Fe^{3+}_{tet} cations couple antiferromagnetically via superexchange. Therefore, the macroscopic moment of Fe_3O_4 of 4.07 $\frac{\mu_B}{\text{f.u.}}$ originates from the ferromagnetic order of the Fe^{2+}_{oct} cations [113].

Due to this magnetic properties, magnetite is a long-standing candidate to contribute to all-oxide thin-film spintronic devices, as a source for spin-polarized currents [7–12]. These kinds

of devices utilize the fact that many metal oxides with varying electronic and magnetic properties grow in spinel or rock-salt structures – such as the conducting ferrimagnets Fe_3O_4 and γ-Fe_2O_3, the insulating ferrimagnets $NiFe_2O_4$ and $CoFe_2O_4$, the insulating antiferromagnets NiO, CoO and FeO, or the non-magnetic insulators MgO and $MgAl_2O_4$ –, which all share a cubic close-packed oxygen lattice with very similar lattice constants [7]. This allows epitaxial growth of film stacks with a large variety of spinelectronic functionality, but with little strain and thus supposedly well-matching interfaces.

However, a drawback of this concept is that the structural similarity of these metal oxides also means that undesired modifications at their interfaces are difficult to detect, such as interdiffusion of Mg [36], Ni [34, 188] or Co [169] into Fe_3O_4 films, or the transformation of the different iron oxides into each other [21, 144]. All-oxide spintronic devices with Fe_3O_4 electrodes did indeed not prove to be very successful yet; their shortcomings were speculated to stem from magnetic dead layers at the substrate interface [17] or other interface effects [12].

One particular functional interface, which is important, for instance, for magnetic tunnel junctions, is the interface between ferromagnetic and antiferromagnetic films, e.g. Fe_3O_4 and NiO, respectively, exhibiting exchange bias [23, 130–132]. This effect causes a shift of the coercive fields of the ferromagnetic film, and can be used to pin its magnetization state.

In this study, we investigate the structural and magnetic properties of the Fe_3O_4/NiO and Fe_3O_4/MgO interfaces. We grow Fe_3O_4 single layers and Fe_3O_4/NiO bilayers on MgO(001) by reactive molecular beam epitaxy (RMBE), and investigate the distribution and magnetic order of the three cations Fe^{2+}_{oct}, Fe^{3+}_{tet} and Fe^{3+}_{oct} of Fe_3O_4 by x-ray resonant magnetic reflectivity (XRMR), combined with charge-transfer multiplet analysis of x-ray magnetic circular dichroism (XMCD) spectra.

7.2. Experimental details

The deposition and characterization methods of the samples followed the ones presented in Refs. [23, 34]. We prepared Fe_3O_4/MgO(001) and Fe_3O_4/NiO/MgO(001) samples in a multichamber ultra-high-vacuum system with a base pressure of $p_0 < 1 \times 10^{-8}$ mbar. Before deposition, the MgO(001) substrates were annealed at 400°C in an oxygen atmosphere of 1×10^{-4} mbar for 1 hour. Our films were grown by RMBE. For the NiO, we deposited nickel in an oxygen pressure of 1×10^{-5} mbar, and for the Fe_3O_4 we deposited iron in an oxygen pressure of 5×10^{-6} mbar. We limited the substrate temperature to 250°C, in order to avoid interdiffusion of Mg into the films [36]. After growth, the electronic structure of the samples were characterized *in situ* by x-ray photoelectron spectroscopy (XPS), using a Phoibos HSA 150 hemispherical analyzer and an Al Kα anode, and their surface structure by low-energy electron diffraction (LEED). The Fe 2p XPS spectra show the Fe^{2+} and the Fe^{3+} features typical for Fe_3O_4, and the LEED patterns confirm the characteristic $(\sqrt{2} \times \sqrt{2})$R45° surface structure [110, 189] (both not shown here). Fe_3O_4/MgO(001) and Fe_3O_4/NiO/MgO(001) samples were transported under ambient conditions to BESSY II for x-ray absorption spectroscopy (XAS), XMCD, x-ray reflectivity (XRR) and XRMR on the XUV diffractometer at beamline UE46_PGM-1 [173]. The samples were placed between two permanent magnets in a magnetic field of 200 mT at room temperature. The x-rays had a degree of 90% circular polarization. Additionally, we measured XAS and XMCD in total fluorescence yield mode (TFY) and reflection mode at Diamond Light Source (DLS), on the RASOR diffractometer of

	BESSY II UE46_PGM-1		DLS I10
	Fe_3O_4/MgO	Fe_3O_4/NiO/MgO	Fe_3O_4/NiO/MgO
$d_{Fe_3O_4}$(nm)	25.2 ± 0.3	9.3 ± 0.1	17.6 ± 0.1
d_{NiO}(nm)	–	4.3 ± 0.1	27.3 ± 0.2
$\sigma_{surface}$ (Å)	3.3 ± 0.5	3.2 ± 0.5	2.0 ± 0.6
$\sigma_{Fe_3O4/NiO}$ (Å)	–	3.0 ± 0.2	4.2 ± 0.8
$\sigma_{substrate}$ (Å)	3.5 ± 0.5	2.7 ± 0.5	2.5 ± 0.3

Tab. 7.1: Film thicknesses d_i and rms roughnesses σ_i of the investigated samples, obtained from off-resonant XRR measurements recorded at 1000 eV. Corresponding data and fits for the UE46_PGM-1 samples are shown in Fig. 7.2.

beamline I10. The samples were placed in a similar magnet setup under the same conditions. Here, the x-rays had a degree of circular polarization of 99%. All XAS and XMCD spectra were recorded in total electron yield (TEY) mode with an incidence glancing angle of 30°. XRR and XRMR curves were obtained by θ-2θ scans in the range $2\theta = 0° - 140°$ at selected resonant photon energies with both right and left circularly polarized x-rays. The structural properties of the samples (thickness d, roughness σ) obtained by XRR at an off-resonant energy (1000 eV, cf. Fig. 7.2) are summarized in Tab. 7.1.

7.3. Data analysis

7.3.1. XMCD

To obtain cation- and lattice-site-selective magnetooptical depth profiles, first the XMCD spectra have to be analyzed. Figures 7.1(a) and (b) show XAS and XMCD spectra, respectively, of the Fe $L_{2,3}$ edge of the Fe_3O_4/NiO/MgO sample. Charge-transfer multiplet calculations of the three Fe cations of Fe_3O_4 using the Thole code [177] with assistance of CTM4XAS [28,178] provide the three individual XAS and XMCD spectra shown below the data. For these calculations, we assumed the three-cation model, with crystal field energies of $10Dq^{oct} = 1.0\,eV$ in octahedral and $10Dq^{tet} = -0.6\,eV$ in tetrahedral coordination. The splittings between the initial and final charge-transfer states were $\Delta_{init} = 6\,eV$ and $\Delta_{final} = 5\,eV$ [23]. We used an exchange splitting $g \cdot \mu_B$ of $12 \pm 1\,meV$. The multiplet states resulting from these calculations were compared to the experimental data by assuming a Gaussian instrumental broadening of 0.25 eV, and a Lorentzian lifetime broadening of 0.3 eV at L_3 and 0.6 eV at L_2. Adding the three individual cation spectra with a 1:1:1 ratio valid for Fe_3O_4 results in total spectra (orange lines), which fits both the XAS and the XMCD data well. The multiplet analysis reveals that at those energies where the XMCD spectrum has its extrema (708.4 eV, 709.5 eV, 710.2 eV), most of the XMCD signal originates from one dominant cation(cf. Chap. 6. The individual XMCD contributions of each cation species to the spectrum at these three energies can be found in Tab. 7.2. Therefore, XRMR measurements on those energies are mostly sensitive to one specific cation species, allowing conclusions about distinct features of the individual cations.

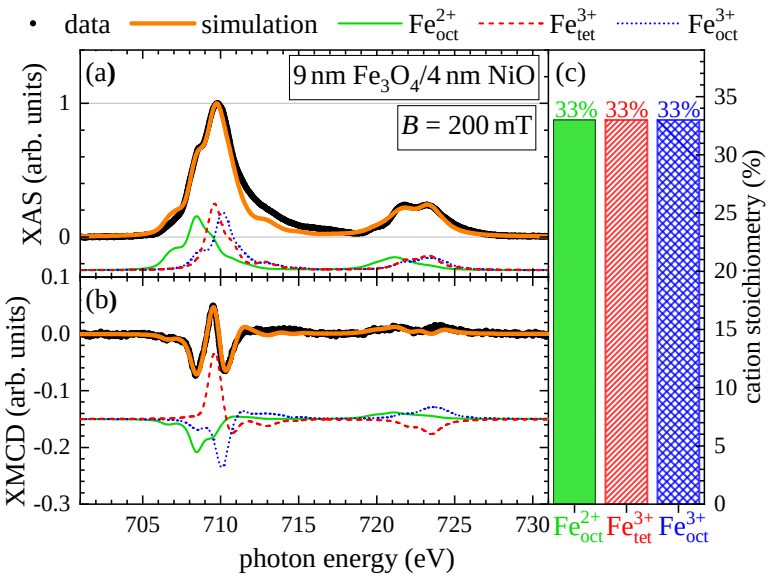

Fig. 7.1: (a) XAS and (b) XMCD spectrum at the Fe $L_{2,3}$ edge for the Fe_3O_4/NiO/MgO sample, taken at 200 mT external magnetic field, at room temperature and in TEY mode. A step function was subtracted from the XAS spectrum. Black circles are data points; green, red and blue spectra are multiplet calculations for the three cation species of Fe_3O_4, assuming a 1:1:1 stoichiometry, the orange line is their sum. The cation spectra are offset for better visibility.

Since the TEY mode has a probing depth of about 3 nm in Fe_3O_4 [71], the TEY signal from the buried NiO film was strongly attenuated at the Ni $L_{2,3}$ edge. For a clearer signal, we brought a 18 nm Fe_3O_4/27 nm NiO/MgO sample to beamline I10 of DLS, and measured XAS and XMCD in TFY mode, whose probing depth is only limited by the x-ray attenuation length in Fe_3O_4 of about 80 nm [48], at a fixed incident angle of 30° (cf. Figs. 7.3(a),(b)). Simultaneously, we measured the reflected intensity, in order to obtain an estimate of the dichroism in reflection (cf. Figs. 7.3(c),(d)).

7.3.2. XRMR

The XRMR data were recorded by measuring XRR curves at resonant photon energies E_i with extrema in the XMCD signal (maximum at 708.4 eV, minimum at 709.5 eV, maximum at 710.2 eV, see Fig. 7.1(b)) with both left and right circularly polarized x-rays. Resonant 'non-dichroic' XRR curves were obtained by averaging the signals from both helicities

$$I = (I^{\text{right}} + I^{\text{left}})/2 \tag{7.1}$$

Energy	Fe^{2+}_{oct}	Fe^{3+}_{tet}	Fe^{3+}_{oct}
708.4 eV	$73 \pm 5\%$	$8 \pm 3\%$	$19 \pm 5\%$
709.5 eV	$18 \pm 3\%$	$64 \pm 3\%$	$18 \pm 3\%$
710.2 eV	$4 \pm 3\%$	$16 \pm 8\%$	$80 \pm 10\%$

Tab. 7.2: Contributions of the three cation species to the extrema in the XMCD spectrum in Fig. 7.1(b), as obtained by the multiplet analysis.

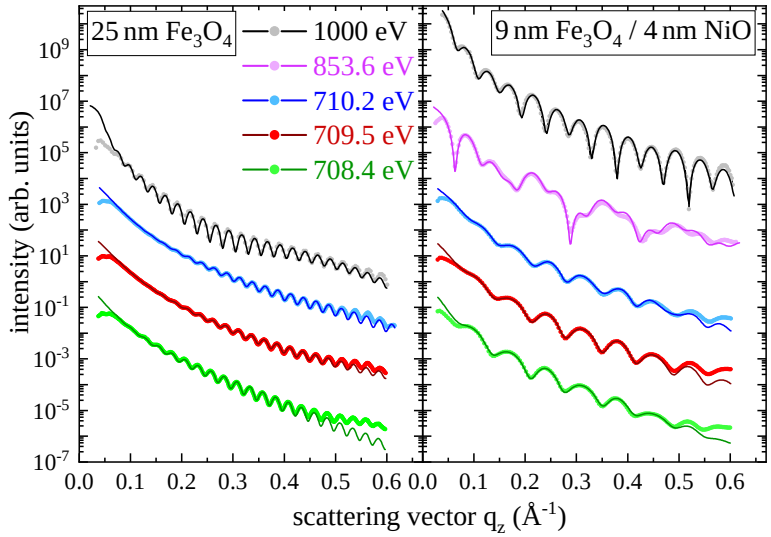

Fig. 7.2: XRR measurements of the two samples recorded at the three resonant energies of the Fe L_3 XMCD spectrum of Fe_3O_4 (708.4 eV, 709.5 eV, 710.2 eV), the energy of the Ni L_3 maximum (853.6 eV) and at an off-resonant energy (1000 eV).

and the XRMR asymmetry ratios by subtracting and normalizing them:

$$\Delta I = \frac{I^{\text{right}} - I^{\text{left}}}{I^{\text{right}} + I^{\text{left}}}. \tag{7.2}$$

These curves were then fitted with the Zak matrix formalism using the software ReMagX [30] to determine the depth profiles of the complex refractive index $n(z)$

$$n(z) = 1 - \delta(z) + i\beta(z) \tag{7.3}$$

along the film height z. The optical dispersion δ and the optical absorption β can be split into non-magnetic parts δ_0, β_0 and magnetooptical parts $\Delta\delta$, $\Delta\beta$. In the case of an in-plane magnetic field longitudinal to the x-ray beam, they can be written as [30]

$$\delta(z) = \delta_0(z) - \Delta\delta(z) \cdot \cos(\theta) \tag{7.4}$$

$$\beta(z) = \beta_0(z) + \Delta\beta(z) \cdot \cos(\theta) \quad , \tag{7.5}$$

where the magnetooptical contributions depend on the x-ray incidence glancing angle θ. The optical absorption β_0 is proportional to the XAS signal, while the magnetooptical absorption $\Delta\beta$ is proportional to the XMCD signal. Thus, $\Delta\beta(z)$ is a measure of the magnetization along the film depth. A detailed review of the XRMR method and the software is given in Ref. [30], and a conclusive recipe for fitting XRMR data can be found in Refs. [90, 190].

7.4. Results

Figure 7.3(a) shows the XAS spectra of the 18 nm Fe_3O_4/27 nm NiO/MgO sample recorded with left and right circularly polarized x-rays in TFY mode, and Fig. 7.3(b) shows their difference. The XMCD signal is about 3% of the XAS maximum. In reflection, the dichroism becomes even more apparent. Note that the data are recorded at fixed incidence angle, therefore the scattering vector q_z changes along with the energy. At the Ni L_3 resonant

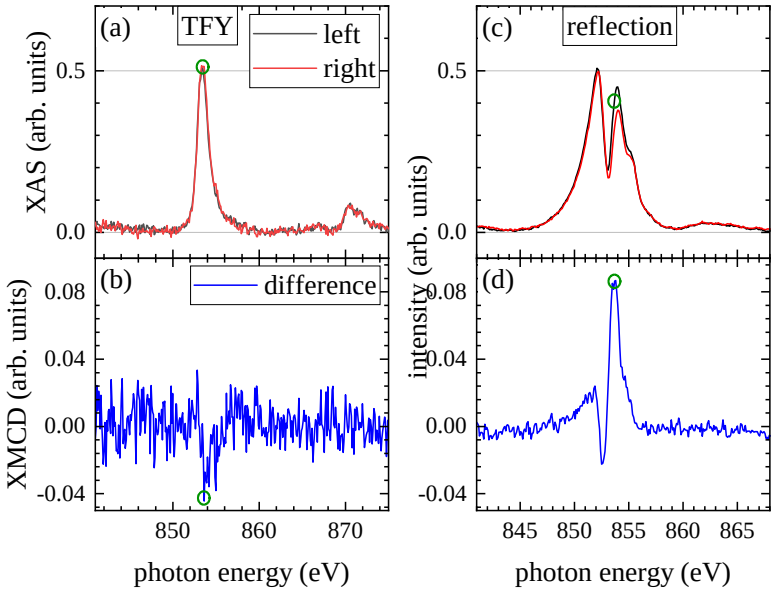

Fig. 7.3: (a) XAS and (b) XMCD spectra in TFY mode at the Ni $L_{2,3}$ edge for a 18 nm Fe_3O_4/27 nm NiO/MgO sample. (c) Energy scans of the reflected intensity for left and right circularly polarized x-rays. (d) Difference of the curves in (c). The green circles circles indicate the energy at which the XRMR curves were taken (853.6 eV). The XAS data are normalized to the maximum of the XAS spectrum $XAS^{left}+XAS^{right}$. All data are recorded at a fixed incidence glancing angle of 30°.

energy of 853.6 eV, the dichroism in reflection ranges up to about 8%, demonstrating a strong magnetic signal from NiO. This energy was chosen for the XRMR measurements at the Ni L_3 resonance, and is indicated by the green circles in Fig. 7.3.

The data and fits of the resonant XRR measurements can be found in Fig. 7.2, alongside with the off-resonant XRR curves. Figures 7.4(a) and (b) show the XRMR data for the Fe_3O_4/MgO and the Fe_3O_4/NiO/MgO samples at the three Fe resonant energies 708.4 eV, 709.5 eV and 710.2 eV, and the Ni L_3 resonant energy 853.6 eV, together with their respective fits, which describe the data very well. The fits in Fig. 7.4(b) were obtained from the magnetooptical depth profile models which are displayed in Fig. 7.5(a) for all four energies of the Fe_3O_4/NiO/MgO sample. The grey line represents the optical absorption $\beta_{\text{off-res}}$ obtained from the off-resonant XRR measurement, and represents the structural depth profiles of the sample. It has three plateaus, corresponding to the MgO substrate, the NiO film and finally the Fe_3O_4 film, as illustrated by the sketch on top of the panel. The filled areas are the magnetooptical depth profiles $\Delta\beta(z)$ at the resonant energies of the three iron cation species and the Ni L_3 energy, obtained from the XRMR asymmetry ratios.

One notable feature of these magnetooptical depth profiles is found at the surface of the Fe_3O_4 films. Here, a thin layer of enhanced magnetooptical absorption is observed at both 709.5 eV and 710.2 eV. This effect is discussed in detail in Chap. 6 for Fe_3O_4/MgO(001), but is not the subject of this study, which focuses on the interfaces.

Figure 7.5(b) shows the interface region of the magnetooptical depth profiles of the Fe_3O_4/MgO sample, according to the fits in Fig. 7.4(a). Both the interfaces of the magnetooptical depth profile at 708.4 eV (green) and of the one at 710.2 eV (blue) are collocated with the structural interface (grey line) at $z = 0$ Å. However, the interface of the magnetooptical depth profile at 709.5 eV is shifted by a distance $\Delta z_{709.5\,\text{eV}} = 3.2 \pm 1.3$ Å away from the interface into the Fe_3O_4 film. The roughnesses of magnetooptical depth profiles at both Fe^{3+} resonances follow the structural depth profile. In contrast, the roughness of the magnetooptical depth

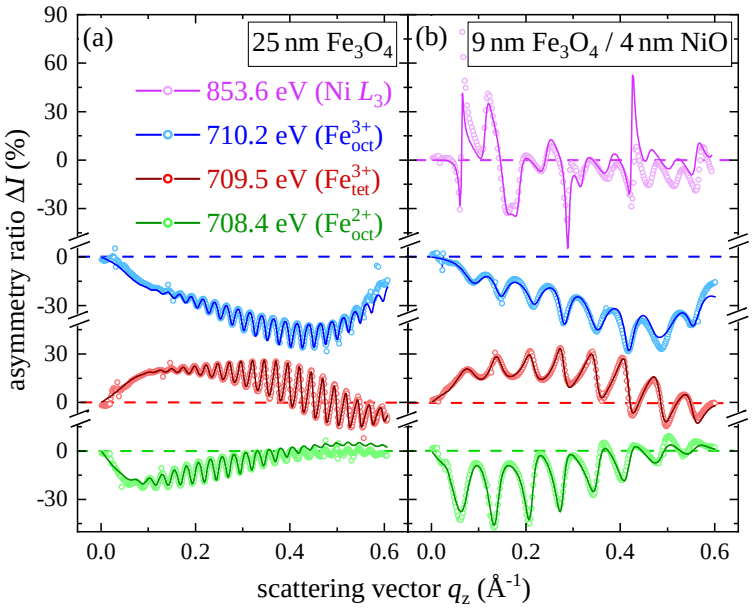

Fig. 7.4: XRMR data (open circles) and fits (solid lines) from (a) the Fe_3O_4/MgO and (b) the Fe_3O_4/NiO/MgO sample, recorded at the three resonant energies of the Fe XMCD L_3 edge and the Ni L_3 edge. The magnetooptical depth profile models corresponding to the fits in (a) are displayed in Fig. 7.5(b), and the interface regions of the magnetooptical depth profiles corresponding to the fits in (b) are shown in Fig. 7.5(c).

profile recorded at the Fe^{2+}_{oct}energy, $\sigma_{708.4\,eV} = 4.4 \pm 0.2$ Å is slightly larger than the structural roughness $\sigma_{substrate} = 3.5 \pm 0.5$ Å.

For the Fe_3O_4/NiO/MgO film, the results are slightly different. Figure 7.5(c) shows the Fe_3O_4/NiO interface region of the Fe_3O_4/NiO/MgO sample. The XRMR data at the Ni L_3 edge can be well fitted with a homogeneous magnetization profile throughout the NiO film. The interfaces of the magnetooptical depth profiles at the Ni L_3 edge and at the Fe^{2+}_{oct}-related resonance at 708.4 eV are collocated with the structural interface, indicating intact structural and magnetic order for both species. Notably, both their roughnesses are slightly higher, $\sigma_{708.4\,eV} = 6$Å, $\sigma_{853.6\,eV} = 4.6$ Å, compared to the structural roughness $\sigma_{Fe_3O_4/NiO} = 3$ Å.

In contrast to the magnetooptical depth profile at 708.4 eV, which directly follows the structural profile, the profiles at 709.5 eV and 710.2 eV are rising with shifts of $\Delta z_{tet} = 2.6 \pm 0.9$ Å and $\Delta z_{oct} = 3.3 \pm 1.4$ Å, respectively, apart from the interface, pointing to a lack of magnetooptical absorption of both Fe^{3+}_{oct} and Fe^{3+}_{tet} at the interface.

7.5. Discussion

For the Fe_3O_4/MgO sample, it is shown in Fig. 7.5(b) that the magnetooptical depth profile recorded at a photon energy of 709.5 eV is displaced from the interface into the Fe_3O_4 film by a shift $\Delta z_{709.5\,eV}$. From the quality of the fits, we can determine this shift to the range $\Delta z_{709.5\,eV} = 3.2 \pm 1.3$Å. Since this resonance is governed by the tetrahedrally coordinated Fe ions, this result is consistent with a B-terminated interface, having octahedrally coordinated cations in the Fe_3O_4 interface layer: Figure 7.6(a) shows the ideal stacking order at a B-terminated Fe_3O_4/MgO(001) interface. The oxygen lattice of the substrate continues as the oxygen lattice of the film. In [001] direction, Fe_3O_4 can be described as a stack of subsequent B layers, consisting of a row of O^{2-} anions as well as Fe^{2+}_{oct} and Fe^{3+}_{oct} cations, and A layers, containing Fe^{3+}_{tet} cations, with a distance of 1.05 Å between them. These layers are depicted as blue and red shaded areas in Fig. 7.6(a), with the interface layer being a B layer

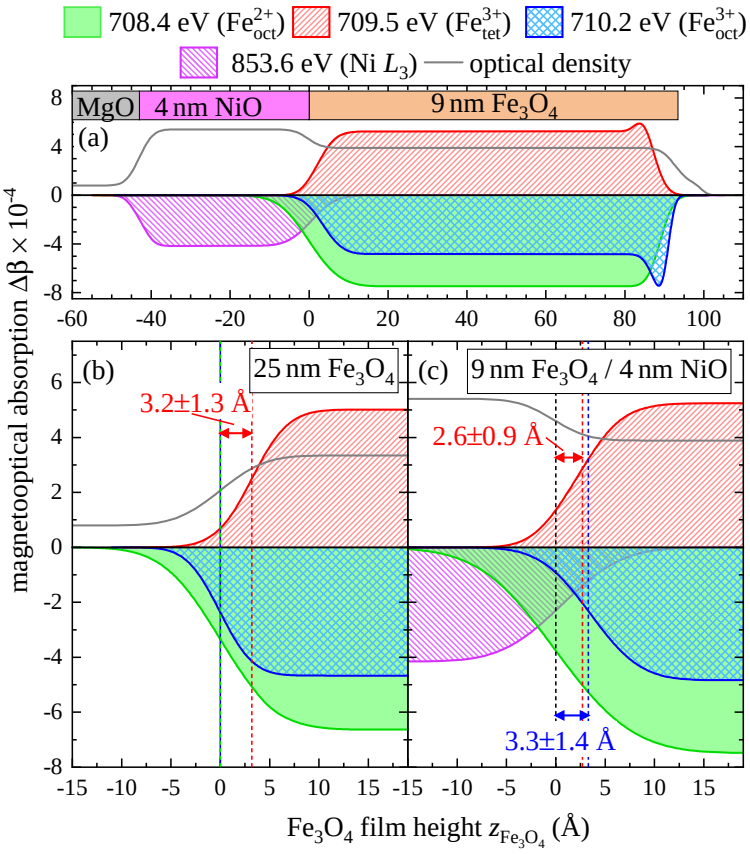

Fig. 7.5: (a) $\Delta\beta(z)$ depth profiles at the three Fe L_3 resonant energies and the Ni L_3 energy of the Fe_3O_4/NiO/MgO sample, corresponding to the fits in Fig. 7.4(b). (b) Close-up of the interface region of the Fe_3O_4/MgO film, obtained from the fits in Fig. 7.4(a). (c) Close-up of the Fe_3O_4/NiO interface region of the magnetooptical depth profiles in (a). The grey lines indicate the optical absorption profiles $\beta_{\text{off-res}}(z)$ obtained by off-resonant XRR fits. Dashed lines highlight the interface positions of the magnetooptical depth profiles.

(B-termination). Simulated cation depth profiles following this model, using an interface roughness of $\sigma = 3.5$ Å, corresponding to the experimentally determined roughness of the Fe_3O_4/MgO interface, are shown in Fig. 7.6(b). The rising edge of the Fe^{3+}_{tet} depth profile is shifted by $\Delta z_{tet} = 1.05$ Å from the interfaces of the Fe^{2+}_{oct} and Fe^{3+}_{oct} profiles into the Fe_3O_4 film. Because of the overlap of the individual cation spectra (cf. Fig. 7.1(b)), the expected magnetooptical depth profiles do not follow this behavior exactly. By taking into account the magnetooptical contributions as derived from the multiplet calculations of each cation at each of the three energies, the expected magnetooptical depth profiles of a B-terminated Fe_3O_4/MgO(001) interface can be calculated. They are shown in Fig. 7.6(c). The expected shift of the magnetooptical depth profile at 709.5 eV is $\Delta z_{709.5\,\text{eV}} = 2.5$ Å, consistent with the experimental result of $\Delta z_{709.5\,\text{eV}} = 3.2 \pm 1.3$ Å. Therefore, the magnetooptical depth profiles indicate a B-terminated Fe_3O_4/MgO(001) interface with no interlayer, and evidently, also no magnetic dead layer. The magnetic order of all three sublattices have bulk properties down to the interface. The simulations of the B-terminated interface also predict that the roughness $\sigma_{708.4\,\text{eV}}$ of the magnetooptical depth profiles at 708.4 eV appears to be about 0.5 Å larger than the structural profile $\sigma_{\text{substrate}}$. This offers an explanation for the slight mismatch of these two rougnesses observed in the experiment.

Both the Fe_3O_4/MgO and the Fe_3O_4/NiO interfaces have been studied by various methods. Spintronic devices require interfaces that are structurally, but especially also magnetically sharp. Therefore, focus has been laid on the possible presence of interlayers and intermixing at the interfaces. In the case of Fe_3O_4/MgO, the formation of FeO interlayers have been

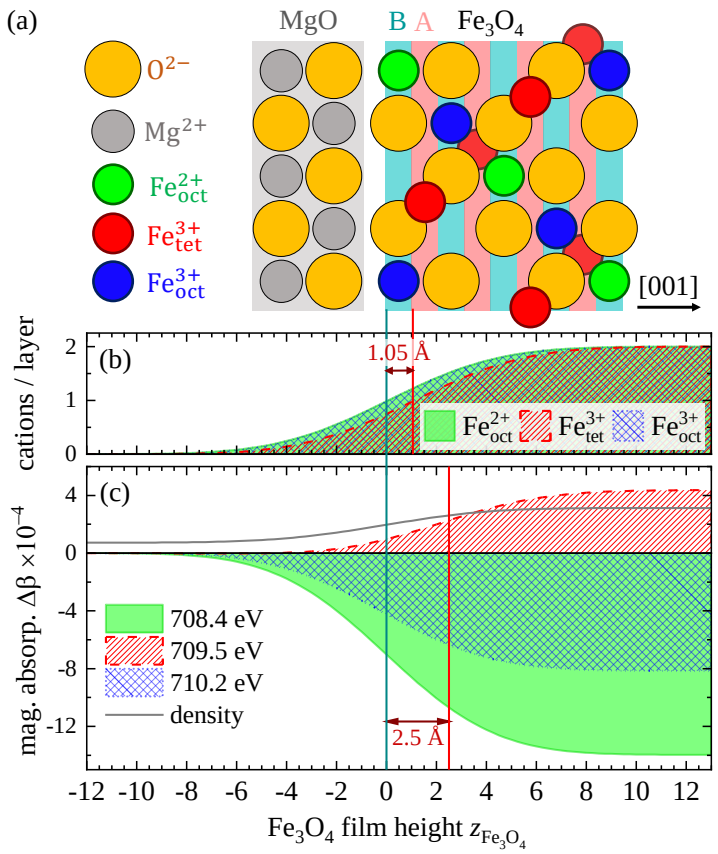

Fig. 7.6: (a) Illustration of the stacking order at a B-terminated Fe_3O_4/MgO(001) interface. The blue and red shaded areas indicate octahedral and tetrahedral layers, respectively. (b) Simulated cation profiles at the interface of a Fe_3O_4 film with a roughness of σ = 3.5 Å, in scale with (a). (c) Expected magnetooptical depth profiles at the three resonant energies of the Fe L_3 edge, stemming from the cation profiles in (b), and assuming the magnetooptical absorption contributions of the individual cation spectra in Fig. 7.1(b).

reported on both metal and oxide substrates [159,160,162], but also on MgO(001) for films deposited at room temperature [21]. In the growth study presented in Chap. 5, it has been observed that a thin $Fe_{1-\delta}O$ layer of about 2–3 unit cells forms at the beginning of the growth. However, tr-HAXPES data suggested that this interlayer might not be retained after the growth is concluded. The possibility of a single atomic $Fe_{1-\delta}O$ interlayer is discussed in the following. The corresponding magnetooptical depth profiles are simulated in Figs. 7.7(a)-(f) for two scenarios. $Fe_{1-\delta}O$ is paramagnetic at room temperature. Therefore, the first reasonable scenario is that it forms a magnetic dead layer at the interface, presented in Figs. 7.7(a)-(c). Figure 7.7(a) shows an illustration of the stacking order, Fig. 7.7(b) the cation depth profiles simulated with a roughness of σ = 3.5 Å, and Fig. 7.7(c) the resulting magnetooptical depth profiles. Due to the magnetically dead $Fe_{1-\delta}O$ layer, the rising edges of the magnetooptical depth profiles at both 708.4 eV and 710.2 eV are shifted about 2 Å into the Fe_3O_4 film compared to the structural interface (cf. dashed black and solid green line in Fig. 7.7(c)), not consistent with the observed profiles in Fig. 7.5(b).

The second scenario assumes that the magnetic order of the Fe^{2+}_{oct} sublattice is extended into the FeO layer. The resulting magnetooptical depth profiles differ even more from the observed ones (cf. Figs. 7.7(d)-(f)). Our data therefore do not indicate any magnetically dead layers, which had been considered to be the cause of the magnetization reduction in Fe_3O_4 ultrathin films [71,80,191,192], or interlayers of FeO. Since it has already been shown that the magnetooptical depth profiles can be explained without an interlayer, it is unlikely that a FeO interlayer of more than a single atomic layer is present. This implies that the

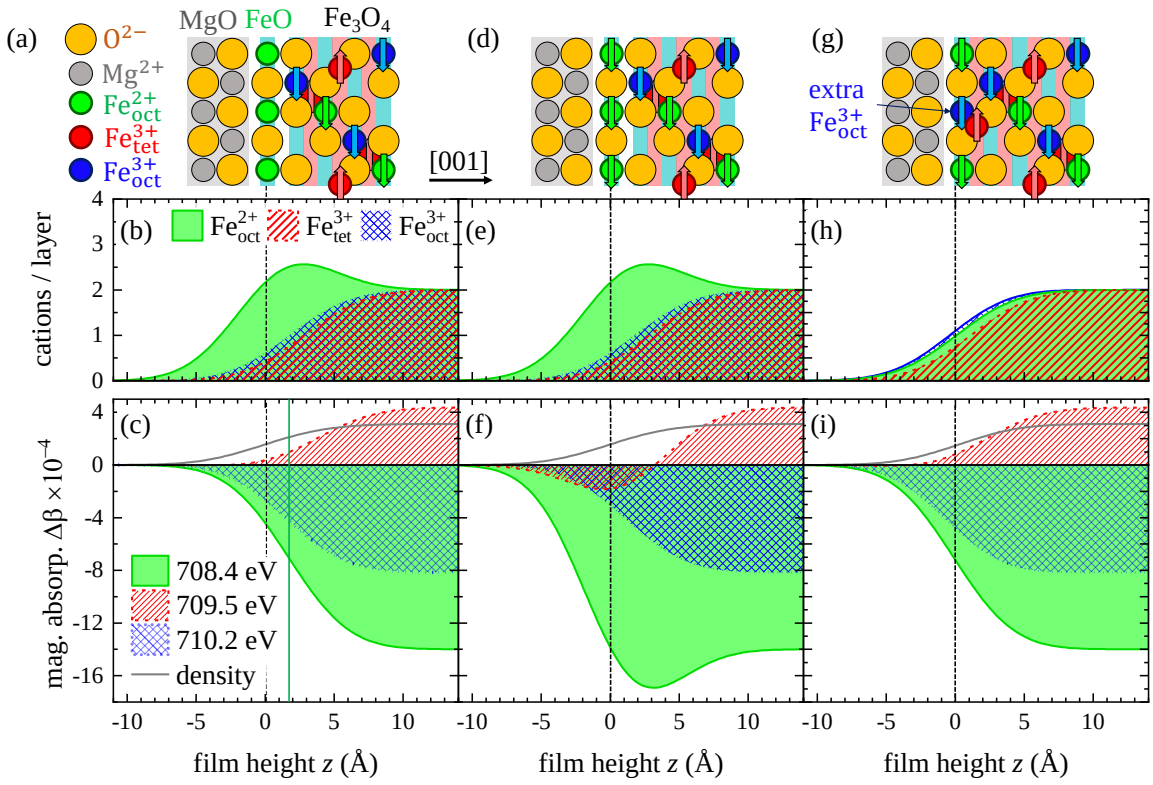

Fig. 7.7: Simulated magnetooptical depth profiles for three models of the Fe_3O_4/MgO interface. (a),(d),(g) Illustrations of the stacking orders of Fe_3O_4/MgO interfaces (a) with a single non-magnetic $Fe_{1-\delta}O$ interlayer, (d) with a single magnetic $Fe_{1-\delta}O$ interlayer, (g) with an additional Fe^{3+}_{oct} cation in the interface layer, following the model of Chang et al [80]. (b),(e),(h) Cation depth profiles corresponding to the illustrations in (a),(d),(g), respectively. (c),(f),(i) Magnetooptical profiles resulting from the cation profiles in (b),(e),(h), respectively.

$Fe_{1-\delta}O$ layers forming at the beginning in the early growth process, as reported in Chap. 5, do not persist in the film after deposition, consistent with the tr-HAXPES data.

Another interesting model, which was proposed by Chang et al. for the growth dynamics of Fe_3O_4 [80], shall also briefly be mentioned here. This model suggests the first interface layer to contain an additional Fe^{3+}_{oct} cation per unit formula $[(Fe^{2+}_{oct})_2(Fe^{3+}_{oct})_3O_8$ instead of $(Fe^{2+}_{oct})_2(Fe^{3+}_{oct})_2O_8]$. An illustration can be seen in Fig. 7.7(g). Both the cation depth profiles and the simulated magnetooptical depth profiles resulting from this model, presented in Figs. 7.7(h),(i), hardly differ from the B-terminated interface shown in Figs. 7.6(b),(c). Although XRMR would in principle be an ideal method to test this model, the lacking spatial resolution in our experiments can neither confirm nor reject a faint phenomenon like an additional Fe^{3+}_{oct} cation in the interface layer.

For the Fe_3O_4/NiO/MgO(001) sample, a noteworthy finding is the dichroic signal of the NiO film. Bulk NiO is an antiferromagnet at room temperature and should not show any circular dichroism. However, as demonstrated in Fig. 7.3, we do observe a dichroism in both TFY mode and in reflection at the Ni L_3 edge. Interestingly, we can exclude the XMCD signal to stem from uncompensated surface spins, since the magnetooptical depth profiles clearly

show a homogeneous magnetization of the entire film. Size-effects of the magnetic properties of NiO, including ferromagnetic behaviour at room temperature, have been frequently reported before, mostly for NiO nanoparticles [134–138]. For Fe_3O_4/NiO ultrathin films, a spin-flop coupling of NiO to the Fe_3O_4(001) interface has been reported [132]. In that case, the antiferromagnetic order of NiO aligns perpendicular to the magnetization of Fe_3O_4, but with a canting of the Ni^{2+} moments, resulting in a magnetization component parallel to the ferrimagnet. This reaction of NiO to outer magnetic fields has also been confirmed by spin-hall magnetoresistance measurements [128, 139], and can explain the presence of the observed XMCD signal.

The interface of Fe_3O_4/NiO has mostly been discussed regarding the presence of a $NiFe_2O_4$ interlayer. In reports by Gatel et al. [131] and Pilard et al. [133], high-resolution transmission electron microscopy (HRTEM) images show generally sharp interfaces between the rock salt structure of NiO and the spinel structure of Fe_3O_4. However, this only partly solves the question, because the lack of chemical and magnetic contrast cannot exclude, for instance, the formation of a rock salt $(Fe, Ni)O$ phase or a spinel $NiFe_2O_4$ phase. Gatel et al. adressed this issue by performing both HRTEM and electron energy loss spectroscopy (EELS) [131]. For a NiO/Fe_3O_4/MgO(001) sample, for which the NiO film was deposited at a substrate temperature of 700°C, indeed an intermediate $NiFe_2O_4$ phase was observed. For a Fe_3O_4/NiO/MgO(001) stack, which had the Fe_3O_4 film deposited at 400°C, the interface appeared to be chemically sharp, with at most minor interdiffusion [131]. The $NiFe_2O_4$ phase they observe in the NiO/Fe_3O_4/MgO(001) stack is likely caused by thermal interdiffusion due to the high deposition temperature [34]. A formation of a well-ordered $NiFe_2O_4$ interlayer does not match our observations. $NiFe_2O_4$ crystallizes in the same inverse spinel structure as Fe_3O_4, but with Ni^{2+}_{oct} cations instead of Fe^{2+}_{oct} sharing the B-sites with Fe^{3+}_{oct}. Analogous to Fe_3O_4, the magnetic moments of the Ni^{2+}_{oct} and Fe^{3+}_{oct} cations on the B-sites align antiferromagnetically to the magnetic moments of the Fe^{3+}_{tet} cations on the A-sites. For the magnetooptical depth profiles, this would imply a decrease of Fe^{2+}_{oct} cations and thus of the magnetooptical absorption at 708.4 eV, while the magnetooptical absorption depth profiles for 709.5 eV and 710.2 eV should stay constant in a $NiFe_2O_4$ layer. Instead, we observe a reduction of the magnetooptical absorption at 709.5 eV and 710.2 eV as compared to the case of the Fe_3O_4/MgO interface. This behavior, together with the increased roughnesses of the magnetooptical depth profiles at the Fe^{2+}_{oct} and the Ni^{2+} energies, might indicate a slight interdiffusion of Fe^{2+}_{oct} into the rock salt structure of NiO. However, this effect may not extend farther than a single atomic layer. Notably, the ferromagnetic order of the Fe^{2+}_{oct} cations is retained down to the interface regardless of the intermixing.

7.6. Conclusion

We have prepared ultrathin Fe_3O_4/MgO(001) and Fe_3O_4/NiO/MgO(001) films by RMBE and performed XMCD and XRMR measurements to extract magnetooptical depth profiles for Fe_3O_4's individual cation species Fe^{2+}_{oct}, Fe^{3+}_{tet} and Fe^{3+}_{oct} as well as for Ni^{2+}. These magnetooptical depth profiles show that for Fe_3O_4/MgO(001), the magnetic order of all three cation species is stable for the entire film with no interlayer or magnetic dead layer at the interface. For Fe_3O_4/NiO films, we observe a magnetooptical absorption at the Ni L_3 in the NiO film corresponding to a ferromagnetic order throughout the entire NiO film. The magnetooptical profiles of the iron cations reveal an intact magnetic order for the Fe^{2+}_{oct} cation species down to

the interface, while the magnetooptical depth profiles at the Fe^{3+}_{oct} and the Fe^{3+}_{tet} resonances are shifted about 3 Å into the Fe_3O_4 film, possibly indicating a single intermixed layer containing both Fe^{2+} and Ni^{2+} cations.

Acknowledgments

Financial support from the Bundesministerium für Bildung und Forschung (FKZ 05K16MP1) is gratefully acknowledged. We are also grateful for the kind support from the Deutsche Forschungsgemeinschaft (DFG under No. KU2321/6-1, and No. WO533/20-1). The authors would like to thank Diamond Light Source for beamtime (proposal SI19173-1), and the staff of beamline I10 for assistance with data collection of the XMCD data on the Ni L edge. We thank HZB for the allocation of synchrotron beamtime at beamline UE46_PGM-1 (181/06266ST/R) where we recorded the XRMR curves and the XMCD measurements on the Fe L edge.

8. Summary and outlook

This work investigated the growth dynamic of the reactive beam epitaxy of Fe_3O_4 films, and its impact on the cation distribution, as well as on the magnetic and structural properties at the surface and the interfaces.

In order to study the structure and composition of Fe_3O_4 films during growth, time-resolved HEXRD and time-resolved HAXPES measurements were used to monitor the deposition process of Fe_3O_4 ultrathin films on $SrTiO_3(001)$, MgO(001) and NiO/MgO(001). It is found that the initial growth stage of $Fe_3O_4/SrTiO_3(001)$ can be divided into 3 steps: First, the film grows in disordered islands of unknown structure. Second, at a coverage of about 1.5 nm, they display the rock salt structure and show an excess of Fe^{2+}, likely being a $Fe_{1-\delta}O$ phase. Beyond thicknesses of 2.8 nm, the film grows in an inverse spinel structure in [001] direction, and develops (111) nanofacets on the surface. The films on MgO(001) and NiO/MgO(001) show a similar result, with the exception that the films are not disordered in the early growth stage. They grow initially in an island mode as well, and form a closed layer after the deposition of about $2-3$ nm. However, in contrast to $Fe_3O_4/SrTiO_3(001)$, these islands immediately exhibit a crystalline $Fe_{1-\delta}O$ phase up to a thickness of 1 nm. After that, the films grown in the inverse spinel structure of Fe_3O_4 on both MgO(001) and NiO/MgO(001). Additionally, the tr-HAXPES measurements of $Fe_3O_4/SrTiO_3(001)$ demonstrate that the $Fe_{1-\delta}O$ phase is only stable during the deposition process, but turns into a Fe_3O_4 phase when the deposition is interrupted. This suggests that this $Fe_{1-\delta}O$ layer is a strictly dynamic property of the growth process, and might not be retained in the as-grown films.

In order to characterize the as-grown films, a technique was introduced to extract the cation depth distribution of Fe_3O_4 films from magnetooptical depth profiles obtained by fitting XRMR curves. To this end, XAS/XMCD spectra were recorded as well as XRMR curves to obtain magnetooptical depth profiles. To attribute these magnetooptical depth profiles to the depth distribution of the cations, multiplet calculations were fitted to the XMCD data. From these calculations, the cation contributions at the three resonant energies of the XMCD spectrum can be evaluated. Recording XRMR curves at those energies allows to resolve the magnetooptical depth profiles of the three iron cation species in Fe_3O_4.

This technique was used to resolve the the cation stoichiometry at the surface of Fe_3O_4/MgO(001) films (cf. Chap. 6). It is found that both Fe^{3+} species show an enhanced signal in a $\approx 3.9 \pm 1.0$ Å thick layer, with the Fe^{3+}_{tet} layer located about 2.9 ± 0.4 Å underneath the Fe^{3+}_{oct} layer. This is attributed to the first unit cell from the surface containing an excess of Fe^{3+} cations, likely related to the SCV reconstruction of the $Fe_3O_4(001)$ surface. The magnetic order of the Fe^{3+}_{oct} and Fe^{3+}_{tet} species appears to be not disturbed in this reconstructed layer. The excess of Fe^{3+} cations at the surface can skew the results of data obtained from surface-sensitive spectroscopic techniques, and has to be taken into account during the analysis.

In Chap. 7, the same XRMR method was employed to study the interface region of Fe_3O_4/MgO(001) and Fe_3O_4/NiO/MgO(001) films. XMCD and XRMR measurements were performed to ex-

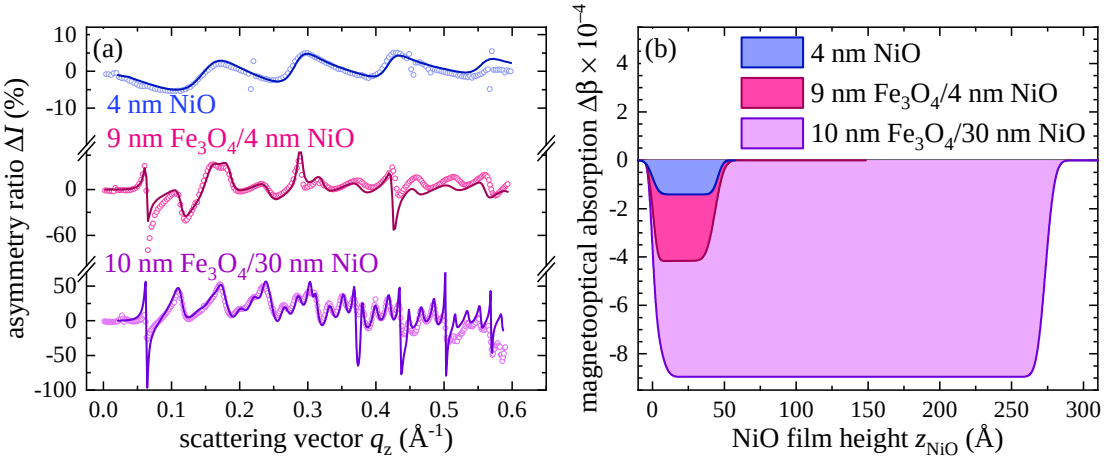

Fig. 8.1: (a) XRMR data recorded on the Ni L_3 edge with fits for a 4 nm NiO/MgO(001), a 9 nm Fe_3O_4/4 nm NiO/MgO(001) and a 10 nm Fe_3O_4/30 nm NiO/MgO(001) sample, recorded in an outer magnetic field of 200 mT. (b) Magnetooptical depth profiles $\Delta\beta(z)$ corresponding to the fits in (a). Preliminary results.

tract magnetooptical depth profiles for the Fe^{2+}_{oct}, Fe^{3+}_{tet} and Fe^{3+}_{oct} cation species as well as for Ni^{2+}. It is found that for Fe_3O_4/MgO(001), the magnetic order of all three cation species is stable for the entire film with no interlayer or magnetic dead layer at the interface, demonstrating that in fact the $Fe_{1-\delta}O$ layer vanishes during the growth process. For Fe_3O_4/NiO films, we observe a magnetooptical absorption at the Ni L_3 in the NiO film corresponding to a ferromagnetic order throughout the entire NiO film. This unexpected behavior for NiO, which is antiferromagnetic in the bulk, might be related to a spin-flop coupling of the NiO film to the Fe_3O_4 film. The magnetooptical profiles of the iron cations reveal an intact magnetic order for the Fe^{2+}_{oct} cation species down to the interface, while the magnetooptical depth profiles at the Fe^{3+}_{oct} and the Fe^{3+}_{tet} resonances are shifted about 3 Å into the Fe_3O_4 film, possibly indicating a single intermixed layer containing both Fe^{2+} and Ni^{2+} cations.

For this work, two techniques were demonstrated that grant access to the structural, chemical and magnetic properties of ultrathin films, but they were so far only used for Fe_3O_4. In Chap. 7, it has been shown that a homogeneous magnetization is observed across the NiO film in a 9 nm Fe_3O_4/4 nm NiO/MgO(001) film. Figure 8.1 repeats the results from that sample together with preliminary results from a 4 nm NiO/MgO(001) and a 10 nm Fe_3O_4/30 nm NiO/MgO(001) sample, obtained by XRMR measurements on the Ni L_3 edge. All three samples are displaying the same behavior, with the magnetization of the NiO film strongly increasing with addition of a neighboring Fe_3O_4 film, and with sample thickness. The origin and the exact behavior of this effect is not yet quite clear. For the immediate future, another XRMR experiment is planned to study more carefully this unexpected ferromagnetic signal in NiO films.

It would also be very interesting to use the CTM-assisted XRMR technique for other complex oxide materials, such as $NiFe_2O_4$ or $CoFe_2O_4$, in order to observe the distribution and magnetic properties of not only iron, but also Ni and Co through the film. Preliminary data for $NiFe_2O_4$/MgO(001) suggest a more complex cation distribution, requiring new modeling strategies.

A particularly interesting question is posed by the transient $Fe_{1-\delta}O$ layer observed during the early growth stage of Fe_3O_4. For Fe_3O_4/MgO(001) grown at room temperature, it has been reported that the wüstite interlayer remains present [21]. As has been discussed in the introduction, interface effects have been speculated to be the cause for the poor performance of Fe_3O_4-based tunnel junctions [12, 18, 19]. This suspicion is fueled by the finding that Fe_3O_4 seems to have a tendency to form an interface layer. If the exact circumstances of the formation of this interlayer and its magnetic properties could be understood, magnetoresistance measurements on a series of well-characterized Fe_3O_4/MgO /Fe_3O_4 junctions, prepared with and without interlayer, might shed light on the low tunneling spin-polarization of the half-metal magnetite.

A. Origin of XMCD

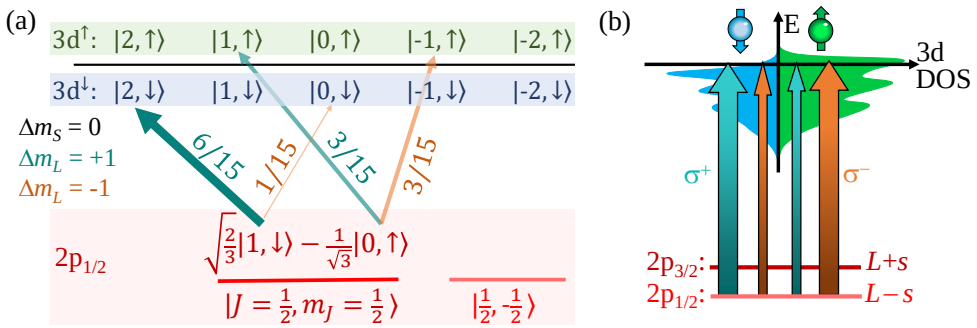

Fig. A.1: (a) Transition scheme from the $|J{=}1/2,m_J{=}1/2\rangle$ 2p state (red) into a 3d band without spin-orbit coupling ($m_S{=}\ 1/2$ states in green, $m_S{=}\ -1/2$ in blue). Cyan and orange arrows indicate transitions with σ^+ and σ^- x-rays, respectively. Numbers on arrows denote the respective transition probabilities. (b) Sketch of the excitation from a spin-orbit split 2p state into a spin-polarized 3d band without spin-orbit coupling.

In order to understand the origin of the XMCD effect, on top of the additional selection rules the matrix elements of the transitions have to be taken into account. An instructive example is offered in Fig. A.1(a), which shows the transition from a $2p_{1/2}$ state into a 3d band. For the simplicity of the argument, all multiplet effects are neglected for now (no Coulomb interaction between the electrons). The 2p spin-orbit interaction couples the orbital angular momentum $L = 1$ and the spin $S = 1/2$ to $J = 1/2$ and $J = 3/2$, represented by states of the form $|J, m_J\rangle$. Since in transition metals, the 3d spin-orbit coupling is typically weak (cf. Tab. 2.3), it is a qualitatively reasonable approximation to neglect the 3d spin-orbit coupling. The 3d states experience no spin-orbit coupling and remain in the LS basis. Such a 3d state is written short as $|L = 1, S = 1/2, m_L, m_S\rangle = |m_L, m_S\rangle$ in green for $m_S = 1/2 =\uparrow$ and in blue for $m_S = -1/2 =\downarrow$ in Fig. A.1(a). In order to enable transitions between these states, the J basis of the 2p states needs to be rewritten in the LS basis, as is done in the bottom of Fig. A.1(a) [193]. In the LS basis, the selection rules require $\Delta m_S = 0$ and $\Delta m_L = +1$ for σ^+ x-ray photons and $\Delta m_L = +1$ for σ^+ x-ray photons. Cyan and orange arrows indicate transitions using σ^+ and σ^- helicities, respectively. Each initial state in $2p_{1/2}$ has one allowed final state in the 3d band for both helicities, however, the transition probabilities are different[1]. This is visualized by the thicknesses of the arrows, and leads to an asymmetric excitation efficiency into the spin-up and spin-down band for the two helicities. Thus, a spin-polarization can be probed by comparing the two helicity channels.

[1] The matrix elements $|\langle L, m_L|\hat{p}|L, m_L\rangle|^2$ have been calculated to be [193]
$|\langle 2,2|\hat{p}^{\sigma+}|1,1\rangle|^2 = |\langle 2,-2|\hat{p}^{\sigma-}|1,-1\rangle|^2 = 6/15$
$|\langle 2,1|\hat{p}^{\sigma+}|1,0\rangle|^2 = |\langle 2,-1|\hat{p}^{\sigma-}|1,0\rangle|^2 = 3/15$
$|\langle 2,0|\hat{p}^{\sigma+}|1,-1\rangle|^2 = |\langle 2,0|\hat{p}^{\sigma-}|1,1\rangle|^2 = 1/15$

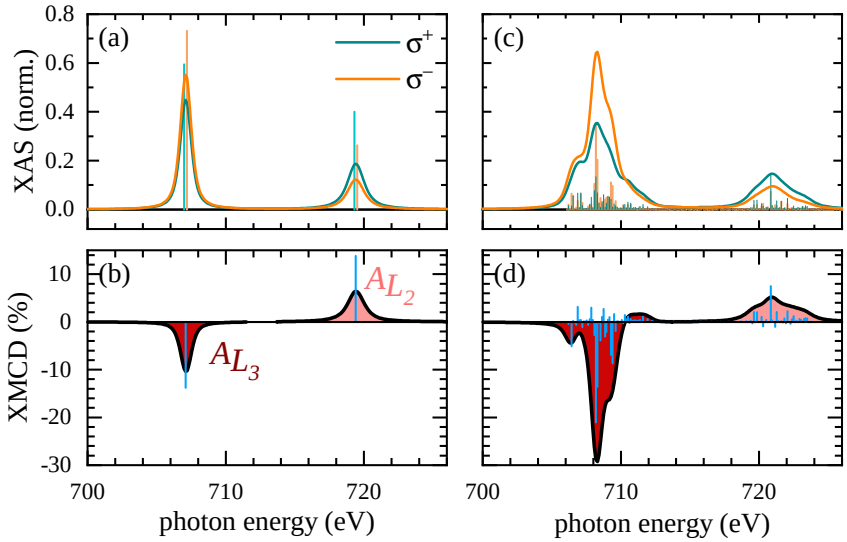

Fig. A.2: (a),(b) Multiplet calculations of the (a) XAS and (b) XMCD spectrum with only 2p spin-orbit coupling for an Fe^{2+} cation. (c),(d) Full CTM calculations of the (c) XAS and (d) XMCD spectra of a Fe^{2+}_{oct} cation. XA spectra are displayed for both σ^+ and σ^- helicities, normalized to the maximum of the unpolarized XA spectrum (cf. Eq. (2.41)). Dark red and light red shaded areas are the integreal below the L_3 and L_2 XMCD spectra, respectively.

The situation explained above applies for any atom, even non-magnetic ones. However, a non-magnetic sample will not yield an XMCD signal, because the orientation of the spins of the atoms will be random, and the probed electrons do not distinguish between the x-ray helicities. A finite XMCD signal is only found if the 3d states are spin-polarized in regards to the quantization axis. This is illustrated in Fig. A.1(b). The 3d band is spin-polarized and has more free spin-up ($m_S =\uparrow$) than spin-down ($m_S =\downarrow$) states at the Fermi energy. Electrons are excited by both helicities into both 3d bands, but with different efficiencies, so that a substraction of $I^{\sigma+} - I^{\sigma-}$ yields a finite signal. In the case of a Fe^{2+} cation with exclusively 2p spin-orbit coupling, which was discussed in Fig. A.1(a), the resulting XAS and XMCD spectra are shown in Figs. A.2(a),(b). Interestingly, the XAS ratio between L_3 and L_2 shows the typical $2:1$ ratio, but the XMCD ratio is $A_{L_3} : A_{L_2} = -1:1$ (dark and light red areas underneath the XMCD spectrum). To directly see this, it is necessary to work through all matrix elements for the transitions from all 6 states of $2p_{1/2}$ and $2p_{3/2}$, as exemplarily done for the $|1/2, 1/2\rangle$ state in Fig. A.1(a). However, an intuitive understanding is offered by the fact that $2p_{3/2}$ gathers the states with $J = L + S$ and $2p_{1/2}$ the states with $J = L - S$, and the $-$ sign in front of the spin S is exactly reflected in the XMCD spectrum. This $-1:1$ ratio remains true as long as the XMCD signal stems exclusively from the spin moment, but is lifted as soon as 3d spin-orbit coupling enters and a non-zero orbital moment emerges. Figures A.2(c),(d) show full CTM calculations of a Fe^{2+}_{oct} cation. The overall features remain the same, but the $A_{L_3} : A_{L_2}$ ratio changes and more spectral features occur.

Literature

[1] A. G. Roca, R. Costo, A. F. Rebolledo, S. V. Verdaguer, P. Tartaj, T. G. no, M. P. Morales and C. J. Serna. "Progress in the preparation of magnetic nanoparticles for applications in biomedicine". *J. Phys. D Appl. Phys.*, 42(22), 2009.

[2] R. Mejías, S. Pérez-Yagüe, L. Gutiérrez, L. I. Cabrera, R. Spada, P. Acedo, C. J. Serna, F. J. Lázaro, A. Villanueva, M. P. Morales and D. F. Barber. "Dimercaptosuccinic acid-coated magnetite nanoparticles for magnetically guided in vivo delivery of interferon gamma for cancer immunotherapy". *Biomaterials*, 32, 2938–2952, 2011.

[3] H. He, Y. Zhong, X. Liang, W. Tan, J. Zhu and C. Y. Wang. "Natural Magnetite: an efficient catalyst for the degradation of organic contaminant". *Sci. Rep.*, 5(10139), 2015.

[4] M. Munoz, Z. M. de Pedro, J. Casas and J. J. Rodriguez. "Preparation of magnetite-based catalysts and their application in heterogeneous Fenton oxidation - A review". *Appl. Catal. B*, 176-177, 249–265, 2015.

[5] Z. Zhang and S. Satpathy. "Electron states, magnetism, and the Verwey transition in magnetite". *Phys. Rev. B*, 44, 13319, 1991. doi:10.1103/PhysRevB.44.13319.

[6] W. Wang, J.-M. Mariot, M. C. Richter, O. Heckmann, W. Ndiaye, P. De Padova, A. Taleb-Ibrahimi, P. Le Fèvre, F. Bertran, F. Bondino, E. Magnano, J. Krempaský, P. Blaha, C. Cacho, F. Parmigiani and K. Hricovini. "Fe t_{2g} band dispersion and spin polarization in thin films of Fe_3O_4(0 0 1)/MgO(0 0 1): Half-metallicity of magnetite revisited". *Phys. Rev. B*, 87, 085118, 2013. doi:10.1103/PhysRevB.87.085118.

[7] J.-B. Moussy. "From epitaxial growth of ferrite thin films to spin-polarized tunnelling". *J. Phys. D Appl. Phys.*, 46, 143001, 2013. doi:10.1088/0022-3727/46/14/143001.

[8] J. M. D. Coey and C. L. Chien. "Half-Metallic Ferromagnetic Oxides". *MRS Bulletin*, 28, 720, 2003. doi:10.1557/mrs2003.212.

[9] M. Bibes and A. Bartheélemy. "Oxide spintronics". *IEEE Trans. Electron Devices*, 54, 1003, 2007. doi:10.1109/TED.2007.894366.

[10] I. Žutić, J. Fabian and S. D. Sarma. "Spintronics: Fundamentals and applications". *Rev. Mod. Phys.*, 76, 323, 2004. doi:10.1103/RevModPhys.76.323.

[11] J. A. Moyer, R. Gao, P. Schiffer and L. W. Martin. "Epitaxial growth of highly-crystalline spinel ferrite thin films on perovskite substrates for all-oxide devices". *Sci. Rep.*, 5, 10363, 2015.

[12] L. Marnitz, K. Rott, S. Niehörster, C. Klewe, D. Meier, S. Fabretti, M. Witziok, A. Krampf, O. Kuschel, T. Schemme, K. Kuepper, J. Wollschläger, A. Thomas, G. Reiss and T. Kuschel. "Sign change in the tunnel magnetoresistance of $Fe_3O_4/MgO/Co-Fe-B$ magnetic tunnel junctions depending on the annealing temperature and the interface treatment". *AIP Adv.*, 5, 047103, 2015. doi:10.1063/1.4917018.

[13] J. Fabian, A. Matos-Abiague, C. Ertler, P. Stano and Žutić. "Semiconductor Spintronics". *Acta Phys. Slov.*, 57, 565, 2007.

[14] E. Y. Tsymbal, O. N. Mryasov and P. R. LeClair. "Spin-dependent tunnelling in magnetic tunnel junctions". *J. Phys. Condens. Matter*, 15, R109, 2003. doi:10.1088/0953-8984/15/4/201.

[15] S. Datta and B. Das. "Electronic analog of the electrooptic modulator". *Appl. Phys. Lett.*, 56, 665, 1990. doi:10.1063/1.102730.

[16] H. C. Koo, J. H. Kwon, J. Eom, J. Chang, S. H. Han and M. Johnson. "Control of Spin Precession in a Spin-Injected Field Effect Transistor". *Science*, 325, 1515, 2009. doi:10.1126/science.1173667.

[17] P. van der Zaag, P. Bloemen, J. Gaines, R. Wolf, P. van der Heijden, R. van de Veerdonk and W. de Jonge. "On the construction of an Fe_3O_4-based all-oxide spin valve". *J. Magn. Magn. Mater.*, 211, 301, 2000. doi:10.1016/S0304-8853(99)00751-9.

[18] G. Hu and Y. Suzuki. "Negative Spin Polarization of Fe_3O_4 in Magnetite/Manganite-Based Junctions". *Phys. Rev. Lett.*, 89, 276601, 2002. doi:10.1103/PhysRevLett.89.276601.

[19] T. Kado. "Large room-temperature inverse magnetoresistance in tunnel junctions with a Fe_3O_4 electrode". *Appl. Phys. Lett.*, 92, 092502, 2008. doi:10.1063/1.2890852.

[20] P. LeClair, H. J. M. Swagten, J. T. Kohlhepp, R. J. M. van de Veerdonk and W. J. M. de Jonge. "Apparent Spin Polarization Decay in Cu-Dusted Co/Al_2O_3/Co Tunnel Junctions". *Phys. Rev. Lett.*, 84, 2933, 2000. doi:10.1103/PhysRevLett.84.2933.

[21] F. Bertram, C. Deiter, O. Hoefert, T. Schemme, F. Timmer, M. Suendorf, B. Zimmermann and J. Wollschläger. "X-ray diffraction study on size effects in epitaxial magnetite thin films on MgO(0 0 1)". *J. Phys. D Appl. Phys.*, 45, 395302, 2012. doi:10.1088/0022-3727/45/39/395302.

[22] O. Kuschel, W. Spiess, T. Schemme, J. Rubio-Zuazo, K. Kuepper and J. Wollschläger. "Real-time monitoring of the structure of ultrathin Fe_3O_4 films during growth on Nb-doped $SrTiO_3$(001)". *Appl. Phys. Lett.*, 111, 041902, 2017. doi:10.1063/1.4995408.

[23] K. Kuepper, O. Kuschel, N. Pathé, T. Schemme, J. Schmalhorst, A. Thomas, E. Arenholz, M. Gorgoi, R. Ovsyannikov, S. Bartkowski, G. Reiss and J. Wollschläger. "Electronic and magnetic structure of epitaxial Fe_3O_4(001)/NiO heterostructures grown on MgO(001) and Nb-doped $SrTiO_3$(001)". *Phys. Rev. B*, 94, 024401, 2016. doi:10.1103/PhysRevB.94.024401.

[24] C. Kittel. *Einführung in die Festkörperphysik*. Oldenbourg Verlag München Wien, 14. edition, 2006.

[25] A. Rockett. *Thin Film Growth Processes*, pages 455–503. Springer, Boston, MA, 2008. doi:10.1007/978-0-387-68650-9_10.

[26] J. M. D. Coey. *Magnetism and magnetic materials*. Cambridge University Press, The Edinburgh Building, Cambridge CB2 8RU, UK, 1. edition, 2009.

[27] F. de Groot. "X-ray absorption and dichroism of transition metals and their compounds". *J. Electron Spectros. Relat. Phenomena*, 67, 529, 1994. doi:10.1016/0368-2048(93)02041-J.

[28] F. de Groot. "Multiplet effects in X-ray spectroscopy". *Coord. Chem. Rev.*, 249, 31, 2005. doi:10.1016/j.ccr.2004.03.018.

[29] F. de Groot and A. Kotani. *Core Level Spectroscopy of Solids*. CRC Press, Taylor & Francis Group, 2008.

[30] S. Macke and E. Goering. "Magnetic reflectometry of heterostructures". *J. Phys. Condens. Matter*, 26, 363201, 2014. doi:10.1088/0953-8984/26/36/363201.

[31] J. Als-Nielsen and D. McMorrow. *Elements of Modern X-ray Physics*. John Wiley & Sons, Ltd, Chichester, 2. edition, 2011.

[32] I. K. Robinson and D. J. Tweet. "Surface X-ray diffraction". *Rep. Prog. Phys.*, 55, 599, 1992. doi:10.1088/0034-4885/55/5/002.

[33] R. Gross and A. Marx. *Festkörperphysik*. De Gruyter Oldenbourg, 2. edition, 2014.

[34] O. Kuschel, R. Buß, W. Spiess, T. Schemme, J. Wöllermann, K. Balinski, A. T. N'Diaye, T. Kuschel, J. Wollschläger and K. Kuepper. "From Fe_3O_4/NiO bilayers to $NiFe_2O_4$-like thin films through Ni interdiffusion". *Phys. Rev. B*, 94, 094423, 2016. doi:10.1103/PhysRevB.94.094423.

[35] J. Rodewald, J. Thien, T. Pohlmann, M. Hoppe, F. Timmer, F. Bertram, K. Kuepper and J. Wollschläger. "Formation of ultrathin cobalt ferrite films by interdiffusion of Fe_3O_4/CoO bilayers". *Phys. Rev. B*, 100, 155418, 2019. doi:10.1103/PhysRevB.100.155418.

[36] N.-T. Kim-Ngan, A. Balogh, J. Meyer, J. Brötz, M. Zajac, T. Ślezak and J. Korecki. "Thermal and irradiation induced interdiffusion in magnetite thin films grown on magnesium oxide (001) substrates". *Surf. Sci.*, 603, 1175, 2009. doi:10.1016/j.susc.2009.02.028.

[37] G. S. Parkinson, P. Lackner, O. Gamba, S. Maaß, S. Gerhold, M. Riva, R. Bliem, U. Diebold and M. Schmid. "$Fe_3O_4(110) - (1 \times 3)$ revisited: Periodic (111) nanofacets". *Surf. Sci.*, 649, L120, 2016. doi:10.1016/j.susc.2016.02.020.

[38] J. Lapujoulade and B. Salanon. *The Roughening Transition on Surfaces*, pages 217–246. Springer, Boston, MA, 1991. doi:10.1007/978-1-4684-5970-8_13.

[39] L. Pedemonte, G. Bracco and R. Tatarek. "A critical discussion about the roughening temperature estimation: the Ag(110) case". *Surf. Sci.*, 377-379, 524, 1997. doi:10.1016/S0039-6028(96)01430-6. European Conference on Surface Science.

[40] J. B. Maxson, D. E. Savage, F. Liu, R. M. Tromp, M. C. Reuter and M. G. Lagally. "Thermal Roughening of a Thin Film: A New Type of Roughening Transition". *Phys. Rev. Lett.*, 85, 2152–2155, 2000. doi:10.1103/PhysRevLett.85.2152.

[41] R. People and J. C. Bean. "Calculation for critical layer thickness versus lattice mismatch for Ge_xSi_{1-x}/Si strained-layer heterostructures". *Appl. Phys. Lett.*, 47, 322, 1985. doi:10.1063/1.96206.

[42] A. K. Lindquist, J. M. Feinberg, R. J. Harrison, J. C. Loudon and A. J. Newell. "Domain wall pinning and dislocations: Investigating magnetite deformed under conditions analogous to nature using transmission electron microscopy". *J. Geophys. Res. Solid Earth*, 120, 1415, 2015. doi:10.1002/2014JB011335.

[43] D. Chicot, J. Mendoza, A. Zaoui, G. Louis, V. Lepingle, F. Roudet and J. Lesage. "Mechanical properties of magnetite (Fe_3O_4), hematite (α-Fe_2O_3) and goethite (α-

FeO · OH) by instrumented indentation and molecular dynamics analysis". *Mater. Chem. Phys.*, 129, 862, 2011. doi:10.1016/j.matchemphys.2011.05.056.

[44] J. P. Hirth and X. Feng. "Critical layer thickness for misfit dislocation stability in multilayer structures". *J. Appl. Phys*, 67, 3343, 1990. doi:10.1063/1.345371.

[45] F. Y. Huang. "Theory of Strain Relaxation for Epitaxial Layers Grown on Substrate of a Finite Dimension". *Phys. Rev. Lett.*, 85, 784–787, 2000. doi:10.1103/PhysRevLett.85.784.

[46] M. Orchin, R. S. Macomber, A. Pinhas and R. M. Wilson. *Atomic Orbital Theory*, pages 3–17. John Wiley & Sons, Inc., Hoboken, New Jersey, 2005. doi:10.1002/0471713740.

[47] R. Shankar. *Principles of quantum mechanics*. Springer Science+Business Media, Inc., 233 Spring Street, New York, NY 10013, USA, 2. edition, 1994.

[48] B. Henke, E. Gullikson and J. Davis. "X-ray interactions: photoabsorption, scattering, transmission, and reflection at E=50-30000 eV, Z=1-92". *At. Data Nucl. Data Tables*, 54, 181–342, 1993. doi:10.1006/adnd.1993.1013.

[49] G. van der Laan. *Hitchhiker's Guide to Multiplet Calculations*, page 143. Springer Berlin Heidelberg, Berlin, Heidelberg, 2006. doi:10.1007/3-540-33242-1_7.

[50] M. Liska, P. Pelikán and L. Turi Nagy. "Systematic determination of the Slater-Condon parameters of atoms and ions with K(2)L(8)3sm3pn configurations". *Chem. Pap.*, 29, 577, 1975.

[51] P. S. Miedema and F. M. de Groot. "The iron L edges: Fe 2p X-ray absorption and electron energy loss spectroscopy". *J. Electron Spectros. Relat. Phenomena*, 187, 32, 2013. doi:10.1016/j.elspec.2013.03.005.

[52] M. Taguchi, A. Chainani, S. Ueda, M. Matsunami, Y. Ishida, R. Eguchi, S. Tsuda, Y. Takata, M. Yabashi, K. Tamasaku, Y. Nishino, T. Ishikawa, H. Daimon, S. Todo, H. Tanaka, M. Oura, Y. Senba, H. Ohashi and S. Shin. "Temperature Dependence of Magnetically Active Charge Excitations in Magnetite across the Verwey Transition". *Phys. Rev. Lett.*, 115, 256405, 2015. doi:10.1103/PhysRevLett.115.256405.

[53] T. Fujii, F. M. F. de Groot, G. A. Sawatzky, F. C. Voogt, T. Hibma and K. Okada. "In situ XPS analysis of various iron oxide films grown by NO_2-assisted molecular-beam epitaxy". *Phys. Rev. B*, 59, 3195–3202, 1999. doi:10.1103/PhysRevB.59.3195.

[54] SPECS GmbH. *PHOIBOS 100/150 - Manual*, 4.0 edition, 2012.

[55] S. Tanuma, C. J. Powell and D. R. Penn. "Calculations of electron inelastic mean free paths (IMFPS). IV. Evaluation of calculated IMFPs and of the predictive IMFP formula TPP-2 for electron energies between 50 and 2000 eV". *Surf. Interface Anal.*, 20, 77, 1993. doi:10.1002/sia.740200112.

[56] M. P. Seah and W. A. Dench. "Quantitative electron spectroscopy of surfaces: A standard data base for electron inelastic mean free paths in solids". *Surf. Interface Anal.*, 1, 2, 1979. doi:10.1002/sia.740010103.

[57] M. Trzhaskovskaya, V. Nefedov and V. Yarzhemsky. "Photoelectron angular distribution parameters for elements Z=1 to Z=54 in the photoelectron energy range 100-5000 eV". *At. Data Nucl. Data Tables*, 77, 97, 2001. doi:10.1006/adnd.2000.0849.

[58] J. Moulder. "The impact of the scanning XPS microprobe on industrial applications of X-ray photoelectron spectroscopy". *J. Electron Spectros. Relat. Phenomena*, 231, 43, 2019. doi:10.1016/j.elspec.2018.04.003.

[59] J. Rodewald, J. Thien, T. Pohlmann, M. Hoppe, F. Bertram, K. Kuepper and J. Wollschläger. "Real-time monitoring the growth of strained off-stoichiometric $Ni_xFe_{3-x}O_4$ ultrathin films on MgO(001)". *Appl. Phys. Lett.*, 117, 011601, 2020. doi:10.1063/5.0013925.

[60] J. Thien, J. Bahlmann, A. Alexander, M. Hoppe, T. Pohlmann, K. Ruwisch, C. Meyer, F. Bertram, K. Küpper and J. Wollschläger. "Effects of Post-deposition Annealing on Epitaxial CoO/Fe_3O_4 Bilayers on $SrTiO_3(001)$ and Formation of Thin High-Quality Cobalt Ferrite-like Films". *J. Phys. Chem. C*, 124, 23895, 2020. doi:10.1021/acs.jpcc.0c05503.

[61] V. N. Antonov, B. N. Harmon and A. N. Yaresko. "Electronic structure and x-ray magnetic circular dichroism in Fe_3O_4 and Mn-, Co−, or Ni-substituted Fe_3O_4". *Phys. Rev. B*, 67, 024417, 2003. doi:10.1103/PhysRevB.67.024417.

[62] S. Yamamoto, H. Yokogawa and H. Hashimoto. "Cylindrical Mirror Analyzer for Measuring Energy Spectrum of Photostimulated Exoelectrons". *Jpn. J. Appl. Phys*, 24, 281, 1985. doi:10.7567/jjaps.24s4.281.

[63] P. de Vera and R. Garcia-Molina. "Electron Inelastic Mean Free Paths in Condensed Matter Down to a Few Electronvolts". *J. Phys. Chem. C*, 123, 2075, 2019. doi:10.1021/acs.jpcc.8b10832.

[64] SPECS GmbH. *XR 50 NAP - Manual*, 3.1 edition, 2016.

[65] "μ-FOCUS 500/600 NAP", https://www.specs-group.com/nc/specs/products/detail/u-focus-500600-nap/, 2020.

[66] C. Schlueter, A. Gloskovskii, K. Ederer, I. Schostak, S. Piec, I. Sarkar, Y. Matveyev, P. Lömker, M. Sing, R. Claessen, C. Wiemann, C. M. Schneider, K. Medjanik, G. Schönhense, P. Amann, A. Nilsson and W. Drube. "The new dedicated HAXPES beamline P22 at PETRA III". *AIP Conf. Proc.*, 2054, 040010, 2019. doi:10.1063/1.5084611.

[67] C. T. Chantler. "X-Ray Form Factor, Attenuation, and Scattering Tables". *J. Phys. Chem Ref. Data*, 24, 71, 1995.

[68] C. T. Chantler. "Detailed Tabulation of Atomic Form Factors, Photoelectric Absorption and Scattering Cross Section, and Mass Attenuation Coefficients in the Vicinity of Absoprtion Edges in the Soft X-Ray (Z=30-36, Z=60-89, E=0.1 keV-10 keV), Adressing Convergence Issues of Earlier Work". *J. Phys. Chem. Ref. Data*, 29, 597, 2000. doi:10.1063/1.1321055.

[69] P. Zimmermann, S. Peredkov, P. M. Abdala, S. DeBeer, M. Tromp, C. Müller and J. A. van Bokhoven. "Modern X-ray spectroscopy: XAS and XES in the laboratory". *Coord. Chem. Rev.*, 423, 213466, 2020. doi:10.1016/j.ccr.2020.213466.

[70] Y. Chihiro, I. Hideshi, N. Koji, W. Iwao, K. Kazuo and O. Toshiaki. "Partial Fluorescence Yield XAFS Measurements in Soft X-ray Region Using a Large-Area Silicon Drift Detector". *AIP Conf. Proc.*, 14, 111, 2012.

[71] G. F. M. Gomes, T. E. P. Bueno, D. E. Parreiras, G. J. P. Abreu, A. de Siervo, J. C. Cezar, H.-D. Pfannes and R. Paniago. "Magnetic moment of Fe_3O_4

films with thicknesses near the unit-cell size". *Phys. Rev. B*, 90, 134422, 2014. doi:10.1103/PhysRevB.90.134422.

[72] T. J. Regan, H. Ohldag, C. Stamm, F. Nolting, J. Lüning, J. Stöhr and R. L. White. "Chemical effects at metal/oxide interfaces studied by x-ray-absorption spectroscopy". *Phys. Rev. B*, 64, 214422, 2001. doi:10.1103/PhysRevB.64.214422.

[73] R. M. Trevorah, C. T. Chantler and M. J. Schalken. "Solving self-absorption in fluorescence". *IUCrJ*, 6, 586, 2019. doi:10.1107/S2052252519005128.

[74] S. Eisebitt, T. Böske, J.-E. Rubensson and W. Eberhardt. "Determination of absorption coefficients for concentrated samples by fluorescence detection". *Phys. Rev. B*, 47, 14103–14109, 1993. doi:10.1103/PhysRevB.47.14103.

[75] F. de Groot, M. Arrio, P. Sainctavit, C. Cartier and C. Chen. "Distortions of X-ray absorption spectra measured with fluorescence yield". *Physica B Condens. Matter*, 208-209, 84, 1995. doi:10.1016/0921-4526(94)00638-C. Proceedings of the 8th International Conference on X-ray Absorption Fine Structure.

[76] R. Aeschlimann, D. Preziosi, P. Scheiderer, M. Sing, S. Valencia, J. Santamaria, C. Luo, H. Ryll, F. Radu, R. Claessen, C. Piamonteze and M. Bibes. "A Living-Dead Magnetic Layer at the Surface of Ferrimagnetic DyTiO3 Thin Films". *Adv. Mater.*, 30, 1707489, 2018. doi:10.1002/adma.201707489.

[77] M. Kallmayer, H. Schneider, G. Jakob, H. J. Elmers, K. Kroth, H. C. Kandpal, U. Stumm and S. Cramm. "Reduction of surface magnetism of Co2Cr0.6Fe0.4Al Heusler alloy films". *Appl. Phys. Lett.*, 88, 072506, 2006. doi:10.1063/1.2175486.

[78] M. Kallmayer, K. Hild, H. J. Elmers, S. K. Arora, H.-C. Wu, R. G. S. Sofin and I. V. Shvets. "Magnetic moment investigations of epitaxial magnetite thin films". *J. Appl. Phys.*, 103, 07D715, 2008. doi:10.1063/1.2838982.

[79] Y. Teramura, A. Tanaka and T. Jo. "Effect of Coulomb Interaction on the X-Ray Magnetic Circular Dichroism Spin Sum Rule in 3 d Transition Elements". *J. Phys. Soc. Jpn.*, 65, 1053, 1996. doi:10.1143/JPSJ.65.1053.

[80] C. F. Chang, Z. Hu, S. Klein, X. H. Liu, R. Sutarto, A. Tanaka, J. C. Cezar, N. B. Brookes, H.-J. Lin, H. H. Hsieh, C. T. Chen, A. D. Rata and L. H. Tjeng. "Dynamic Atomic Reconstruction: How Fe_3O_4 Thin Films Evade Polar Catastrophe for Epitaxy". *Phys. Rev. X*, 6, 041011, 2016. doi:10.1103/PhysRevX.6.041011.

[81] P. Carra, B. T. Thole, M. Altarelli and X. Wang. "X-ray circular dichroism and local magnetic fields". *Phys. Rev. Lett.*, 70, 694, 1993. doi:10.1103/PhysRevLett.70.694.

[82] C. T. Chen, Y. U. Idzerda, H.-J. Lin, N. V. Smith, G. Meigs, E. Chaban, G. H. Ho, E. Pellegrin and F. Sette. "Experimental Confirmation of the X-Ray Magnetic Circular Dichroism Sum Rules for Iron and Cobalt". *Phys. Rev. Lett.*, 75, 152, 1995. doi:10.1103/PhysRevLett.75.152.

[83] B. T. Thole, P. Carra, F. Sette and G. van der Laan. "X-ray circular dichroism as a probe of orbital magnetization". *Phys. Rev. Lett.*, 68, 1943, 1992. doi:10.1103/PhysRevLett.68.1943.

[84] D. J. Huang, C. F. Chang, H.-T. Jeng, G. Y. Guo, H.-J. Lin, W. B. Wu, H. C. Ku, A. Fujimori, Y. Takahashi and C. T. Chen. "Spin and Orbital Magnetic Moments of Fe_3O_4". *Phys. Rev. Lett.*, 93, 077204, 2004. doi:10.1103/PhysRevLett.93.077204.

[85] E. Goering, S. Gold, M. Lafkioti and G. Schütz. "Vanishing Fe 3d orbital moments in single-crystalline magnetite". *EPL*, 73, 97, 2006. doi:10.1209/epl/i2005-10359-8.

[86] L. Martín-García, R. Gargallo-Caballero, M. Monti, M. Foerster, J. F. Marco, L. Aballe and J. de la Figuera. "Spin and orbital magnetic moment of reconstructed $\sqrt{2}\times\sqrt{2}R45°$ magnetite(001)". *Phys. Rev. B*, 91, 020408, 2015. doi:10.1103/PhysRevB.91.020408.

[87] L. G. Parratt. "Surface Studies of Solids by Total Reflection of X-Rays". *Phys. Rev.*, 95, 359, 1954. doi:10.1103/PhysRev.95.359.

[88] L. Névot and P. Croce. "Caractérisation des surfaces par réflexion rasante de rayons X. Application á l'étude du polissage de quelques verres silicates". *Rev. Phys. Appl.*, 15, 761, 1980. doi:10.1051/rphysap:01980001503076100.

[89] F. Bertram. *Röntgenreflektometrie an ultradünnen Schichten.* Bachelor's thesis, Universität Osnabrück, 2007.

[90] C. Klewe, T. Kuschel, J.-M. Schmalhorst, F. Bertram, O. Kuschel, J. Wollschläger, J. Strempfer, M. Meinert and G. Reiss. "Static magnetic proximity effect in $Pt/Ni_{1-x}Fe_x$ bilayers investigated by x-ray resonant magnetic reflectivity". *Phys. Rev. B*, 93, 214440, 2016. doi:10.1103/PhysRevB.93.214440.

[91] W. H. Bragg and W. L. Bragg. "The reflection of X-rays by crystals". *Proc. Math. Phys. Eng. Sci.*, 88, 428, 1913. doi:10.1098/rspa.1913.0040.

[92] W. Friedrich, P. Knipping and M. Laue. "Interferenz-Erscheinungen bei Röntgenstrahlen". *Die Naturwissenschaften*, 346, 971, 1913. doi:10.1002/andp.19133461004.

[93] P. J. Brown, A. G. Fox, E. N. Maseln, M. A. O'Keefe and B. T. M. Willis. "Intensity of diffracted intensities". *International Tables for Crystallography*, C, 2006. doi:10.1107/97809553602060000600.

[94] F. Bertram. *The structure of ultrathin iron oxide films studied by x-ray diffraction.* Phd thesis, Universität Osnabrück, 2012.

[95] P. Scherrer. "Bestimmung der Größe und der inneren Struktur von Kolloidteilchen mittels Röntgenstrahlen". *Nachrichten von der Gesellschaft der Wissenschaften zu Götting, Mathematisch-Physikalische Klasse*, 1918, 98, 1918. doi:10.1007/978-3-662-33915-2_7.

[96] B. Ingham and M. Toney. *1 - X-ray diffraction for characterizing metallic films*, pages 3 – 38. Woodhead Publishing, 2014. doi:10.1533/9780857096296.1.3.

[97] R. M. Cornell and U. Schwertmann. *The Iron Oxides: Structure, Properties, Reactions, Occurences and Uses.* WILEY-VCH Verlag GmbH & Co. KGaA, Weinheim, 2. edition, 2003.

[98] K. Momma and F. Izumi. "VESTA 3 for three-dimensional visualization of crystal, volumetric and morphology data". *J. Appl. Crystallogr.*, 44, 1272, 2011. doi:10.1107/S0021889811038970.

[99] G. Ketteler, W. Weiss, W. Ranke and R. Schlögl. "Bulk and surface phases of iron oxides in an oxygen and water atmosphere at low pressure". *Phys. Chem. Chem. Phys.*, 3, 1114, 2001. doi:10.1039/B009288F.

[100] A. Rohatgi. "Webplotdigitizer: Version 4.4", https://automeris.io/WebPlotDigitizer, 2020.

[101] S. Alraddadi, W. Hines, T. Yilmaz, G. Gu and B. Sinkovic. "Structural phase diagram for ultra-thin epitaxial Fe_3O_4/MgO(001) films: thickness and oxygen pressure dependence". *J. Phys. Condens. Matter*, 28, 115402, 2016. doi:10.1088/0953-8984/28/11/115402.

[102] Y. Gao, Y. J. Kim and S. A. Chambers. "Preparation and charaterization of epitaxial iron oxide films". *J. Mater. Res.*, 13, 2003, 1998. doi:10.1557/JMR.1998.0281.

[103] T. Pollenske. *Untersuchung von elektronischen Transporteigenschaften an Magnetit- und Nickelferritschichten, Bachelor's thesis.* Bachelor's thesis, Universität Osnabrück, 2020.

[104] G. Tarrach, D. Bürgler, T. Schaub, R. Wiesendanger and H.-J. Güntherodt. "Atomic surface structure of Fe_3O_4(001) in different preparation stages studied by scanning tunneling microscopy". *Surf. Sci.*, 285, 1, 1993. doi:10.1016/0039-6028(93)90908-3.

[105] P. W. Tasker. "The stability of ionic crystal surfaces". *J. Phys. C: Solid State Phys.*, 12, 4977, 1979. doi:10.1088/0022-3719/12/22/036.

[106] C. Noguera. "Polar oxide surfaces". *J. Phys. Condens. Matter*, 12, R367, 2000. doi:10.1088/0953-8984/12/31/201.

[107] C. Wöll. "The chemistry and physics of zinc oxide surfaces". *Prog. Surf. Sci.*, 82, 55, 2007. doi:10.1016/j.progsurf.2006.12.002.

[108] R. Wiesendanger, I. V. Shvets, D. Bürgler, G. Tarrach, H. J. Güntherodt, J. M. D. Coey and S. Gräser. "Topographic and Magnetic-Sensitive Scanning Tunneling Microscope Study of Magnetite". *Science*, 255, 583, 1992. doi:10.1126/science.255.5044.583.

[109] S. Chambers and S. Joyce. "Surface termination, composition and reconstruction of Fe_3O_4(001) and γ-Fe_2O_3(001)". *Surf. Sci.*, 420, 111, 1999. doi:10.1016/S0039-6028(98)00657-8.

[110] R. Bliem, E. McDermott, P. Ferstl, M. Setvin, O. Gamba, J. Pavelec, M. A. Schneider, M. Schmid, U. Diebold, P. Blaha, L. Hammer and G. S. Parkinson. "Subsurface cation vacancy stabilization of the magnetite (001) surface". *Science*, 346, 1215, 2014. doi:10.1126/science.1260556.

[111] G. S. Parkinson. "Iron oxide surfaces". *Surf. Sci. Rep.*, 71, 272, 2016. doi:10.1016/j.surfrep.2016.02.001.

[112] M. L. Néel. "Propriétés magnétiques des ferrites ; ferrimagnétisme et antiferromagnétisme". *Ann. Phys.*, 12, 137, 1948. doi:10.1051/anphys/194812030137.

[113] Weiss, Pierre and Forrer, R. "La saturation absolue des ferromagnétiques et les lois d'approche en fonction du champ et de la température". *Ann. Phys.*, 10, 279, 1929. doi:10.1051/anphys/192910120279.

[114] V. C. Rakhecha and N. S. Murthy. "Spin-transfer due to covalency for the tetrahedral-site Fe^{3+} ions in Fe_3O_4". *J. Phys. C: Solid State Phys.*, 11, 4389, 1978. doi:10.1088/0022-3719/11/21/015.

[115] J. García and G. Subías. "The Verwey transition—a new perspective". *J. Phys. Condens. Matter*, 16, R145, 2004. doi:10.1088/0953-8984/16/7/r01.

[116] A. Rosencwaig. "Double Exchange and the Metal-Nonmetal Transition in Magnetite". *Phys. Rev.*, 181, 946, 1969. doi:10.1103/PhysRev.181.946.

[117] S. Celotto, W. Eerenstein and T. Hibma. "Characterization of anti-phase boundaries in epitaxial magnetite films". *Eur. Phys. J. B*, 36, 271, 2003. doi:10.1140/epjb/e2003-00344-7.

[118] M. A. Gilleo. "Superexchange Interaction Energy for Fe^{3+}-O^{2-}-Fe^{3+} Linkages". *Phys. Rev.*, 109, 777, 1958. doi:10.1103/PhysRev.109.777.

[119] P. D. Battle and A. K. Cheetham. "The magnetic structure of non-stoichiometric ferrous oxide". *J. Phys. C: Solid State Phys.*, 12, 337, 1979. doi:10.1088/0022-3719/12/2/021.

[120] C. Wilkinson, A. K. Cheetham, G. J. Long, P. D. Battle and D. A. O. Hope. "Polarized neutron diffraction and Moessbauer effect study of the magnetic ordering in wustite, FeyO". *Inorg. Chem.*, 23, 3136, 1984. doi:10.1021/ic00188a023.

[121] H. Bowen, D. Adler and B. Auker. "Electrical and optical properties of FeO". *J. Solid State Chem.*, 12, 355, 1975. doi:10.1016/0022-4596(75)90340-0.

[122] A. N. Shmakov, G. N. Kryukova, S. V. Tsybulya, A. L. Chuvilin and L. P. Solovyeva. "Vacancy Ordering in γ-Fe_2O_3: Synchrotron X-ray Powder Diffraction and High-Resolution Electron Microscopy Studies". *J. Appl. Crystallogr.*, 28, 141, 1995. doi:10.1107/S0021889894010113.

[123] R. Grau-Crespo, A. Y. Al-Baitai, I. Saadoune and N. H. D. Leeuw. "Vacancy ordering and electronic structure of γ-Fe_2O_3(maghemite): a theoretical investigation". *J. Phys. Condens. Matter*, 22, 255401, 2010. doi:10.1088/0953-8984/22/25/255401.

[124] A. U. Gehring, H. Fischer, M. Louvel, K. Kunze and P. G. Weidler. "High temperature stability of natural maghemite: a magnetic and spectroscopic study". *Geophysical Journal International*, 179, 1361, 2009. doi:10.1111/j.1365-246X.2009.04348.x.

[125] T. Yamashita and P. Hayes. "Analysis of XPS spectra of Fe2+ and Fe3+ ions in oxide materials". *Appl. Surf. Sci.*, 254, 2441, 2008. doi:10.1016/j.apsusc.2007.09.063.

[126] T. Pohlmann, T. Kuschel, J. Rodewald, J. Thien, K. Ruwisch, F. Bertram, E. Weschke, P. Shafer, J. Wollschläger and K. Küpper. "Cation- and lattice-site-selective magnetic depth profiles of ultrathin Fe_3O_4(001) films". *Phys. Rev. B*, 102, 220411, 2020. doi:10.1103/PhysRevB.102.220411.

[127] W. L. Roth. "Neutron and Optical Studies of Domains in NiO". *J. Appl. Phys*, 31, 2000, 1960. doi:10.1063/1.1735486.

[128] G. R. Hoogeboom, A. Aqeel, T. Kuschel, T. T. M. Palstra and B. J. van Wees. "Negative spin Hall magnetoresistance of Pt on the bulk easy-plane antiferromagnet NiO". *Appl. Phys. Lett.*, 111, 052409, 2017. doi:10.1063/1.4997588.

[129] G. A. Sawatzky and J. W. Allen. "Magnitude and Origin of the Band Gap in NiO". *Phys. Rev. Lett.*, 53, 2339, 1984. doi:10.1103/PhysRevLett.53.2339.

[130] J. Keller, P. Miltényi, B. Beschoten, G. Güntherodt, U. Nowak and K. D. Usadel. "Domain state model for exchange bias. II. Experiments". *Phys. Rev. B*, 66, 014431, 2002. doi:10.1103/PhysRevB.66.014431.

[131] C. Gatel, E. Snoeck, V. Serin and A. Fert. "Epitaxial growth and magnetic exchange anisotropy in Fe_3O_4/NiO bilayers grown on MgO(001) and Al_2O_3(0001)". *Eur. Phys. J. B*, 45, 157–168, 2005. doi:10.1140/epjb/e2005-00073-y.

[132] I. P. Krug, F. U. Hillebrecht, M. W. Haverkort, A. Tanaka, L. H. Tjeng, H. Gomonay, A. Fraile-Rodríguez, F. Nolting, S. Cramm and C. M. Schneider. "Impact of

interface orientation on magnetic coupling in highly ordered systems: A case study of the low-indexed Fe_3O_4/NiO interfaces". *Phys. Rev. B*, 78, 064427, 2008. doi:10.1103/PhysRevB.78.064427.

[133] M. Pilard, O. Ersen, S. Cherifi, B. Carvello, L. Roiban, B. Muller, F. Scheurer, L. Ranno and C. Boeglin. "Magnetic properties of coupled ultrathin NiO/Fe_3O_4 (001) films". *Phys. Rev. B*, 76, 214436, 2007. doi:10.1103/PhysRevB.76.214436.

[134] R. H. Kodama, S. A. Makhlouf and A. E. Berkowitz. "Finite Size Effects in Antiferromagnetic NiO Nanoparticles". *Phys. Rev. Lett.*, 79, 1393, 1997. doi:10.1103/PhysRevLett.79.1393.

[135] E. Winkler, R. D. Zysler, M. V. Mansilla and D. Fiorani. "Surface anisotropy effects in NiO nanoparticles". *Phys. Rev. B*, 72, 132409, 2005. doi:10.1103/PhysRevB.72.132409.

[136] L. Li, L. Chen, R. Qihe and G. Li. "Magnetic crossover of NiO nanocrystals at room temperature". *Appl. Phys. Lett.*, 89, 134102, 2006. doi:10.1063/1.2357562.

[137] P. Ravikumar, B. Kisan and A. Perumal. "Enhanced room temperature ferromagnetism in antiferromagnetic NiO nanoparticles". *AIP Adv.*, 5, 087116, 2015. doi:10.1063/1.4928426.

[138] N. Rinaldi-Montes, P. Gorria, D. MartÃnez-Blanco, A. B. Fuertes, I. Puente-Orench, L. Olivi and J. A. Blanco. "Size effects on the NÃ©el temperature of antiferromagnetic NiO nanoparticles". *AIP Adv.*, 6, 056104, 2016. doi:10.1063/1.4943062.

[139] J. Fischer, O. Gomonay, R. Schlitz, K. Ganzhorn, N. Vlietstra, M. Althammer, H. Huebl, M. Opel, R. Gross, S. T. B. Goennenwein and S. Geprägs. "Spin Hall magnetoresistance in antiferromagnet/heavy-metal heterostructures". *Phys. Rev. B*, 97, 014417, 2018. doi:10.1103/PhysRevB.97.014417.

[140] M. Kurth, P. Graat and E. Mittemeijer. "The oxidation kinetics of magnesium at low temperatures and low oxygen partial pressures". *Thin Solid Films*, 500, 61, 2006. doi:10.1016/j.tsf.2005.11.044.

[141] J. M. D. Coey, M. Venkatesan and P. Stamenov. "Surface magnetism of strontium titanate". *J. Phys.: Condens. Matter*, 28, 485001, 2016. doi:10.1088/0953-8984/28/48/485001.

[142] J. Rodewald. *Advancement of growth and characteristics of ultrathin ferrite films*. Phd thesis, Universität Osnabrück, 2020.

[143] M. Monti, M. Sanz, M. Oujja, E. Rebollar, M. Castillejo, F. J. Pedrosa, A. Bollero, J. Camarero, J. L. F. Cuñado, N. M. Nemes, F. J. Mompean, M. Garcia-Hernández, S. Nie, K. F. McCarty, A. T. N'Diaye, G. Chen, A. K. Schmid, J. F. Marco and J. de la Figuera. "Room temperature in-plane ⟨100⟩ magnetic easy axis for Fe3O4/SrTiO3(001):Nb grown by infrared pulsed laser deposition". *J. Appl. Phys*, 114, 223902, 2013. doi:10.1063/1.4837656.

[144] F. Bertram, C. Deiter, K. Pflaum, M. Suendorf, C. Otte and J. Wollschläger. "In-situ x-ray diffraction studies on post-deposition vacuum-annealing of ultra-thin iron oxide films". *J. Appl. Phys*, 110, 102208, 2011. doi:10.1063/1.3661655.

[145] F. Bertram, C. Deiter, T. Schemme, S. Jentsch and J. Wollschläger. "Reordering between tetrahedral and octahedral sites in ultrathin magnetite films grown on MgO(001)". *J. Appl. Phys*, 113, 184103, 2013. doi:10.1063/1.4803894.

[146] D. T. Margulies, F. T. Parker, M. L. Rudee, F. E. Spada, J. N. Chapman, P. R. Aitchison and A. E. Berkowitz. "Origin of the Anomalous Magnetic Behavior in Single Crystal Fe_3O_4 Films". *Phys. Rev. Lett.*, 79, 5162, 1997. doi:10.1103/PhysRevLett.79.5162.

[147] J. G. Tobin, S. A. Morton, S. W. Yu, G. D. Waddill, I. K. Schuller and S. A. Chambers. "Spin resolved photoelectron spectroscopy of Fe_3O_4: the case against half-metallicity". *J. Phys. Condens. Matter*, 19, 315218, 2007. doi:10.1088/0953-8984/19/31/315218.

[148] S. K. Arora, H. Wu, H. Yao, W. Y. Ching, R. J. Choudhary, I. V. Shvets and O. N. Mryasov. "Magnetic Properties of Ultrathin Magnetite Films Grown by Molecular Beam Epitaxy". *IEEE Trans. Magn.*, 44, 2628, 2008. doi:10.1109/TMAG.2008.2003173.

[149] S. Kale, S. M. Bhagat, S. E. Lofland, T. Scabarozi, S. B. Ogale, A. Orozco, S. R. Shinde, T. Venkatesan, B. Hannoyer, B. Mercey and W. Prellier. "Film thickness and temperature dependence of the magnetic properties of pulsed-laser-deposited Fe_3O_4 films on different substrates". *Phys. Rev. B*, 64, 205413, 2001. doi:10.1103/PhysRevB.64.205413.

[150] J. Rubio-Zuazo, L. Onandia, E. Salas-Colera, A. Muñoz Noval and G. R. Castro. "Incommensurate Growth of Thin and Ultrathin Films of Single-Phase $Fe_3O_4(001)$ on $SrTiO_3(001)$". *J. Phys. Chem. C*, 119, 1108, 2015. doi:10.1021/jp510615j.

[151] W. Eerenstein, T. T. M. Palstra, T. Hibma and S. Celotto. "Origin of the increased resistivity in epitaxial Fe_3O_4 films". *Phys. Rev. B*, 66, 201101, 2002. doi:10.1103/PhysRevB.66.201101.

[152] W. Eerenstein, T. T. M. Palstra, S. S. Saxena and T. Hibma. "Spin-Polarized Transport across Sharp Antiferromagnetic Boundaries". *Phys. Rev. Lett.*, 88, 247204, 2002. doi:10.1103/PhysRevLett.88.247204.

[153] T. Hibma, F. C. Voogt, L. Niesen, P. A. A. van der Heijden, W. J. M. de Jonge, J. J. T. M. Donkers and P. J. van der Zaag. "Anti-phase domains and magnetism in epitaxial magnetite layers". *J. Appl. Phys*, 85, 5291, 1999. doi:10.1063/1.369857.

[154] G. J. Strijkers, J. T. Kohlhepp, P. A. A. van der Heijden, H. J. M. Swagten, W. J. M. de Jonge and J. M. Gaines. "Magnetization of Fe_3O_4/MgO multilayers studied with Mössbauer spectroscopy". *J. Appl. Phys*, 85, 5294, 1999. doi:10.1063/1.369858.

[155] W. Eerenstein, T. T. M. Palstra, T. Hibma and S. Celotto. "Diffusive motion of antiphase domain boundaries in Fe_3O_4 films". *Phys. Rev. B*, 68, 014428, 2003. doi:10.1103/PhysRevB.68.014428.

[156] K. P. McKenna, F. Hofer, D. Gilks, C. Chen, Z. Wang and Y. Ikuhara. "Atomic-scale structure and properties of highly stable antiphase boundary defects in Fe_3O_4". *Nat. Commun.*, 5, 599, 2014. doi:10.1038/ncomms6740.

[157] A. V. Singh, B. Khodadadi, J. B. Mohammadi, S. Keshavarz, T. Mewes, D. S. Negi, R. Datta, Z. Galazka, R. Uecker and A. Gupta. "Bulk Single Crystal-Like Structural and Magnetic Characteristics of Epitaxial Spinel Ferrite Thin Films with Elimination of Antiphase Boundaries". *Adv. Mater.*, 29, 1701222, 2017. doi:10.1002/adma.201701222.

[158] M. Luysberg, R. G. S. Sofin, S. K. Arora and I. V. Shvets. "Strain relaxation in $Fe_3O_4/MgAl_2O_4$ heterostructures: Mechanism for formation of antiphase boundaries in an epitaxial system with identical symmetries of film and substrate". *Phys. Rev. B*, 80, 024111, 2009. doi:10.1103/PhysRevB.80.024111.

[159] S. Gota, E. Guiot, M. Henriot and M. Gautier-Soyer. "Atomic-oxygen-assisted MBE growth of $\alpha-Fe_2O_3$ on $\alpha-Al_2O_3(0001)$: Metastable FeO(111)-like phase at subnanometer thicknesses". *Phys. Rev. B*, 60, 14387, 1999. doi:10.1103/PhysRevB.60.14387.

[160] J. Karunamuni, R. L. Kurtz and R. L. Stockbauer. "Growth of iron oxide on Cu(001) at elevated temperature". *Surf. Sci.*, 442, 223, 1999. doi:10.1016/S0039-6028(99)00921-8.

[161] G. Waddill and O. Ozturk. "Epitaxial growth of iron oxide films on Ag(111)". *Surf. Sci.*, 575, 35, 2005. doi:10.1016/j.susc.2004.10.050.

[162] C. Schlueter, M. Lübbe, A. Gigler and W. Moritz. "Growth of iron oxides on Ag(111) - Reversible Fe2O3/Fe3O4 transformation". *Surf. Sci.*, 605, 1986, 2011. doi:10.1016/j.susc.2011.07.019.

[163] ebmpapst. "Make it quick", https://mag.ebmpapst.com/en/industries/refrigeration-ventilation/fan-upgrade-diamond-light-source_8651/, 2014.

[164] H. Wang, P. Bencok, P. Steadman, E. Longhi, J. Zhu and Z. Wang. "Complete polarization analysis of an APPLE II undulator using a soft X-ray polarimeter". *J. Synchrotron Radiat.*, 19, 944, 2012. doi:10.1107/S0909049512034851.

[165] S. Sasaki. "Analyses for a planar variably-polarizing undulator". *Nucl. Instrum. Methods. Phys. Res. B*, 347, 83, 1994. doi:10.1016/0168-9002(94)91859-7.

[166] U. Englisch, H. Rossner, H. Maletta, J. Bahrdt, S. Sasaki, F. Senf, K. Sawhney and W. Gudat. "The elliptical undulator UE46 and its monochromator beam-line for structural research on nanomagnets at BESSY-II". *Nucl. Instrum. Methods. Phys. Res. B*, 467-468, 541, 2001. doi:10.1016/S0168-9002(01)00407-7. 7th Int.Conf. on Synchrotron Radiation Instrumentation.

[167] SPECS GmbH. *EBE-1 Single Pocket Electron Beam Evaporator - Manual*, 2.3 edition, 2013.

[168] T. Schemme, O. Kuschel, F. Bertram, K. Kuepper and J. Wollschläger. "Structure and morphology of epitaxially grown Fe_3O_4/NiO bilayers on MgO(001)". *Thin Solid Films*, 589, 526, 2015. doi:10.1016/j.tsf.2015.06.018.

[169] J. Rodewald, J. Thien, T. Pohlmann, M. Hoppe, F. Timmer, F. Bertram, K. Kuepper and J. Wollschläger. "Formation of ultrathin cobalt ferrite films by interdiffusion of Fe_3O_4/CoO bilayers". *Phys. Rev. B*, 100, 155418, 2019. doi:10.1103/PhysRevB.100.155418.

[170] picclick.de. "Flex-Wellbalg-ISO-K_DN100-Edeltstahl-L", https://picclick.de/Flex-Wellbalg-ISO-K-DN100-Edelstahl-L%C3%A4nge-200-mm-173631280592.html, 2020.

[171] N. Schell, A. King, F. Beckmann, T. Fischer, M. Müller and A. Schreyer. "The High Energy Materials Science Beamline (HEMS) at PETRA III". In "Mechanical Stress Evaluation by Neutrons and Synchrotron Radiation VI", volume 772 of *Materials Science Forum*, pages 57–61. Trans Tech Publications Ltd, 2014. doi:10.4028/www.scientific.net/MSF.772.57.

[172] J. Gustafson, M. Shipilin, C. Zhang, A. Stierle, U. Hejral, U. Ruett, O. Gutowski, P.-A. Carlsson, M. Skoglundh and E. Lundgren. "High-Energy Surface X-ray Diffraction for Fast Surface Structure Determination". *Science*, 343, 758, 2014. doi:10.1126/science.1246834.

[173] E. Weschke and E. Schierle. "The UE46 PGM-1 beamline at BESSY II". *Journal of large-scale research facilities*, 4, A127, 2018. doi:10.17815/jlsrf-4-77.

[174] D. A. Shirley. "High-Resolution X-Ray Photoemission Spectrum of the Valence Bands of Gold". *Phys. Rev. B*, 5, 4709, 1972. doi:10.1103/PhysRevB.5.4709.

[175] A. E. Bocquet, T. Mizokawa, K. Morikawa, A. Fujimori, S. R. Barman, K. Maiti, D. D. Sarma, Y. Tokura and M. Onoda. "Electronic structure of early 3d-transition-metal oxides by analysis of the 2p core-level photoemission spectra". *Phys. Rev. B*, 53, 1161, 1996. doi:10.1103/PhysRevB.53.1161.

[176] M. Suendorf. *Investigation of the growth process of thin iron oxide films: Analysis of X-ray Photoemission Spectra by Charge Transfer Multiplet calculations.* Phd thesis, Universität Osnabrück, 2012.

[177] G. van der Laan. "Theory of simple spectra". *J. Electron Spectros. Relat. Phenomena*, 86, 41, 1997. doi:10.1016/S0368-2048(97)00047-9.

[178] E. Stavitski and F. M. de Groot. "The CTM4XAS program for EELS and XAS spectral shape analysis of transition metal L edges". *Micron*, 41, 687, 2010. doi:10.1016/j.micron.2010.06.005.

[179] M. I. Litter and M. A. Blesa. "Photodissolution of iron oxides. IV. A comparative study on the photodissolution of hematite, magnetite, and maghemite in EDTA media". *Can. J. Chem.*, 70, 2502, 1992. doi:10.1139/v92-316.

[180] L. Pauling and S. B. Hendricks. "The crystal structure of hematite and corundum". *J. Am. Chem. Soc.*, 47, 781, 1925. doi:10.1021/ja01680a027.

[181] F. Koch and J. B. Cohen. "The defect structure of $Fe_{1-x}O$". *Acta Crystallogr., Sect. B: Struct. Sci., Cryst. Eng. Mater.*, 25, 275, 1969. doi:10.1107/S0567740869002111.

[182] H. Yanagihara, M. Hasegawa, E. Kita, Y. Wakabayashi, H. Sawa and K. Siratori. "Iron Vacancy Ordered γ-Fe_2O_3(001) Epitaxial Films: The Crystal Structure and Electrical Resistivity". *J. Phys. Soc. Jpn.*, 75, 054708, 2006. doi:10.1143/JPSJ.75.054708.

[183] R. Takahashi, H. Misumi and M. Lippmaa. "Self-Template Growth of Orientation-Controlled Fe3O4 Thin Films". *Cryst. Growth Des.*, 12, 2679, 2012. doi:10.1021/cg300287r.

[184] R. Takahashi, H. Misumi and M. Lippmaa. "Growth temperature effect on the structural and magnetic properties of Fe3O4 films grown by the self-template method". *J. Appl. Phys*, 116(3), 033918, 2014. doi:10.1063/1.4890510.

[185] M. Roelsgaard, A.-C. Dippel, K. A. Borup, I. G. Nielsen, N. L. N. Broge, J. T. Röh, O. Gutowski and B. B. Iversen. "Time-resolved grazing-incidence pair distribution functions during deposition by radio-frequency magnetron sputtering". *IUCrJ*, 6, 299, 2019. doi:10.1107/S2052252519001192.

[186] G. Renaud, R. Lazzari and F. Leroy. "Probing surface and interface morphology with Grazing Incidence Small Angle X-Ray Scattering". *Surf. Sci. Rep.*, 64(8), 255, 2009. doi:10.1016/j.surfrep.2009.07.002.

[187] Z. Jiang. "Theory of GISAXS". Lecture, 2014.

[188] R. F. C. Farrow, M. J. Carey, R. F. Marks, P. M. Rice and D. J. Smith. "Enhanced blocking temperature in NiO spin valves: Role of cubic spinel ferrite layer between pinned layer and NiO". *Appl. Phys. Lett.*, 77, 1191, 2000. doi:10.1063/1.1289660.

[189] G. Mariotto, S. Murphy and I. V. Shvets. "Charge ordering on the surface of $Fe_3O_4(001)$". *Phys. Rev. B*, 66, 245426, 2002. doi:10.1103/PhysRevB.66.245426.

[190] T. Kuschel, C. Klewe, J.-M. Schmalhorst, F. Bertram, O. Kuschel, T. Schemme, J. Wollschläger, S. Francoual, J. Strempfer, A. Gupta, M. Meinert, G. Götz, D. Meier and G. Reiss. "Static Magnetic Proximity Effect in $Pt/NiFe_2O_4$ and Pt/Fe Bilayers Investigated by X-Ray Resonant Magnetic Reflectivity". *Phys. Rev. Lett.*, 115, 097401, 2015. doi:10.1103/PhysRevLett.115.097401.

[191] P. van der Heijden, P. Bloemen, J. Gaines, J. van Eemeren, R. Wolf, P. van der Zaag and W. de Jonge. "Magnetic interface anisotropy of MBE-grown ultra-thin (001) Fe_3O_4 layers". *J. Magn. Magn. Mater.*, 159, L293, 1996. doi:10.1016/0304-8853(96)00376-9.

[192] Y. Zhou, C. McEvoy, R. Ramos and I. V. Shvets. "The magnetic and magnetoresistance properties of ultrathin magnetite films grown on MgO substrate". *J. Appl. Phys*, 99, 08J111, 2006. doi:10.1063/1.2176313.

[193] S. Pizzini. "X-ray magnetic circular dichroism: basic concepts and theory for rare earths and 3d metals". Lecture, 2003.

Danksagung

Vielen Dank an all die Leute, die mir bei dieser Arbeit geholfen haben! Und das sind eine ganze Menge. Zuallererst geht mein herzlichster Dank an meinen lieben Professor, Joachim Wollschläger, der sich immer – oder sagen wir: meistens – geduldig mein Bedenkenträgertum über meine Daten angehört und mit messerscharfem Auge meine Arbeiten durchgesehen hat; was manchmal wirklich bitter nötig war. Aber nicht nur seine fachliche Hilfe war etwas Besonderes: Wir beide haben zusammen auch zwei wunderbare Indienurlaube verbracht, in denen wir uns entweder Tempel, Eisenbahnen oder alte Städte hoch im berauschend schönen Himalaja angesehen oder uns an laufend nachgeliefertem Kardamom-Chai im Physiklabor gütlich getan haben, während Kanchan uns zeigen musste, wie man Magnetgelee kocht – wer feiern kann, der kann auch anderen bei der Arbeit zugucken. Ich bin sehr, sehr glücklich, einen solchen Doktorvater gehabt zu haben[2].

Ebenso wertvoll war mir mein großes Vorbild Florian Bertram, der mich an meinem Arbeitsplatz am DESY angeleitet hat, und immer mein erster Ansprechpartner war für alle Beugungsfragen, aber eigentlich auch für alles andere. Zusammen haben wir außerdem zig Messzeiten durchgemacht, die später in meine Arbeit gingen, und ohne die ich nicht so weit gekommen wäre – oder, noch schlimmer, noch mehr Forschung an Magneten hätte machen müssen. Aber im Ernst, ich kann schwer in Worte fassen, was für ein fantastischer, zuverlässiger Betreuer Florian war, der innerhalb kürzester Zeit jede noch so alberne Frage oder Anfrage gewürdigt hat. Im Übrigen muss ihm zu Gute gehalten werden, dass er die neunschwänzige BNC-Peitsche, von der er seit Jahren träumt, nie zum Einsatz gebracht hat.

Außerdem möchte ich mich sehr herzlich bei Karsten Küpper bedanken, der mir Ladungstransfer-Multiplett-Rechnungen beigebracht hat und mit mir im Russlandurlaub war, und bei Robin Steinigeweg, der sich sofort bereit erklärt hat, an meiner Prüfungskommission teilzunehmen, obwohl er mich noch nie gesehen hat. Vielen Dank dafür, das weiß ich sehr zu schätzen.

Mein nächster Dank muss unbedingt an meinen Büro- und Labor- und eigentlich Universalkollegen Martin Hoppe gehen, der mit mir am DESY gemeinsam unsere schöne gute Kammer aufgebaut hat, und mit dem zusammen ich viele Nächte Eisen beim Verdampfen zugesehen habe. Auch tausend Dank an all die anderen lieben Kollegen am DESY, an Jan Röh, Olof Gutowski und René Kirchhof, die unerlässliche Hilfen für unsere P07-Experimente waren, und an meine P08-Kollegen Sergey Volkov, Chen Shen und Arka Dey, und an Oliver Seeck und an Sonia Francoual, und all die anderen, die ich nicht alle aufzählen kann.

Aber auch wenn ich selbst fast immer am DESY war, so war wenigstens mein halbes Herz auch stets bei meinen tollen Kollegen in Osnabrück, allen voran bei Jannis Thien und Jari Rodewald, mit denen ich viel zu viele viel zu schöne Messzeiten verbracht habe, und mit denen ich mich, auch nachdem Corona die Kneipen dicht gemacht hatte, noch jede Woche im Internet getroffen habe, wo wir uns weiter über unsere Doktorarbeiten austauschten, zusammen weinten und lacht... naja, schon vor allem weinten. Außerdem schönsten Dank an Kevin Ruwisch, dessen seelischen Beistand vor allem am ESRF ich niemals vergessen werde, und an Gregor Steinhoff, bei dem unser Förderkoffer stand und der immer die Scherereien hatte, wenn wir in Hamburg was einkaufen wollten. Aber auch allen anderen AG Woll-Schlägertypen mein herzlichster Dank: Wann immer ich bei euch war, war es wie nach Hause

[2] Naja, noch bin ich ja nicht ganz durch, also sagen wir: einen solchen Doktorvater gehabt haben zu werden.

zu kommen. Außerdem habe ich dauernd euren Kaffee getrunken, meistens ohne was in die Kasse zu tun. Und ein besonderer Dank geht an meinen Teilzeitmentor Timo Kuschel, der mich erst an XRMR herangeführt hat und für alle Magnetfragen zur Verfügung stand – unsere Beziehung fühlte sich eigentlich meist dergestalt an, dass er mich wie einen Gaul vor seinen Karren spannte, aber mir als Ausgleich auch immer mal ein paar Mohrrüben zufütterte. Im Rückblick habe ich aber einen großen Teil meiner Doktorstrecke als Gaul vor seinem XRMR-Karren zurückgelegt, und dafür möchte ich ihm herzlich danken.

Zuletzt möchte ich mich bei meinem Vater und meiner Mutter bedanken für ihr Verständnis dafür, dass ich nichts Ordentliches gelernt habe und stattdessen 30 Jahre zur Schule gegangen bin, und am allermeisten vielen Dank an meine liebe, liebe Frau Elin, die meine viele Abwesenheit während der Messzeiten ertragen musste und – womöglich schlimmer – meine viele Anwesenheit während des Zusammenschreibens. Du bist die Schönste und die Beste!